AD
# 746638

DISCLAIMER NOTICE

THIS DOCUMENT IS THE BEST
QUALITY AVAILABLE.

COPY FURNISHED CONTAINED
A SIGNIFICANT NUMBER OF
PAGES WHICH DO NOT
REPRODUCE LEGIBLY.

DOCUMENT CONTROL DATA - R & D

(Security classification of title, body of abstract and indexing annotation must be entered when the overall report is classified)

1 ORIGINATING ACTIVITY (Corporate author)	2a. REPORT SECURITY CLASSIFICATION
Division of Engineering and Applied Physics Harvard University Cambridge, Massachusetts	Unclassified
	2b. GROUP

3 REPORT TITLE

THE STRUCTURE OF TETRAHEDRALLY COORDINATED AMORPHOUS SEMICONDUCTORS

4. DESCRIPTIVE NOTES (Type of report and inclusive dates)
Interim technical report

5. AUTHOR(S) (First name, middle initial, last name)

Nigel J. Shevchik

6 REPORT DATE	7a. TOTAL NO. OF PAGES	7b. NO. OF REFS
July 1972	355	204

8a. CONTRACT OR GRANT NO.	9a. ORIGINATOR'S REPORT NUMBER(S)
N00014-67-A-0298-0012 and ARPA	
b. PROJECT NO. DAHC 15-67-C-0219	Technical Report No. HP-29 Technical Report No. ARPA-44
c.	9b. OTHER REPORT NO(S) (Any other numbers that may be assigned this report)
d.	

10 DISTRIBUTION STATEMENT

Reproduction in whole or in part is permitted by the U. S. Government. Distribution of this document is unlimited.

11 SUPPLEMENTARY NOTES	12. SPONSORING MILITARY ACTIVITY
	Office of Naval Research

13 ABSTRACT

Not until we have a better knowledge of the details of the short range order (SRO) and the distribution of defects in amorphous solids will we be able to interpret the results of electrical and optical measurements with any certainty. The purpose of this report is to enlarge upon our knowledge of the structure of tetrahedrally coordinated amorphous semiconductors (among those investigated are Si, Ge, InSb, GaP, GaAs, GaSb, InSb, and GeSn) by employing high angle x-ray diffraction from which the radial distributions functions (RDF) are deduced, and by employing small angle x-ray scattering (SAS) from which the sizes and concentrations of voids are deduced.

Methods of analysis of the high angle diffraction data have been devised which almost totally eliminate termination errors in the RDF Also, in deducing the coherently scattered radiation, the incident beam energy profile has been taken into account. It is shown that its effect is to simply modify the monochromator efficiency by a constant amount.

A Kratky small angle scattering (SAS) camera has been built which allows data to extend to as high as 12°, thus permitting the SAS data to be normalized to electronic units by matching them on to the high angle data. Also, a numerical method has been devised which can make collimation corrections to the SAS data for a general smearing function.

The experimental diffraction curves of Ge, GaAs, GaP and GeSn have first peak positions in k-space that fall close to the positions of the (111) peaks in their crystalline forms, and have second peak positions that fall close to the average position of the (220) and (311) peaks in their crystalline forms. However, for InSb and GaSb, it has been found that the first diffraction peak positions have changed by 11% and 5% respectively to higher k values than the (111) peak position of their crystalline forms.

The F(k)'s and RDF's of Ge, GaAs, GaP, GaSb, GeSn, and InSb are found to be similar in shape, suggesting that all have the same structure. In each case, the short range order is similar to that of the crystalline forms up to the second nearest neighbors. The bond lengths are only slightly distorted, the bond angles are distorted an rms amount from 10-17°, and the dihedral angles are randomly rotated.

The currently accepted structural models for Ge all contain five membered rings. Hence, if these models correctly describe the structure of Ge and other tetrahedrally coordinated semiconductors, then it is likely that the amorphous III-V compounds contain wrong bonds, i.e. bonds between like atoms.

In Chapter 6, it is shown that voids occur in various sizes and concentrations depending on the method of preparation. The density deficit as determined from the SAS is in good agreement with that found from hydrostatic weighing. In the III-V compounds, there is little evidence for phase separation. The connection between the ESR signals and the voids determined from the SAS is reexamined.

With increasing temperature of anneal, the SAS of amorphous Ge increases at smaller angles while decreasing at larger angles, indicating the condensation of smaller voids into larger voids. The generally weak SAS in all but evaporated Si and Ge indicates that these materials are homogeneous, and hence, it is unlikely that they are microcrystalline.

In Chapter 7, the results of a computer simulation of the deposition process are presented which show that several different continuous random networks may exist, which differ in the dihedral angle distribution. For the most physically reasonable assumed deposition process, the resulting RDF of the cluster generated fits the experimental RDF of amorphous Ge in every major detail.

DD FORM 1473 (PAGE 1)
1 NOV 65

0102-014-6700

D-23822

14 KEY WORDS	LINK A		LINK B		LINK C	
	ROLE	WT	ROLE	WT	ROLE	WT
Random networks						
Disordered materials						
Amorphous semiconductors						
Computer Models						
X-ray structural determination						
Ge, and other tetrahedral semiconductors						

THE STRUCTURE OF TETRAHEDRALLY
COORDINATED AMORPHOUS SEMICONDUCTORS

By

Nigel J. Shevchik

July 1972

D D C

AUG 18 1972

B

Technical Report No. HP-29

Technical Report No. ARPA-44

Division of Engineering and Applied Physics

Harvard University · Cambridge, Massachusetts

TABLE OF CONTENTS

v

LIST OF FIGURES

LIST OF TABLES

CHAPTER 1

INTRODUCTION AND HISTORICAL REVIEW

A. Introduction

The... "fundamental understanding for many solid state problems is achieved when four questions can be answered:

(1) What are the atoms involved and how are they arranged?

(2) How did this arrangement come into being?

(3) How does this arrangement lead to certain mechanisms of electronic and atomic motion?

(4) How do these mechanisms give rise to the observed properties?"[1]

When Shockley wrote this in 1950, he most likely had crystalline materials in mind, but today the answers to the first two questions are of particular importance to those investigating amorphous semiconductors.

The periodicity of the structures of crystalline solids allows for both their easy experimental determination and analytical representation thus allowing question (1) to be answered easily. However, for disordered systems, we cannot experimentally find the exact position of each constituent and question (1) remains unanswered for all amorphous solids. For disordered systems, the most direct structural information available is embodied in the radial distribution func-

tion (RDF) which, due to the experimental averaging over a large number of atoms, contains information on only the radial structure about the average atom. To fill in the details of the short range order, such as the local angular correlations, the best we can do at present is to fit the experimental RDF with a model. Unfortunately such a fit may not be unique. This difficulty is further compounded by the inaccuracies in the experimental RDF's which admit a still wider range of structural possibilities.

Amorphous semiconductors often contain microscopic inhomogeneities, either voids or phase separated regions on the scale of a few to several hundred angstroms, in concentrations which strongly depend on the deposition conditions. Since these inhomogeneities can seriously alter the electronic properties of the ideal homogeneous material, it is imperative to establish the homogeneity of the sample before its electronic properties can be interpreted with any certainty. Unfortunately the number of papers concerning the inhomogeneities in amorphous semiconductors is rather meager in comparison to the number reporting the electronic properties of these materials.

Not only are we confronted with large uncertainties in both the structure and the experimental results concerning the electronic properties, but the mathematical difficulties involved in solving the Schrödinger equation in three dimensions for disordered systems appear to be, at least for now, intractable. Hence the bulk of the theories on the electronic prop-

erties of the amorphous state are either on models so idealised that they bear little resemblence to anything real, or they are so lacking in mathematical detail that they are no more than conjectures and outright guesses.

In spite of the large expenditures of effort in the last three years on the study of the electronic properties of amorphous semiconductors, it is not surprising that little has been finally settled, either experimentally or theoretically. Spurred by the large experimental inconsistencies and the lack of adequate explanations for them, solid state physicists are finding it necessary to develop new experimental methods and theories to treat the amorphous state, and in particular, to spend more effort on answering questions 1 and 2.

It is likely that further theoretical developments will have difficulty progressing until we better understand the amorphous structure so that less effort need be wasted on inapplicable models. On the experimental side, the call for a full structural characterization is a necessary prerequisite before the full significance of the observed electronic properties can be appreciated.

Since the electronic properties depend upon the structure and the structure in turn depends upon a deposition process, an understanding of both the deposition process and the structure is helpful, and sometimes necessary, in the investigation of the properties of these complex disordered materials.

In this thesis we examine the amorphous structure and the deposition process in detail, and correlate, as much as pos-

sible, the observed electronic properties to the structure, and the structure to the deposition process. In the remainder of this chapter, we review the reported electronic properties and theories, the structural tools available to the experimentalist, and the structural models proposed for tetrahedrally coordinated amorphous solids. In Chapter 2 we discuss how the films investigated here have been made. In Chapter 3, we discuss how the RDF's can be obtained from the high angle x-ray diffraction, and in Chapter 5 we present the RDF's of eight amorphous semiconductors. In Chapter 4 we discuss how information concerning the sizes and concentration of inhomogeneities can be obtained from the small angle x-ray diffraction (SAS), and in Chapter 6 we present the results of the SAS experiments performed on ten amorphous semiconductors. Finally, in Chapter 7, we develop a computer simulation of the deposition process, which generates structures in good agreement with experiment.

B. Types of disorder

Ziman[2] stresses that the types of disorder are quite different mathematically, and effects occurring in one type may not necessarily occur in another; the types of materials of interest in this investigation are those with no long range order. A precise definition of long range disorder is given by consideration of the density function $\rho(r)$, which specifies the positions of the atoms comprising the solid. If no long range order exists then the correlation function $\langle \rho(r)\rho(r+R)\rangle$

is expected to go to its limiting value ρ_o^2 as R becomes large, where ρ_o is the average atomic density. If it does not, then long range order must exist. Since the diffraction pattern of a solid is the Fourier transform of the correlation function, examination of it can tell us something about the asymptotic behavior of the correlation function.

If the diffraction pattern is discontinuous and contains delta function singularities, then the density function ρ (r) contains terms which oscillate without decaying, and hence, the correlation function cannot go to its limiting value at large r. However, if there is some breadth to the diffraction peaks, aside from instrumental broadening, its transform must decay in r space. Hence, a necessary and sufficient condition that the structure possess no long range order is that its diffraction pattern contain no sharp peaks.

Some of the types of disorder are schematically represented in Figure 1-1 by one dimensional arrays of square wells, where each well represents an atomic position. Adjacent to each well is the corresponding k-space structure factor, which, upon multiplication by the atomic form factor, gives the diffraction pattern.

Figure 1-1a shows the ordered elemental crystal in which there is uncertainty neither in the well depths nor separations. Long range order exists since the uncertainty in any two wells n wells apart is zero, no matter how large n is chosen. In k-space the identifying characteristic of such a 1 dimensional chain is a series of delta functions, all of the same height, occur-
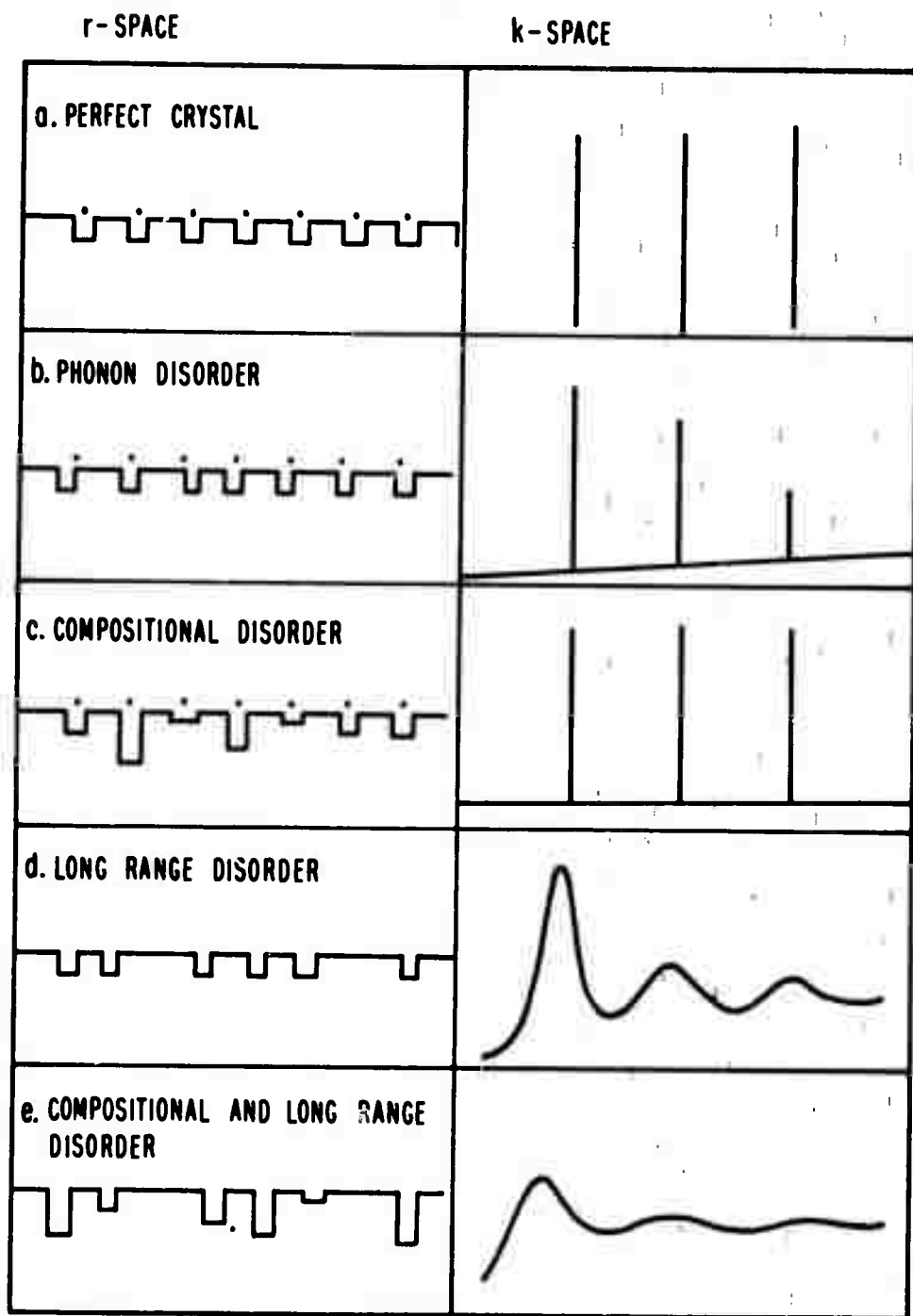
FIG. 1-1 r-SPACE AND k-SPACE STRUCTURES FOR VARIOUS DISORDERED 1 DIMENSIONAL CHAINS.

ring at regular intervals.

In Figure 1-1b, the potential wells are slightly dis-placed away from their crystalline equilibrium positions. This type of disorder is called phonon disorder. The short range order is reduced because the interwell separation is uncertain; however, long range order still persists because the uncertainty in the positions of wells far apart does not grow, but remains equal to twice the uncertainty of each well about its equilibrium position. The existence of long range order is shown by the sharp peaks in k-space. The uncertain-ty in the well positions leads to a decrease in the height of the peaks and to an increase of a smooth background as k in-creases. It must be remembered that phonon disorder occurs in all solids, both ordered and disordered.

In the next set of wells, shown in Figure 1-1c, the peri-odicity of the lattice still exists, but the depth of each well is still random. This kind of disorder is called com-positional, and occurs in disordered crystalline alloys. In k-space the delta functions of the crystal still persist, but now there is a flat continuous background, the value of which depends upon the well depth fluctuations.

Phonon and compositional disorder fall into a class of disorder called cellular disorder. In both cases, the length of the unit cell remains well defined, but the disorder takes place only within the unit cell. In no way can long range order be eliminated with this type of disorder.

In Figure 1-1d, not only are the interwell separations

random, but the position of each well is statistically dependent upon the position of the well adjacent to it. This type of disorder is called long range disorder, since the uncertainty in the positions of wells far apart grows as their separation increases. Here, as opposed to the case of phonon disorder, where the spacing between the wells is also random, no lattice exists. This type of disorder occurs in the elemental amorphous semiconductors such as Si, Ge, and Se. In k-space, as has already been discussed, the distinguishing characteristics of the long range disorder are the broad diffraction peaks.

Finally, in Figure 1-1e, is shown the most disordered of all the chains, in which occurs both compositional and positional disorders. Such disorder occurs in amorphous alloys, such as the chalcogenide glasses. Because a different atom can be found at any site, the depths of the wells are random. Because of the differences in the sizes of the wells, a further uncertainty is added to the interatomic spacing, thereby increasing the long range disorder. In k-space the oscillations decay even faster than for the case of the monoatomic long range disorder, and, as for the case of compositional disorder, there is also a background intensity which depends on the uncertainty in the well depths.

It is the last two types of disorders which are of interest in this investigation. Although the one dimensional structure factors are very similar to the structure factors observed for real three dimensional materials, their simi-

larities in r-space are much less, since in one dimension the long range disordering mechanism is limited to bond length fluctuations. In three dimensions, in addition to bond length fluctuations, bond angle distortions and rotations also can contribute to the disorder. One dimensional systems are unable to represent topological disorder, which has meaning only in higher dimensions.

For topological disorder, the coordination of the atom is maintained, but it is the connectivity of the network which is disordered. It is readily identified by the occurrence of rings with different numbers of members, as shown in Figure 1-2b. Note that for this type of disorder, it is absolutely necessary to break bonds to transform the atoms back into the crystalline arrangement shown in Figure 1-2a. Figure 1-2c shows the crystal lattice which is positionally distorted so as to eliminate long range order. Note that in this case, all the rings contain six members only, and hence, topological disorder is absent.

It appears that this structure is unstable and can easily spring back into the crystalline configuration, whereas the structure containing the topological disorder cannot just easily spring back into the crystalline configuration. Drummond[3] found that he was unable to build with plastic tetrahedra a two dimensional amorphous network with six membered rings only and that the crystalline arrangement always resulted. It is believed that the topological disorder is essential in the stabilization of the amorphous structure.
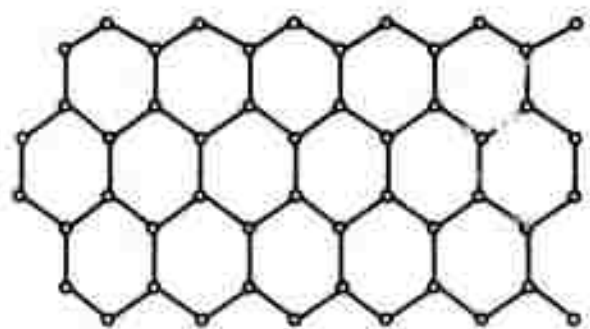
a. PERFECT CRYSTALLINE ORDER
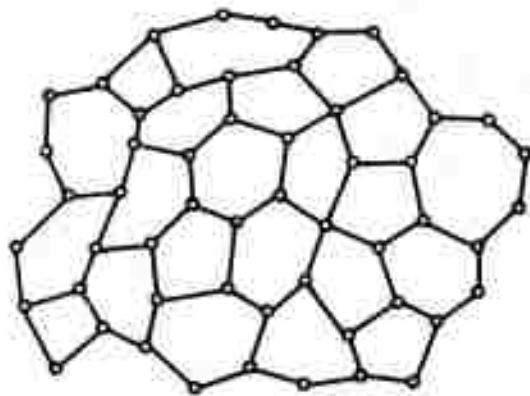
b. TOPOLOGICAL DISORDER
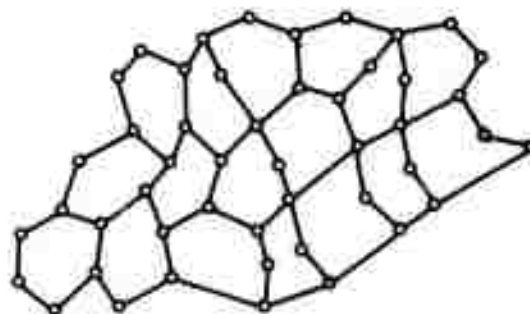
c. LONG RANGE POSITIONAL DISORDER
WITHOUT TOPOLOGICAL DISORDER

FIG. 1-2 PERFECT CRYSTALLINE ORDER, TOPOLOGICAL
DISORDER, AND LONG RANGE POSITIONAL
DISORDER WITHOUT TOPOLOGICAL DISORDER.

C. What has theory told us?

Since most of the theoretical calculations concerning electrons in disordered systems are difficult to follow, they will be mentioned here only briefly. This section will be weighted by the author's own unpublished calculations, not because they have provided anything new or outstanding, but because the author feels they serve a useful function as a pedagogical aid in introducing some of the theoretical problems involved. Two questions to which theoreticians have addressed themselves are: (1) Is the energy gap maintained as the long range order is reduced?, and (2) What is the nature of the eigenstates?

The existence of a band gap in systems with no long range order has been postulated by Ioffee and Regel to be solely dependent upon the short range order, i.e., the nearest neighbor environment.[4] A similar idea has been recently formulated by Weaire,[5] who argues that in systems with topological disorder only, the existence of a gap is solely contingent upon the maintenance of the nearest neighbor tetrahedral coordination everywhere; however, his proof is in the tight binding approximation, treating only nearest neighbor interactions. The inclusion of higher order terms which incorporate bond angle distortions and rotations may destroy the gap.[5] Gubanov[6], using a structural model in which the crystal lattice is weakly perturbed, has argued that the gap is maintained for small disorders, but it is unlikely that the true amorphous structures resemble a slightly disordered crys-

tal. Edwards[7], using a Green's function formulism, on the other hand, has shown that states are introduced into the gap for the slightest disordering of the crystalline lattice.

The nature of the eigenstates, whether they be extended or localized, has received even more attention than the question of states in the gap.[8-14] In his controversial as well as difficult paper, Anderson[8] has claimed that in the tight binding approximation, electrons are unable to diffuse away from their initial positions if the fluctuation in energy of the potential wells is sufficiently large. This localization effect has come under attack by Bonch-Bruevich,[9] Lloyd,[10] and Brouers,[11] who have argued that in regions where the density of states remains finite, localization is difficult, if not impossible. Economu and Cohen,[12] Thouless,[13] and Ziman[14] have joined Anderson in arguing for localization, but still no final resolution of the question appears to be in sight.

Often it is difficult to determine which properties are intrinsic to real disordered materials and which are artifacts of either the mathematical approximations or the structural models. The questions concerning states in the gap and the nature of the states in disordered systems are unresolved theoretically, and must await improvements on both structural models and mathematical techniques before they can be answered.

Very little has been established concerning the effects of quantitative disorder in higher dimensions. Only Weaire's[5] result concerning the existence of an energy gap in a topologically disordered system that has nearest neighbor inter-

actions only has been rigorously established.

Only for the one dimensional systems has anything concerning quantitative disorder been rigorously established, since there, no mathematical approximation need be made and the effects of disorder can be examined with certainty. In addition, after years spent on elaborate computer calculations, there has been a recent return to the one dimensional systems since they provide a simple, convenient means to expose the physics involved in the problem, and in many cases they have been found to describe many properties of real systems with surprising accuracy.[15] Aside from being a valuable pedagogical aid, they also serve as a testing ground for analytical methods which are supposed to extend to higher dimensions. Already they have shown Edwards's[7] Green's function techniques to be invalid by demonstrating that his method gives states in a region of energy where there are known to be none.[16-18]

Although the effects of disorder can be investigated relatively free of analytical approximation, apart from numerical round off errors and the finite size of the system, the conclusions reached in these systems can not always be safely extended to three dimensions, since it is apparent that an electron propagating in 1 dimension is confined to a given trajectory and must encounter all barriers, which in higher dimensions it might otherwise avoid. Nevertheless, many results established in 1 dimension may carry over to real solids.

The exact wave function for a finite one dimensional system can be found in a variety of ways, and from it, the den-
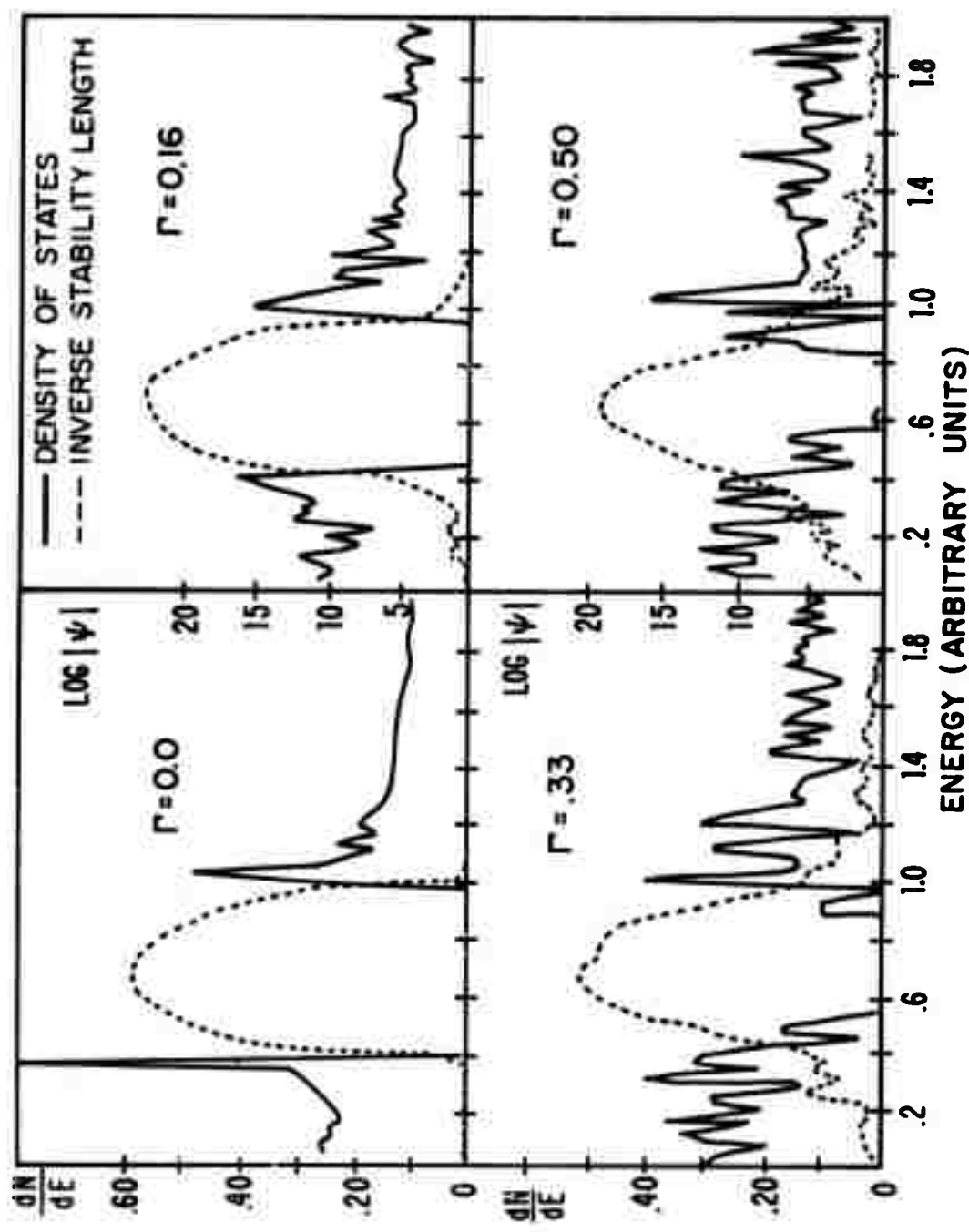
FIG. 1-3 DENSITY OF STATES AND INVERSE OF THE STABILITY LENGTH FOR VARIOUS LONG RANGE DISORDERS.

sity of states. The density of states, as discussed by James and Ginzberg,[19] is simply $\frac{dN(E)}{dE}$ where $N(E)$ is the number of zeroes in the wave function. Figure 1-3 shows the resulting density of states along with the inverse of the stability length as a function of increasing long range disorder, which is characterized by Γ, a measure of the fractional uncertainty in the well positions.[20] The stability length is a measure of how strongly the wave function is damped and reflected as it attempts to propagate. Mott[21] suggests that this length is the one commonly inserted into the usual formulas to get the mobility.

For the perfectly ordered lattice, as is shown in Figure 1-3a, a well defined energy gap appears, bounded on each side by a high density of states. For energies outside the gap, the solutions are stable (i.e. have infinite stability length) but inside the gap they are unstable, growing by several orders of magnitude over the length of the chain. Since the density of states is zero in this region, electrons cannot occupy these unstable regions. However, as the disorder is introduced, the density of states curve tails into the unstable region, while the unstable region expands further into the region of non-zero density of states.

Figure 1-3 shows that as the disorder increases, the width of the gap decreases, but within the computational error, the gap is still retained even for bond length fluctuation greater than can occur in a real solid. Borland[17] has shown that an energy gap does continue to persist in one dimension provided
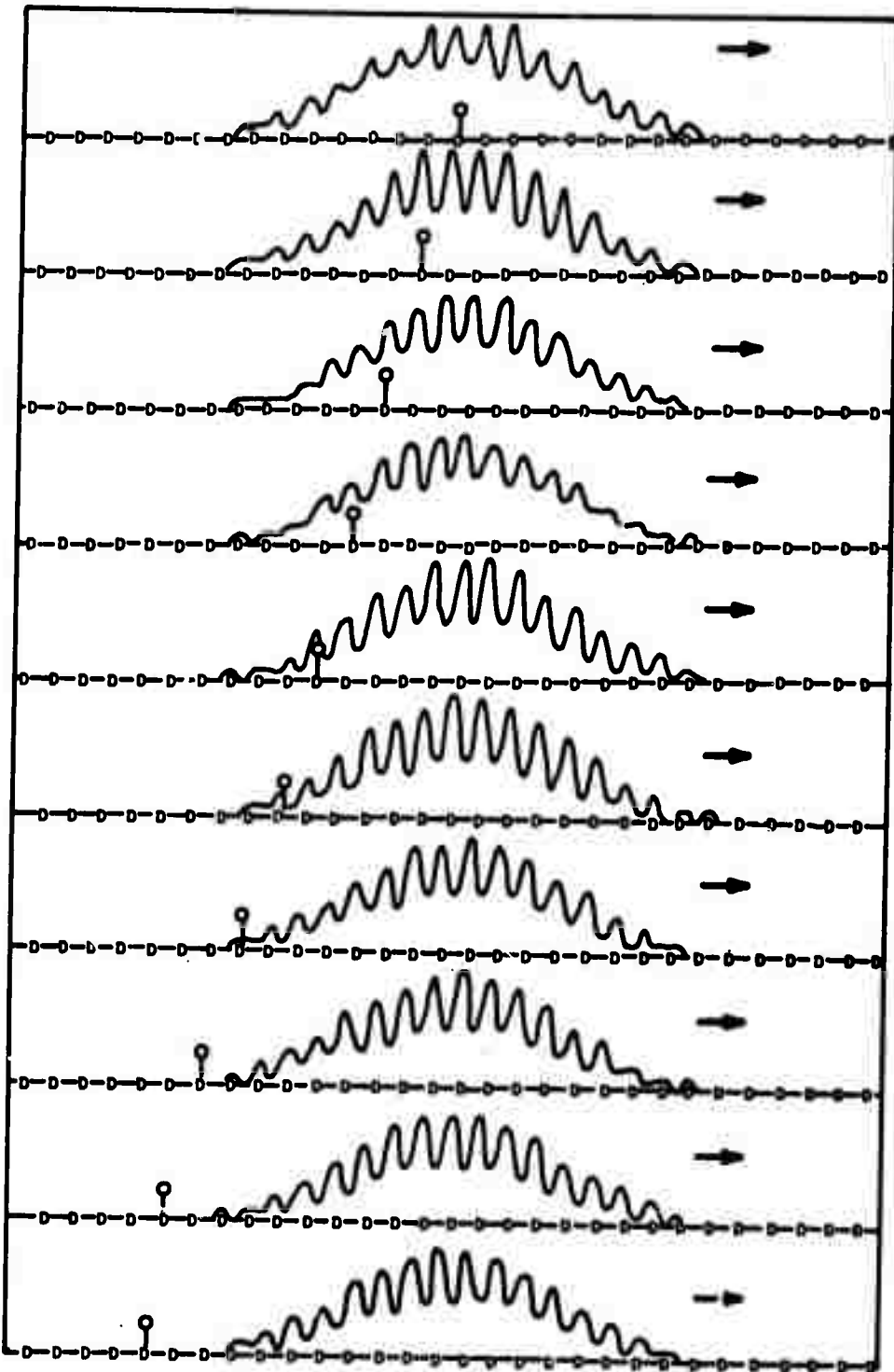
FIG. 1-4 WAVE PACKET IN AN ORDERED LATTICE AS
A FUNCTION OF POSITION AND TIME.
THE ARROW → AND THE LAMP POST
DENOTE THE VELOCITY AND INITIAL
POSITION RESPECTIVELY OF THE PACKET.

that the maximum deviation of the distances between atoms is less than a critical value; in addition, Halperin[22] has shown that an energy gap exists in a disordered chain provided that there is a range of energies which lies in the band gap of every crystal that can be constructed from each unit cell occurring in the disordered chain. Both of these conditions set forth by Borland and Halperin have been met in the calculations of the density of states curve in Figure 1-3.

These results imply that perhaps in a structure having a cut off in the quantitative disordering mechanism (such as a maximum bond angle distortion), no states should appear in the gap. However, the introduction of defects (such as a void) that cause fluctuations beyond those found in this structure puts states into the gap.

This result is complementary to Weaire's result[5] that topological disorder cannot destroy the gap.

The instability of the solutions has led to the speculation that, as a consequence of the disorder, the states become localized.[21,24] Mott and Twose[24], recognizing this instability, have argued that localized states could always be constructed by adjusting the energy so as to match solutions, one decaying to the right and the other to the left of an arbitrary point.

Some information concerning the nature of the eigenstates can be obtained in one dimension by iterating the time dependent Schrödinger equation according to the method developed by Goldberg et al.[25] Figure 1-4 shows that indeed a wave packet placed into a crystalline array of atoms retains its initial

gaussian shape and has no difficulty in propagating.[20]

However, we see that in Figure 1-5 the packet in the one dimensional disordered lattice quickly decays into a very irregular shape and that it quickly undergoes a Bragg reflection. The reflection occurs because the packet has encountered a region in the lattice that has a periodicity that tends to exclude the packet from it, while in other regions the wave packet encounters fluctuations that give it no difficulty in propagating. This is very different to the crystal where the packet can propagate in all regions equally well and never encounters such reflecting barriers.

Note that with increasing disorder, the structure in the density of states increases. Performing the same calculations with another set of wells gives a different structure in the density of states, although the width of the gap region still remains about the same. This tells us that a small region containing about 100 atoms in a disordered material has a structured density of states, whereas a similar sized region in an ordered material does not. Averaging several such disordered segments will give a smooth density of states similar to the ones found by Borland and Bird.[23]

It is less likely that an electron having an energy occurring at the depressions in the density of states curve will be found in this chain; hence to a degree, quantization, which is to be expected for localized states, has occurred. The concept of a spatially varying density of states function has been the basis of the more recent models to be discussed later.
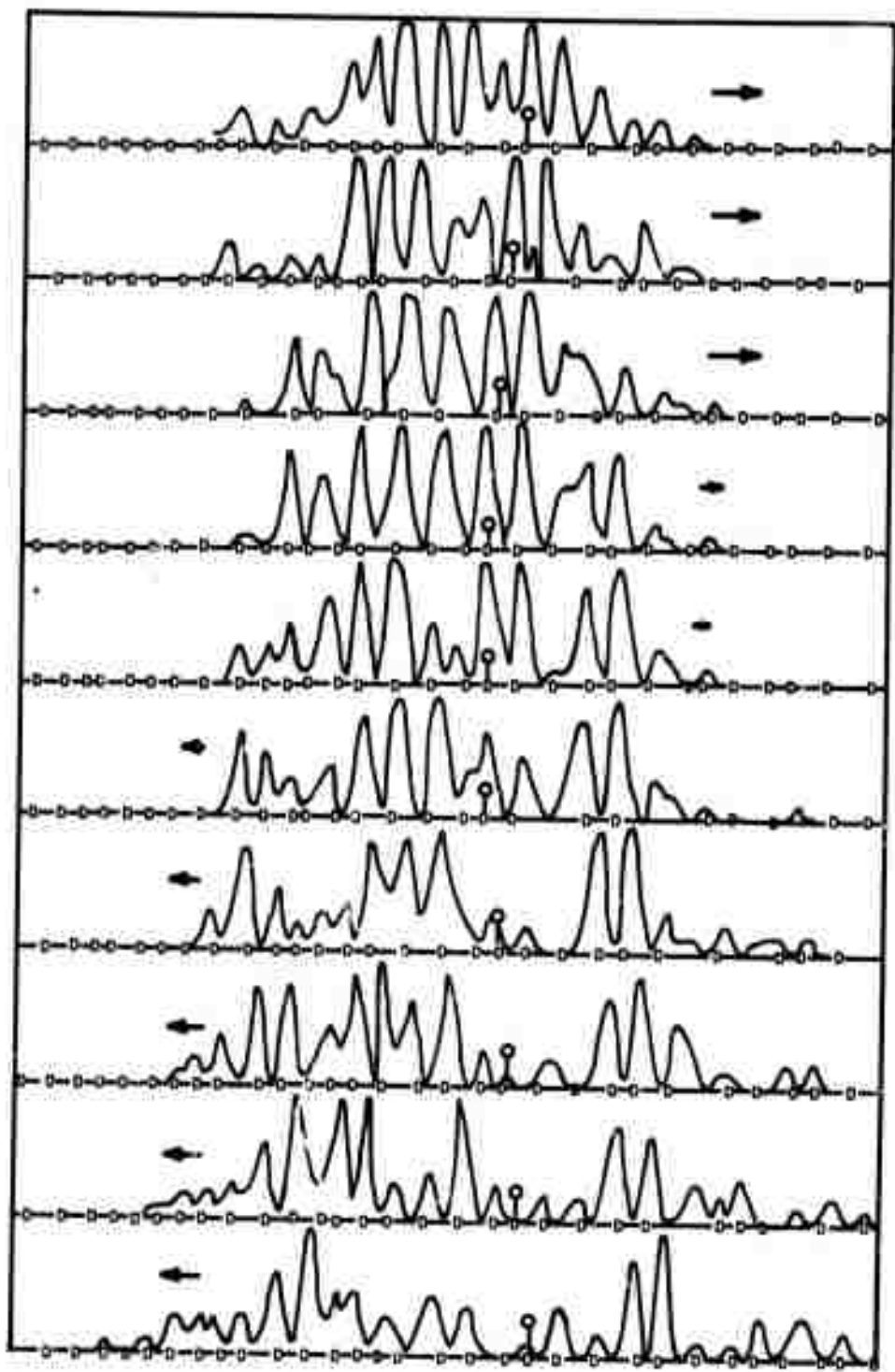
FIG. 1-5 WAVE PACKET IN A DISORDERED LATTICE
AS A FUNCTION OF POSITION AND TIME.
THE ARROW ⟶ AND THE LAMP POST ⸙
DENOTE THE VELOCITY AND INITIAL
POSITION RESPECTIVELY OF THE PACKET.

Summarizing, the results rigorously established in one dimension are:

1. The width of the band gap decreases with disorder, but remains greater than zero as long as there is a cut off in the distributions of the bond lengths and well depths and the disorder remains sufficiently small.

2. All solutions that were stable in the ordered lattice become increasingly unstable as the disorder increases.

3. As the disorder is increased, the density of states curve for a segment of a few tens of atoms becomes increasingly structured.

D. Models for the electronic states

The current popular model of the density of states distribution in real amorphous solids, of which some of the general features have already been revealed in the one dimensional model, is shown in Figure 1-6. This model was first suggested by Banyai,[26] but a great deal of the credit seems to have been attributed to Mott, Cohen, Fritzsche. and Ovshinshky, since the model is now commonly referred to as the Mott-CFO model.[27,28] Because of the structural and mathematical difficulties involved, the model as originally proposed remained necessarily imprecise, serving only as a basic framework about which our thinking on amorphous semiconductors was to be formulated.

It is speculated that as a result of the disorder, states tail into the gap from the conduction and valence bands possibly to such an extent that they overlap in energy,[27,28] thus making the assignment of conduction and valence bands in this
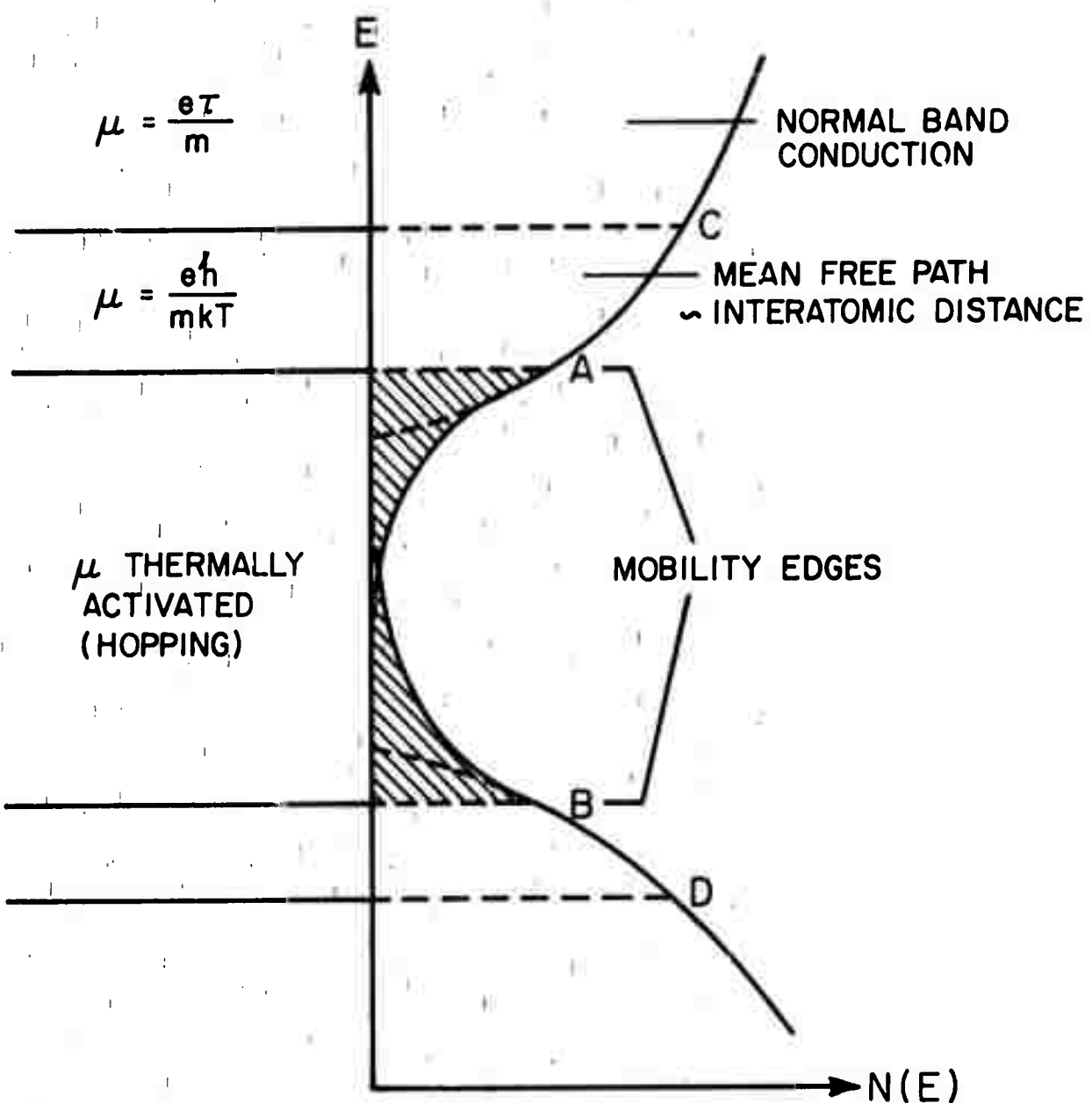
FIG. 1-6 SCHEMATIC OF THE MOTT-CFO MODEL FOR THE
DENSITY OF STATES.

region difficult. The definitions used in the CFO model are that those states which are neutral when occupied belong to the valence band, and those which are neutral when empty belong to the conduction band. For energies above C and below D, the electronic states are extended and approximately described by plane waves which undergo occasional scattering with a well defined mean free path (MFP), as is so with their crystalline counterparts. In regions A-C and B-D conduction can take place without thermal activation, but because of the high degree of disorder, the phase of the wave function is random from site to site, resulting in a diffusive electronic motion. Closer to the gap in regions AC and BD, the interaction with the disorder becomes so strong that the MFP becomes comparable to the interatomic spacing. Mott[21] has conjectured that when the MFP becomes shorter than the interatomic spacing the states become localized.

Mott[21,28] recognized that with the onset of localization a drop in mobility should concur so that, although the energy gap may disappear, a mobility gap is retained. Conduction in the mobility gap can take place only by thermally activated hopping between localized states. However, at high temperatures carriers are excited into the conduction band, and hence, the conductivity is expected to behave as $\sigma_o e - \frac{E_{qc}}{kT}$, where E_{qc} is the conductivity gap, defined to be the shortest distance in energy between the Fermi level and the conducting states.

Fritzsche[29] has recently extended the Mott-CFO model in

order to reconcile the electrical measurements, which suggested
a high density of states in the gap, with the optical measure-
ments, which suggested a low density of states in the gap.
He has argued that the amplitude and the absolute energy of
the gap varies with position, and hence, filled localized and
channel states, i.e. states that extend throughout the volume
but are excluded from some regions, occupy different regions
in space than unfilled localized and channel states. Thus,
optical transitions between them are suppressed.

Inglis and Williams[30] have recently proposed an alterna-
tive model to the Mott-CFO model in which they have been able
to calculate the wavefunctions. They start with the crystalline
lattice and potential and superpose over this crystalline po-
tential, fluctuations on a scale of about 100 Å. Such fluc-
tuations, they show, lead to localized wave functions near the
band edge which behave like harmonic oscillator functions.
The mobility gap occurs at an energy where fluctuations cause
the electronic wave functions to become damped. In contrast
to the Fritzsche model, transitions are allowed between the
localized states. As long as the strength of the fluctuations
does not exceed that of the crystalline band gap, a well de-
fined energy gap remains. Although their model is at the out-
set structurally incorrect, it cannot be disregarded because
most of the observed properties of amorphous semiconductors are
explained as a natural consequence of the superposition of this
100 Å fluctuation. Moreover, it is the first model in which
one is able to describe quantitatively some of the properties

of amorphous semiconductors, and hence, it can be more easily tested than the Mott-CFO model.

Essential to all of the models are the spatial fluctuations in the potential, of which the details and origin have not been specified. In Chapter 6, we will discuss the possible origin of some of them.

E. What has experiment told us?

Now we will discuss the experimental electronic properties, not so much to test Mott-CFO model, as to see what deductions can be made concerning the structure. Early experimenters, proceeding under the beliefs that the as-deposited structure of amorphous semiconductors was well defined[32] and that annealing only caused recrystallization of the films,[35,36] limited most of their investigations to as-deposited films.

1. Transport properties

It has been found that the high temperature conductivity of most amorphous semiconductors is well fitted by the intrinsic conduction law $\sigma_0 e^{\frac{-E}{kT}}$, where σ_0 is the high temperature limit of the conductivity found by extrapolation of the experimental data to $1/T=0$.[30] Stuke[30] has pointed out that σ_0 is about $10^3 - 10^4$ ohm^{-1} cm^{-1} for all amorphous semiconductors. An adequate explanation of this result has not been given.

In general, it has been found that the low temperature conductivity is not a straight line when plotted against $1/T$, but shows a progressively increasing activation energy from a few hundredths of an ev at 30° K to a few tenths of an ev

at room temperature.[30-34] A classic example of such a curve is that of amorphous Ge found by A.H. Clark,[32] as is shown in Figure 1-5. The same data plotted against $1/T^{1/4}$ give a straight line, which at first glance seems to indicate the hopping conduction predicted by Mott.[28] However such an interpretation has been questioned by Chopra and Bahl[33] who have shown that the same data may be plotted in at least three other ways with an equally good, or better, fit.

A limited number of high frequency conductivity experiments have indicated the presence of a hopping mechanism in several amorphous semiconductors.[33,35,38] However, high frequency measurements often entail experimental difficulties which make the results less believable.

The dominant carrier in most amorphous semiconductors is uncertain since the Hall effect measurements have on occasion indicated electronic conduction when thermoelectric measurements were indicating hole conduction.[39] This same anomaly has also been observed in crystalline semiconductors. It appears that, whereas Hall effect and thermopower experiments will give the same sign of carrier when the carriers occupy simple band extrema, this is not the case for carriers on Fermi surfaces which have a complicated dependence on energy and k-vector. The situation regarding amorphous semiconductors is less clear. Allgaier[39] suggests that the difficulty is that we do not yet understand the Hall effect in disordered systems, and that the thermopower measurements give a more reliable indication of the type of carrier since they are less
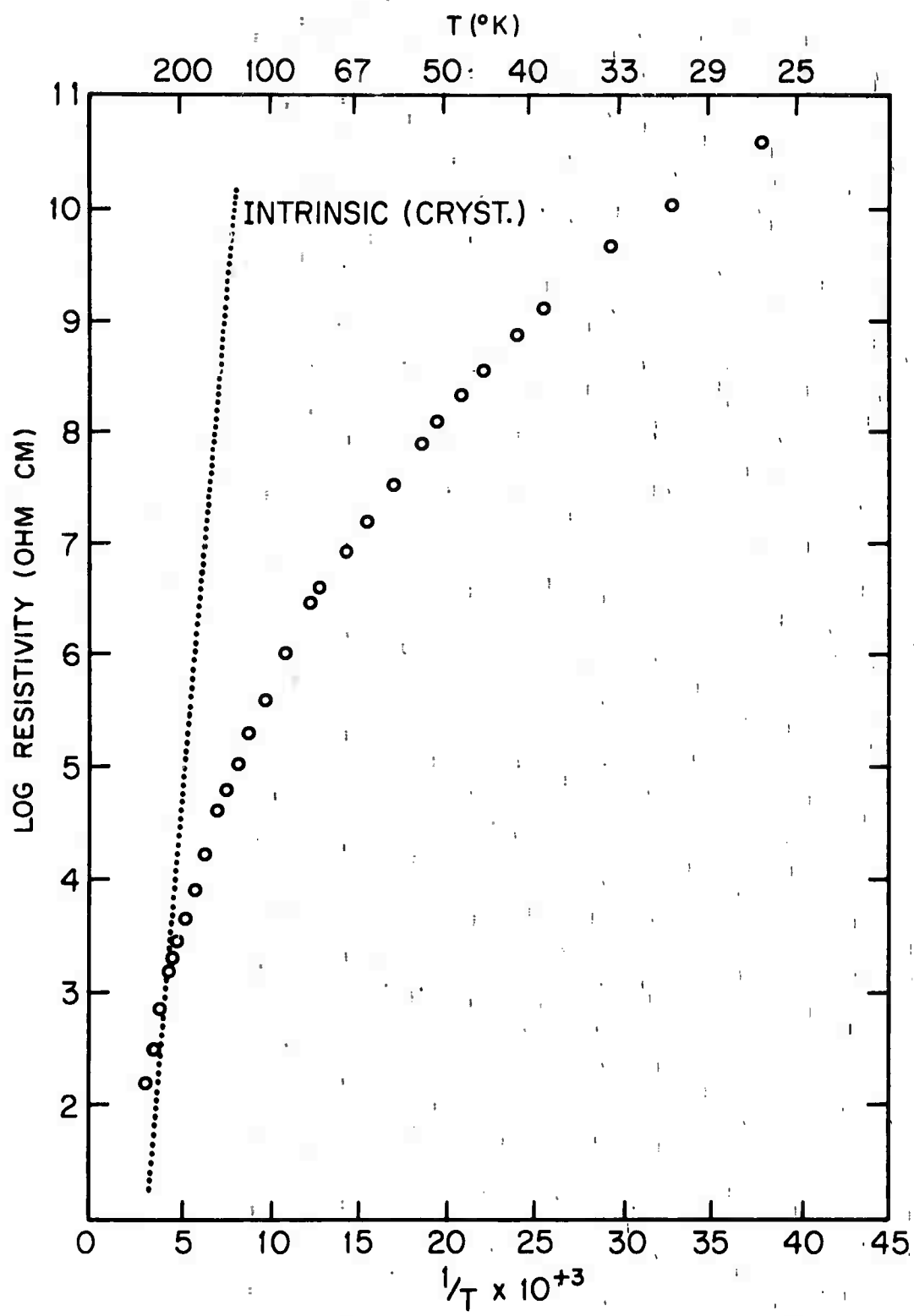
FIG. 1-7. R vs. $1/T$ FOR AMORPHOUS Ge.

sensitive to the details of the disorder.

Also typical of most amorphous semiconductors is the high field behavior of the conductivity, which can often be adequately fitted by theories based on the Poole-Frenkel theory of the field assisted emission of electrons out of traps into free wave-like states,[33-36,41-47] In addition, many power law dependences of the conductivity on the electric field have been found, some of which have been interpreted as space charge limited conduction arising from a high density of localized states distributed in energy near the conduction band.[41] Several other power law dependences still have no adequate explanation. However, all of these preliminary conductivity vs. field experiments suggest a large number of localized states in the gap regions that may be associated with structural defects.

The onset of the optical absorption and the onset of the photoconductivity in amorphous materials often do not coincide as they do in crystalline materials.[37,48,49] In the Mott-CFO model, this can be attributed to the absorption at low energies taking place between localized states, the excitation of which cannot add to the conductivity. At higher energies the absorption takes place between states of higher mobility, resulting in the onset of a noticible photoconduction. However, recent measurements show that the photoconductivity of amorphous GeTe[50], InSb,[51] and Ge[52] does follow the optical absorption edge. This suggests that more statistics must be accumulated to establish whether the photoconduction behavior

is intrinsic to the ideal material or to the defects.

It has been found that the resistivity of amorphous semi-conductors compared to that of crystals, is relatively in-sensitive to doping.[21,53] As suggested by Gubanov,[6] with a high density of states in the gap, the added impurity electron or hole leaves its parent atom and takes up residence in some non-conducting localized state at the Fermi level instead of near   or valence
the conduction band as it would do in a crystal. An alterna-tive possibility suggested by Mott is that the insensitivity to doping arises from the ability of each atom to satisfy its valency requirement during the formation of the amorphous state so that all impurity electrons become embedded into the valence band.[21]

The evidence from all the transport measurements indicate that there exists a high density of states in the gap, but as to whether these states are intrinsic to the ideal amorphous solid or to defects has remained unresolved.

2. Optical properties

The most striking difference between the crystalline and amorphous ϵ_2 spectra is the lack of structure in the amorphous ϵ_2 spectra. Most amorphous materials exhibit a single broad ϵ_2 peak which is not simply a broadened spectrum of their cry-stalline forms, but exhibits a strong red shift. The position of the peak maximum in the tetrahedrally coordinated semicon-ductors frequently is near the energy corresponding to transi-tions associated with the (111) directions in the crystal.

Stuke[54] has argued that since the (111) directions corres-
pond to the directions of the nearest neighbor bonds, which
are disturbed very little from their ideal tetrahedral posi-
tions, features associated with the (111) directions are con-
served. However, a simple diffraction theory tells us that
all energy gaps in the crystal near the Fermi level are pri-
marily caused by a second order interaction of the (111)
pseudopotential components; hence, the existence of all of the
gaps is contingent upon retention of order in the (111) direc-
tion.[55]

Despite the frequently observed red shift in most of the
ε_2 spectra, the static dielectric constant usually remains
within about 10% greater than/the corresponding crystalline value.[56-62]
Since it has been found that the density of most amorphous
semiconductors usually remains within about 10% of the crystal's
we expect the moment $\int_0^\infty \omega \varepsilon_2 d\omega$ to be nearly the same value
as for the crystal.[56,57] A striking exception has been GeTe,
in which the static dielectric constant changes from 36 in the
crystalline form to 4.5 in the amorphous form.[63] The key to
the explanation of this change surely lies in the recent
structural measurements which indicate that the amorphous
phase of GeTe has a shorter nearest neighbor distance and a
lower coordination number than the crystalline phase.[64,65] A
decreased dielectric constant has also been found in amorphous
Te and Se.[66]

Most as-deposited amorphous semiconductors exhibit ex-
ponential absorption edges with slopes that vary by not much

more than a factor of 2, as is shown in Figure 1-8 for a variety of amorphous materials.[37,48,57-61,67-69] Why this is so remains unknown. The frequent occurrence of the exponential edge has led to the suggestion that this edge is intrinsic to amorphous materials. This type of absorption is also consistent with the tailing density of states postulated in the Mott-CFO model. However, in contradiction with what one expects from the one dimensional models, amorphous InSb has been found to have a sharp optical absorption edge occurring at twice the energy at which it occurs in the crystalline material.[51] It has been found also that the first diffraction peak in InSb is shifted to higher k values than in the crystal, indicating some difference in the short range order, but no correlations of the optical properties to this shift have been made.[51]

3. Dependence of the electronic properties on deposition conditions and thermal history

The reported variations in the electronic properties of amorphous semiconductors are consistent with the expectation that the structure and chemical composition will depend on the deposition conditions and thermal history. It has been found that the annealing of amorphous semiconductors short of crystallization usually changes the resistivity by several orders of magnitude and increases the activation energy of the resistivity.[34-37,70] Walley and Jonscher[34] have found that the resistivity of their as-deposited amorphous Ge films
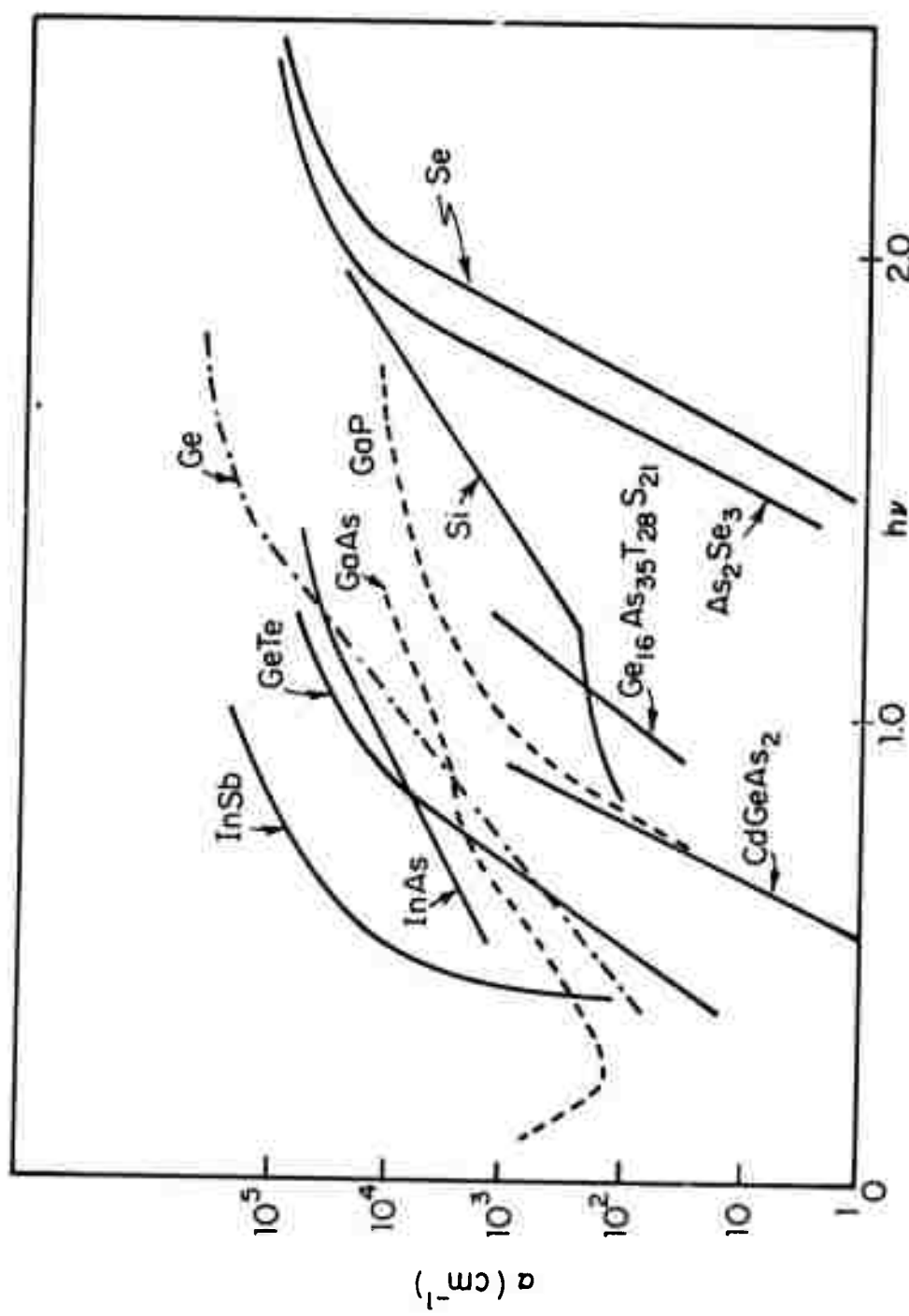
FIG. 1-8 ABSORPTION EDGES FOR SOME AS DEPOSITED AMORPHOUS SEMICONDUCTORS.

References for the absorption edges in Fig. 1-8

Material	ref.no.
As_2Se_3	67
$CdGeAs_2$	57
Ge	37
GeTe	64
$Ge_{16}As_{35}Te_{28}S_{21}$	68
GaAs	58
GaP	59
InAs	60
InSb	51
Se	48
Si	37

depends upon the deposition rate, and that at room temperature, the resistivity changes by a factor of 3 over several days. Brodsky et al.[71] have shown that the changes brought about by annealing/the electrical resistance, ESR signal, the refractive index, and the optical absorption edge in amorphous Si are correlated. Tauc et al.[72] have found that the method of preparation influences the infrared absorption in Ge.

Davey and Pankey[58,59] have shown that the positions of the optical absorption edges of amorphous GaP and GaAs are dependent upon the substrate temperature and are sensitive to annealing.

For years the position and shape of the optical absorption edge in amorphous Ge has' been in dispute. In Figure 1-9 are plotted some of the reported absorption edges as of 1970.[31,32,36,55,72-74] From this we see that the slopes and relative magnitudes of the edges vary over a wide range.

However the tone of the dispute changed when M.L. Theye[76] in a systematic investigation of the preparation and annealing dependence of amorphous Ge showed that the differences could be explained by the preparation conditions. More importantly, she found that the as-deposited films usually exhibited exponential edges which, with annealing, became sharper and shifted to higher energies, and that the films continued to display diffuse scattering lines, and hence remained amorphous. She found that in the best annealed films the edges were not only sharp, but also lay at higher energies than the crystalline edge.
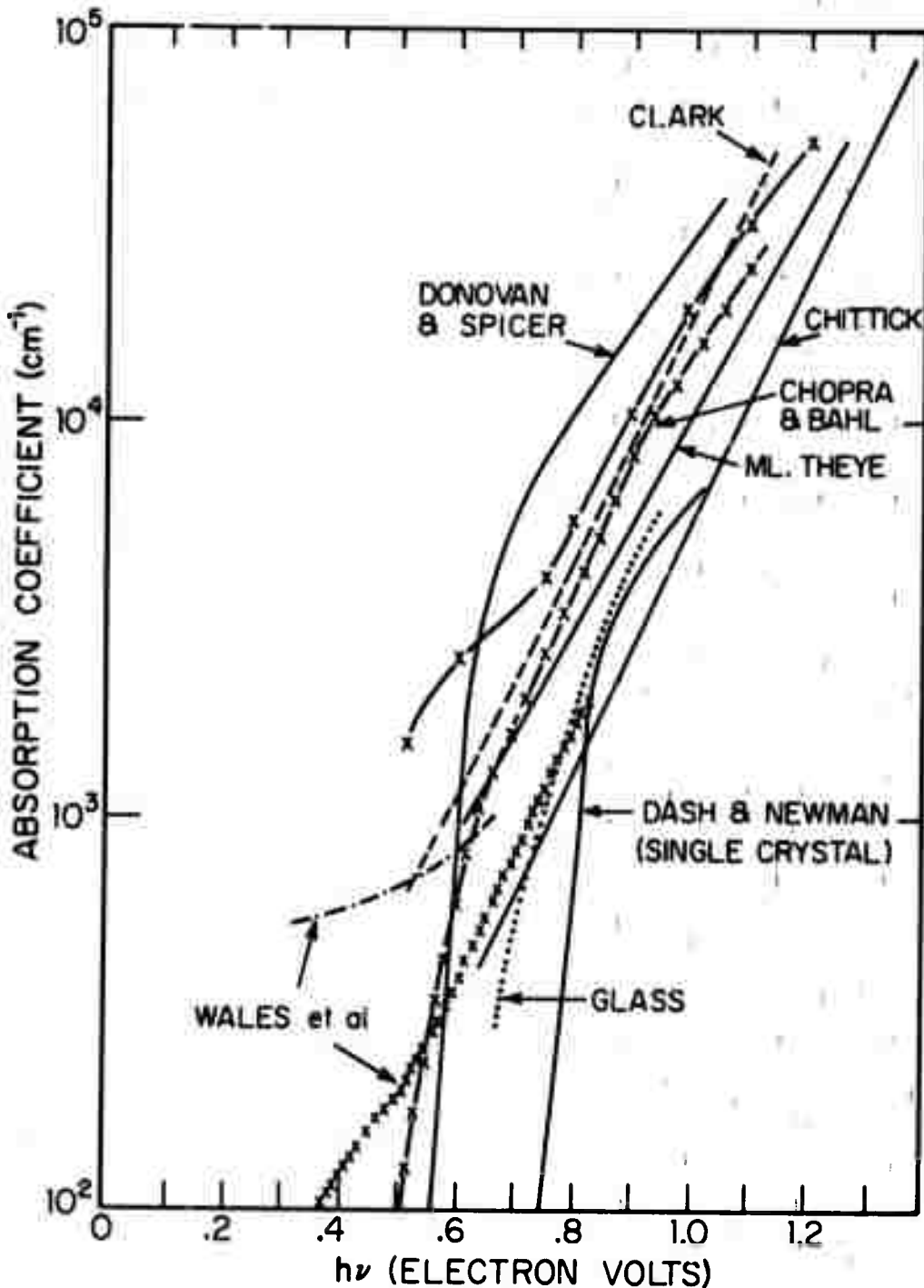
FIG. 1-9 REPORTED ABSORPTION EDGES IN AMORPHOUS Ge As OF 1970.

A little later Connell and Paul[77] and Paul et al.[78] showed that the optical edge of amorphous Ge films prepared by sputtering, electrodeposition, and evaporation initially exhibited different absorption edges but the edges tended toward the same curve with annealing, suggesting that perhaps the structure of the ideal state was a well defined quantity independent of the method of preparation.

From these investigations emerged the idea that annealing does not bring about recrystallization, but that defects in the network are healed by the slight thermal agitation, and that the network may subsequently tend toward some ideal defect free structure.

More recent results by Bauer and Galeener indicate that the ϵ_2 spectra to 10 ev are sensitive to the density of the film, which they find to depend on the substrate temperature. According to their analysis, the presence of voids can significantly alter the behavior of ϵ_2.[79]

The optical and electrical measurements have indicated that the structure is sensitive to annealing and to deposition conditions, and direct structural measurements have confirmed this to be so. The early work of Richter and Breitling[80] has demonstrated that the details of the short range order of amorphous Ge, As, Se, embodied in the RDF, depend upon the method of deposition and also the thermal history. Moss and Graczyk[81] have shown that slight changes occur in the RDF of amorphous Si with annealing while large changes occur in the small angle scattering, indicating the

presence and redistribution of voids. Chen and Turnbull[82] have found that the small angle scattering of electrolytic Ge films is less than that of evaporated films, indicating a smaller void density in the electrolytic Ge.

We conclude, from both the electronic and structural measurements, that the as-deposited films do not have a unique structure, but have a varying number of defects which are incorporated into the structure during deposition and which can significantly alter the electronic properties. The present trend is to attempt production of ideal amorphous material which is void free. However even if this goal is achieved, we will not be much further along if we find that there is a variety of ideal structures.

But for the present, a full structural characterization is needed before any experimental results concerning the electronic properties can be interpreted with any certainty. It is insufficient to just state the sample's method of preparation or thermal history, or to note the absence of diffuse diffraction lines, since these in themselves appear to be quite inadequate in characterizing the structure. Unless structural characterizations are performed on each sample to give information on amorphicity, density, void size and concentration, phase separation, all further experimental results will be greatly diminished in value.

F Attempts to fit the photoemission and optical data

The attempts to fit the optical and photoemission data have

met with only limited success possibly because of the inade-
quate models used. Herman and Van Dyke[83] have attempted to
explain the experimental density of states, obtained from
photoemission by Donovan and Spicer,[84] by attributing the then
believed 30% density deficit to a 10% increase in the cry-
stalline interatomic spacing and modifying the crystalline
band structure accordingly. In no way have they attempted
to introduce spatial disorder. Since the resulting theoreti-
cal density of states has no energy gap and also has pro-
nounced structure, its agreement with experiment must be con-
sidered only qualitative at best.

Brust,[85] on the other hand, has attempted to introduce
into a pseudopotential calculation a spatial disorder by
superimposing on the crystalline structure a frozen in pho-
non disorder 12 times greater than that occurring at room
temperature. As discussed on page 1-6, phonon disorder is
not equivalent to long range disorder; however, the agree-
ment of the calculated ϵ_2 spectra to experiment appears to
be good. Donovan and Spicer[85] have replied that partial re-
tention of a k vector, such as has been done in Brust's cal-
culation, results in a strong modulation in the photoemission
spectrum, while this modulation is not observed experimentally.

Chakraverty[86] has attempted to explain the optical pro-
perties in terms of a microcrystalline model. He has contended
that a sharp edge is retained because of the crystalline order
within the crystallite, but that the ϵ_2 spectra shift to the
red because the large numbers of broken bonds on the surfaces

of the microcrystallites leads to an overall reduction of the binding. However it would appear that a large number of broken bonds would produce a large density of states in the gap with a non-sharp absorption edge.

So far the most daring attempt to describe the optical properties has been made by Kramer,[88] who has introduced long range disorder by smearing the corresponding crystalline k-space structure, and has used this model directly in a pseudo-potential calculation, employing novel mathematical techniques. He has found the ϵ_2 spectra to be very sensitive to the degree of disorder, but those degrees of disorder which give the best fit to the optical data, also are nearly equal to those observed experimentally. The degree to which the k-space structure of amorphous semiconductors resembles that of the crystal will determine the validity of this approach. In Chapter 5, it will be shown that some amorphous materials have a k-space structure different from their crystalline forms.

Phillips[89] has suggested that the isotropic/amorphous solid can be approximately formulated as a one dimensional system, and the ϵ_2 spectrum is the same as that expected for an ordered 1 dimensional system, but smeared and shifted to lower energies. The smearing and the shift to lower energies are caused by bond angle distortions and missing atoms. He has been able to explain quantitatively the position of the peak maximum in the ϵ_2 spectrum for amorphous Ge and further has suggested that under more ideal deposition conditions, films

could be made that have an ϵ_2 peak maximum close to that observed in the crystal. He also claimed that the dielectric constant at zero frequency remains unchanged since the reduction in the mean gap is compensated for by a corresponding reduction in the oscillator strength.

However Connell and Paul[78] have disagreed with Phillips's conclusions. They have calculated the effective heat of crystallization by taking into account the known bond angle distortions of several amorphous semiconductors and the known force constants for the corresponding crystalline materials. By equating the calculated heat of crystallization to the difference in the total electronic energy of the crystalline and amorphous forms of various semiconductors based on the Penn model,[90] they have been able to show that the average (or Penn) energy gap changes by no more than 10% due to the disorder. Hence, since the mass density, and therefore the plasma frequency is changed little, they have argued that $\epsilon_1(0)$ should change little also.

Much effort has been expended in attempting to explain the frequently observed exponential absorption edge in amorphous semiconductors. Tauc[91] has suggested that internal electric fields, arising from either frozen in longitudinal optical phonons or charged centers, aid the optical transitions in such a way as to give an exponential edge. Dow and Redfield[92] have proposed that internal electric fields broaden the excitonic transitions into an exponential edge. By imposing a random fluctuation having a spatial correlation

length of 6 angstroms on the potential of crystalline Si, Stern[93] has not only been able to obtain the exponential edge in amorphous Si but has been able to explain its annealing behavior in terms of a reduction of this fluctuation.

G. Structural measurements

1. Direct and indirect structural measurements

Since no single structural measurement can uniquely specify the structure, it is necessary to utilize as much information available from all types of measurements to set bounds on the proposed structural models. The structural measurements can be broken into two kinds: direct and indirect. Direct measurements involve observations of some property which is a direct consequence of the position of the atoms, such as the diffraction pattern obtained in a scattering experiment, whereas indirect measurements involve detection of an electronic or a vibrational property which is structure sensitive. The types of structural measurements available along with the information they give are listed below.

2. Density

Density measurements tell how efficiently the solid is packed. A density deficit may indicate either the presence of voids or a net expansion of the lattice, whereas a density excess may indicate a lattice contraction, or in the case of the amorphous alloys may indicate a precipitation of the constituents. Densities have generally been measured by hydro-

static techniques, and by separately measuring the weight and volume. More sophisticated, but less accurate, methods employ reductions of the high angle and small angle diffraction data. Two of these methods will be discussed in Chapters 3 and 4.

3. Microscopy

The direct observations of fluctuations down to a scale of 1 micron with an optical microscope, down to a scale of 200 $\overset{\circ}{A}$ with a scanning electron microscope, and down to a scale of 10 $\overset{\circ}{A}$ with an electron microscope are possible. Optical and scanning electron microscopes can be used on both thick and thin films, whereas the electron microscope, can be used only on films sufficiently thin to pass an electron beam. High resolution dark field electron microscopy allows the diffraction properties of very small regions 10 $\overset{\circ}{A}$ to be investigated. With these methods, it is sometimes possible to directly observe voids and crystalline regions in an amorphous matrix.

4. Small angle diffraction

Small angle diffraction in regions where the momentum transfer vectors are such that $k < 1.0 \overset{\circ}{A}{}^{-1}$, is sensitive to electronic fluctuations on a scale greater than the interatomic separations. As will be discussed in Chapter 6 this measurement, supplemented with density measurements, allows identification of the electronic charge density associated with the complementary particles producing the scattering,

whether they be voids or phase separated regions. With such
identification, the total void volume may be found, and hence,
the density of the void free material. With proper normali-
zation techniques, it is most useful for determining both the
size and number of the scatterers. From such distributions,
the total volume and surface of the scatterers can be measured,
and hence a lower bound on the number of broken bonds can be
estimated.

5. High angle diffraction

To obtain the average atomic radial environment, high
angle diffraction, either by x-rays, electrons, or neutrons
is the most valuable technique. The intensity functions
themselves are of use to theoreticians for direct incorpora-
tion into theories formulated in k-space. Inversion of the
intensity functions gives a radial distribution function from
which some of the features of the short range order may be
deduced, such as the nearest neighbor separations and numbers.
With additional analysis of the RDF, the bond angle distri-
butions and rotations may also be deduced. By a suitable in-
version of the high angle data, without the inclusion of the
small angle data, the density of the void free material may
be found.

In principle, the radial distribution functions for each
constituent in a multi-component system can be found by ex-
ploiting the dependence of the atomic scattering factor on
the wavelength of the incident radiation. However this has

never been done, perhaps for two good reasons: first, the
dependence of the magnitude of the scattering factors on the
wave length of the incident radiation is no more than about
10%; and second, to get a change this large, it is necessary
to use an incident radiation of long wave length, where the
resolving power in r-space is very poor.

6. <u>X-ray absorption spectroscopy</u>

The oscillations on the high side of the K absorption
edge have been found to be sensitive to the local environ-
ment of the atom.[94] Comparison of its absorption spectra to
that of its crystalline forms has shown that glassy GeO_2 has
a short range order much like its hexagonal crystalline
form.[95] Recently Sayers et al.[96] have successfully inverted
the fine edge structure of both crystalline and amorphous
Ge to obtain a radial density function, which has demonstrated
that the nearest neighbor separation in amorphous Ge is with-
in 1% of that of the crystal. The method, however, is in-
accurate in obtaining information concerning the higher co-
ordination shells since the data at low k values are obscured
by strong scattering and other effects. The method is limited
by the availability of adequate detectors and samples of suf-
ficient thickness so that the absorption is large enough.
In principle, its greatest advantage is in application to multi-
phase systems where it permits the local order of each com-
ponent to be investigated separately.

7. NMR and ESR

Nuclear magnetic resonance and electron spin resonance techniques have been successfully employed by chemists for years to identify particular functional groups in liquids. The resonance techniques are somewhat less useful in solid state because of the line broadening of multiplet levels. Their application to some of the borate glasses has been useful in the identification of the local coordinations of the boron atom.[97] Senturia et al.[98] have found differences in the chemical shifts in the NMR signals between the crystalline and amorphous forms of materials used in memory switching, and interpret this as indicating large changes in bonding, and hence, the structure. Koma et al.[99] have attributed a new line appearing in the NMR spectra of amorphous Te to atoms on the end of small Te chains. This NMR technique may be useful in detecting wrong bonds i.e., bonds between like atoms in the amorphous III-V's and II-VI's, since the wrong bonds are expected to produce chemical shifts in the resonance lines.

Brodsky et al.[71] have found that the ESR signals are observable in Ge, Si and SiC, and have attributed these signals to dangling bonds on internal surfaces, although this connection has never been well demonstrated. If the ESR signal is caused by internal surface, ESR offers a simpler and more sensitive method to detect surface than small angle scattering. In Chapter 6 we re-examine this connection between the ESR signal and internal surface.

8. Raman scattering

Raman scattering by the vibrational modes of the solid may provide a means to probe the local binding. Shifts in the energy of the Raman scattering peaks away from their crystalline counterparts may indicate a change in binding, which may be caused by a change in the nearest neighbor distance or coordination. Discrete structural units may be identified by comparison with known spectra. Non stoichiometric regions in the compound semiconductors may show the spectra characteristic of the phase separated materials. Wihl et al.[100] have observed vibrational spectra characteristic of crystalline antimony in amorphous GaSb films which are, according to the small angle scattering to be presented in Chapter 6, not phase separated and according to x-ray fluorescence measurements contain, within a few percent, equal numbers of Sb and Ga atoms. This result suggests that bonds between like atoms may occur even in films which are homogeneous and stoichiometric. In Chapter 5, we will present some structural measurements which support this notion.

However, it is difficult to use Raman scattering as a quantitative tool since little is known about the Raman cross section for most materials. The usefulness of the Raman scattering method is further limited by the extreme broadness of the spectra in the amorphous state, making the separation and identification of some peaks difficult, if not impossible.

Aside from small shifts in the peak positions, the spectra

observed in the tetrahedrally coordinated amorphous semicon-
ductors because of the relaxation of the k-vector selection
rules are simply a smeared version of the corresponding cry-
stalline single phonon density of states.[100,101] This sug-
gests that the nearest neighbor separation and coordination
of these materials are the same as those of the crystal. In
Chapter 5, some RDF's will be presented which confirm this
for some III-V semiconductors.

9. Optical absorption

IR absorption has been found useful in the identification
of discrete structural units by the comparison of the unknown
spectra with known.[72,102,103] For example, by comparing the
IR spectrum of amorphous Se with those of its two crystal-
line forms, Zallen and Lucovsky have almost conclusively
shown that the SRO of amorphous Se is the same as that of its
monoclinic crystalline form.[103] Tauc et al.[72] have observed
IR absorption bands which they have attributed to local a-
tomic configurations or intrinsic defects characteristic of
amorphous Ge. They have suggested that the band occurring at
.23ev may be from the same defect that is induced by radia-
tion damage into crystalline Ge. Since the bands they found
are of different strengths/ depending on the preparation,
this method may also provide a
sensitive means of detecting small structural differences bet-
ween different films.

It has been speculated that the ideal amorphous state is
characterized by a sharp absorption edge and that the pre-
sence of defects modifies this edge by introducing states in-

to the gap.[77] If this is so, observation of the optical edge provides a very sensitive measure of the degree of perfection of the amorphous solid. Since most direct structural measurements at best have an accuracy of only a few percent, the optical measurements may be the only means to determine the necessary perfection of the solid.

10. Calorimetry

Calorimetry gives us the total energy involved in the amorphous to crystalline transformation, and an estimate of the crystallization temperature. The behavior of the specific heat as a function of temperature may also indicate some structural transformation going on before the onset of crystallization.

H. Structural models

To gain the details of the structure, small models constructed with physical units are useful. At the present level of sophistication, model builders are content to fit only the gross structural characteristics of the experimental RDF's.[104-106] Experimental RDF's are deficient because they indicate only the ensemble average radial fluctuations. The extraction of angular information, such as the distribution of bond rotations, is somewhat uncertain. Detailed angular information and other local structural correlations can only be gained if a 3 dimensional model is constructed which adequately describes the experimental RDF. Unfortunately, the fitting of the experimental RDF is not by any means proof

that the model represents the true structure, since such a fit may not be unique; however, the greater the number of peaks in the RDF that can be explained by the model, the more credible becomes the model.

The usefulness of such models has been demonstrated by Bell and Dean[105] who have calculated the configurational entropy of their sticks and balls model of SiO_2. Henderson and Herman[106] have been employing small clusters of disordered atoms, periodically extended to fill all space, to calculate the electronic properties of amorphous Ge.

The types of structural models proposed for the amorphous state fall into two categories; first, the domained structures, in which the solid is believed to be comprised of ordered domains of dimensions of about 10-15 Å; and second, the continuously connected networks in which no regular structural unit occurs except for the five atom tetrahedral unit. It is believed that for formation of the domain networks, the atoms first prefer to conglomerate into small clusters which are more energetically stable, and then these clusters become embedded into the bulk of the structure without any further association into larger units. In the continuous network structures, on the other hand, it is believed that during deposition the atoms quickly become part of the surface by permitting its bonds to distort so as to enable it to satisfy its bonding and to maximize the connectivity of the network.[107]

The microdomain model is at first the easiest to visualize until one attempts to describe how these domains are to be

connected so as to maintain both incoherent diffraction between themselves and the number of broken bonds minimal. As of now, no one has been able to give a prescription on how to do this. For the size of the domain indicated by diffraction, about half of the atoms must reside on the surface of the domains. Unless there is some mechanism to satisfy these bonds, the increase in energy would be intolerably high. In the continuous networks, however, connectivity is essentially the building prescription, but this connectivity must be paid for energetically by allowing bond angle distortions. Which of the two types of models is more energetically favorable cannot be determined until detailed specification of each is available.

The early workers on the amorphous state, perhaps biased by their previous experiences with crystalline solids, realized that very small crystallites gave broad diffraction lines typical of amorphous structures and suggested that the amorphous state was made of an assembly of crystals 10 - 15 Å in size.[108]

Richter and Breitling[80] have suggested the existence of a two phase system consisting of small microcrystals separated by completely random regions. The details of the random regions and how they connect with the crystallites have not been specified. Moss and Grazyk[81] have shown that the scattering from a single isolated microcrystal can not reproduce the experimental scattered intensity. Since they did not include inter-particle scattering, which becomes large when the size of the domains becomes small and the number

of surface atoms becomes large, their results are not con-
clusive. In Chapter 5 we present the results of a calcula-
tion   which includes the interparticle scattering almost
exactly for an assumed random correlation between micro-
crystals.

The strongest evidence against the microcrystal model is
the absence of the 3rd crystalline nearest neighbor peak in
the RDF of the amorphous material. [80,81] Grigorovid and
Manaila[109] realizing this inadequacy of the microcrystal-
line model and noting the prevalence of the peaks at 6.1 Å
and 8.0 Å in the amorphous RDF (see Chapter 5) have suggested
that the domains are not crystalline but are amorphon clusters,
i.e., pentagonal dodecahedrons. They have postulated that
the structure is characterized by three properties:

1) the nearest neighbors preserve the tetrahedral form, but
   the bond lengths are expanded by 3-5%.

2) the rotations of the dihedral angle cannot be arbitrary
   in order to preserve 1.

3) the rotations must either be staggered or eclipsed.

To fill in some regions in the RDF in which no amorphon dis-
tance occurs, they have found it necessary to introduce some
diamond-like structure. The resulting structure is assumed
to be made of domains of diamond, wurtzite and amorphonic
structure continuously connected to one another.

Turnbull and Polk[107] have pointed out that the density
of such a network is much lower than observed since it in-
corporates large holes into the structure. In Chapter 7,

some computer generated models will be presented which show that the Grigorovici-Manaila[104] models cannot fit the experimental RDF's.

The microdomain models had been losing popularity until their recent revival by M.L. Rudee,[110] who has observed spots in his micrographs corresponding to regions about 10-15 $\overset{o}{A}$ in diameter. He has interpreted this as evidence of coherent diffraction effects taking place on a scale of 10-15 A, which can only be explained by ordered regions of this size, or by microcrystals. However it is not evident that this should not also be expected of a continuous network model. In Chapter 5 a radial distribution function of Ge made in exactly the same way as one of the films investigated by Rudee[110], will be presented which shows that the short range order is not the same as that of the crystal.

Using common plastic tetrahedra as the basic structural unit, Polk[111] has constructed an almost entirely connected network which he believes represents the ideal random structure. That is, random in the sense that we have no recognizable structural unit beyond the basic tetrahedron. The structure is then defined statistically in terms of bond lengths, and angles, dihedral angles and perhaps numbers of n membered rings. The basic characteristics of this model are:

1) the first nn distance is spread no more than .03 $\overset{o}{A}$.

2) the rms bond angle distortion of the tetrahedron is 10°

3) the distribution of the dihedral angle, as well as it can be defined, appears to be flat.

4) the density deficit, as constructed, is 7%, while the average nearest neighbor position is expanded by 1% over that of the crystal.

5) the density deficit, after imposing the constraint that the average nearest neighbor position be equal to the crystalline, becomes 3%.

Unfortunately, this model is small and its RDF does not extend beyond the 4th crystalline coordination shell; hence, it is not known whether this model can reproduce the crucial peaks at 6.1 and 8.0 $\mathring{A}$. It is somewhat difficult to imagine that such a model with a flat dihedral angle distribution can give these peaks, since if the 3rd and 4th crystalline peaks were washed out, the higher order coordination peaks should be washed out even more. Until his RDF is extended to show these peaks, it cannot be fully accepted as representing the true structure. At this time, however, the great merit of this construction is that it shows that it is at least geometrically possible to complete the valency of every atom without too severe bond distortions.

Much less work has been done on the alloy systems for two reasons: first the interpretation of the experimental RDF is very complicated for a homogeneous multicomponent system; and second, the possibility of the coexistence of separate phases adds to this complexity. The work that has been done on amorphous GeTe and GeSe has been most successfully interpreted in terms of a random covalent model in which each atom

satisfies its bonding requirements without caring to which type of atom it bonds.[65,112]

The microcrystal models at first appear to be the most likely candidates for ionic materials, since they can easily allow the atoms to retain their ionic bonding. The continuous random network models, as well as those proposed by Grigorovici,incorporate large numbers of 5 membered rings, making it necessary that large numbers of wrong bonds be found. In an alloy structure, wrong bonds are those between like atoms. Drummond[3] has found that in order to maintain the stoichiometry of a III-V or similar compound in the model constructed by Polk, a minimum of 12% of the bonds must be wrong.

It is of interest to see if increasing the difference in ionicity of the constituents in any way alters the structure. In Chapter 5 RDF's will be presented which answer this question.

REFERENCES

1. W. Shockley, preface to Electrons and Holes in Semi-conductors, D. Van Nostrand Co. Inc., New York 1950

2. J.M. Ziman, J. Phys. C., 2, 1784 (1969)

3. C. Drummond, private communication

4. A.F. Ioffe and A.R. Regel in Progress in Semiconductors (Wiley, New York, 1960) Vol. 4, 237

5. D. Weaire, Phys. Rev. Lett. 26, 1841 (1971)

6. A.E. Gubanov, Quantum Electron Theory of Amorphous Con-ductors, (Consultants Bureau, New York, 1965)

7. S.F. Edwards, Phil. Mag. 6, 617 (1961)

8. P.W. Anderson, Phys. Rev. 109, 1442 (1959)

9. V.L. Bonch-Bruevich, Phys. Lett. 18, 260 (1969)

10. P. Lloyd, J. Phys. C. Ser 2, 2, 1717 (1964)

11. F. Broers, J. Non-Cryst. Solids 4, 428 (1970)

12. E.N. Economou and M.H. Cohen, Phys. Rev. Lett. 16, 1445 (1970)

13. D.J. Thouless, J. Phys. C. 3, 1554 (1970)

14. J.M. Ziman, J. Phys. C. 2, 1230 (1969), Ibid 1, 1532 (1968)

15. D.L. Camphausen, G.A.N. Connell, and W. Paul, Phys. Rev. Lett. 26, 184 (1971)

16. K. Hiroike, Phys. Rev. 138A, 422 (1965)

17. R.E. Borland, Proc. Phys. Soc. (London) A78, 926 (1961)

18. A.P. Roberts and R.E.B. Mackinson, Proc. Phys. Soc. (London), A79, 630 (1962)

19. H.M. James and A.S. Ginsburg, J. Phys. Chem. 57, 840 (1953)

20. N.J. Shevchik, to be published

21. N.F. Mott, Adv. in Phys. 16, 49 (1967)

22. B.I. Halperin, Adv. in Chem. Phys. 102, 123 (1967)

23. R.E. Borland and N.F. Bird, Proc. Phys. Soc., 83, 23 (1969)

24. N.F. Mott and W.D. Twose, Adv. in Phys. 10, 107 (1961)

25. A. Goldberg, H.M. Schey, J.L. Schwartz, J. Amer. Phys. 35, 177 (1967)

26. L. Banyal, Seventh International Conference on the Physics of Semiconductors, Paris, 1964, (Academic Press, New York, 1965) p. 417

27. M.H. Cohen, H. Fritzsche, S.R. Ovshinsky, Phys. Rev. Lett. 22, 1065 (1970)

28. N.F. Mott, Phil Mag. 8, 24 (1971), Ibid 19, 835 (1970) and J. Non-Cryst. Solids, 1, 2 (1968)

29. H. Fritzsche, J. Non-Cryst. Solids, 6, 49 (1971)

30. G.B. Inglis and F. Williams, Phys. Rev. Lett. 25, 1275, (1970) and J. Non-Cryst. Solids, 5, 313 (1971)

31. J. Stuke, J. Non-Cryst. Solids 4, 1, 1970

32. A.H. Clark, Phys. Rev. 154, 750 (1967)

33. K.L. Chopra and S.K. Bahl, Phys. Rev. B2, 2545 (1970)

34. R. Grigorovici, Mat. Res. Bull. 3, 13 (1968)

35. P.A. Walley and A.K. Jonscher, Thin Solid Films, 1, 367 (1968)

36. P.A. Walley, Thin Solid Films 2, 327 (1968)

37. R.C. Chittick, J. Non-Cryst. Solids 3, 255 (1970)

38. F. Argall and A.K. Jonscher, Thin Solid Films 2, 185 (1968)

39. R.S. Allgaier, J. Vac. Sci. and Tech. 8, 113 (1971)

40. E.A. Davis and N.F. Mott, Phil. Mag. 22, 903 (1970)

41. A.K. Jonscher, Thin Solid Films 1, 213 (1967)

42. N. Croitoru and L. Vescan, Thin Solid Films, 3, 269 (1969)

43. R.M. Hill, Phil. Mag. 23, 59 (1971)

44. G.A.N. Connell, D.L. Camphausen and W. Paul, Phil. Mag., to be published

45. C.J. Adkins, S.M. Freake, E.M. Hamilton, Phil. Mag. 22, 183 (1970)

46. K. Moorjani and C. Feldman, J. Non-Cryst. Solids, 4, 248 (1970)

47. M. Morgan and P.A. Walley, Phil. Mag. 22, 661, (1971)

48. J.L. Hartke and P.J. Regensburger, Phys. Rev. 139A, 970 (1965)

49. D.L. Camphausen, G.A.N. Connell, and W. Paul, J. Non-Cryst. Solids, in press

50. W.E. Howard and R. Tsu, Phys. Rev. B1, 4709 (1970)

51. W.E. Eckenbach, W. Fuhs, J. Stuke, J. Non-Cryst. Solids, 5, 264 (1971)

52. J.E. Fisher, T.M. Donovan, J. Non-Cryst. Solids, in press

53. D. Adler, H.K. Bauen, L.P. Ferrao, D.D. Marchant, and R.N. Singh, J. Non-Cryst. Solids, in press

54. J. Stuke, Proc. of the Tenth International Conference on the Physics of Semiconductors, (Cambridge, Mass 1970) USAEC Div., Tech Inform. Oak Ridge, Tenn. 1970

55. V. Heine and R.O. Jones, J-Phys. C2, 719 (1968)

56. T.M. Donovan, W.E. Spicer, J.M. Bennett and E.J. Ashley, Phys. Rev. B2, (1970)

57. J. Tauc, L. Stourac, V. Vorlicek, M. Zavetova, Ninth International Conference on the Physics of Semiconductors, Moscow, 1968, (Novka Leningrad 1968) 1251

58. J.E. Davey and T. Pankey, J. Appl. Phys. 35, 2203 (1964); T. Pankey and J.E. Davey, J. Appl. Phys. 37, 1507 (1966)

59. J.E. Davey and T. Pankey, J. Appl. Phys. 40, 212 (1969)

60. R.P. Howson, Brit. J. Appl. Phys. D1, 15 (1968)

61. I.H. Khan, Surface Sci. 9, 306 (1968)

62. G.A.N. Connell and W. Paul, J. Non-Cryst. Solids, in press

63. S.K. Bahl and K.L. Chopra, J. Appl. Phys. 40, 4440 (1969)

64. D.B. Dove, M.B. Heritage, K.L. Chopra, and S.K. Bahl, Appl. Phys. Lett. 16, (19⁻0)

65. F. Betts, A. Bienenstock, and S.R. Ovshinsky, J. Non-Cryst. Solids, 2, 347 (1970)

66. J. Feinleib and S.R. Ovshinsky, J. Non-Cryst. Solids, 4, 564 (1970)

67. J.T. Edmond, Brit. J. Appl. Phys. 17, 979 (1966)

68. E.A. Fagen and H. Fritzsche, J. Non-Cryst. Solids 2, 180 (1970)

69. R. Tsu, W.E. Howard, L. Esaki, J. Non-Cryst. Solids 4, 322 (1970)

70. C.J. Mogab and W.D. Kingery, J. Appl. Phys. 39, 3640 (1968)

71. M.H. Brodsky, R. Title, K. Weiser, G.D. Pettit, Phys. Rev. B1, 2632 (1970)

72. J. Tauc, A. Abraham, R. Zallen, and M. Slade, J. Non-Cryst. Solids, 4, 279 (1970)

73. A.M. Glass, Canad. J. Phys. 43, 1068 (1965)

74. C. Wales, G.J. Lowitt, R.A. Hill, Thin Solid Films, 1, 137 (1967)

75. W.C. Dash and R. Newman, Phys. Rev. **99**, 1151 (1955)

76. M.L. Theye, Mat. Res. Bull. **6**, 103 (1971) and Optics Comm. **2**, 7, 329, 1970

77. W. Paul, G.A.N. Connell and N.J. Shevchik, Bull Amer. Phys. Soc. **16**, 347 (1971)

78. G.A.N. Connell and W. Paul, J. Non-Cryst. Solds, in press

79. R. Bauer and F. Galeener, J. Non-Cryst. Solids, in press

80. H. Richter and G. Breitling, Z. Naturforschg. **139**, 988 (1958) and Mat. Res. Bull. **4**, 19 (1969)

81. S.C. Moss and J.F. Graczyk, (Tenth Internation Conference on the Physics of Semiconductors), Cambridge, Mass. 1970, U.S.A.E.C. Div., Tech. Inform. Oak Ridge, Tenn. 1970, 658

82. H.S. Chen and D. Turnbull, J. Appl. Phys. **40**, 4214 (1969)

83. F. Herman and J.P. Van Dyke, Phys. Rev. Lett. **21**, 1578 (1970)

84. T.M. Donovan and W.E. Spicer, Phys. Rev. Lett. **21**, 861 (1970)

85. D. Brust, Phys. Rev. **186**, 768 (1964) and Phys. Rev. Lett. **23**, 1232 (1969)

86. W.E. Spicer and T.M. Donovan, Phys. Rev. Lett. **24**, 595 (1970)

87. B.K. Chakraverty, Proc. Congress. Int. sur les Couches Minces, Cannes, October, 1970 S.F.I.T.V., Paris, 1970 427

88. B. Kramer, Phys. Stat. Sol. **41**, 649 (1970) Ibid **41**, 725 (1970); and J. Non-Cryst. Solids, in press

89. J.C. Phillips, Phys. Stat. Sol. b44, kl (1971)

90. J.C. Phillips and J.A. Van Vechten, Phys. Rev. B2, 2147 (1970)

91. J. Tauc, Mat. Res. Bull. 3, 37 (1968)

92. J.D. Dow and D. Redfield, Phys. Rev. B1, 3358 (1970)

93. F. Stern, Phys. Rev. 3, 2636 (1971)

94. L.V. Azavoff, Rev. Mod. Phys. 35, 1021 (1963)

95. W.F. Nelson and I. Siegel, Phys. Rev. 127, 2025 (1962)

96. D.E. Sayers, F.W. Lytle, E.A. Stern, Phys. Rev. Lett. 27, 1204 (1971); J. Non-Cryst. Solids, in press; and in Advances in X-ray Analysis, Vol. 13, Plenum Press (1970)

97. P.J. Bray and A.H. Silver, in Modern Aspects of the Vitreous State, ed. J.P. Mackensie, (Butterworth, London, 1960) Vol. 1, p. 92

98. S.D. Senturia, C.R. Howes and D. Adler, J. Appl. Phys. 41, 430 (1970)

99. A. Koma, O. Mizumo, S. Tanaka, Phys. Stat. Sol. B46, 225, (1971)

100. M. Wihl, J. Tauc and M. Cardona, J. Non-Cryst. Solids, in press

101. J.E. Smith, M.H. Brodsky, B. Crowder and M.I. Nathan, J. Non-Cryst. Solids, in press

102. G. Lucovsky, Mat. Res. Bull. 4, 505 (1964)

103. R. Zallen and G. Lucovsky, in Selenium, W.C. Cooper and R.A. Zingavo, Eds. Van Nostrand Reinhold, New York 1971

103. D.L. Evans, S.V. King, Nature 212, 1353 (1966)

105. R.J. Bell and P. Dean, Nature 212, 1354 (1966)

106. D. Henderson and F. Herman, J. Non-Cryst. Solids, in press

107. D. Turnbull and D.E. Polk, J. Non-Cryst. Solids, in press

108. J.T. Randall, H.P. Rookesby. B.S. Cooper, J. Soc. Glass Tech. 14, 219 (1930)

109. R. Grigorovici and R. Manaila, Thin Solid Films 1, 343 (1967)

110. M.L. Rudee, Phys. Stat. Solidi 46b, K1 (1971)

111. D.E. Polk, J. Non-Cryst. Solids, 5, 365 (1971)

112. R.W. Fawcett, G.S. Cargill III, C.N.J. Wagner, J. Non-Cryst. Solids, in press.

CHAPTER 2

SAMPLE PREPARATION

A. Introduction

Each of the tetrahedrally coordinated amorphous semiconductor of the amorphous Ge family has been prepared by one of more of the following methods: electrodeposition,[1-3] sputtering,[4] ion bombardment,[5] evaporation, and decomposition of its hydrides with a glow discharge.[6] None of the tetrahedrally coordinated semiconductors, Ge,Si, and the III-V's, has been prepared by quenching from the melt as has been a variety of other materials, such as Se, Te and glasses based on these elements. In this investigation, three methods of preparation have been used: electrodeposition to prepare amorphous Ge; sputtering to prepare amorphous Ge, GeSn, GaAs, GaP, GaSb, and InSb; and evaporation tc prepare amorphous Ge. The first step common to these three processes is the dispersal of the constituents into atomic form and aggregates consisting of a few atoms, and the second is their collection on a substrate held at sufficiently low temperatures so that crystallization is inhibited.

In the electrodeposition process, the dispersal of the atoms is achieved by the ionization of a metallic salt containing the element to be deposited in a fluid having a high static dielectric constant. The positive metallic ions are then drawn to the cathode which is held at a negative potential. When the ion comes close enough to the cathode, an

electron is transferred from the cathode to the ion, thereby neutralizing the ion into a free atom. This atom is then free to wander about the surface of the cathode until it bonds with a favorable site on the surface of the cathode. In this way, a thick deposit can be built up atom by atom.

Contamination can arise in this process by incorporation of impurities within the solvent or of the solvent itself. Also, in some cases the co-evolution of H at the anode makes it likely that films prepared by electrodeposition are heavily contaminated with H gas.

So far, of the materials investigated here, only amorphous Ge and Se have been successfully electrodeposited.[1-3] In this investigation, Ge has been electrodeposited by the technique devised by Szekely[1] (Szekely[1] was apparently unaware that the films produced by his method were amorphous, It was Chen[10] who later discovered their amorphous nature). Application of this method to the electrodeposition of the III-V compounds appears to be impossible because the large electrochemical potential differences between group III and group V elements makes it virtually impossible to maintain stoichiometry.[11]

In the sputtering process, the dispersal of the atoms is achieved by bombarding the source target, which is made of material to be deposited, with inert gas ions having energies from 500 to 10,000 electron volts.[12] Upon colliding with the target, the ions knock away several atoms which are then collected on a cooled substrate.

Contamination can arise from an inadequate vacuum and even from incorporation of the inert gas into the structure. Also, electron bombardment of the substrate during deposition can significantly affect the structure of the resulting film.[12]

The advantage of sputtering is that every solid material can be deposited, including alloys and compounds, without severe stoichiometry problems. Since the stoichiometry of the reulting film is usually close to that of the starting target material, it is easy to make compound materials starting from a pressed powdered mixtures of two or more elements.

In the evaporation process, the dispersal of the atoms is achieved by raising the temperature of the source material sufficiently so that the vapor pressure of the source material increases to a point where a large number of atoms can leave the source material. The evaporated atoms are subsequently collected nearby onto a cooled substrate. The evaporation of a single element is easily achieved with this method, but for the deposition of alloys and compounds, care must be taken so that the stoichiometry of the deposited material is maintained.

Flash evaporation, in which the compound material is entirely vaporized as soon as it hits the crucible, insures that equal numbers of each type of atom are evaporated. However, it is difficult to obtain films several microns thick with this method. On the other hand, the three temperature method,

as discussed by Gunther and Fueller[13] in which two sources
are heated separately and the temperature of the substrate
is held so that one of the components is volatile, allows
thick, stoichiometric, amorphous films to be made.[7-8]

In the evaporation process contamination can be caused
by a poor vacuum, and also, the radiant heat emitted from the
heated source material may effect the structure of the film.

B. Electrodeposition

1. The electrodeposition system

The schematic of the electrodeposition system, consisting
of DC power supply and current stabilizer, a temperature
sensor and controller, a Fisher Thermix, and an electrode-
position cell, is shown in Figure 2-1. The General Radio
power supply, capable of delivering 25 amps from 0 to 100
volts DC, serves as an adequate constant voltage supply; under
normal operating conditions, 60 volts and 1 amp, the ripple
in the output has been found to be less than 0.1%. However,
the plating process is governed by the current density, not
the applied voltage, and it is essential to keep the current
as stable as possible. Since the supply's output is at con-
stant voltage, and since during deposition the resistance of
the cell changes, it is impossible to maintain constant cur-
rent with the DC power supply alone. The current is stabi-
lized to 0.02 amps by employing between the deposition cell
and the DC power supply a simple cathode follower circuit
using a Motorola 2N1365 power transistor.
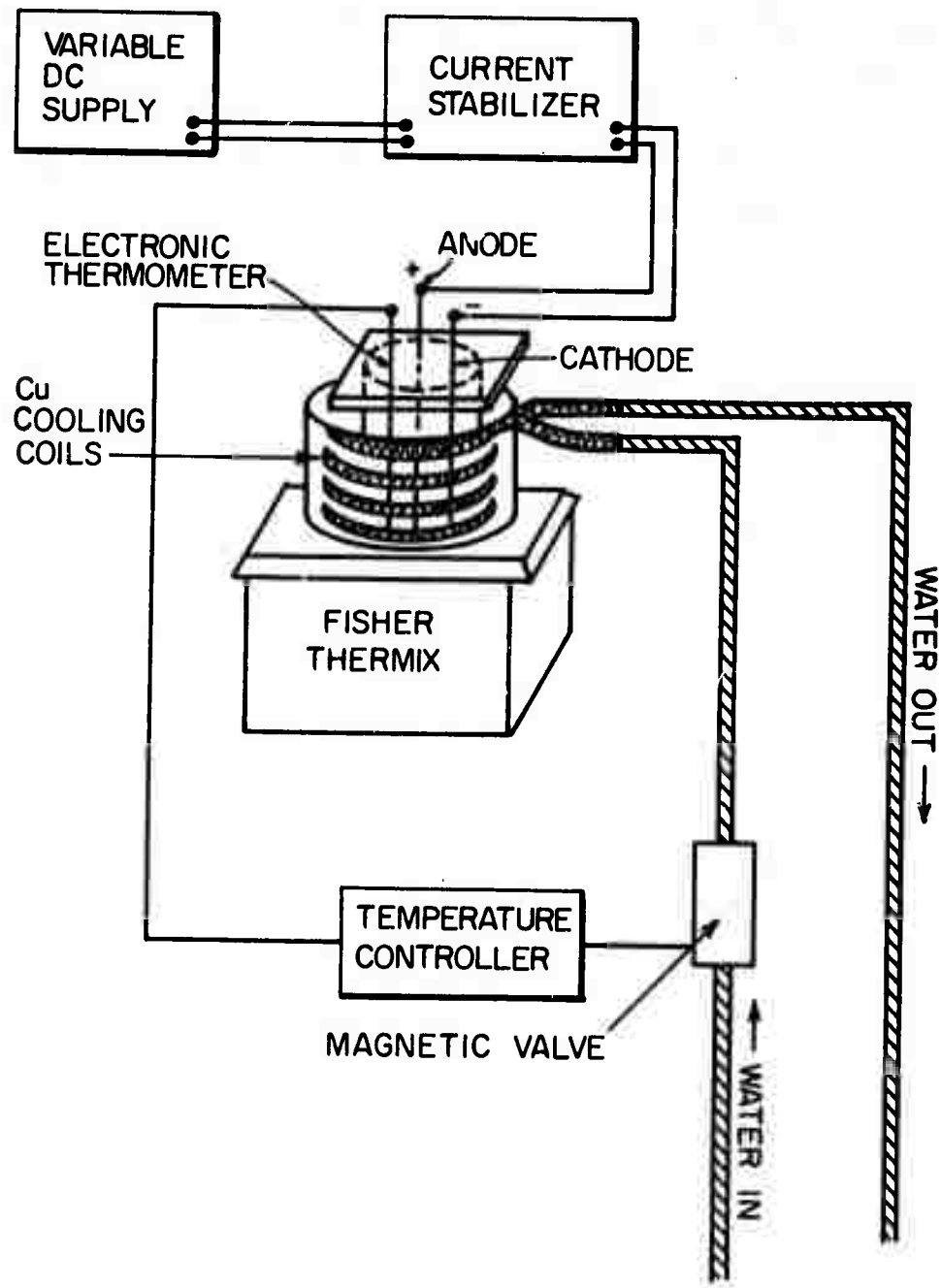
FIG. 2-1 SCHEMATIC OF ELECTRODEPOSITION SYSTEM

The temperature of the electrolytic bath is monitored with an electronic thermometer, consisting of a Fenwall JA33J1 thermistor placed into a glass tube, which is then immersed into the electrolytic bath. When the bath temperature becomes greater than some temperature, T_c, determined by the dial setting on the temperature controller, the controller opens the magnetic valve allowing water to flow through the Cu cooling coils. When the temperature falls below T_c, the controller closes the watervalve and the heat generated by the deposition process raises the temperature of the cell to T_c again. In this way the temperature of the electrolytic bath is held stable to $\pm 2^{\circ}$ C.

Since the resistance of the cell depends strongly on the temperature of the bath and the amount of heat generated depends upon the resistance of the bath, it is necessary to regulate both the temperature and the current if stable operating conditions are to be achieved.

The electrodeposition cell is shown in more detail in Figure 2-2. The arrangement of the electrodes is admittedly not the ideal for electrodeposition, (when both the anode and cathode would be infinite planes[13]), but the necessity of having to produce thick films at a reasonable cost requires that a small cathode, and hence, non-ideal geometry be used. The anode consists of a high purity graphite rod, 1/4" in diameter. The mercury thermometer serves to check the temperature of the bath and as a standard to set the temperature controller.
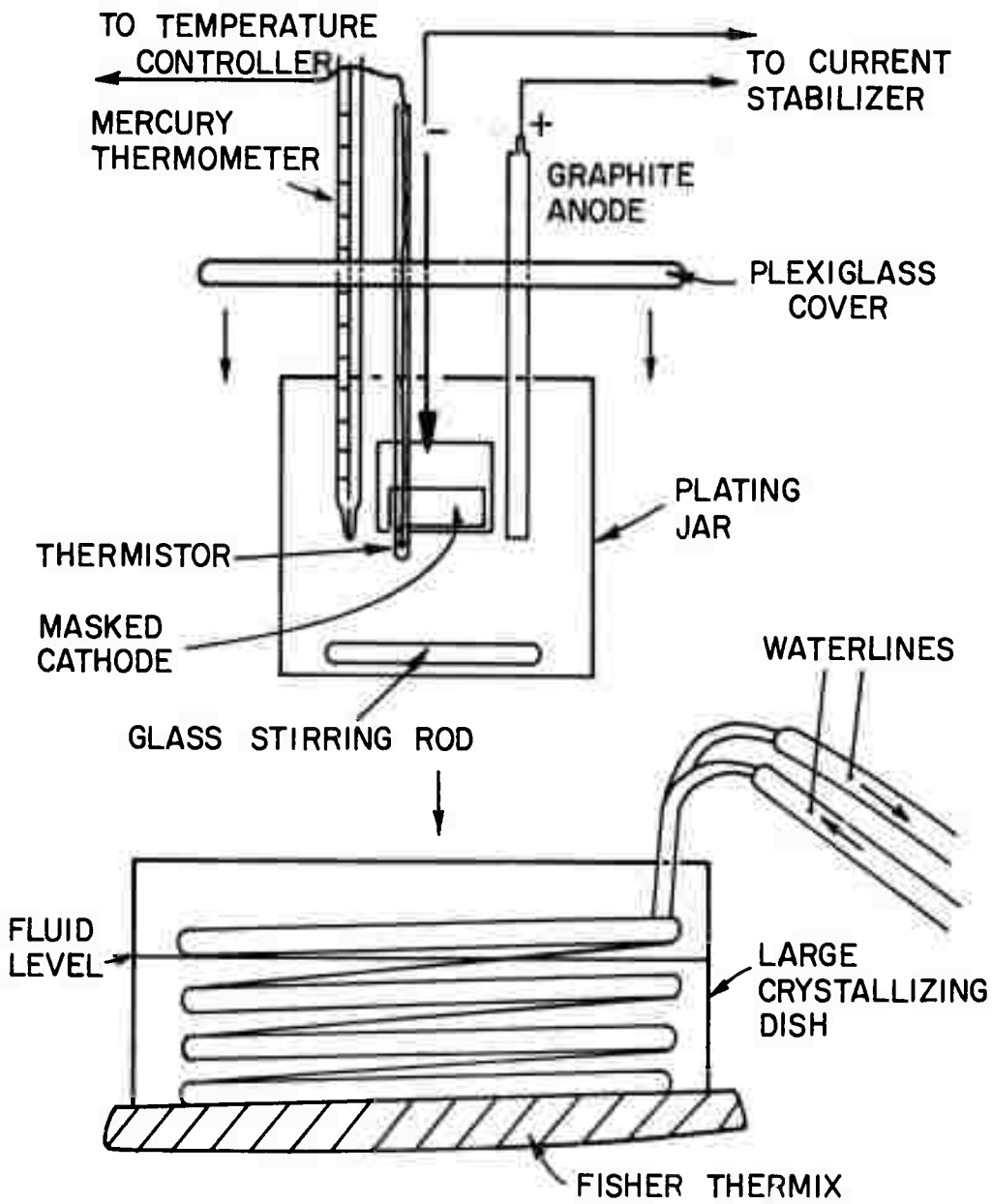
FIG. 2-2 SCHEMATIC OF ELECTRODEPOSITION CELL

The mercury thermometer, high purity graphite anode, electronic thermometer, and cathode wires all passing through holes drilled into a plexiglass plate, together comprise the top assembly, which is placed over the mouth of the jar during deposition. To prevent contamination of the bath with plexiglass, the underside of the plexiglass plate is thoroughly coated with "Microshield" (from Michigan Chrome and Chemical). In the bottom of the cell lies a stirring rod consisting of a magnetic rod sealed in a glass tube. During deposition, the cell is placed into the large crystallizing dish containing the Cu coils and propylene glycol. The Fisher Thermix drives the magnetic rod and provides heat to the solution when necessary.

2. Electrodeposition procedure

After the substrate is sanded with fine sandpaper and polished with Linde A to produce a shiny surface, it is ultrasonically cleaned in trichloroethylene, and then, in methanol. The substrate is then weighed on a Christian Becker equal arm balance to 0.001 gram, an alligator clip and a wire are attached, and all but the usual 1 cm by 2 cm plating area is covered with a thick coat of Microshield, which is then permitted to dry for a minimum of 12 hours. Attempts to use the substrate before allowing the Microshield to set for at least 12 hours have been unsuccessful since the Microshield comes off the substrate after a few hours of deposition.

The propylene glycol is added to the cell and heated to

the proper operating temperature, while the agitation of the magnetic stirring rod keeps the temperature uniform throughout the solution. The $GeCl_4$ (99.999% purity, obtained from Alpha Chemical, now a division of Ventron) is added and given about three minutes to mix. With the voltage applied between the anode and cathode, the top assembly is placed onto the top of the jar, and the heights of the mercury and electronic thermometers, the anode, and cathode are adjusted until their ends are immersed in about 1" of the electrolyte. Inserting the anode and cathode into the electrolyte with no voltage applied would allow some of the cathode material to dissolve into the solution where it can later plate back with the Ge film, thereby contaminating the film. Inserting the cathode and anode into the electrolyte with a voltage applied helps to reduce contamination from the cathode by allowing a deposit of Ge to commence rapidly.

After a satisfactory amount of Ge has been deposited, the film is removed from the solution, allowed to cool to room temperature, and then bathed in acetone to remove the Microshield. The sample and substrate are then weighed, and the amount of sample deposited is determined. When required, the Ge is removed from the Cu substrate by dissolving it in a solution of 500 grams of chromic acid and 27 ml of sulphuric acid in 1000 ml of water. After the substrate dissolves away, the Ge film usually breaks up into several smaller pieces, the largest of which measure about $0.2 \times .5 \ cm^2$. The break-up of the film is believed to be caused by the different ther-

mal expansions between Ge and Cu which leads to strains which finally are relieved when the supporting substrate is removed.

3. Some comments on the electrodeposition procedure

The substrate normally consists of a rectangular Cu sheet about 1" square and 15 mils thick. Thinner substrates about 5 mils thick always warp badly during the deposition process. For thicker more rigid substrates, about 30-50 mil and thicker, the warpage is reduced or is absent, but the Ge film shatters off the substrate during deposition, making the surface rough and inadequate for diffraction experiments. The 15 mil thick Cu substrates are about optimum for off-setting the effects of thermal expansion and warpage.

The deposition has been found to be successful on Ta and Mo; it has been found to be/unsuccessful on Zn, Al and Ni, possibly because these materials appear to be attacked by the electrolytic solution.

Chen[10] found it necessary to change solutions of $GeCl_4$ and propylene glycol several times during a run to achieve a 50 micron thickness.[11] However, this thickness has been achieved often from a single bath of 7 ml of $GeCl_4$ in 100 ml of propylene glycol operating at a current density of 0.4 amps/cm^2 onto a substrate with an area 2cm^2 at a deposition temperature of 55° C. It has also been found unnecessary to fractionally distill the propylene glycol (from Fisher Scientific, cat. no. P-354) before using it in the bath solution. Chen's reduced rate of plating may be attributed to

the use of an evacuated plating cell. Since at atmospheric pressure the boiling point of $GeCl_4$ is 77° C, and since normal operating temperature is about 50° C, appreciable amounts of $GeCl_4$ may have boiled out of Chen's solutions.[10]

The maximum thickness obtained from any single bath is 50 microns. One of the limiting factors is an increasing sample resistance due to its increasing thickness, which requires a higher power input to maintain the same current density, and hence a larger amount of heat need be dissipated. The system used here is limited to a power dissipation of about 50 watts, limiting the operating current to 0.8 amps. The growth of the film is also limited by the eventual deterioration of the Microshield masking agent. When the Microshield deteriorates the Ge begins to plate on areas that had been masked with the Microshield rather than on the desired area. At an operating temperature of 50° the Microshield deterioration appears to be slight, but at temperatures of 60° and above the lifetime of the Microshield is only a few hours.

C. Sputtering

1. The DC sputtering system

The schematic of the arrangement used for sputtering is shown in Figure 2-3. The sputtering module, a R.D. Mathis SP210 triode system, is evacuated by a Welch 3101A turbo-molecular pump having a 200 liter/sec pumping speed. The bottled 99.999% pure Argon gas is fed via a regulator and
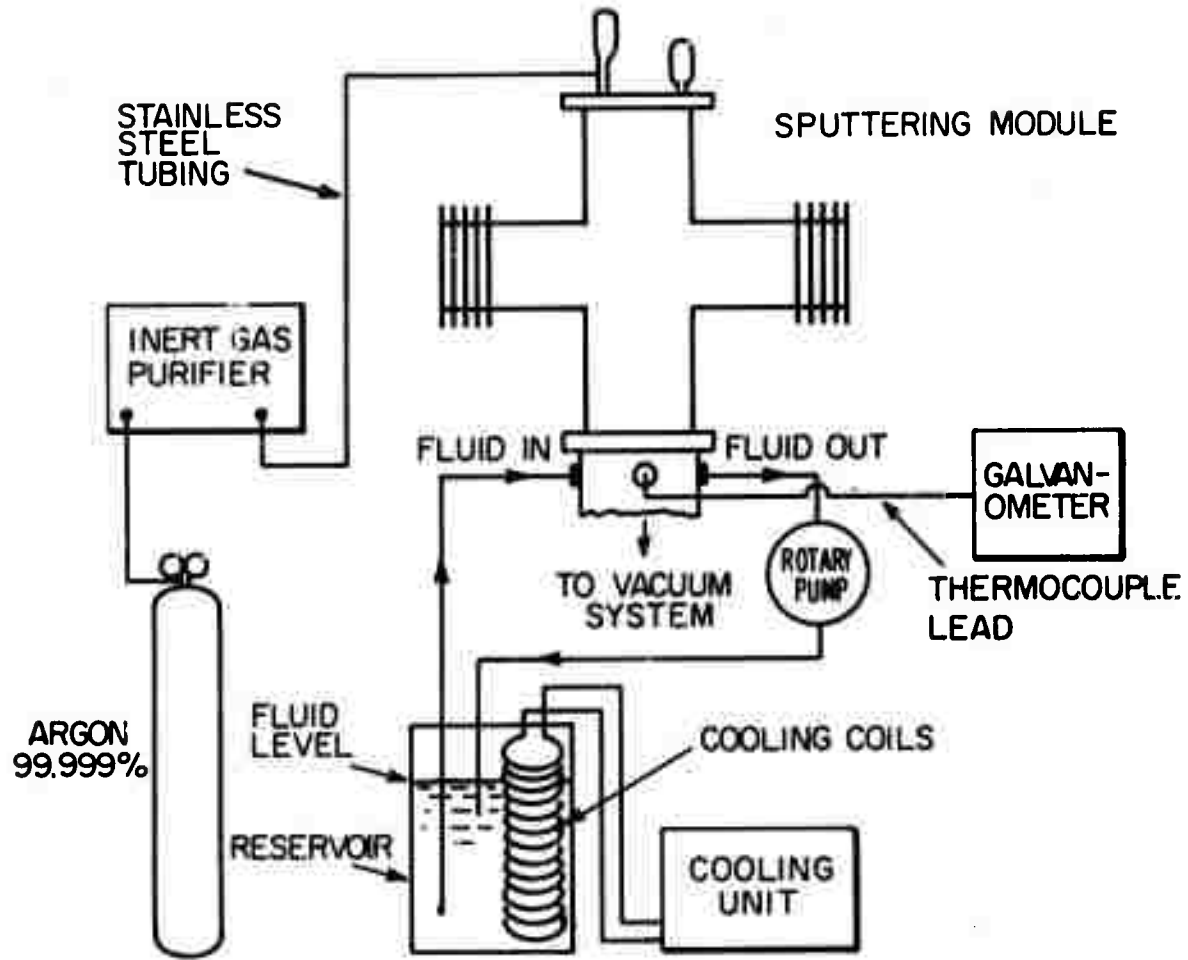
FIG. 2-3 SCHEMATIC OF SPUTTERING DEPOSITION SYSTEM

copper tube into an R.D. Mathis inert gas purifier, where the purification of the gas, according to R.D. GP100 Mathis Co., is increased to 1 part per million. The purified gas then travels through a stainless steel tube to the needle valve on top of the sputtering module through which it is fed into the bell jar. The temperature of the cooling fluid, a 50/50 mixture of tap water and ethylene glycol, is controlled by a Blue M Constant Flow Portable Cooling Unit. The cooling fluid is circulated through the sputtering module and returned to the reservoir by the Teel rotary pump. The substrate temperature is monitored by the galvanometer reading of the copper-constatan thermocouple.

The details of the sputtering module are shown in Figure 2-4. The cooling stage consists of a hollow cylindrical block through which circulates the cooling fluid, by entering and leaving through the port holes in the base plate. The substrates are placed on top of the substrate plate which is held at ground potential. The thermocouple is placed to measure the temperature of the top of the substrate plate. The tungsten filaments supply the thermionic electrons which are accelerated towards the anode, thereby colliding with argon atoms producing a glow discharge. The magnetic field coils produce a field which serves to increase the total path length of the thermionic electrons, thereby increasing the probability that they will ionize the argon gas. The target is fastened with a thermally conductive epoxy to the end of a cylindrical copper block, which is then screwed onto the copper
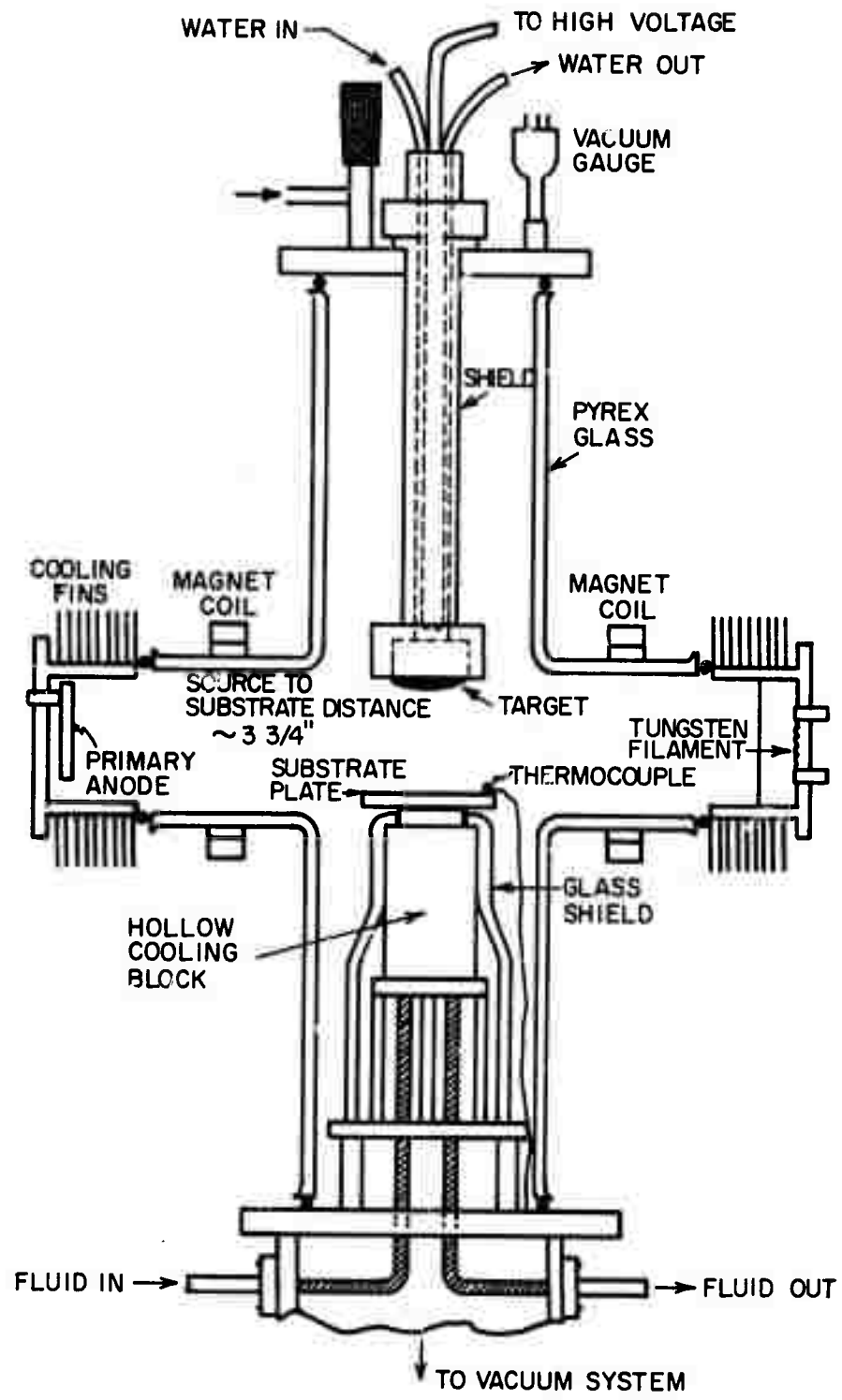
FIG. 2-4 SCHEMATIC OF SPUTTERING MODULE

rod. The aluminum target shield is held at ground potential
to prevent the sputtering of the rod and block holding the
target in place.

2. Sputtering procedure

The gas purifier and the cooling unit are turned on se-
veral hours before the commencement of a sputtering run to
allow each unit to reach equilibrium running conditions. The
substrates, after they have been polished and cleaned, are
attached to the substrate plate with a thin layer of Apiezon
N vacuum grease. After the inside of the bell jar has been
thoroughly etched to remove any contamination from the pre-
vious run and the filaments replaced, a light coat of Apiezon
N is applied to the rubber gaskets at the top and bottom of
the bell jar, and the bell jar is placed on top of the pumping
station. The target is inserted into the target holding
assembly and the target shield is put in place. This top
plate, which holds the bleeder valve, the vacuum gauge and
the target assembly, is then placed on top of the bell jar.

The bell jar is roughed down to 100 microns and the high
vacuum valve is opened to engage the turbomolecular pump,
which then pulls the vacuum down to about 10^{-6} torr in an
hour. The Teel rotary pump is started to circulate the fluid
through the cooling block after this vacuum has been achieved.
The filament current is set to 7.2 amps for about 15 minutes
and is closed again to allow the vacuum to go down to 10^{-6}
torr. The filament current is adjusted to 7.4 amps, the anode

current set to midscale, and the needle valve opened until the glow discharge is ignited (this usually occurs at a pressure of 1-5 microns). The magnetic field coils are then turned on full scale and the needle valve adjusted until the gas pressure stabilizes near one micron. Occasionally, arcing due to residual contamination occurs, but it usually subsides within about 15 minutes. The target is slowly raised to the operating voltage, usually 2000-3000 volts, and allowed to condition, i.e., some of its surface is sputtered away for a time dependent upon its nature and preparation. After the target has been sufficiently conditioned, the shutter shielding the samples is removed and the deposition commences.

After a sufficient thickness has been deposited, the high voltage is slowly decreased and turned off, the anode voltage and the filament current are turned off, and the needle valve is closed. The rotary pump which circulates the cooling fluid is turned off and the substrate is allowed to slowly warm up to room temperature under a vacuum. The high vacuum valve is closed and argon gas is slowly admitted to the bell jar until atmospheric pressure is reached. The bell jar is removed from the pumping station and the samples removed from the substrate plate.

3. Preparation of sputtering targets

The targets used for sputtering have been prepared in three ways: by cold pressing mixed powders of the constituents, by melting pieces of the bulk material into the proper shape, and by mounting the larger pieces available directly onto the target holders.

It has been found that 50-50 mix of Ge and Sn powders, and a 50-50 mix of In and Sb powders are successfully pressed into targets by the apparatus described in John Fan's[15] thesis. Attempts to press a 25%-75% Sn-Ge mix have been unsuccessful since the resulting targets are powdery to the touch. This suggests that cold pressing of mixed powders is successful only when at least one of the materials is soft and in sufficient concentration to bind the target together. Attempts to cold press InSb and ZnS powders have resulted in unsatisfactory targets which are usually broken into several pieces and crumble when touched.

InSb targets have been successfully produced by melting together in a vacuum RF induction furnace small pieces of InSb placed in a high purity graphite mold.

Large pieces of polycrystalline GaSb, GaAs, and GaP were available that could be used directly as sputtering targets.

D. Evaporation

1. Evaporation system

The system used for the production of the evaporated Ge films consists of a NRC 3166 vacuum system, with an electron gun powered by a Veeco VeB-6C power supply. As is schematically shown in Figure 2-5, the source material is placed into a high purity graphite crucible, which sits on top of a water cooled copper block. The electron beam strikes the source material raising it to sufficiently high temperature such that large numbers of atoms are evaporated from the surface. The atoms then condense onto the substrate
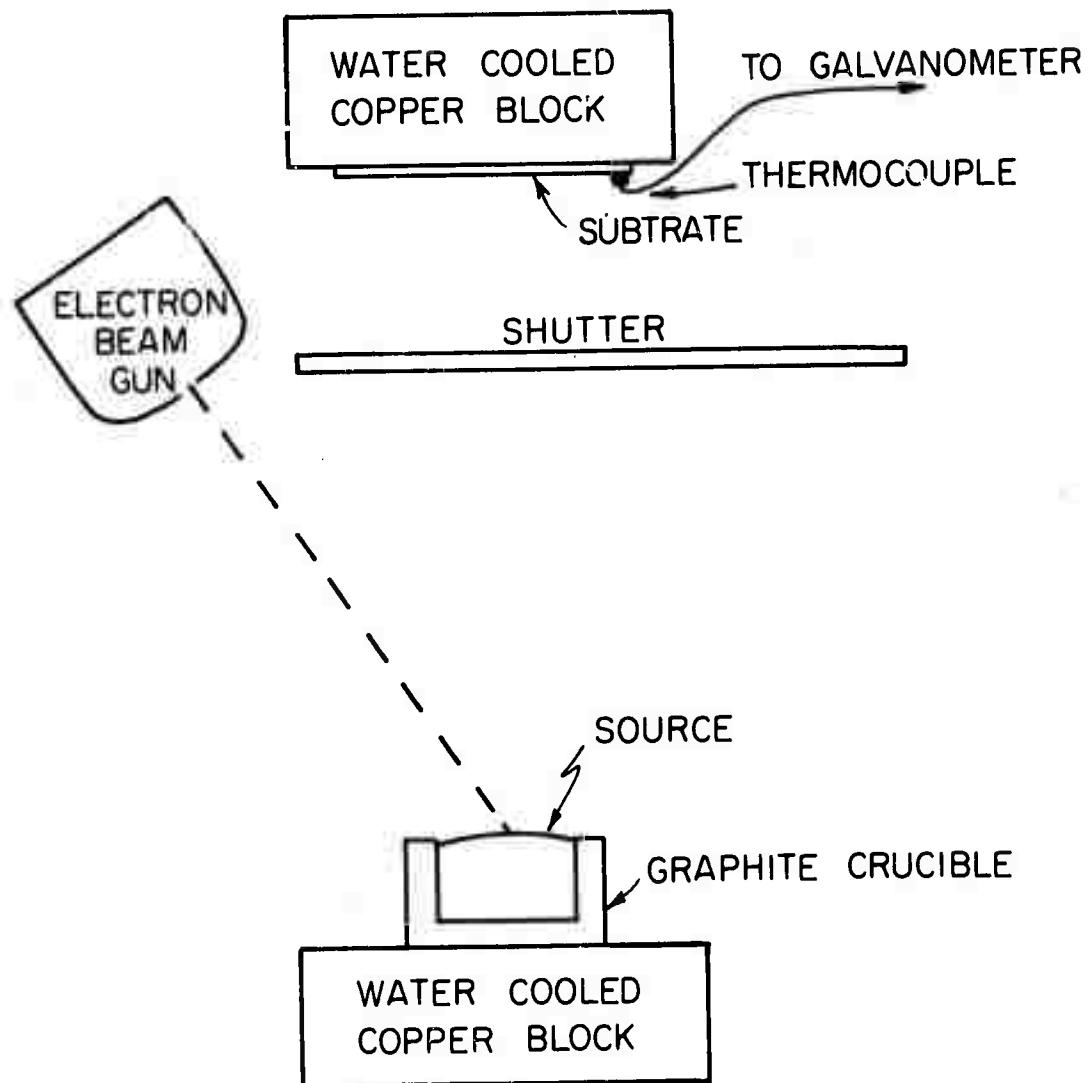
FIG. 2-5 SCHEMATIC OF ELECTRON BEAM
EVAPORATION SYSTEM

fastened to the water cooled block, which is about 12" away from the source. A copper-constantan thermocouple attached to the substrate allows the temperature to be monitored. The shutter, manually controlled with a lever on the outside of the pumping station, serves to shield the substrate from the source when necessary.

2. Evaporation procedure

The Ge used for the evaporation source has consisted of high purity 40 ohm cm Ge material, which has been etched with CP4 prior to use to remove any surface contamination. The crucible and source material are carefully aligned on the copper block to ensure that the electron beam strikes the source material. The substrates, consisting of freshly cleaved mica, are attached to the lower side of the copper cooling block with silver paint. The thermocouple is then attached to the substrate. The steel bell jar is lowered and the system is pumped down to 10^{-5} torr. The current in the electron beam is slowly increased until the substrate temperature reaches 50°C. This restriction on the substrate temperature limits the deposition rate so that it takes about 1 hour to deposit 5 microns. It is necessary to monitor the current during the entire run so that the temperature does not stray above 50°C, or the film may possibly crystallize. After a sufficient amount of material has been deposited, the electron beam gun is turned off, and the system is allowed to cool for about an hour. Air is then slowly admitted to the bell jar and the samples are removed.

E. Sample purity

Detailed purity analyses, unfortunately, have not been performed on all the films produced here, mainly because of the great expense and the frequent unreliability of the techniques currently applied.

The purity of the electrolytic films was investigated with mass and emission spectroscopy. The mass spectroscopy test was kindly performed by Dr. M. Hunt of the Air Force Cambridge Research Laboratory and the emission spectrographic test was performed by the commercially available facilities at the Jarrel-Ash Division of Fisher Scientific at Waltham Mass. The mass spectrographic/listed analysis in Table 2-1 shows that the resulting films have a total impurity content of about 8 atomic percent. However, the absolute values of the impurity concentrations are accurate to only a factor of three so the total impurity level may be as low as two percent. The impurities H,C and O could have come from the incorporation of the propylene glycol into the structure, but we cannot account for the high concentrations of the other impurities.

The Jarrel Ash emission spectrograph analysis shows that some of the materials detected with the mass spectrograph - particularly Na, B, K, Ti - have not been detected. The concentrations of Al, Si and Cr, according to this analysis are an order of magnitude less than those detected by the mass spectrographic analysis.

However, consistent with all these analyses is the Cu con-

contamination of about 0.1%, which is an order of magnitude less than the Cu impurity level reported by Tauc et al.[15] in their films. Connell[16] has been unable to find any vibrations in the infrared which can be conclusively identified as Ge-O vibrations. Thus we believe the oxygen contamination may be smaller than the value given in Table 2-1.

Connell[16] has been unable to find any lines in the IR spectra of the sputtered films which can conclusively be identified as vibrations from oxygen. The stoichiometries of the sputtered InSb, GaAs, GaSb films have been checked by comparing the x-ray fluorescence lines with those emitted from their corresponding crystals. These results show that the stoichiometries of the amorphous sputtered films are maintained to within the experimental accuracy of 2%. It has been impossible to check the stoichiometry in GaP since the P emission line could not be detected with the detectors currently available. Also no measurements have been made to estimate the argon content of our films. However, recent sputter ion source mass spectrographic analysis performed on our sputtered films by F.G. Satkiewicz of GCA of Bedford, Mass, shows no evidence for argon contamination.

Table 2-1

Summary of Mass Spectrographic Analysis / of electrodeposited Ge. Data has been

normalized so that concentration of Ge = 100%

Impurity	Atomic % *
H	0.1
B	0.01
C	3.0
O	1.0
F	-
Na	0.2
Al	1.3
P	-
Si	0.4
K	0.07
Ca	-
Ti	1.0
Cr	0.2
Mn	-
Fe	.06
Cu	.08
Ge	100.00

* Estimated accuracy is to within a factor of 3

JARRELL-ASH DIVISION/FISHER SCIENTIFIC COMPANY
590 LINCOLN STREET, AT ROUTE 128 WALTHAM, MASSACHUSETTS 02154 USA

Certificate of Analysis

TO: Harvard University
Gordon McKay Labs- 9 Oxford St.

Cambridge, Mass. 02138

Att: Mr. Nigel J. Shevchik

DATE REPORTED: 1-19-70

DATE RECEIVED: 1-16-70

ORDER NO. 093144

SAMPLE DESCRIPTION: Ge metal flakes #35

Li	ND			Zn	ND			Sb	ND			Lu			
Be	ND			Ga	ND			Te	ND			Hf	ND		
B	ND			Ge	H			Cs	ND			Ta	ND		
Na	ND			As	ND			Ba	ND			W	ND		
Mg	VVFT			Rb	ND			La				Ra	ND		
Al	VVFT VFT			Sr	ND			Ce				Os	ND		
Si	VFT			Y				Pr				Ir	ND		
K	ND			Zr	ND			Nd				Pt	ND		
Ca	FT			Nb	ND			Sm				Au	ND		
Ti	ND			Mo	ND			Eu				Hg	ND		
V	ND			Ru	ND			Gd				Tl	ND		
Cr	FT			Rh	ND			Tb				Pb	VFT		
Mn	ND			Pd	ND			Dy				Bi	VVFT		
Fe	VFT			Ag	VFT FT			Ho				Th			
Co	ND			Cd	ND			Er				U			
Ni	ND			In	ND			Tm				P	ND		
Cu	L			Sn	FT			Yb							

REMARKS:

KEY:

ND - Not Detected		T	.01 -.1%
VVFT < .0001%		L	.1- 1%
VFT .0001% - .001%		M	1% -10%
FT .001% - .01%		H	>10%

STAFF ANALYST

SUPERVISOR,
TESTING LABS

TL 21-103

REFERENCES

1. G. Szekely, J. Electro Chem. Soc. 98, 318 (1951)

2. C.C. Fink and V.M. Dokras, J. Electro. Chem. Soc. 95, 80 (1949)

3. A.K. Graham, H.L. Pinkerton, H.J. Boyd, J. Electro. Chem. Soc. 106, 65 (1951)

4. G.A.N. Connell and W. Paul, J. Non-Cryst. Solids(1972), (in the press)

5. J.E. Smith Jr., M.H. Brodsky, B.L. Crowder, and M.I. Nathan, J.Non-Cryst. Solids, (1972), (in the press)

6. R.C. Chittick, J. Non-Cryst. Solids 3, 255 (1970)

7. T. Pankey and J.E. Davey, J. Appl. Phys. 37, 1507 (1966)

8. J.E. Davey and T. Pankey, J. Appl. Phys. 40, 212 (1969)

9. R.P. Howson, Brit. J. Appl. Phys. Ser 2, 1, 15 (1968)

10. H.S. Chen, PhD. Thesis, Harvard University (1969)

11. A. Brenner, Electrodeposition of Alloys, Principles and Practice, (Academic Press Inc., New York, 1963)

12. R.W. Berry, P.M. Hall, M.J. Harris, Thin Film Technology, (D. Van. Nostrand C O, Inc., Princeton N.J. (1968))

13. K.G. Gunther and H. Fueller, Proc. Congress. Int. sur les Couches Minches, Cannes,1970, Paris

14. J. Fan, Ph.D. Thesis, Harvard University (1972)

15. J. Tauc, A. Abraham, R. Zallen, M. Slade, J. Non-Cryst. Solids, 4, 279, (1970)

16. G.A.N. Connell, (Private communication)

17. M.H. Brodsky, (Private communication)

CHAPTER 3

HIGH ANGLE X-RAY DIFFRACTION - THEORY AND EXPERIMENT

A. Introduction

An ideal amorphous solid is postulated to be a conti-
nuously connected network of atoms, homogeneous over at
least a scale of a few tens of angstroms; in it all bonds
are satisfied, but the atoms are arranged so that the un-
certainty in the separation of an arbitrary atom and its
nth nearest neighbor increases as n increases. However, in
real solids this ideal structure rarely occurs, since
throughout the real solid may be many density fluctuations,
either voids or phase separated regions. To fully specify
the structure of a real solid, it is necessary to have two
distributions: one specifying the concentrations and sizes
of the density fluctuations, and the other specifying the
arrangements of the atoms within each phase.

Diffraction, either by electrons, neutrons or x-rays
provides some direct information concerning these two dis-
tributions. It is fortunate that in most cases, the scat-
tered intensity curve can be broken into two regions; one
occurring at small angles where the scattering is dominated
by the density fluctuations having dimensions of several
atomic diameters, and the other occurring at higher angles
where the intensity is dominated by the interatomic inter-
ferences. This allows one to determine with diffraction some

information concerning both the density fluctuations and the arrangements of the atoms.

However, since the diffraction experiments require the sampling of a large volume, they give information on only the average structure, making it difficult, and in some cases impossible, to extract separate information on the environment of each type of atom comprising the solid. Since amorphous solids are macroscopically isotropic, much information concerning the short range order is lost in the experimental averaging process, and hence, the most we can expect to obtain from diffraction experiments concerning the arrangements of the atoms is the radial distribution function (RDF).

The RDF is the distribution of the distances between the average atom and its nearest neighbors. From this distribution we can obtain the positions and spreads of the first and second neighbor distributions, the numbers of first and second neighbors, the bond angle and its spread, and other indications of short range order.

In this Chapter, we discuss how the RDF can be obtained from high angle diffraction, and in the next Chapter, we discuss how the sizes and concentrations of the density fluctuations can be obtained from small angle diffraction.

B. Theoretical discussion of the high angle scattered intensity

As has been discussed by Kaplow et al.,[1] the theoretical 1st order coherently scattered intensity for an isotropic system can be written as:

$$I_{coh}^{(1)}(k) = <f^2> + \frac{<f>^2}{k} \int_0^\infty 4\pi r (h(r,k) - \rho_0) \sin(kr)\, dr \quad (3-1)$$

where $I_{coh}^{(1)}(k)$ = 1st order coherently scattered intensity per atom in electron units

$h(r,k)$ $= \sum\limits_{ij} \omega_{ij}(k) \rho_{ij}(r)$

ω_{ij} $= x_i \dfrac{f_i(k) f_j(k)}{<f>^2}$

$<f^2>$ $= \sum\limits_{i} x_i f_i^2(k)$

$<f>$ $= \sum\limits_{i} x_i f_i(k)$

r = radial distance from an arbitrary atom

k $= \dfrac{4\pi \sin\theta}{\lambda}$

λ = wavelength of incident radiation

2θ = angle between the incident and scattered beams

x_i = atom fraction of element i

f_i = scattering factor of element i

ρ_0 = average atomic density

$\rho_{ij}(r)$ = average number of atoms of type j per unit volume a distance r away from an atom of type i

Equation 3-1 can be inverted to give:

$$G(r) = 4\pi (\hat{\rho}(r) - \rho_0) r = \frac{2}{\pi} \int_0^\infty F(k) \sin(kr)\, dk \qquad (3-2a)$$

where

$$F(k) = k\left(\frac{I_{coh}^{(1)} - <f^2>}{<f>^2}\right) \qquad (3-2b)$$

The advantage of using this particular inversion is that it allows the average atomic density ρ_o, to be determined. For r less than the smallest interatomic distance, all $\rho_{ij}(r) = 0$, and hence, $G(r) = -4\pi\rho_o r$. The average atomic density is simply determined from the slope of $G(r)$ in this region. With the density thus determined, the RDF is given by:

$$4\pi r^2 \hat{\rho}(r) = 4\pi r^2 \rho_o + rG(r) \qquad (3-3)$$

However, the unavoidable disadvantage of this inversion is that since the $\omega_{ij}(k)$'s are k dependent, the deduced $\hat{\rho}(r)$ is not simply a linear sum of the $\rho_{ij}(r)$'s but is a convolution of the $\rho_{ij}(r)$'s with the transform of the $\omega_{ij}(k)$'s. The $\omega_{ij}(k)$'s may sharpen or broaden the peaks in the observed RDF or may shift their positions and alter their strengths. When the $\omega_{ij}(k)$'s are strongly k dependent, then one must resort to the more complicated methods of Warren[14] to deduce the true density functions. With this method, one first guesses the $\rho_{ij}(r)$'s, substitutes them into Equation 3-1, and calculates the scattered intensity. One then transforms this calculated intensity with Equation 3-2 to obtain an RDF which is then compared with the experimental RDF. By successively adjusting the assumed $\rho_{ij}(r)$'s one can eventually fit the RDF, thereby possibly obtaining the true density functions.

When the $\omega_{ij}(k)$'s are only weakly k dependent, it suffices to settle for the RDF given by the inversion of Equations 3-2 and 3-3. However, in interpreting it, we must bear in mind

that the observed RDF is a convolution of the true density functions with the $\omega_{ij}(k)$'s. When the $\omega_{ij}(k)$'s are weakly k dependent, the $\frac{f_i f_j}{<f>^2}$ factors may be approximately replaced by their average value over the range of integration.[14] In this case, the ω_{ij}'s become constants and:

$$\hat{\rho}(r) = \sum_{ij} <\omega_{ij}> \rho_{ij}(r) \qquad (3-4)$$

In this approximation the observed RDF is just a weighted linear sum of the density functions. We note that when the $\omega_{ij}(k)$'s are k dependent, $\hat{\rho}(r)$ is not just a linear sum of the $\rho_{ij}(r)$'s. Even with this simple approximation, we still have too many unknowns to specify the local correlations uniquely for each constituent.

However, we note that in the case of a single constituent, $h(r) = \rho(r)$ and $<f>^2 = <f^2>$; thus, the coherent intensity reduces to:

$$I_{coh}^{(1)} = f^2 + \frac{f^2}{k} \int_0^\infty 4\pi r (\rho(r) - \rho_o) \sin(kr) dr \qquad (3-5)$$

The inversion to obtain the RDF is again given by Equation 3-2. We note that in this case, the RDF can in principle be obtained exactly. For compounds in which the atomic constituents have nearly the same atomic number, such as in InSb and GaAs, the true RDF is very close to that obtained with Equations 3-2 and 3-3.

C. Interpretation of the observed RDF for a binary solid

The systems of interest here are those containing one
and two atomic constituents. We have just discussed how the
inversion and the subsequent interpretation of the experi-
mental data of compounds having atoms with widely different
scattering factors are more complex than for monoatomic
solids.   Since the number of unknown density functions ex-
ceeds the number of known ones available from a single dif-
fraction experiment, we must make assumptions concerning
the structure of the local environment about each type of
atom and see how well the consequences of the assumptions
agree with experimental results. It is unfortunate that
usually several assumed structures of the local environ-
ment may adequately fit the experimental data, and, to com-
pound this difficulty, the limited accuracy of the RDF admits
a still wider range of possibilities.

We pause here to demonstrate that in some cases the dif-
ferences in the scattering factors may, in fact, be useful
in determining the correlations between unlike atoms if the
coordination number can be determined by other independent
methods.

We consider a solid comprised of equal numbers of A and
B atoms with each type of atom having the same coordination
number, CN. Amorphous solids that are expected to have such
constituents are alloys based on Si and Ge, and Ge and Sn
and perhaps the III-V's. (In Chapter 5 we will present an
RDF of a Ge-Sn alloy that supports this belief).

Assuming that the ratio of the scattering factors of

elements A and B is constant, we derive some simple expressions relating the observed coordination number, interatomic separation and spread to the true coordination number, interatomic separation and spread. Integrating both sides of Equation 3-4 over the first coordination sphere gives for the observed coordination number of this system:

$$C_{obs} = \frac{1}{2} \left\{ \frac{f_A^2}{<f>^2} C_{AA} + \frac{2f_A f_B}{<f>^2} C_{AB} + \frac{f_B^2}{<f>^2} C_{BB} \right\} \qquad (3-6)$$

where

$$C_{obs} \qquad = \quad \text{observed coordination number}$$

$$C_{AA} \qquad = \quad \text{average number of AA bonds per A atom}$$

$$C_{BB} \qquad = \quad \text{average number of BB bonds per B atom}$$

$$C_{BA} = C_{AB} \qquad = \quad \text{average number of AB bonds per A or B atom}$$

We have used the fact that since the coordination numbers of the A and B atoms are the same, then $C_{AB} = C_{BA}$. We see that since each type of bond is weighted by a separate factor, the observed coordination number depends on the number of each type of bond. There are three limiting cases which are useful to consider.

First we have the case of total phase separation, denoted by the superscript "PS", where B atoms are surrounded only by B atoms and A atoms are surrounded only by A atoms. In this case, $C_{AA} = C_{BB} = CN$, $C_{AB} = 0$, and the observed coordination number becomes:

$$C_{obs}^{PS} = \{1 + \frac{1}{4} \frac{<f_A - f_B>^2}{<f>^2}\} \; CN \qquad (3-7)$$

Hence, the observed coordination number is greater than the actual coordination number.

Now suppose that each element is randomly dispersed, denoted by superscript "R", throughout the structure so that on the average $C_{AA} = C_{BB} = C_{AB} = CN/2$, then the observed coordination becomes:

$$C_{obs}^{R} = \frac{1}{2} \frac{CN}{2} \{\frac{f_A^2 + 2f_A f_B + f_B^2}{<f>^2}\} = \frac{CN}{4} \left(\frac{2f}{f}\right)^2 = CN \qquad (3-8)$$

In this case, the observed coordination becomes equal to the **true** coordination number.

In what we shall call the totally ionic case, denoted by the superscript "I", where A atoms are surrounded only by B atoms and B atoms are surrounded only by A atoms, we have $C_{AA} = C_{BB} = 0$, and $C_{AB} = CN$, the observed coordination number becomes:

$$C_{obs}^{I} = CN \{1 - \frac{1}{4} \frac{<f_A - f_B>^2}{<f>^2}\} \qquad (3-9)$$

which is less than the true coordination number, CN.

From these results we see that if we are able to deduce the true coordination number by other methods[*], then the observed coordination number can tell us something about the

---

[*] One such way to determine the coordination number is by finding from the experimental RDF both the nearest neighbor position and the density. One can then find a coordination number that is consistent with these two measurements.

relative ordering of the two constituents. For the general case, it is easy to show that the observed coordination number is given by:

$$C_{obs}(x) = CN \left\{ 1 + \frac{1}{4}(2x - 1)\left(\frac{\langle f_A - f_B \rangle}{\langle f \rangle}\right)^2 \right\} \qquad (3-10)$$

where x is the fraction of AA or BB bonds, per A or B atom.

It should also be noted from Equation 3-4 that the effect of the scattering factors is to weigh more heavily in the observed RDF those distances occurring between the heavier elements. Assuming that the ratio of the scattering factors is constant, it is easy to show from Equation 3-4 that the observed average nearest neighbor separation is:

$$\overline{r_1} = \frac{x(f_A^2 r_{AA} + f_B^2 r_{BB}) + 2(1 - x)f_A f_B r_{AB}}{x(f_A^2 + f_B^2) + 2(1 - x)f_A f_B} \qquad (3-11)$$

and the mean square first neighbor separation is:

$$\overline{r_1^2} = \frac{x(f_A^2 r_{AA}^2 + f_B^2 r_{BB}^2) + 2(1 - x)f_A f_B r_{AB}^2}{x(f_A^2 + f_B^2) + 2(1 - x)f_A f_B} \qquad (3-12)$$

The rms spreading of the first neighbor peak caused by the existence of more than one type of bond length is:

$$\sqrt{\overline{\Delta r_1^2}} = \sqrt{\overline{r_1^2} - \overline{r_1}^2} \qquad (3-13)$$

Note that when x=0, the case when only AB bonds exist, the spread

of the peak is zero. Note also that, when x increases, the width of the nearest neighbor distribution increases, and, provided that the larger element is also the heaviest, and $r_{AB} = r_A + r_B$, as is generally the case, the average position also increases.

D. Experimental arrangement

The experimental arrangement used for the high angle diffraction experiments is shown in Figure 3-1. It consists of an x-ray source, a Norelco diffractometer, which employs Bragg-Bratano geometry, a diffracted beam monochromator, a scintillation counter and associated electronics. The x-ray source, a sealed stationary anode type employing either Cu or Mo targets, is powered by an Eindhoven type Pw1010 generator, which has been measured to have a 1% stability over a period of a week.[2] The scattered intensity is monochromated with an AMR Model 3-302 diffracted beam monochromator, which employs a bent LiF crystal set to reflect the 200 plane. The x-rays are detected with a scintillation counter, the output of which is analysed by a pulse height analyser, which removes most of the counter noise and $\frac{\lambda}{2}$ wavelength component passed by the monochromator.

E. Data collection

The samples, which were usually 1 x 2 cm^2 in area and of various thicknesses, depending upon the availability of the material, were carefully shimmed into the sample holder so as to ensure their tangency to the focusing circle. (See
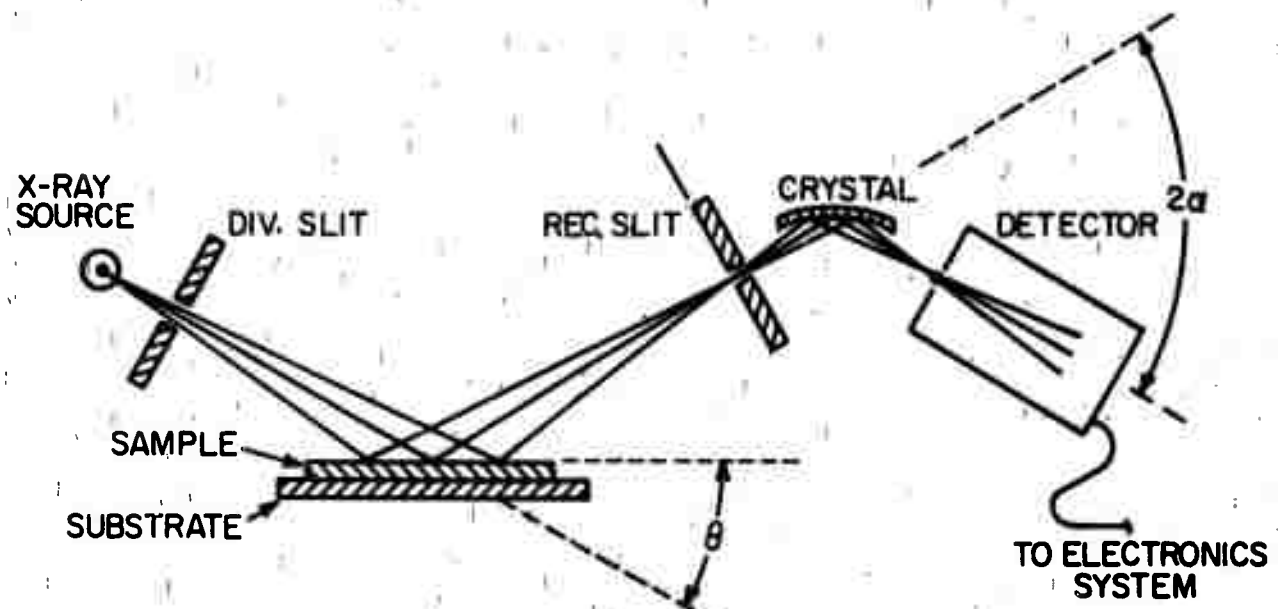
FIG. 3-1 EXPERIMENTAL DIFFRACTION ARRANGEMENT

"Operations Manual for the Norelco Diffractometer"). Runs were made with both Cu and Mo radiation. The runs with the Cu radiation were made to ensure that the peak positions and relative heights of the first two peaks, which were sensitive to alignment and surface roughness, could be more accurately estimated.[3] In order to obtain data at high k values, it was necessary to use MoK_α radiation.

Often the samples were of insufficient thickness to prevent radiation scattered from the substrate from coming through the sample at high angles. To circumvent this difficulty, after the intensity at low k values had been obtained with Cu and Mo radiation, pieces of additional sample material were glued to the surface of the original sample with a dilute mixture of watch crystal cement and methanol in order to increase the effective thickness of the sample. With the sample thus modified, the data at high angles could be accumulated without encountering any serious scattering from the substrate. However, the intensity obtained from such samples was inadequate at low angles since the surface roughness and shadow effects from such a layered film could produce large errors in the data at low angles.[3] The data obtained from the sample to which no pieces had been glued was matched at intermediate angles onto the data obtained from the sample to which extra pieces had been glued.

The data were collected by step scanning, usually with 0.25° intervals between 7° and 70° and with 0.5° intervals between 60° and 115°. Sufficient counts were taken to keep

the statistical error per degree to less than 1.4%

After the completion of a run, the sample was removed from its holder and the intensity was measured with 1^O intervals from $2\theta = 7^O$ to 115° to get an estimate of the background intensity as a function of angle.

The incident beam energy profile which was necessary to estimate correctly the total Compton scattered intensity, was found by measuring the energy reflected from a LiF single crystal as a function of angle.

F. The contributions to the total observed intensity

1. The total observed intensity

The determination of $I_{coh}^{(1)}$ is complicated since the experimentally observed intensity is the sum of several contributions, which are given by:

$$I_{exp} \propto (1-e^{\frac{-2ut}{sin\theta}})(PF^{(1)}(I_{coh}^{(1)} + I_{incoh}^{(1)}) + PF^{(2)}(I_{coh}^{(2)} + I_{incoh}^{(2)})$$

$$+ e^{-\frac{2ut}{sin\theta}} I_{sub} + I_{back} + I_{Fluor} \qquad (3-14)$$

where

I_{exp} = experimentally observed intensity

u = inverse absorption length of the x-ray beam in the sample

t = thickness of the sample

2θ = angle between the incident and scattered beam direction

$PF^{(1)}$ = polarization factor of the first order scattered radiation

$I_{coh}^{(1)}$ = intensity of the first order coherently scattered radiation

$I_{incoh}^{(1)}$ = intensity of the first order incoherently scattered radiation

$PF^{(2)}$ = polarization factor of the second order coherently scattered radiation

$I_{coh}^{(2)}$ = intensity of the second order coherently scattered radiation

$I_{incoh}^{(2)}$ = intensity of the second order incoherently scattered radiation

I_{sub} = intensity scattered from the substrate with no sample on its surface

I_{back} = background intensity

I_{fluor} = fluorescence radiation produced by the sample and substrate

The relative contribution of these components depends on the sample's geometry and atomic constituents. Since the combined corrections to the intensity scattered from the materials investigated here are at worst 20% of I_{coh}, they must be taken into account if the data are to be extended to k values of 15.0 $\overset{\circ}{A}^{-1}$. We will now discuss and evaluate each of the terms in Equation 3-14 and how $I_{coh}^{(1)}$ can be deduced from the experimental intensity.

2. **Absorption**

The absorption correction for the intensity of the coherently and incoherently scattered radiation from the sample is given in Equation 3-14 by the term $(1-e^{\frac{-2\mu t}{\sin\theta}})$. The inverse of the absorption length, μ, is given by

$$\mu = \frac{(X_A \cdot AW_A \cdot \mu_A^m + X_B \cdot AW_B \cdot \mu_B^m) \cdot \rho_o}{X_A \cdot AW_A + X_B \cdot AW_B} \tag{3-15}$$

where AW_A and AW_B, and μ_A^m and μ_B^m are the atomic weights and the mass absorption coefficients for elements A and B, respectively.[14] The density, ρ_o, is taken to be equal to the crystalline density, since it has been found that the density of amorphous materials is usually within 10% of the crystalline density. The sample should be sufficiently thick so that the absorption correction remains less than 15% at high angles.

3. **PF$^{(1)}$**

$PF^{(1)}$ is the polarization factor of the detected first order coherently and incoherently scattered x-rays. For a monochromator crystal having reflection planes with a spacing d, the Bragg reflection angle, 2α, is given by

$$2\alpha = 2 \sin^{-1}(\frac{\lambda}{d}) \tag{3-16}$$

The polarization factor of the x-rays detected with the monochromator is:

$$PF^{(1)} = \frac{1 + K(2\alpha)\cos^2(2\theta)}{1 + K(2\alpha)}$$

(3-17)

where $K(2\alpha)$ is the polarization constant, which depends on the degree of perfection of the monochromator crystal and the Bragg angle. For a mosaic crystal, $K_m(2\alpha) = \cos^2(2\alpha)$ and for a perfect crystal, $K_c(2\alpha) = \cos(2\alpha)$. It has been found that some crystals scatter like mosaics, while others scatter between that of a mosaic and that of a perfect crystal.[4] In one case, it has been reported that the monochromator crystal scattered even outside this range.[5] Since most of the prior RDF work has been done using the polarization factor for a mosaic, this factor has been used here also.

We can estimate the possible error introduced in the polarization factor by our lack of information concerning the nature of its scattering behavior as follows. For a LiF crystal with MoKα radiation, $2\theta = 20.2^\circ$, and hence, $K_m = 0.88$ and $K_c = 0.94$. Inserting these values for K into Equation 3-17, one finds that the difference between the two polarization factors for the crystal and the mosaic is at worst only about 3%. Hence, the choice between the two polarization factors is not crucial when using MoKα radiation. However, for CuK radiation, $2\theta = 45^\circ$, and $K_m = 0.49$ and $K_c = 0.71$. The difference between the mosaic and perfect crystal polarization factors is about 10%, and it is in this

case more important to know the correct value of $K(2\alpha)$ for the monochromator.

Fortunately, any error introduced into the polarization factor by a wrong choice of K is slowly varying with k, and hence, such an error is mostly eliminated with the correction procedure to be outlined in Section 4-D.

4. $I_{coh}^{(1)}$

$I_{coh}^{(1)}$ is the first order coherently scattered radiation as is given in Equation 3-1. The atomic form factors are corrected for dispersion by the relation:

$$f_i = (f_{oi} + \Delta f_i') + i\,\Delta f_i''$$

where f_{oi} is the tabulated form factor for element i,[6] and $\Delta f_i'$ and $\Delta f_i''$ are the dispersion corrections for element i which are functions of both the wavelength of the x-ray and the scattering vector.[7]

5. $I_{incoh}^{(1)}$

I_{incoh} is the intensity of the first order Compton scattered radiation, which is produced by those incident photons that lose some of their energy by exciting electrons when scattered. Since the Compton scattered radiation usually has a wide distribution in energy, it can carry no structural information, and its contribution to the total observed scattered intensity must be evaluated and subtracted.

We first assume that the incident beam is monochromatic.

With no monochromator the total Compton scattered intensity is given by:

$$\{ X_A \, f_A^{incoh} + X_B \, f_B^{incoh} \} \, BD \qquad (3\text{-}18)$$

where f_A^{incoh} and f_B^{incoh} are the tabulated incoherent scattering factors for elements A and B respectively, and BD is the Breit-Dirac recoil factor given by:[10]

$$BD = \frac{1.0}{\{1.0 + \frac{2h\lambda}{mc}(\frac{\sin\theta}{\lambda^2})\}^3} \qquad (3.19)$$

where

m = mass of an electron

c = speed of light

h = Planck's constant.

But when a monochromator is used, the detected first order Compton scattered radiation is given by:

$$(Q_A \, X_A \, f_A^{incoh} + Q_B \, X_B \, f_B^{incoh}) \quad BD \qquad (3\text{-}20)$$

where Q_A and Q_B are the monochromator efficiencies, which depend on the binding energy of elements A and B respectively. The monochromator efficiency for any element is given by the formula derived by Ruland:[9]

$$Q_i = \{ (1 + \frac{\Delta\lambda_i}{b})(1 + \frac{\pi^2 \Delta\lambda_c^2}{(\Delta\lambda_i + b)^2}) \}^{-1} \qquad (3\text{-}21)$$

where
$$\Delta\lambda_i = \frac{\lambda'^2}{c} s \, \Delta q(s)$$

$$\Delta q(s) = \Delta q_{max} \frac{s^2}{a^2 + s^2}$$

$$\Delta\lambda_c = \frac{2h}{mc} \sin^2 \theta$$

$$s = \frac{\sin\theta}{\lambda}$$

The width of the Compton profile, Δq_{max}, is taken to be pro-
portional to Z, the atomic number. Using the value calcula-
ted by Duncanson and Coulson[11] for Neon to find the pro-
portionality constant gives:

$$\Delta q_{max} = 0.387 \quad Z \tag{3-22}$$

This approximation to the profile becomes worse for elements
of higher Z; however, it is not crucial to know the exact
profile widths for the heavier elements since at high k, Q
becomes very small and errors in Δq_{max} make negligible dif-
ference to the correction to I_{exp}.

However, in practice the incident beam is not monochro-
matic, but has a high energy shoulder which scatters in-
coherent radiation down into the monochromator pass band.
The incident beam wavelength profile for the x-ray tube used
in the experiments with 2o ma current and an accelerating
voltage of 50 kv is shown in Figure 3-2. Note that the con-
tinuum is about 3% of the $MoK\alpha_1$ peak height, but since the
continuum is much wider, the total power in it is comparable
to that of the $MoK\alpha_1$ peak. The net effect of the Compton
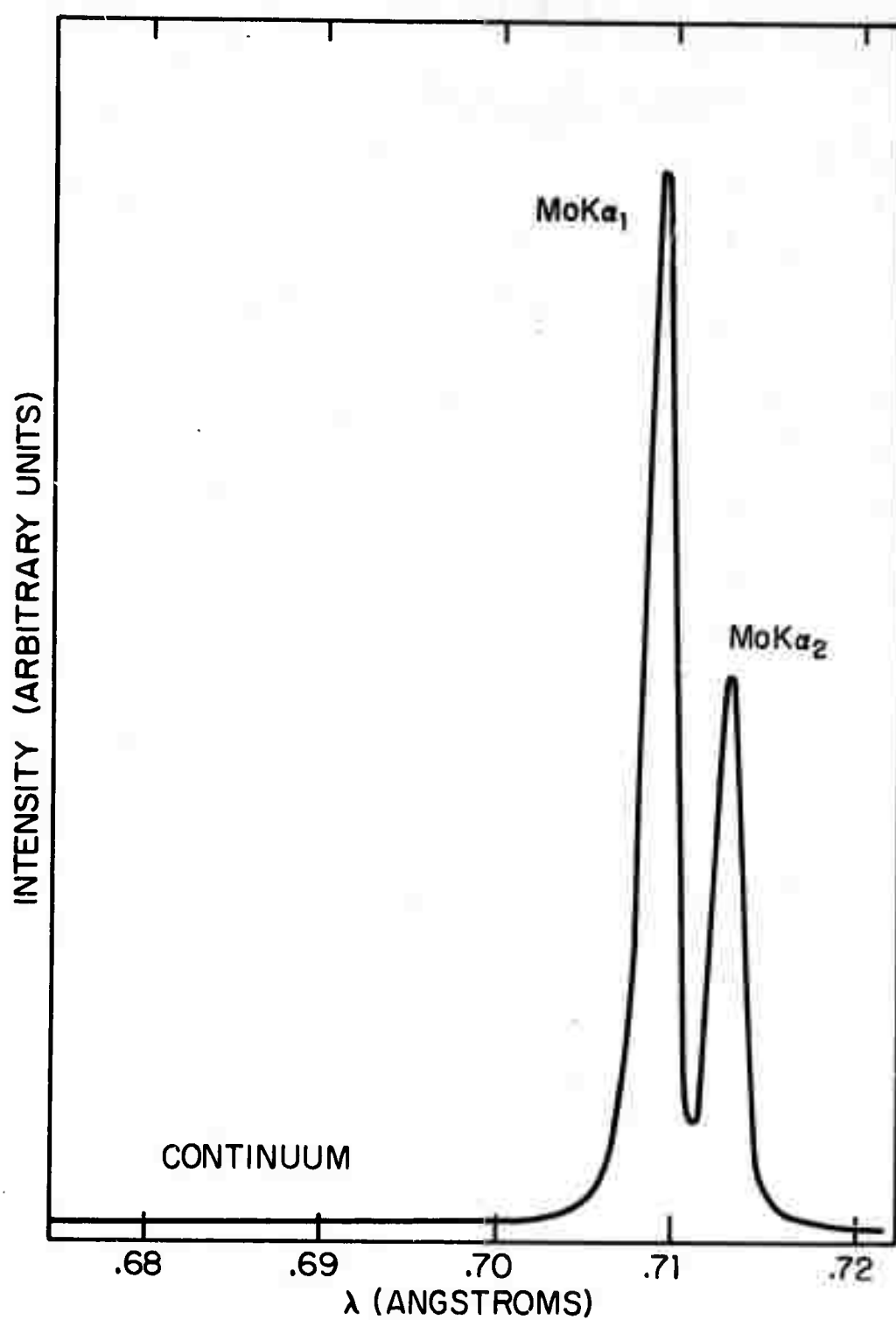
FIG. 3-2 INCIDENT BEAM PROFILE FOR A Mo X-RAY
TUBE AT 20 MA AND 50 kV

scattered radiation produced from this continuum shoulder is to make the monochromator less efficient by adding to each Q_i a constant term, CD. The Compton downscattering ratio, CD, is derived and discussed in more detail in Appendix I.

Taking this Compton downscattering into account, the total observed first order Compton scattered intensity is given by:

$$I_{incoh}^{(1)} = (\ (Q_A + CD)\ X_A\ f_A^{incoh} + (Q_B+CD)\ X_B\ f_B^{incoh})\ BD \qquad (3-23)$$

6. $\underline{I_{coh}^{(2)}}$

The total scattered intensity is the sum of all scattering events to all order, but here we approximate it to be equal to the first and second order terms only. This we can do because the strength of the scattering power of the electron is very weak and the strength of higher order scattering processes decreases geometrically with increasing order.

$I_{coh}^{(2)}$ is the intensity of the radiation that is scattered twice within the sample before it is detected. Following Warren and Mozzi[12] the second order scattering can be written in terms of the first order coherently scattering radiation as:

$$PF^{(2)}\ I_{coh}^{(2)} = W\ PF^{(2)}\ I_{coh}^{(1)} \qquad (3-24)$$

where W is the factor relating the second order scattering

to the first order scattering, and $PF^{(2)}$ is the polarization factor of the second order scattering. If the unpolarized incident beam is first scattered through the angle $2\theta_1$, and rescattered through an angle $2\theta_2$, thus making a total angle of scattering 2θ with the incident beam direction, the polarization factor of the second order coherently scattered radiation is:

$$PF^{(2)} = \frac{\cos^2(2\theta_1) + \cos^2(2\theta_2) + (\cos(2\theta_1)\cos(2\theta_2) - \cos(2\theta))^2}{2}$$

$$(3-25)$$

We neglect the effect that the monochromator has on this polarization factor, since including it leads to a very complicated formula. Besides, with MoKα radiation the polarization effects of the monochromator should be small since it detects both polarization components with nearly equal efficiency.

We evaluate this multiple scattering with the formulas derived by Warren and Mozzi;[12] the ratio of the second order to the first order scattering is given by:

$$W = I_{coh}^{(2)}/I_{coh}^{(1)} = \frac{8e^4 N}{m^2 c^2} \frac{\sin\theta}{(1 + \cos^2 2\theta)(\sum_i X_i \mu_i^m AW_i)J(2\theta)}$$

$$\int_{\phi=0}^{\frac{\pi}{2}} \int_{\epsilon=0}^{\frac{\pi}{2}} \frac{J(p_1) J(p_2) + J(-p_1) J(-p_2)}{\sin\theta + \sin\epsilon} PF^{(2)} \cos\epsilon \, d\epsilon \, d\phi \qquad (3-26)$$

where

$$p_1 = \cos(2\theta_1) = \cos\theta \cos\epsilon \cos\phi - \sin\theta \sin\epsilon$$

$$p_2 = \cos(2\theta_2) = \cos\theta \cos\epsilon \cos\phi + \sin\theta \sin\epsilon$$

e = charge of electron N = Avagadro's Number

$J(p)$ = first order coherently scattered intensity in electron units.

To simplify the computations, $J(p)$ is taken to be equal to the independent scattering per atom given by:

$$J(p) = \langle f(p)^2 \rangle \tag{3-27}$$

This approximation remains good as long as $W \ll 1$, but when the multiple scattering contribution is large, then in order to obtain the first order coherent intensity, we must solve the nonlinear integral equation:

$$I_{exp} = I_{coh}^{(1)} + W \cdot I_{coh}^{(1)} \tag{3-28}$$

where now we must set $J(p) = I_{coh}^{(1)}$. Fortunately for the materials investigated here $W \ll 1$, so we could use the approximation in Equation 3-27 to obtain approximate results for the multiple scattering contribution to I_{exp} without introducing significant error.

7. $I_{incoh}^{(2)}$

$I_{incoh}^{(2)}$ is the intensity of the Compton modified radiation brought about by the incoherent rescattering of the first order coherently scattered radiation. We neglect the contribution to the intensity from the radiation that has been incoherently scattered twice, since after two scattering events, its wavelength is very far shifted from the mono-

chromator pass band, and hence, very little of it should be experimentally detected. We can approximate the ratio of the first order to second order incoherently scattered intensities to be the same as that of the first to second order coherently scattered intensities. This gives for the second order incoherently scattered intensity:

$$PF^{(2)} \quad I^{(2)}_{incoh} = PF^{(1)} \quad I^{(1)}_{incoh} \qquad (3-29)$$

This approximation to $I^{(2)}_{incoh}$ is not quite correct since the monochromator efficiency is not the same for the second order incoherent scattering as it is for the first order. The second order incoherently scattered radiation arises from photons scattered through a distribution of scattering angles, whereas the first order Compton incoherently scattered radiation arises from photons scattered through a single angle. Thus the wavelength distributions for the first and second order intensities are quite different. However, at high angles the monochromator efficiency is limited by the downscattering constant which makes it insensitive to the wavelength distribution of the detected radiation. Hence, in this region the monochromator efficiencies of the first and second order incoherent scatterings become equal, and Equation 3-29 becomes more correct.

8. I_{sub}

When the sample thickness is not several multiples of the absorption length, much radiation can scatter back through

the sample from the substrate. It is then necessary to correct for the substrate scattering. This contribution is given by:

$$e^{\frac{-2\mu t}{\sin\theta}} \cdot I_{SUB} \qquad\qquad (3-30)$$

where I_{sub} is the intensity scattered from the substrate run under the same conditions as the amorphous sample.

9. I_{back}

The background intensity is obtained by removing the sample from its holder and then by recording the intensity as a function of angle with 1° invervals. This picks up spurious radiation scattered from the air column irradiated by the incident beam from the sample guard and scattering slits. This intensity also includes the counter noise. This procedure is not entirely adequate since the removal of the sample does not exactly reproduce the same diffraction conditions as for the sample; however, since at high angles this background is at worst for amorphous Ge no more than 5% of the total scattered intensity, it's precise determination is not essential. For example, suppose we can find the background accurate to only 20%. Since the background is 5% of the total observed intensity, then the total error in the total intensity attributable to the uncertainty in the background is only 1%.

10. I_{fluor}

When the incident radiation contains wavelengths shorter than those needed to excite the inner electrons in the atoms of the sample, the atoms emit their characteristic x-rays, or fluoresce. Usually, the monochromator removes all of the fluorescence radiation, provided that this radiation has a wavelength which is well separated from the central pass band wavelength of the monochromator. For all the experiments conducted here, this has been found to be the case.

11. Summary

Putting all these together gives as the final expression for the experimentally observed intensity:

$$I_{exp} \propto PF^{(1)} (1 - e^{\frac{-2\mu t}{\sin\theta}}) (1 + W) \quad (I_{coh}^{(1)} + I_{incoh}^{(1)}) \quad (3-31)$$
$$+ e^{\frac{-2\mu t}{\sin\theta}} I_{sub} + I_{back}$$

The only unknowns in Equation 3-31 are $I_{coh}^{(1)}$ and the proportionality constant. Rearranging Equation 3-31 gives:

$$I_{coh}^{(1)} + I_{incoh}^{(1)} = XN \left(\frac{I_{exp} - e^{\frac{-2\mu t}{\sin\theta}} I_{sub} - I_{back}}{PF^{(1)} (1 - e^{\frac{-2\mu t}{\sin\theta}}) (1 + W)}\right) \quad (3-32)$$

G. Data reduction

1. Normalization

The only unknown remaining in Equation 3-32 is the scaling factor, XN, which must be evaluated to put the scattered intensity into the correct units. We make use of the fact that at high k, the interference terms are small and the intensity is mostly given by the independent scattering of each constituent. We get a first order estimate of XN by finding the best value which satisfies

$$XN = \frac{1}{N} \sum_{i=1} \frac{(<f^2> + I^{(1)}_{incoh})}{I^{cor}_{exp}} \qquad (3-33)$$

where the sum extends over the last N experimental points. With XN estimated, the coherently scattered intensity is given by:

$$I^{(1)}_{coh} = XN \cdot I^{cor}_{exp} - I^{(1)}_{incoh} \qquad (3-34)$$

This normalization procedure is exact only as long as there are no interference effects at high k, but in some cases, strong oscillations continue to persist and additional means are necessary to improve the normalization. It is helpful to look at the F(k) deduced with the first guess of XN, and to adjust XN until the F(k) properly oscillates about zero.

After the data has been satisfactorily normalized, the F(k) is inverted using an interval dk of 0.025 $\overset{o}{A}^{-1}$ to obtain the G(r) function via the formula:

$$G(r) = \frac{2}{\pi} \int_0^{k_{max}} F(k) \sin(kr) \, dk \qquad (3\text{-}35)$$

The $G(r)$ function is computed by successively increasing k_{max} from 6 Å^{-1} to 9, 12 and 15 Å^{-1} so that errors arising from termination and other spurious effects can be observed.

2. Termination errors - extrapolation procedure

However, it has been found that the persistence of strong oscillations in $F(k)$ at high k results in large termination errors near the first peak in $G(r)$. The standard method of Warren[14] to get around this difficulty is to multiply the $F(k)$ by a damping factor, $e^{-\sigma^2 k^2}$, which has the effect of making the integrand converge faster, thereby reducing termination effects.

Richter and Breitling[15] eliminate termination effects by averaging together 50 RDF's computed by successively raising k_{max} in Equation 3-35 from 2/3 of the maximum experimental k value to the maximum experimental k value. Since the position or phase of termination errors depend upon the upper limit of integration, and since the termination errors are oscillatory about 0, this procedure simply averages them out.

However, the price one pays for employing these methods is to lose some true sharpness of the first peak, which is for interpretation of electronic properties an important parameter to know. Termination errors arise simply because we do not have sufficient data at high k. However, by using

some physical reasoning we can make very good guesses as to what lies beyond the range of the experimental data, and use these guesses to deduce a more accurate RDF. An alternative method will now be discussed which significantly reduces termination effects without broadening the first peak in the RDF.

The $F(k)$ can be written in terms of the RDF as:

$$F(k) = \int_0^{\infty} 4\pi r^2 (\rho(r) - \rho_o) \sin\frac{kr}{r}\, dr \qquad (3\text{-}36a)$$

Now suppose that the RDF can be written as a sum of gaussian functions such that:

$$4\pi r^2 (\rho(r) - \rho_o) = \sum_i \frac{C_i}{\sqrt{2\pi\sigma_i^2}} e^{\frac{-(r-r_i)^2}{2\sigma_i^2}} \qquad (3\text{-}36b)$$

where σ_i and r_i denote the gaussian spread and most probable distance of shell i, and Ci denotes the total number of atoms in this shell. Inserting Equation 3-36b into 3-36a gives an approximate expression for $F(k)$:

$$F(k) = \sum_i \frac{C_i}{r_i} \sin(kr_i) e^{\frac{-\sigma_i^2 k^2}{2}} \qquad (3\text{-}36c)$$

We note that each term in the $F(k)$ is weighted by a gaussian in k; thus for large k, this sum is dominated by the term with the smallest σ_i. This always is the first shell distance in the RDF! Thus at high k, $F(k)$ varies as:

$$F(k) = \frac{C_1}{r_1} \sin(kr_1) e^{\frac{-\sigma_1^2 k^2}{2}} \qquad (3-37)$$

All of these parameters, σ_1, r_1, C_1, are available from just the experimental data. Since the area, C_1, and the position, r_1, of the first peak are somewhat insensitive to termination, we can find r_1 and C_1 by examination of the RDF deduced from inversion of experimental data only. The value of σ_1 can be then obtained by fitting Equation 3-37 to the last experimentally obtained oscillation in the F(k). With these parameters thus obtained, a new RDF can be computed by extending the range of the experimental data with Equation 3-37.

Figure 3-3 demonstrates the effects of the application of this extrapolation procedure. The experimental RDF has been calculated with an F(k) experimentally determined to $k = 12.0 \text{ Å}^{-1}$. In this RDF, there are strong termination oscillations on both sides of the nearest neighbor peak. It appears that there may be a termination bump immediately to the right of the second neighbor distribution at $r = 4.5 \text{ Å}$. The extrapolated RDF has been calculated with values of $C_1 = 2.0$, $r_1 = 2.35 \text{ Å}$ and $\sigma_1 = 0.075 \text{ Å}$ in Equation 3-37. We note that the first peak in the extrapolated RDF has become sharper by about 20% and the termination errors on both sides of it are reduced. Also we note that the bump at $r = 4.5 \text{ Å}$ has disappeared, indicating that it is most likely a termination error.

In general, the effects on the new RDF are to both lessen
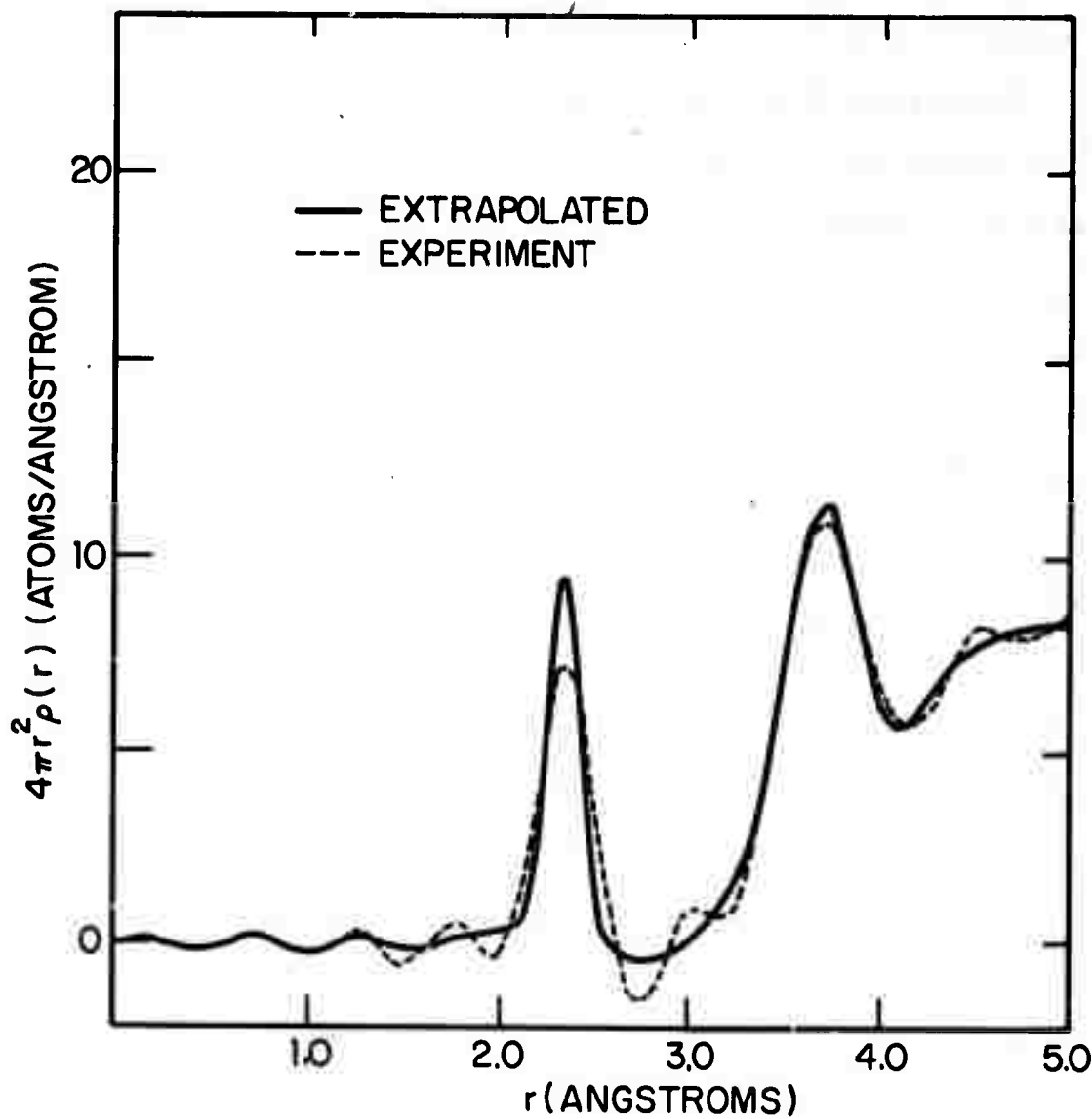
FIG. 3-3 EFFECTS OF TERMINATION EXTRAPOLATION ON
THE RDF OF AMORPHOUS EVAPORATED Se

the size of the termination satellites and to sharpen the first peak more closely to its true sharpness. When this procedure has been used, the data have been extrapolated to $k = 30.0 \overset{\circ}{A}^{-1}$.

We stress that this method is only applicable to the case where there is a single sharp nearest neighbor peak and the experimental data extend to sufficiently high k so that Equation 3-37 becomes a valid approximation to the experimental F(k). Also, we stress that this is only an approximation to the true asymptotic form of F(k) since sometimes the true shape of the first peak in the RDF may not be a gaussian. If this procedure is applied to a case in which the true first peak shape is far from gaussian, it will severely distort the shape of the first peak in the observed RDF.

3.   Slowly varying error correction

Since several corrections must be made to obtain the experimental intensity, it is very easy to introduce an error somewhere. The combined errors produced by alignment, absorption, polarization, normalization, and surface roughness, are all slowly varying with k and introduce a mulplicative error, $\varepsilon(k)$, such that the experimental intensity I_{coh}^{exp}, is related to the true scattered intensity $I_{coh}^{(1)}$ by:

$$I_{coh}^{exp} = (1 + \varepsilon(k)) I_{coh}^{(1)} \qquad (3-38)$$

An error of this general form may be corrected by the following procedure.

Following Kaplow et al.[16] the experimental $F(k)$ is

$$F_{exp}(k) = F(k) + \Delta F(k) = k\left(\frac{I_{coh}^{(1)} \cdot (1 + \epsilon(k)) - \langle f^2 \rangle)}{\langle f \rangle^2}\right) \quad (3\text{-}39)$$

The true $F(k)$ is $k\left(\dfrac{I_{coh}^{(1)} - \langle f^2 \rangle}{\langle f \rangle^2}\right)$ and the error in $F(k)$, $\Delta F(k)$,

is $\dfrac{I_{coh}^{(1)} \epsilon(k) k}{\langle f \rangle^2}$. The two unknowns in $F_{exp}(k)$ are $\epsilon(k)$ and $I_{coh}^{(1)}$

and we look for a way to find them. We now consider the
transform of each of these two terms for $r < r_{max}$, where
r_{max} is the smallest expected interatomic separation. We
have for the experimental $G(r)$, $G(r)^{exp}$,

$$G(r)^{exp} = G(r) + \Delta G(r) = \frac{2}{\pi}\int_{k_{min}}^{k_{max}} F_{exp}(k)\sin(kr)\,dk \quad (3\text{-}40)$$

As has been discussed on Page 3-4, the $G(r)$ vs. r curve
must be a straight line for small r values. For $r < r_{max}$ we
have that $G(r) = -4\pi\rho_o r$, and any deviation of $G^{exp}(r)$ away
from a straight line is a termination or some other kind of
error. Supposing that $\epsilon(k)$ is slowly varying compared to
the oscillations in I_{coh}, then for small r we have:

$$\Delta G(r) = \frac{2}{\pi}\int_{k_{min}}^{k_{max}} k\,\epsilon(k)\,\frac{I_{coh}^{(1)}}{f^2}\sin(kr)\,dk$$

$$(3\text{-}41)$$

$$\approx \frac{2}{\pi}\left\langle\frac{I_{coh}^{(1)}}{f^2}\right\rangle\int_{k_{min}}^{k_{max}} k\,\epsilon(k)\,\sin(kr)\,dk$$

where $\langle \frac{I_{coh}^{(1)}}{f^2} \rangle$ is the long wavelength average of I_{coh}/f^2, which is usually ~ 1. Hence, $\Delta G(r)$ is mostly determined by the function $k \, \varepsilon(k)$, and since $\varepsilon(k)$ is slowly varying with k, $\Delta G(r)$ is confined to mostly small r values below the first neighbor distance.

We must now determine the density. We use:

$$\rho_o = \frac{\int_o^{r_{max}} G^{exp}(r) \, r dr}{\frac{4\pi}{3} \, r_{max}^3} \qquad (3-42)$$

This density is not quite correct since the error in $G^{exp}(r)$ will affect the density somewhat, but we assume that since the error in $G(r)$ is oscillatory about 0 its effect in the determination of the density is small. With the density thus determined, the error in $G^{exp}(r)$ is approximately:

$$\Delta G(r) = +4\pi\rho_o r + G^{exp}(r) \qquad (3-43)$$

Inverting Equation 3-43, we have:

$$k\varepsilon(k) = \int_o^{r_{max}} \Delta G(r) . \sin(kr) dr \qquad (3-44)$$

With $\varepsilon(k)$ determined, the corrected coherent intensity becomes:

$$I_{coh}^{(1)} = \frac{I_{coh}^{exp}(k)}{(1+\varepsilon(k))} \qquad (3-45)$$

The corrected F(k) is:

$$F(k) = F_{exp} - \frac{k\varepsilon(k)}{1+\varepsilon(k)} \quad \frac{I_{exp}(k)}{f^2} = k\left(\frac{I_{coh}^{exp} - (1+\varepsilon(k))<f^2>}{(1+\varepsilon(k))<f>^2}\right) \quad (3-46)$$

However, caution must be used in using this correction procedure to correct the F(k) at high k values, particularly when the F(k) still has strong oscillations at high k. The persistence of the strong oscillations at high k gives rise to termination error satellites about the first peak in the G(r) function. However, we must realize that these termination satellites should not be removed by this procedure, since to do so leads to a correction in the F(k) which is clearly incorrect. This is illustrated in Figure 3-4 where the correction procedure has been applied to the F(k) of amorphous Se at high k values. Note that its effect is to distort the last bump in the F(k) function downward away from its expected oscillatory behavior.

We must realize that the termination satellites arise not from errors in the diffraction pattern, but rather from our incomplete knowledge of the diffraction pattern. These satellites can be more effectively and correctly eliminated by the extrapolation procedure that has been outlined in the last section. Nevertheless, this correction procedure is very powerful in correcting slowly varying errors that are away from k_{max}.
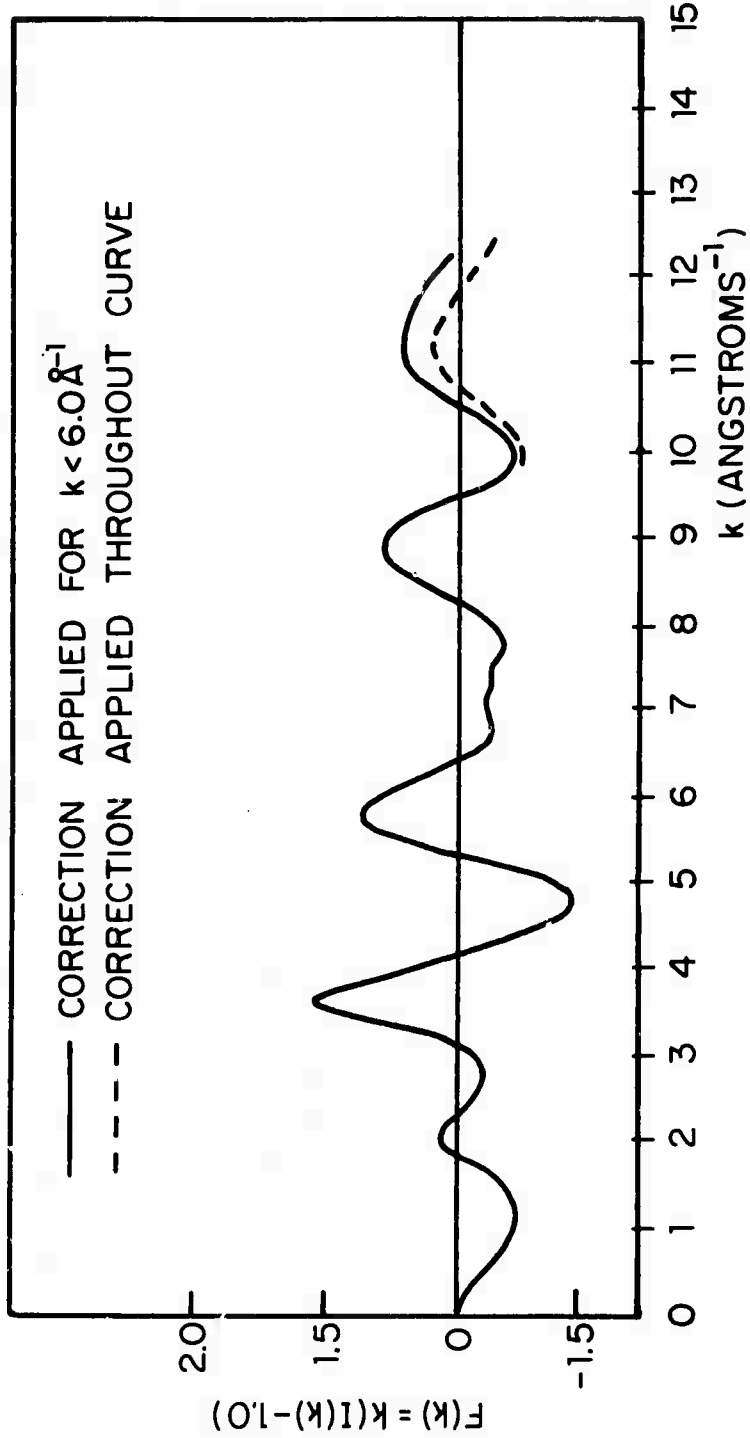
FIG. 3-4 THE EFFECTS OF APPLYING THE CORRECTION PROCEDURE TO THE F(k) OF AMORPHOUS Se NEAR k_{max}.

REFERENCES

1. R. Kaplow, S.L. Strong, and B.L. Averbach, in _Local Atomic Arrangements Studied by Xray Diffraction_ , Edited by J.B. Cohen and J.E. Hilliard, Gordon and Breach, New York (1966)

2. G.S. Cargill III, J. App. Phys., **41**, 12 (1970)

3. P. Trucano and B.W. Batterman, J.Appl. Phys. **41**, 3949 (1969)

4. L.D. Jennings, Acta Cryst. A24, 472 (1968)

5. Miyake , м , S. Togawa, S. Hosoya Acta Cryst. **17**, 1083 (1964)

6. D.T. Cromer and J.T. Waber, Acta Cryst. **18**, 104 (1965)

7. D.T. Cromer, Acta Cryst. **18**, 17 (1965)

8. A.J. Freeman, Acta Cryst. **12**, 969 (1959)

9. W. Ruland, Brit. J. Appl. Phys. **15**, 1301 (1964)

10. H.M. James, _The Optical Principles of the Diffraction of X-rays_, Cornell University Press, Ithaca, New York (1965)

11. W.E. Duncanson and C.A. Coulson, Proc. Phys. Soc. **57**, 190 (1945)

12. B .E. Warren and R.L. Mozzi, Acta Cryst., **21**, 459 (1966)

13. S.L. Strong and Roy Kaplow, Acta. Cryst. **23**, 38 (1967)

14. B.E. Warren, _X-ray Diffraction_, Chapter 10, Addison Wesley, Reading, Mass., (1969)

15. H. Richter and G. Breitling, private communication.

16. R. Kaplow, B.L. Averbach, and S.L. Strong, J. Phys. Chem. Sol. 23, 1195, (1964)

CHAPTER 4

SMALL ANGLE SCATTERING THEORY AND EXPERIMENT

A. Introduction

The ideal amorphous solid is homogeneous over a scale of at least a few tens of angstroms, but in the real amorphous solid this homogeneity is often destroyed by the presence of density fluctuations, such as voids and/or phase separated regions. In this Chapter, we will discuss the detection and analysis of x-ray scattering from such fluctuations.

B. Theoretical discussion of the small angle scattering

1. Scattering from the inhomogeneous solid

Mathematically we can approximate the scattered intensity from an inhomogeneous solid as follows. For a homogeneous monoatomic solid, the coherently scattered intensity normalized to electron units per atom can be written as:

$$I_{coh}(k) = f^2(k)|S^i(k)|^2 \qquad (4-1)$$

where $S^i(k) = \sum_j e^{ik \cdot R_j}$, the index j extends over all the atomic positions characteristic of the homogeneous solid, and f(k) is the electronic form factor of the atoms comprising the solid. The quantity $S^i(k)$ is the structure factor of the homogeneous solid.

Physically, density fluctuations may be introduced into the ideal solid by either removing atoms, by replacing the original atoms with atoms having a different electron density, or by changing in some regions the atomic density by altering

the structure. As long as we can ignore the atomic relaxations brought about by the removal or the insertion of different atoms, the first two mechanisms are equivalent to adding a distribution of charge to the atoms being modified which changes their form factors by the amount Δf. The scattered amplitude for the inhomogeneous solid becomes:

$$f(k)S^i(k) + \Delta f(k)S^c(k) \qquad (4-2)$$

where $S^c(k) = \sum_l e^{ik \cdot R_l}$ and the index l extends over those atoms whose charge density has been modified.

We will henceforth refer to all quantities pertaining to the regions where the charge has been modified by the superscript 'c'. We shall call such regions the complementary particle, realizing that they can be either voids or phase separated regions.

Squaring Equation 4-2, the observed scattered intensity of the inhomogeneous solid becomes:

$$I_{coh}(k) = f^2(k)|S^i(k)|^2 + 2\text{Real}\{f(k)\Delta f^*(k)S^i(k)S^{c*}(k)\} + \Delta f^2(k)|S^c(k)|^2 \qquad (4-3)$$

At first it appears that the intensity from the ideal homogeneous solid cannot be separated from that of the complementary particles. The scattered intensity from the complementary particles must increase or reach a limit with decreasing k provided that there are no interference effects between the complementary particles. The intensity from the homogeneous solid must decrease with decreasing k; thus we can

neglect all terms involving scattering from the ideal homogeneous solid, and to a good approximation the scattering at small angles, $I_{SA}(k)$, is given by the last term in Equation 4-3, or:

$$I_{SA}(k) = \Delta f^2(k) |S^c(k)|^2 \qquad (4-4)$$

In the next section, we discuss for which particle sizes and concentrations the separation of the scattering curve into its contributions from the complementary particles and the ideal, homogeneous solid can be made.

2. Separation of the scattering curves of the homogeneous
    solid and the complementary particles

Figure 4-1 shows the calculated SAS intensity normalized to electron units per atom for a 1% density deficit in amorphous Ge distributed into spherical voids of radius R_0 for various R_0's. Also shown for sake of comparison is the first diffraction peak produced by interatomic interferences in amorphous Ge which represents the scattering from the nearly ideal homogeneous Ge. This peak is approximately a Lorentzian function with a half width of 0.2 $\overset{o}{A}{}^{-1}$. The tailing of this peak to low values is believed to be caused by either the lack of the long range order or by density fluctuations having a spatial extent approximately the size of an atom. For small particles less than 3 $\overset{o}{A}$ radius, it is difficult to separate the two curves since the scattering and the ideal material overlap. As the voids of the small voids/become larger, their SAS intensity becomes
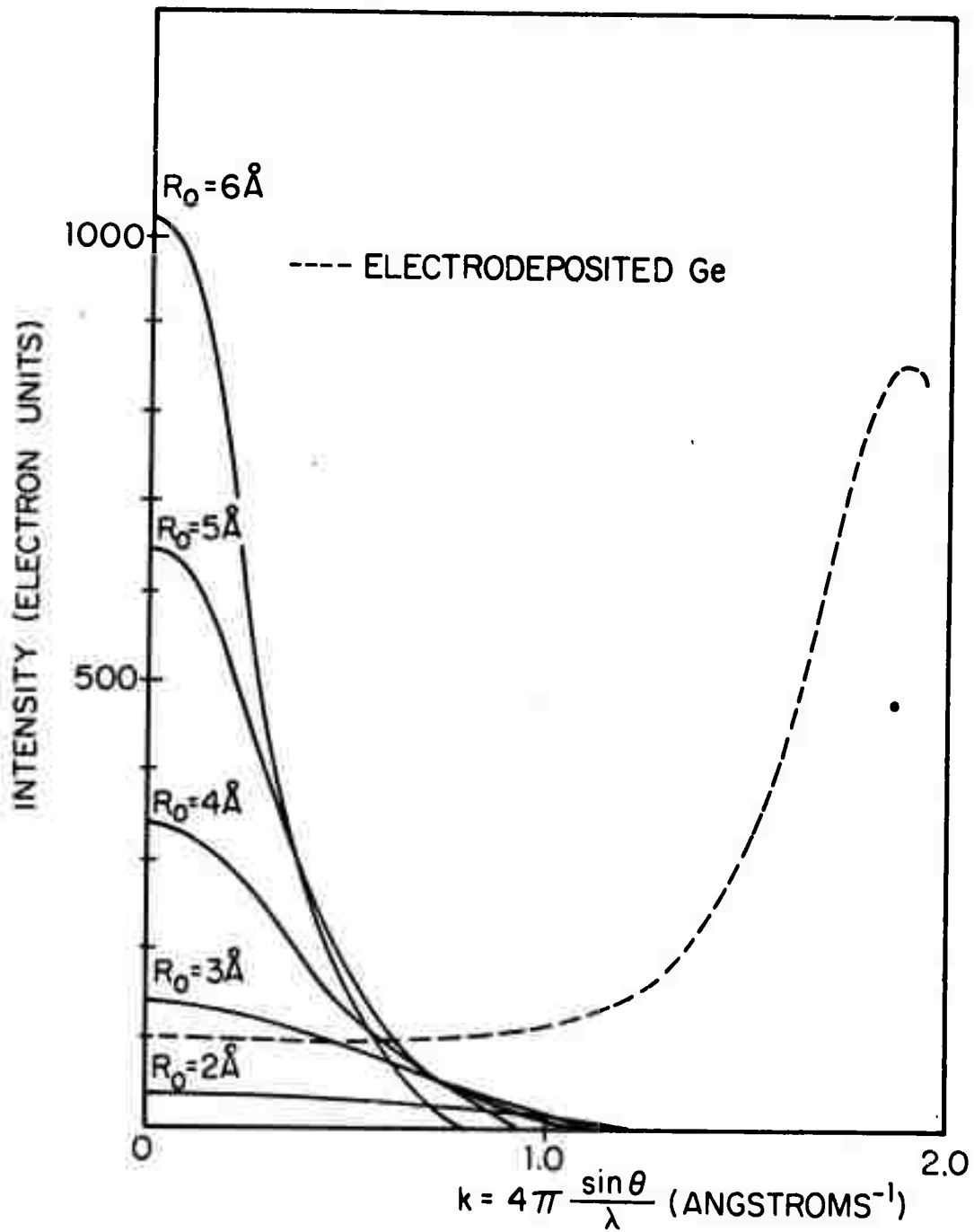
FIG. 4-1 SMALL ANGLE SCATTERING PRODUCED BY 1%
DENSITY DEFICIT DISTRIBUTED IN VOIDS OF
RADIUS R_0 IN AMORPHOUS Ge.

larger and progressively sharper, making the separation from the intensity of the homogeneous easier. Figure 4-1 demonstrates that for a 1% density deficit, the separation does not become accurate until $R_O > 3$ Å.

3. The continuum approximation

When the sizes of the complementary particles are several atomic diameters most of the scattering occurs at k values sufficiently small such that interference effects among atoms within the complementary particles become small. It then becomes simpler to disregard these interference effects and treat the complementary particle as a continuum rather than a collection of discrete atoms. With this assumption, the scattered intensity can be written in terms of a continuous density function $\rho_c(r)$, normalized so that $\rho_c(r) = 1$ for r inside the particle, and $\rho_c(r) = 0$ for r outside the particle.

After all these approximations have been made, the SAS intensity becomes:

$$I_{SA}(k) = |\Delta\rho|^2 \left| \int \rho_c(r) e^{ik \cdot r} d^3 r \right|^2 \tag{4-5}$$

where $\Delta\rho$ is the difference in the electron density between the complementary particle and the homogeneous solid in which it is immersed.

4. Relation of the SAS intensity to the distribution of sizes of the complementary particles

We proceed to specialize Equation 4-5, following Letcher and Schmidt,[2] to treat complementary particles having the

same shape, random positions relative to one another, and random orientations in space.

In the real solid, there may be complementary particles having different values of $\Delta\rho$, but here we restrict the discussion to complementary particles having a single value of $\Delta\rho$. Since the possible values of $\Delta\rho$ are not continuous, but discrete, one type of particle will dominate the SAS. Usually $\Delta\rho$ is the largest for a void, and hence, it is likely that voids will dominate the scattering.

For an ensemble of particles of a single shape with sizes between a and a + da, it can be shown that Equation 4-5 gives as the observed scattered intensity:

$$I_{SA}(k) = \Delta\rho^2 V(a) N(a) da \int_0^\infty 4\pi r^2 \gamma_0\left(\frac{r}{a}\right) \frac{\sin(kr)}{kr} dr \qquad (4-6)$$

where $N(a) da$ = number of voids per unit volume with diameters between a and a + da

$V(a)$ = volume of a particle of diameter a

$\gamma_0\left(\frac{r}{a}\right) = \langle \rho_c(R) \rho_c(R+r) \rangle = \int \rho_c(R) \rho_c(R+r) d^3R$

The quantity $\gamma_0\left(\frac{r}{a}\right)$ gives the probability that for an arbitrary point within a complementary particle of diameter a, a vector of radius r drawn in an arbitrary direction from this point also lies in the particle.[1] As has been discussed by Guinier et al.,[1] $\gamma\left(\frac{r}{a}\right)$ has the property that $\gamma(o) = 1$, and that it monotonically decreases with r, tending very rapidly to 0 with increasing r for r equal to or greater than a.

For particles all having the same shape, but with a dis-

tribution of sizes, the intensity becomes:

$$I_{SA}(k) = \Delta\rho^2 \int_o^\infty \int_o^\infty N(a)V(a)\,\gamma_o(\frac{r}{a})da \;\; 4\pi r^2\frac{\sin(kr)}{kr}dr$$

$$= \Delta\rho^2 \int_o^\infty \gamma(r)\; 4\pi r^2\frac{\sin(kr)}{kr}dr \tag{4-7}$$

where

$$\gamma(r) = \int_o^\infty N(a)V(a)\,\gamma_o(\frac{r}{a})da \tag{4-8}$$

The quantity $\gamma(r)$ is an average shape function in which the $\gamma_o(\frac{r}{a})$ are weighted by the total volume occupied by the complementary particles of size a. By inspection of Equation 4-8, we see that where $\gamma(r)$ becomes equal to zero, then $N(a)\cdot V(a)$ is making a small contribution to the integral, and hence where $\gamma(r)$ goes to 0 indicates the maximum void radius making significant contribution to the total volume of the complementary particles.

Equation 4-7 can be inverted to give:

$$\gamma(r) = \frac{1}{2\pi^2\Delta\rho^2 r} \int_o^\infty k\,\sin(kr)I_{SA}(k)dk \tag{4-9}$$

However, the average of the shape function is not very interesting. We would rather have the distribution $N(r)$ and look for a way to extract it from Equation 4-9. This may be done by operating on both sides of Equation 4-9 with some differential operator, L, such that L satisfies:

$$L\gamma(r) = \int_o^\infty V(a)N(a)L\gamma_o(\frac{r}{a})da = \int_o^\infty S_c(r-a)N(a)da = N(r) \tag{4-10}$$

This relation holds if we choose L to satisfy:

$$V(a)L \, \gamma_o\left(\frac{r}{a}\right) = \delta(r-a) \qquad (4\text{-}11)$$

Using Equation 4-10 and 4-9 the general solution is given by:

$$N(r) = \frac{1}{2\pi^2 \Delta \rho^2} \int_0^\infty kI(k) \, L \, \left(\frac{\sin(kr)}{r}\right) \, dk \qquad (4\text{-}12)$$

In principle, it is necessary to know only the shape of the particles to extract the particle size distribution from the small angle intensity curve. However, there are difficulties in finding L, since there are no known systematic procedures by which it can be found.

Consider the case of spherical particles. We will denote all quantities pertaining to this shape by the superscript 's'. We have for spherical particles:

$$V^s(a) = \frac{\pi a^3}{6} \qquad (4\text{-}13a)$$

$$\gamma_o{}^s\left(\frac{r}{a}\right) = 1 - \frac{3}{2}\frac{r}{a} + \frac{r^3}{2a^3} \quad \text{for } r < a$$

$$= 0 \qquad\qquad \text{for } r > a \qquad (4\text{-}13b)$$

Since the 3rd order derivative of $\gamma_o\left(\frac{r}{a}\right)$ with respect to r at r = a is discontinuous, we have by inspection of Equation 4-13b:

$$\frac{d}{dr}\left(\frac{\gamma_o{}^s\left(\frac{r}{a}\right)}{r}\right) = -\frac{3}{a^3}\delta(r-a) \qquad (4\text{-}14)$$

and hence, by comparison to Equation 4-12, we have:

$$L^s = -\frac{2}{\pi}\frac{d}{dr}\frac{1}{r}\frac{d^2}{dr^2} \qquad (4\text{-}15)$$

Using Equations 4-12 and 4-15 the diameter distribution for spherical particles becomes:

$$N^S(r) = -\frac{1}{2\pi^3 \Delta\rho^2} \int_0^\infty kI(k) \frac{d}{dr} \frac{1}{r}\left(\frac{\sin(kr)}{r}\right)'' dk$$

$$= \frac{1}{\pi^3 \Delta\rho^2} \int_0^\infty k^4 I(k) \alpha(kr) \, dk \qquad (4-16)$$

where

$$\alpha(x) = \cos(x)\left(1 - \frac{8}{x^2}\right) - 4\frac{\sin(x)}{x}\left(1 - \frac{2}{x^2}\right)$$

This same result has been derived by Letcher and Schmidt[2] by using a similar method.

5. <u>SAS for some simple, useful cases</u>

Equations 4-12 and 4-16 are quite general, but are of such complexity that they require a computer to be evaluated. It is helpful to consider a few simple cases which can be directly applied to the data without having to resort to a computer. Guinier et al.[1] show that for a spherical particle of radius R_0, the scattered intensity can be accurately approximated by:

$$I_{SA}(k) = \left(\frac{4\pi}{3} R_0^3 \Delta\rho\right)^2 e^{-\frac{R_0^2 k^2}{5}} \qquad (4-17)$$

Shull and Roess[4] show that when the particles are spherical and their size distribution is a Maxwellian of form:

$$N(r) = \frac{1}{R_0^{n+1}\Gamma\left(\frac{n+1}{2}\right)} \, 2 \, r^n \, e^{-\frac{r^2}{R_0^2}} \qquad (4-18)$$

the scattered intensity becomes:

$$I_{SA}(k) = \frac{constant}{\left[1+\frac{(kR_0)^2}{5}\right]^{(n+4)/2}} \qquad (4-19)$$

Some information concerning the shape and magnitude of the particle size distribution can be obtained by fitting Equations 4-17 and 4-19 to the SAS intensity curves. But when the curves cannot be adequately fitted, then Equation 4-16 must be evaluated to obtain $N(r)$, which is valid only if the complementary particles are almost spherical. As the shape of the particles deviates from sphericity, the fitted parameters, of course, lose their meaning.

6. The volume sum rule

For the interpretation of electronic properties it is important to know the density of the defect free solid. If we can find the charge density of the defect (or complementary particles) and the total volume of the defects, then we can account for the defects' contribution to the measured bulk density to get the density of the ideal solid. The total volume occupied by the complementary particles can be found from the size distribution found from Equation 4-16. If, however, the complementary particles are not spherical, this estimate will be in error.

From Equations 4-8 and 4-9 we have that:

$$\int_0^\infty V(a)\, \gamma_0\left(\frac{r}{a}\right) N(a)\, da = \frac{1}{2\pi^2 \Delta\rho^2} \int_0^\infty kI(k)\frac{\sin(kr)}{r}\, dk \qquad (4-21)$$

We now make use of the properties that as $r \to 0$, $\gamma\left(\frac{r}{a}\right) \to 1$, and

$\sin\frac{kr}{r} \rightarrow k$; hence Equation 4-21 becomes:

$$V_T^{\ C} = \int_0^\infty V(a)N(a)da = \frac{1}{2\pi^2\Delta\rho^2} \int_0^\infty k^2 I(k)\,dk \qquad (4-22)$$

where $V_T^{\ C}$ is the total volume of the complementary particles. Note that this relation is independent of the shapes of the particles and holds equally well for a distribution of shapes, as well as sizes. The only requirement is that the SAS intensity be spherically isotropic.

We note, however, that this volume depends on $\Delta\rho$, which we cannot determine from the SAS alone. But other physical constraints can limit the number of choices of $\Delta\rho$, or can, in some cases, uniquely specify $\Delta\rho$. The $\Delta\rho$ that gives the most physically plausible $V_T^{\ C}$ is chosen to be the correct electronic density.

For example, if we find that $V_T^{\ C}$ is 5% of the sample volume under the assumption that the scattering is from voids, the same data would suggest a $V_T^{\ C}$ of five times the sample volume under the assumption that the scattering is from microcrystals immersed in an ideal amorphous solid with an electron density 90% that of the crystal. Clearly for this case, the scattering cannot possibly be accounted for by micro-crystalline particles.

C. Experimental small angle scattering system

1. Experimental arrangement

The diffractometer arrangement discussed in Chapter 3 is entirely inadequate for obtaining the scattered intensity

at small angles. At small angles, the intensity of
radiation scattered from the air column in the incident beam
can become much larger than the intensity scattered from
the sample. Additional difficulties inherent in the reflec-
tion geometry are that surface roughness and sample mis-
alignment can severely affect the measured coherently
scattered intensity at very small angles. At sufficiently
small angles, total reflection of the x-rays can occur,
making it impossible to obtain the scattered intensity be-
low some minimum angle.

An experimental arrangement devised by Kratky circum-
vents some of these difficulties by employing a geometry in
which the transmitted diffracted beam is detected. This is
the arrangement used here.

2. Description of the small angle scattering equipment

The experimental small angle scattering arrangement,
shown in Figure 4-2, consists of an x-ray generator and
tube, a Kratky collimation system, a vacuum chamber, de-
tector and associated electronics. Two modifications were
made to the system. First, a new vacuum chamber was designed
so that scattering angles as high as 12.5 degrees could be
attained without encountering any spurious peaks produced
by the incident beam striking the bottom of the chamber.
This was achieved by altering the basic design of the commer-
cially available Siemens vacuum chamber by increasing the
length of the back plate of the chamber, while correspondingly
altering the sides and bottom so as to maintain a sealed

chamber. As will be discussed in Section F-3, the purpose for extending these measurements to high angles was to allow the data to be normalized easily to electron untis.

The second modification was the introduction of a stepping motor and platform so that the height of the chamber could be controlled by the Canberra Scan controller. With this modification the data collection was made completely automatic, a necessary convenience since the experiments were usually of several hours duration.

To facilitate further description of the apparatus, it is helpful to trace through an x-ray photon from the point where it is generated until it is recorded. The x-ray source, powered by an Eindhoven type PW1010 generator, is a sealed tube type with a Mo anode. The x-ray photons are produced on a line focal spot characterized by a height h_{fs} and width w_{fs}. The radiation, emanating from the line focus port of the tube, first passes through a Zr filter where the MoKβ component is reduced by a factor of about 10, and then passes through a collimator where the beam is made into a very fine slit of heiglt h_{ib} and width w_{ib}. The beam then passes through the sample, which, usually about 1 cm wide, is chosen to have a thickness such that ut $\sim$ 1, where u is the inverse absorption length of x-rays in the sample.

The direct and the scattered beams then enter through the front window of the vacuum chamber, the direct beam stopping at the rear of the chamber and the scattered beam passing through the window at the rear of the vacuum chamber.

FIG. 4-2 SCHEMATIC OF SMALL ANGLE SCATTERING SYSTEM

chamber. As will be discussed in Section F-3, the purpose for extending these measurements to high angles was to allow the data to be normalized easily to electron untis.

The second modification was the introduction of a stepping motor and platform so that the height of the chamber could be controlled by the Canberra Scan controller. With this modification the data collection was made completely automatic, a necessary convenience since the experiments were usually of several hours duration.

To facilitate further description of the apparatus, it is helpful to trace through an x-ray photon from the point where it is generated until it is recorded. The x-ray source, powered by an Eindhoven type PW1010 generator, is a sealed tube type with a Mo anode. The x-ray photons are produced on a line focal spot characterized by a height h_{fs} and width w_{fs}. The radiation, emanating from the line focus port of the tube, first passes through a Zr filter where the MoKβ component is reduced by a factor of about 10, and then passes through a collimator where the beam is made into a very fine slit of height h_{ib} and width w_{ib}. The beam then passes through the sample, which, usually about 1 cm wide, is chosen to have a thickness such that ut $\sim$ 1, where u is the inverse absorption length of x-rays in the sample.

The direct and the scattered beams then enter through the front window of the vacuum chamber, the direct beam stopping at the rear of the chamber and the scattered beam passing through the window at the rear of the vacuum chamber.

The entrance and exit windows on the vacuum chamber are made of 1 mil thick cellulose acetate foils, which are suffi-ciently strong to hold back the atmosphere in order to main-tain a typical vacuum of 500 microns, but are thin enough so as to produce only negligible scattering.

The scattered beam then passes through the exit slit or receiving slit characterized by a height h_{rs} and a width w_{rs}. After passing through the cellulose acetate window, the scattered radiation passes through another Zr filter, which helps to reduce any fluorescence radiation that has been excited in the sample, and which further filters any other wavelengths that are away from the MoKα wavelength. The scattered radiation is then detected by the scintilla-tion counter, the output of which is analyzed with a pulse height analyzer, thereby adding another stage of filtering to the detected signal.

D. Experimental procedure

The x-ray generator, x-ray tube and vacuum pump are turned on a few hours prior to the commencement of the data collection. If at the end of a few minutes, the vacuum in the vacuum chamber is not at least 800 microns, it becomes necessary to reseal the vacuum chamber. The rear plate on the chamber is removed, the rubber gasket under this plate replaced with a new gasket and the plate then remounted and tightened to the rear of the chamber. The old windows on the front and back of the chamber are removed and new win-dows, consisting of fresh sheets of 1 mil cellulose acetate are glued in place with a dilute solution of rubber cement,

butyl and ethyl acetates. After 15 minutes, when the windows
are firmly in place, the chamber is remounted onto the chamber track, the vacuum hose attached, and the chamber again
is evacuated.

After a sufficient vacuum (500 μ) is attained, a thick
copper foil is inserted directly after the receiving slit.
The chamber height, is adjusted until the intensity detected
through the scintillation counter is maximized. A Siemens
type   monochromator is placed after the Cu attenuator,
and then, the Cu attenuator is removed. The monochromator
is set to pass a band centered about the MoKα component and
the electronics are adjusted to optimize this signal. When
necessary,/the entrance and exit slits are adjusted by the procedure outlined in the Siemens manual, "Kratky small angle
camera". The monochromator is then detuned to make the
counting rate (about 1000 cps) significantly less than the
inverse response time of the scintillation counter. The intensity is then measured, the sample   inserted into the
main beam, and the intensity again recorded. The ratio of
the intensity, with and without the sample in the main beam,
gives the transmission, T, of the sample.

The Cu attenuator is replaced, the monochromator removed, and the chamber height adjusted by hand until the
intensity is again maximized. The scan controller then is
set at 0000 angle, the motor control turned on, the vacuum
chamber electronically raised to 1 mm, the copper attenuator
removed, and the data collection automatically proceeds.

The camera sits at a fixed angle until a predetermined time has passed. Then it is automatically raised by an amount $\Delta\theta$, thus proceeding until the entire angular scan, from about 0.2^O to 12.5^O is covered. At each point the height of the vacuum chamber, the time and counts are recorded on the teletype. The sample is then removed and the experiment repeated to obtain the background intensity.

E. Experimental difficulties

These experiments are designed to see if amorphous semiconductors have dispersed throughout their volume, a high concentration of voids. In order to obtain sufficient intensity to detect the scattering from these voids in a reasonable time, it is necessary to operate with entrance and exit slits of 0.5 mm. This limits the minimum angle at which the scattered intensity is overwhelmed by the main beam to 0.2^O. Since most of the scattering from voids with diameters greater than 60 $\overset{o}{A}$ is confined to angles less than 0.2^O, scattering from voids of this size cannot be observed.

Additional difficulties arise from uncertainties in the background level. Since neither the incident beam nor the diffracted beam is monochromatic, it is hard to be certain that all background scattering is eliminated. Attempts to use a Siemens diffracted beam monochromator to detect the scattered radiation have been unsuccessful, since the intensity observed with this in place after the receiving slit is very small.

Figure 4-3 shows the intensity of the detected unfiltered radiation from an amorphous Ge sample irradiated by x-rays produced by a Mo tube operating at 50 kv. Since the intensity at smaller k values is too large compared to that of the first diffraction peak, this curve cannot be produced solely by a scattering mechanism. Such a curve is expected if there were a large fluorescence component along with the scattered intensity.

When excited with radiation from a Mo x-ray tube, elements such as Ge, Ga, As, and Se emit characteristic fluorescence lines which are approximately 1.2 Å in wavelength. These fluorescence lines are too close in wavelength to the MoKα wavelength to be effectively eliminated by the pulse height analyzer alone. After inserting before the detector a two mil Zr filter, which absorbs wavelengths near 1.2 Å much more strongly than the wavelengths near the Mo Kα wavelength, 0.7 Å, the ratio of the peak to the minimum intensity detected from amorphous Ge is greatly improved, as is shown in Figure 4-3. This supports the contention that the fluorescence radiation has contributed a large signal to the radiation observed from amorphous Ge. A run with a four mil Zr filter indicates that the peak to the minimum intensity is not further changed, suggesting that most of the fluorescence radiation has been already removed by the 2 mil Zr filter. However, as an extra precaution, all the runs have been made using a 4 mil filter directly after the receiving slit.
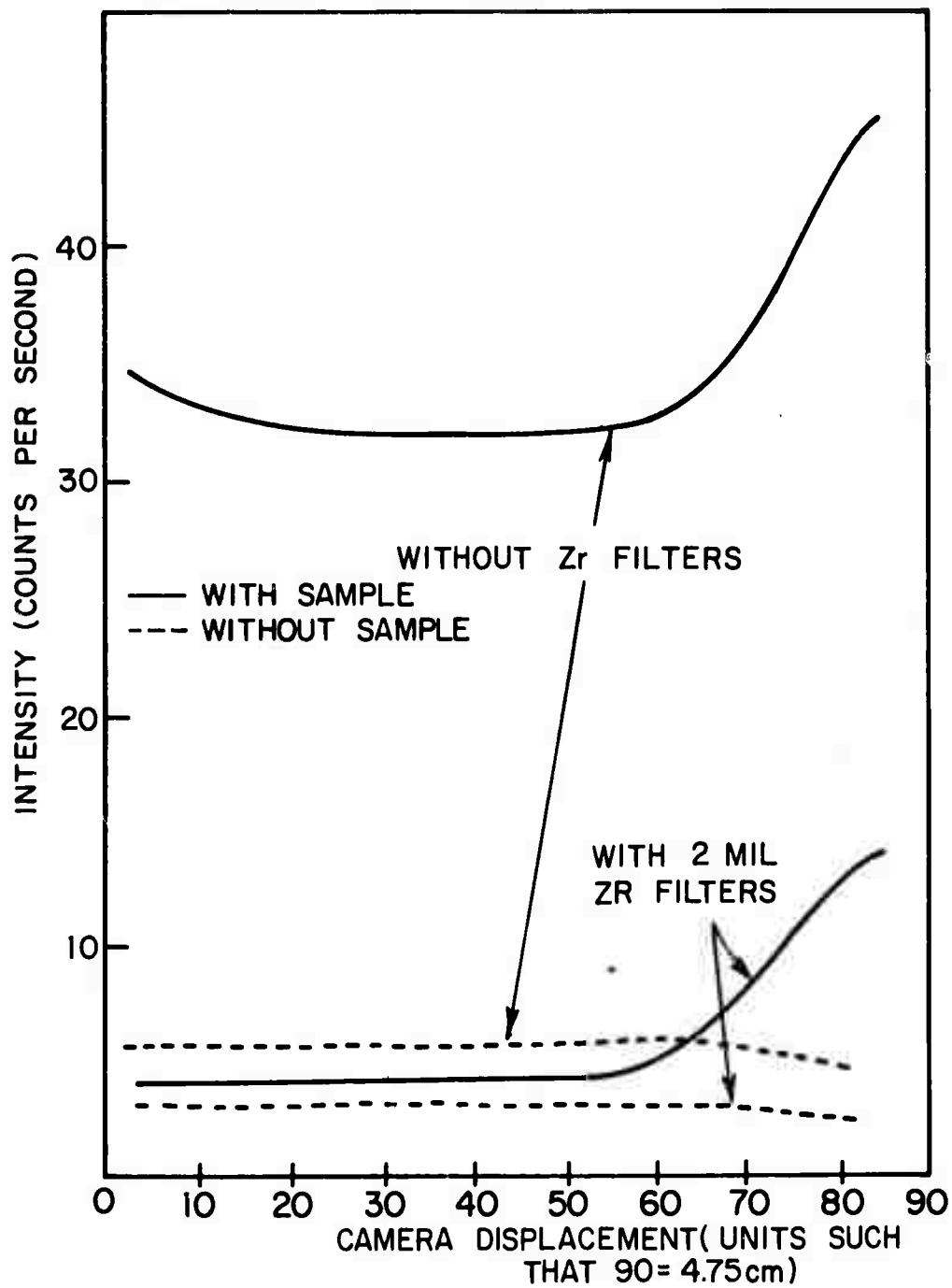
FIG. 4-3   FILTERED AND UNFILTERED RADIATION DETECTED
FROM AN AMORPHOUS GE SAMPLE IRRADIATED
BY RADIATION FROM A M_o X-RAY TUBE.

The fraction of the incident beam intensity that is transmitted through the foil is given by:

$$T = e^{-\mu_m(\lambda)\rho t}$$

where

$\mu_m(\lambda)$ = mass absorption coefficient of the filter material

ρ = density of the filter material

t = thickness of the filter

Figure 4-4 shows that the four mil Zr filter becomes ineffective in attenuating wavelengths shorter than about 0.4 Å. For this reason, it is suggested that the x-ray tube voltage be kept below 40 kv so as not to excite any continuum x-rays with wavelengths less than 0.4 Å. Note that from Figure 4-4, the Ge K α fluorescence line at 1.25 Å is attenuated by the filter about 80 times more than the Mo K α line, thus almost entirely eliminating it.

F. **Data reduction**

1. **Background subtraction**

To obtain the intensity produced by the sample alone, $I_{exp}(y)$, it is necessary to subtract the background intensity from the intensity obtained with the sample. The experimentally observed intensity produced by the sample alone is:

$$I_{exp}(y) = I_s(y) - T I_{back}(y) \qquad (4-23)$$

where $I_s(y)$ = intensity with sample

$$T = e^{-\mu_m(\lambda)\rho t}$$
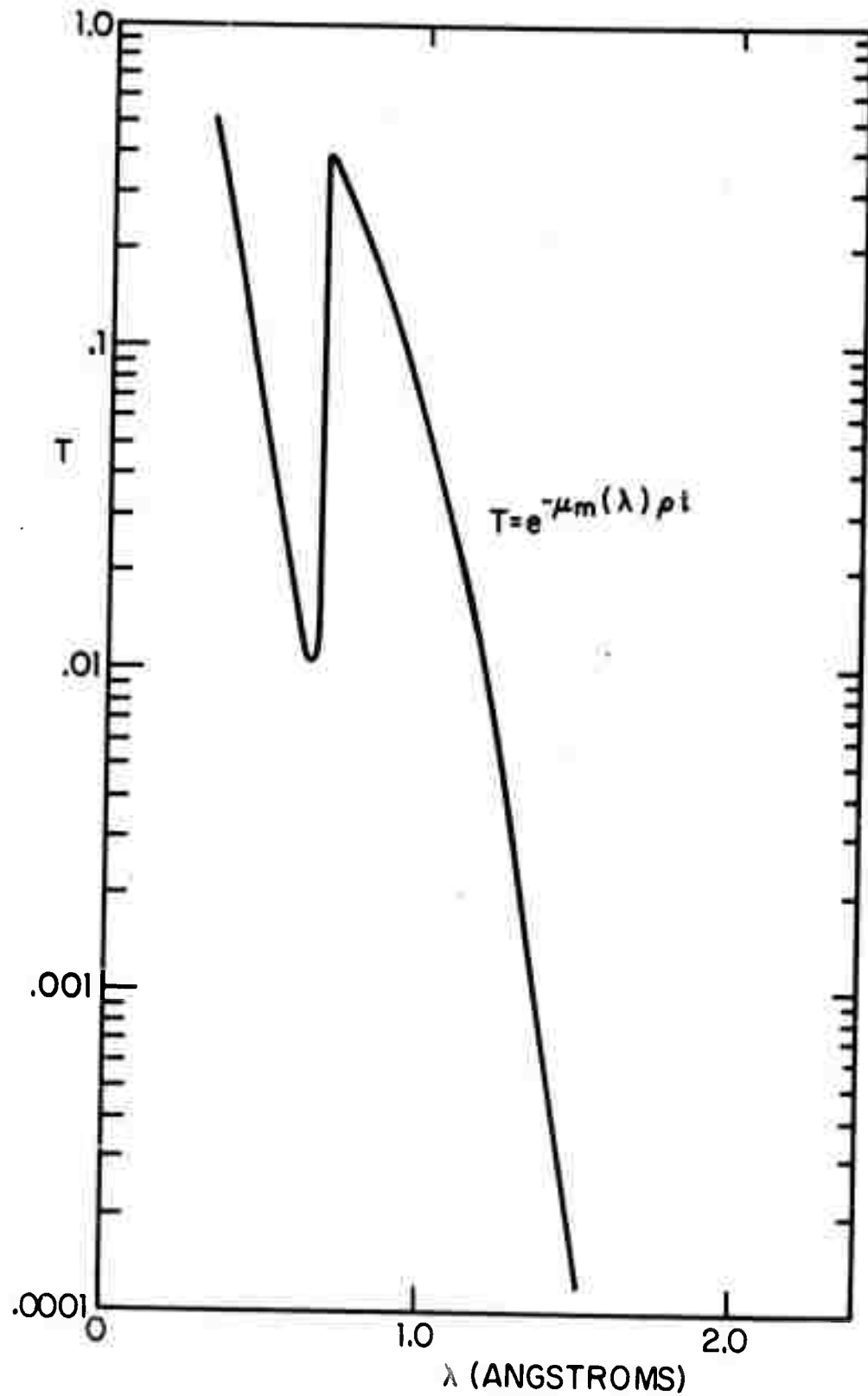
FIG. 4-4   ATTENUATION FUNCTION, T, OF A 4 MIL
ZIRCONIUM FOIL AS A FUNCTION OF THE
X-RAY WAVELENGTH, λ.

$$I_{back}(y) \quad = \quad \text{intensity with no sample}$$

$$T \qquad\qquad = \quad \text{transmission of the sample}$$

$$y \qquad\qquad = \quad \text{vertical displacement of the vacuum}$$

chamber

The intensity is then transformed from dependency on the
variable y to dependency on the scattering vector,k,given
by the relation:

$$k = \frac{4\pi\sin\theta}{\lambda} \quad \text{where } \theta = \frac{1}{2}\sin^{-1}(y/CR) \qquad (4\text{-}24)$$

and where CR is the camera radius, defined to be the distance
between the centers of the sample and the receiving slit.

2. Collimation corrections

The experimentally observed intensity is not directly
given by Equation 4-7. To obtain $I_{SA}(k)$, it is necessary
to correct $I_{exp}(k)$ for the geometry of the focal spot on
the x-ray tube, the incident beam, and the receiving slit.
As far as the incident beam is concerned, only that portion
which intersects the sample produces any scattering and is
therefore relevant. Only when the tube focal spot, the
portion of the sample irradiated by the incident beam, and
the receiving slit are points, is the experimental intensity
exactly given by Equation 4-7.

The path of a typical photon contributing to the inten-
sity is shown in Figure 4-5. At this point, in order to
simplify the discussion, we take the vertical dimensions
of the focal spot, the incident beam, and the receiving
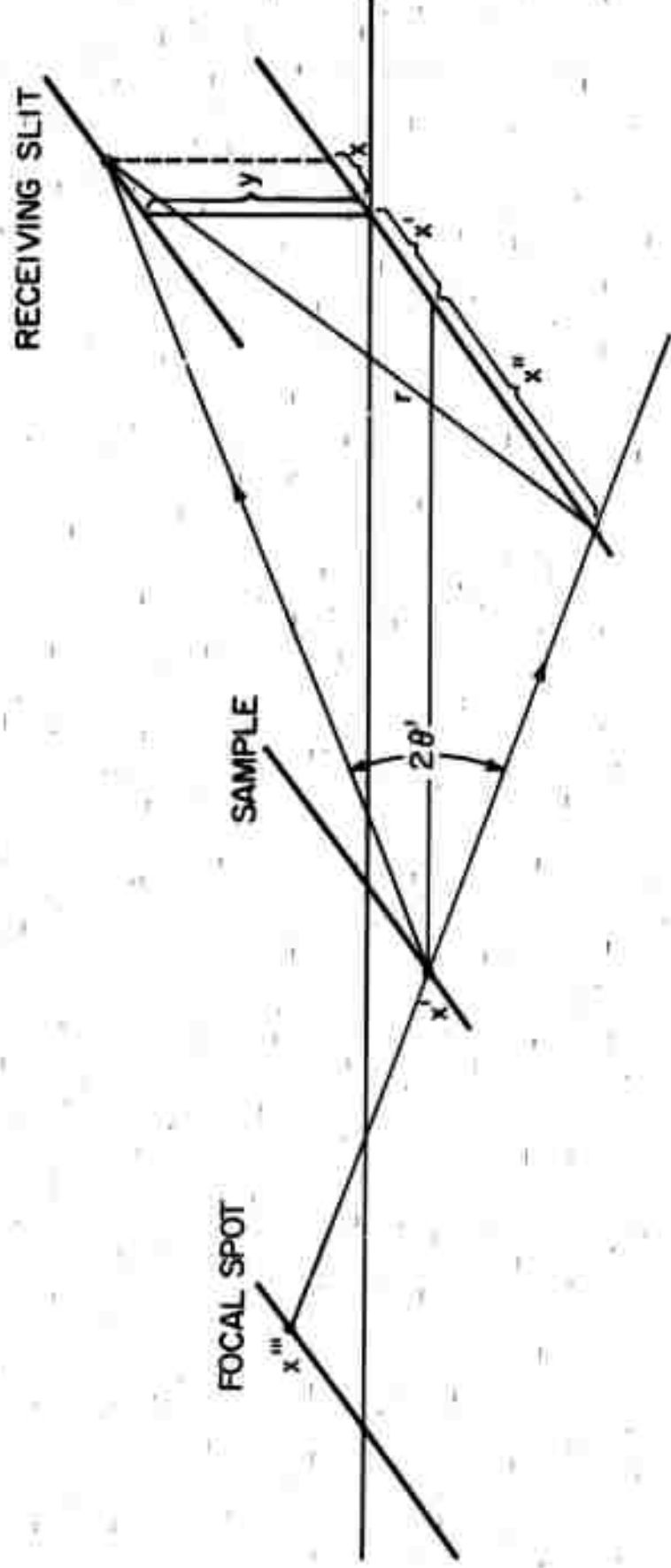
FIG. 4-5 SCHEMATIC REPRESENTATION OF A TYPICAL X-RAY BEAM PATH FOR THE THREE SLIT KRATKY ARRANGEMENT.

slit to be negligible; thus the focal spot, incident beam, and receiving slit reduce to slits, characterized by a long dimension, or height, of h_{fs}, h_{ib}, and h_{rs} respectively. (It may be somewhat disturbing that the long dimensions have been called the heights, rather than what seems to be more natural, the widths. We must refer to the long dimension in this case as the height since this is the convention established in the literature.[1])

An x-ray photon that originates at a point x''' on the focal spot, and scatters at point x' in the sample, and passes through point x at the receiving slit, scatters through an angle given by:

$$\sin(2\theta') = \frac{r}{\sqrt{CR^2 + (x-x'+x'')^2}} = \frac{\sqrt{y^2 + (x-x'+x'')^2}}{\sqrt{CR^2 + (x-x'+x'')^2}}$$

$$\cong \frac{\sqrt{y^2 + (x-x'+x'')^2}}{CR} \qquad (4-25)$$

We have made use of the fact that usually the heights of the slits are much smaller than the camera radius. Note that what determines the scattering angle is not the x''' coordinate on the focal spot, but rather its projection, x'', onto the plane of the receiving slit.

The observed intensity, $I_{exp}(y)$, is given by the sum of the true intensity, $I_{SA}(y)$, over all the ray paths shown in Figure 4-5. The experimentally observed intensity is thus given in terms of $I_{SA}(y)$ as:

$$I_{exp}(y) = \frac{1}{h_{fs} \cdot h_{ib} \cdot h_{rs}} \int_{-\frac{h_{fs}}{2}}^{\frac{h_{fs}}{2}} dx'' \int_{-\frac{h_{ib}}{2}}^{\frac{h_{ib}}{2}} dx' \int_{-\frac{h_{rs}}{2}}^{\frac{h_{rs}}{2}} dx \, I_{SA}\left(\sqrt{y^2 + (x-x'+x'')^2}\right) \qquad (4-26)$$

where x, x' and x'' are as defined in Figure 4-5. For the system used in this investigation, the heights of the receiving slit, the focal spot and the incident beam are the same value, h. In this case, the integral reduces to:

$$I_{exp}(y) = \int_0^\infty I_{SA}(\sqrt{y^2 + u^2}) \; K(v) \; du \qquad (4\text{-}27)$$

where
$$K(u) = \frac{8}{9h^3}\left(\frac{3}{2}h - u\right)^2 \quad \text{for } u < \frac{3h}{2}$$
$$0 \quad \text{for } u > \frac{3h}{2}$$

The knowns in this equation are $I_{exp}(y)$ and $K(u)$, and in principle, we can find $I_{SA}(y)$ from it.

A widely applied technique to correct for the effects of the slit heights is to assume that one of them is infinite,[1] thereby allowing the data to be corrected by a simple integral transform. However, when the data do not fall off sufficiently fast so that the condition:

$$\int_0^h I_{SA}(\sqrt{y^2 + u^2}) \; du \; \approx \; \int_0^\infty I_{SA}(\sqrt{y^2 + u^2}) \; du \qquad (4\text{-}28)$$

is not satisfied,
the infinite slit correction becomes inaccurate and more exact methods must be used. Schmidt and Hight[3] have devised a method where these corrections can be made by assuming that the weighting function, $K(u)$, in Equation 4-27 is a gaussian. However, such an approximation of the weighting function with a one parameter fit can introduce considerable error. Since sample limitations kept h to about 1 cm, we found ourselves in the uncomfortable position where the infinite slit height correction was inadequate,

and had to resort to more precise means to correct the data.

The function $I_{SA}(y)$ can be found by the iteration of the equation:

$$I_{SA}^{n+1}(y) = I_{SA}^{n}(y) + (I_{exp}(y) - M \cdot I_{SA}^{n}(y)) \qquad (4-29)$$

where M denotes the integral operation:

$$M \cdot I_{SA}^{n}(y) = \int_{0}^{\infty} I_{SA}^{n}(\sqrt{y^2 + u^2}) K(u) du \qquad (4-30)$$

We take as the initial guess $I_{SA}^{O}(y) = I_{exp}(y)$. Proof of convergence of Equation 4-29 under certain conditions is outlined in Appendix II.

Equation 4-29 requires about 20 iterations for adequate convergence particularly at small y where the experimental intensity $I_{exp}(y)$ is much less than the actual intensity, $I_{SA}(y)$. In such a case, use of a mulplicative correction procedure instead of an additive speeds up convergence. We assume that the experimental intensity is related to the true intensity by:

$$I_{exp}(y) = a(y) I_{SA}(y) \qquad (4-31)$$

To a first approximation, we then assume that a(y) is given by:

$$a(y) = \frac{M \cdot I_{exp}(y)}{I_{exp}(y)} \qquad (4-3\ )$$

The obvious iteration scheme then becomes:

$$I_{SA}^{n+1}(y) = I_{SA}^{n}(y) + I_{exp}(y) \left(\frac{I_{exp}(y)}{M \cdot I_{SA}^{n}(y)} - 1.0 \right) \qquad (4-3\ )$$

It was found that this mulplicative scheme converged about 10 times faster than the additive scheme given in Equation 4-29. However, this method is not guaranteed to converge and must be used with caution. But, if it does converge, it is necessary that it converges to the true intensity, $I_{SA}(k)$.

3. Normalization

After the data have been corrected for background and collimation, the SAS data are scaled by matching them onto the high angle/which have been obtained on the Norelco diffractometer, and have been scaled by the high angle method. The primary error in this normalization procedure arises from the inaccuracies in the height of the first peak determined from the high angle diffraction. The normalization of the SAS data is expected to be accurate to about ± 10%.

Other normalization techniques require that the scattered intensity from the sample be compared with that from a known standard. It is then necessary to make corrections for the geometry of the sample and absorption in order to scale the scattered intensity to electron units. This high angle method, on the other hand, uses the sample itself as the standard, and hence, it is not necessary to know the details of the geometry of the sample.

4. Extrapolation procedure

Since we obtain data to a minimum scattering angle of $.2^{\circ}$, it is necessary to extrapolate the data to 0 scattering angle

before it can be thoroughly analysed. This is done by making a plot of log I_{exp} vs k^2, drawing a smooth curve through the experimental points, and extrapolating this curve to k = 0 with a French curve.[1] The error introduced by such a procedure should introduce significant error in the particle distribution curves for r > 30 Å only. The intensity found this way is expected to represent a lower bound to the true intensity, for in general the true intensity is expected to be monotonically increasing as k → 0 as long as there are no interference effects between particles.[1]

REFERENCES

1. A. Guinier, G. Fournet, C.B. Walker, K.L. Yudowitch, <u>Small Angle Scattering of X-Rays</u>, John Wiley & Sons, Inc. New York 1955

2. J.H. Letcher and P.W. Schmidt, J.A.P., 37, 649 (1966)

3. P.W. Schmidt and R. Hight, Jr. Acta Cryst. 13, 480 (1960)

4. C.G. Shull and L.C. Roess, J.A.P., 18, 295 (1947)

THE STRUCTURE OF AMORPHOUS
Ge, Se, GaAs, GaP, GaSb, InSb, AND GeSn.

A. Introduction

Most of our knowledge of the structures of amorphous
semiconductors comes from diffraction experiments. The ra-
dial distribution functions (RDF) obtained from curves of
diffracted intensity versus angle give us the nearest
neighbor separations, the coordination numbers, and the bond
angles, all of which are vital parameters for any theory
that hopes to describe in detail the electronic properties
of these materials. Although several structures may give the
same RDF, the RDF's still provide a test for proposed struc-
tural models that are expected to provide some of the details
of the short range order (SRO) that the RDF is unable to pro-
vide directly.

In particular for compound materials such as the III-V's,
it is important to know if there are wrong bonds, i.e. bonds
between like atoms. The structural models that have been
proposed for amorphous Ge have many five membered rings.[1,2]
In a binary compound material, the presence of a five mem-
bered ring requires that at least one wrong bond occur in the
ring. If the III-V compounds exhibit similar RDF's to those
of amorphous Ge, many wrongs bonds are thus likely present
in these materials.

In this investigation, the diffracted intensities, $F(k)$'s and the RDF's of amorphous Ge prepared by electrodeposition and sputtering, of amorphous Se prepared by evaporation, provided by Dr. Robert Gorin of Xerox, and of amorphous GaAs, GaP, GaSb, InSb, and GeSn prepared by sputtering will be presented. Since the procurement of samples adequate in size for diffraction purposes is both costly and difficult, except for Ge only one sample has been investigated for each material, and hence, this investigation must in this sense be regarded as preliminary. We choose to make a scan of the structure of several materials rather than to focus our attention on one material since we feel the present need is to establish at least the gross structural behavior of these materials so that the quickly expanding literature concerning the electronic properties of these materials may have some structural basis for interpretation and speculation. However, we feel that the similarities observed in all the RDF's presented here suggest that these results are typical of what others will find under similar deposition conditions.

In the last section, we will answer some of the charges by Rudee[3] that the diffractionist is unable to obtain an RDF with sufficient accuracy to enable him to distinguish among the various structural models. We will also present some calculations of the interference functions of microcrystalline models taking into account the interparticle interference terms, by assuming a specific correlation between microcrystals. We will show that, despite Moss and

Graczyk's neglect of the interparticle interference terms,[4] their curves are similar to those calculated here; thus their results and conclusions still stand. Finally, we show that the correlations between the microcrystals must be very strong to bring the microcrystalline model into agreement with the experimentally observed RDF of Ge.

B. Comparison of the diffraction peaks of crystalline and amorphous material

Attempts have been made recently to describe the electronic properties of amorphous semiconductors by employing modifications of diffraction theory that require knowledge of the material's k-space structure.[5,6] Since only the spherically averaged k-space structure is experimentally obtainable, the local k-space structure averaged over a few tens of atoms is unknown. To circumvent this difficulty, it has been assumed by some authors that the k-space structure factors of amorphous materials can be represented by a broadened version of the corresponding crystalline k-space structure and that the atomic potential can by represented by the crystalline pseudopotentials.[5,6]

For the results of these theories to be meaningful, it is essential that the peaks in the observed average structure factors of the amorphous material at least have the same positions and strengths as peaks in the spherically averaged structure factors of the crystal. Since the pseudopotential is strongest in the vicinity of the first dif-

fraction peak,[24] it is particularly crucial that the first diffraction peak in the amorphous state be similar to that of the crystal.

Figures 5-1 to 5-7 show the corrected scattered intensities of amorphous evaporated Se and sputtered Ge, GaAs, GaP, GaSb, InSb, and GeSn respectively. Marked on all figures except the figure for amorphous Se, are the diffracted intensity peaks of the corresponding crystalline phase up to the (311) peak. Since GeSn has no corresponding crystalline form, the diffraction peaks for GaSb are included in Figure 5-7. If crystalline GeSn could be made, it would be expected to have an interatomic distance and charge density similar to that of GaSb.

In Table 5-1 are listed the positions in k-space of the first and second diffraction peaks of the amorphous material and the first diffraction peak position of the corresponding crystal, along with the average of the (220) and (311) peak positions weighted by their diffracted intensities.

For amorphous Ge, GaAs, GaP, and GeSn the first peak positions are nearly the same as those observed in their crystalline forms. However, the first peak positions of amorphous GaSb and InSb occur at k values of 5 and 11% respectively greater than the corresponding crystalline positions. A shift of the same size in InSb has also been observed by Eckenbach et al.[7] in thin evaporated films examined by electron diffraction. Clearly, for InSb and GaSb, it is incorrect to represent their k-space structures by

$$k = \frac{4\pi \sin\theta}{\lambda} \text{ (ANGSTROMS}^{-1})$$
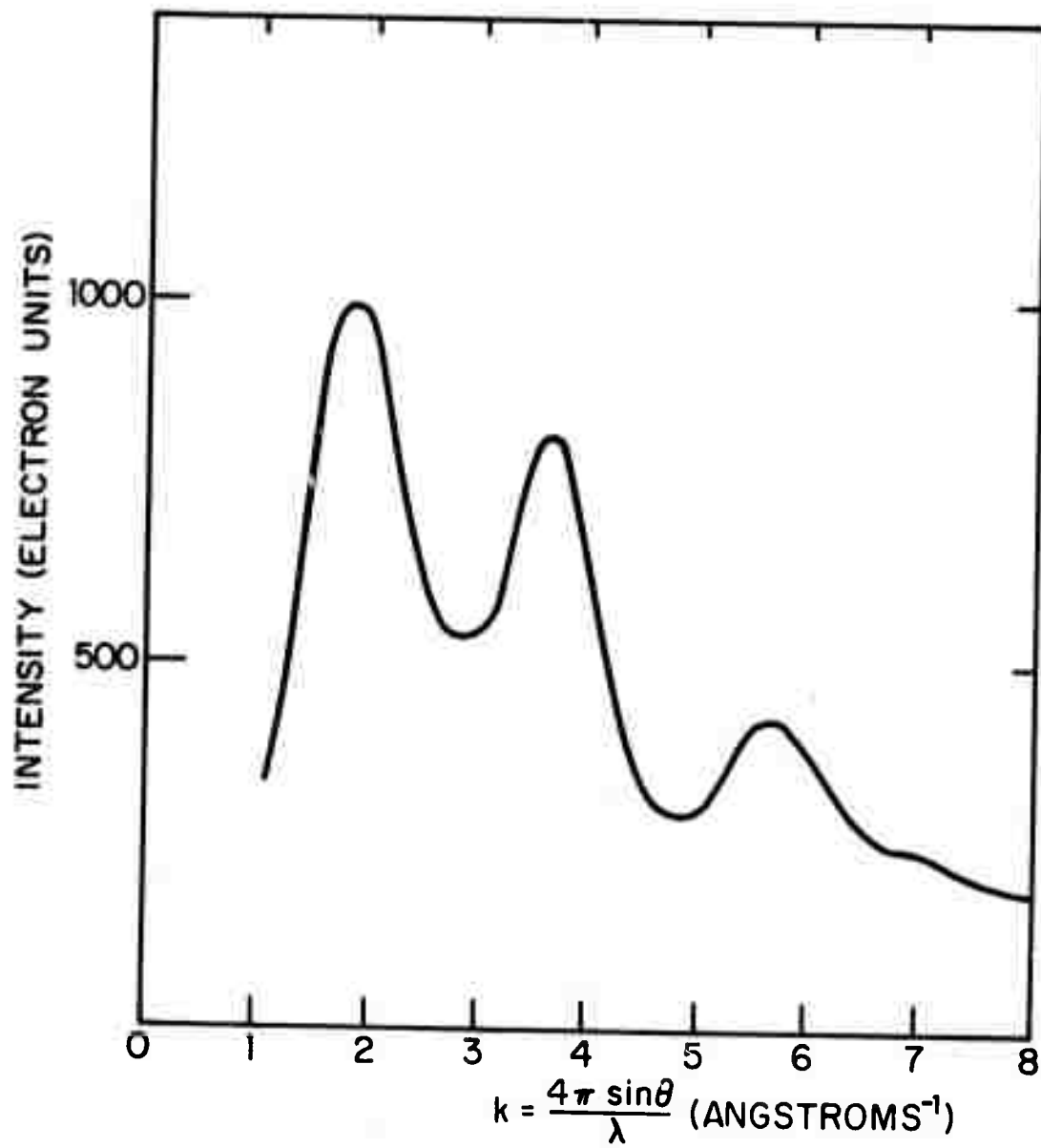
FIG. 5-1 COHERENTLY SCATTERED INTENSITY OF AMORPHOUS EVAPORATED SE.

$$k = \frac{4\pi \sin\theta}{\lambda} \ (ANGSTROMS^{-1})$$
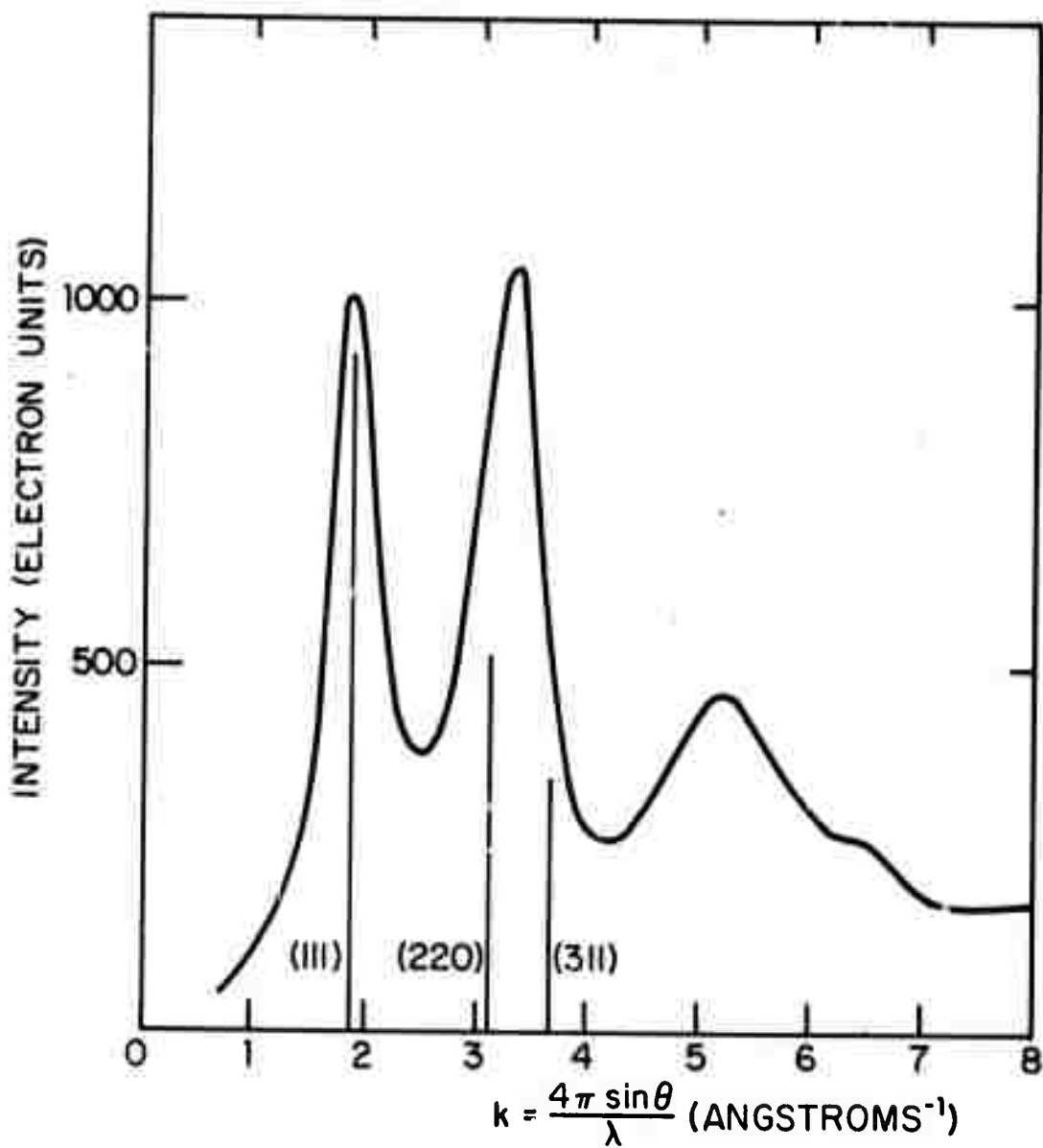
FIG. 5-2 COHERENTLY SCATTERED INTENSITY OF
AMORPHOUS SPUTTFRED GE.
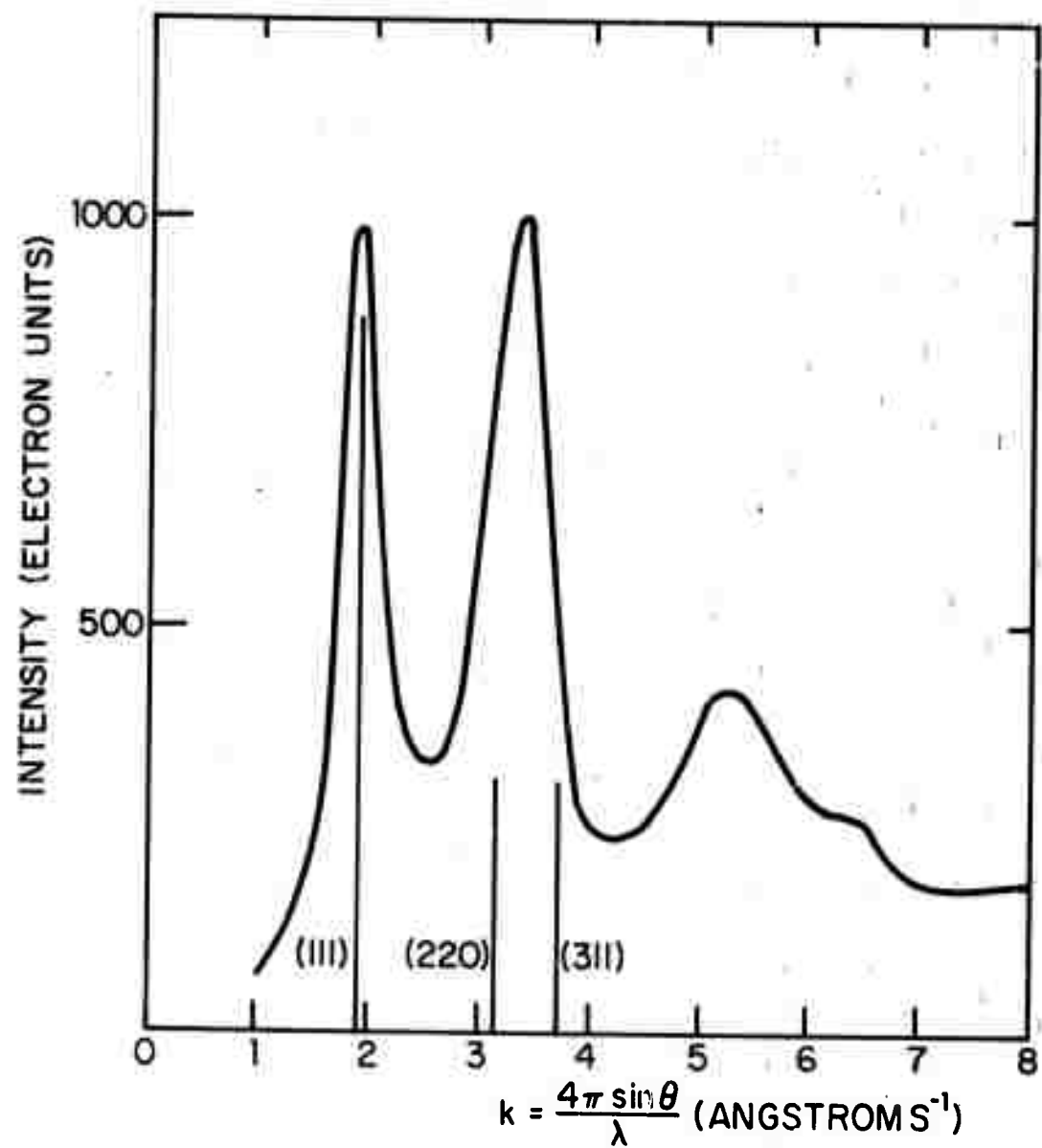
FIG. 5-3 COHERENTLY SCATTERED RADIATION OF AMORPHOUS SPUTTERED GaAs.

$$k = \frac{4\pi \sin\theta}{\lambda} \, (\text{ANGSTROMS}^{-1})$$
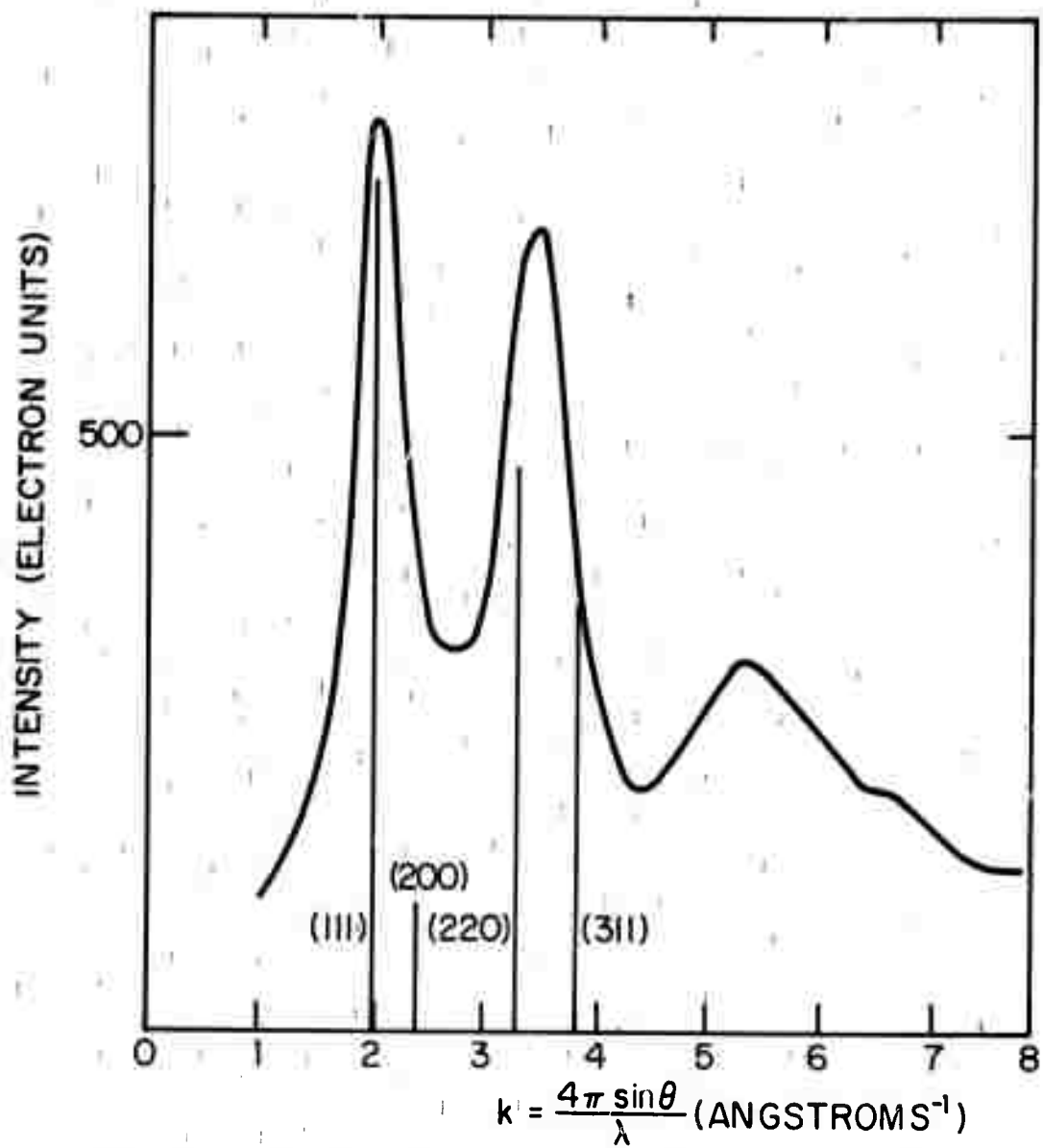
FIG. 5-4 COHERENTLY SCATTERED INTENSITY OF AMORPHOUS SPUTTERED GaP.
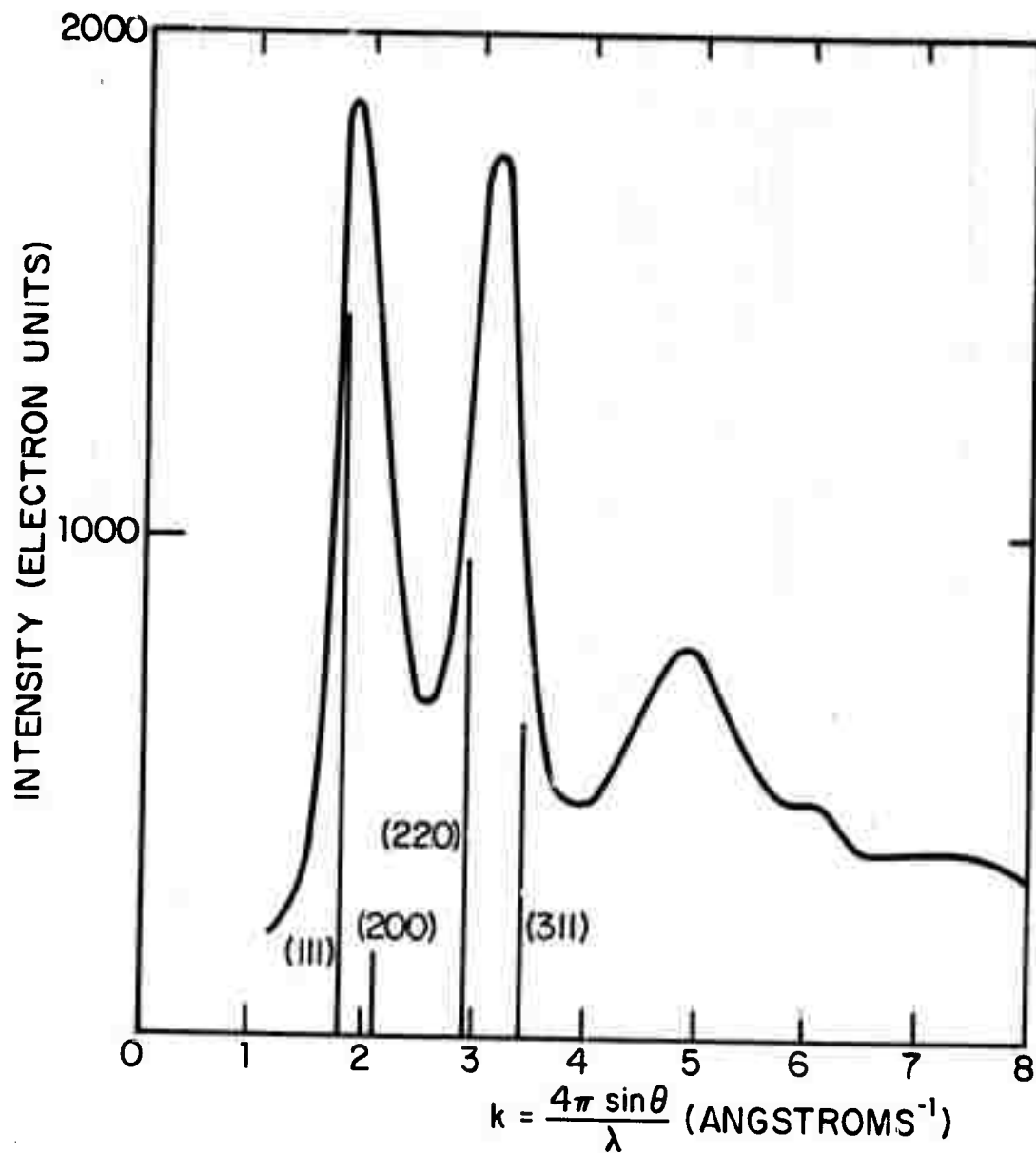
FIG. 5-5 COHERENTLY SCATTERED INTENSITY OF
AMORPHOUS SPUTTERED GaSb.
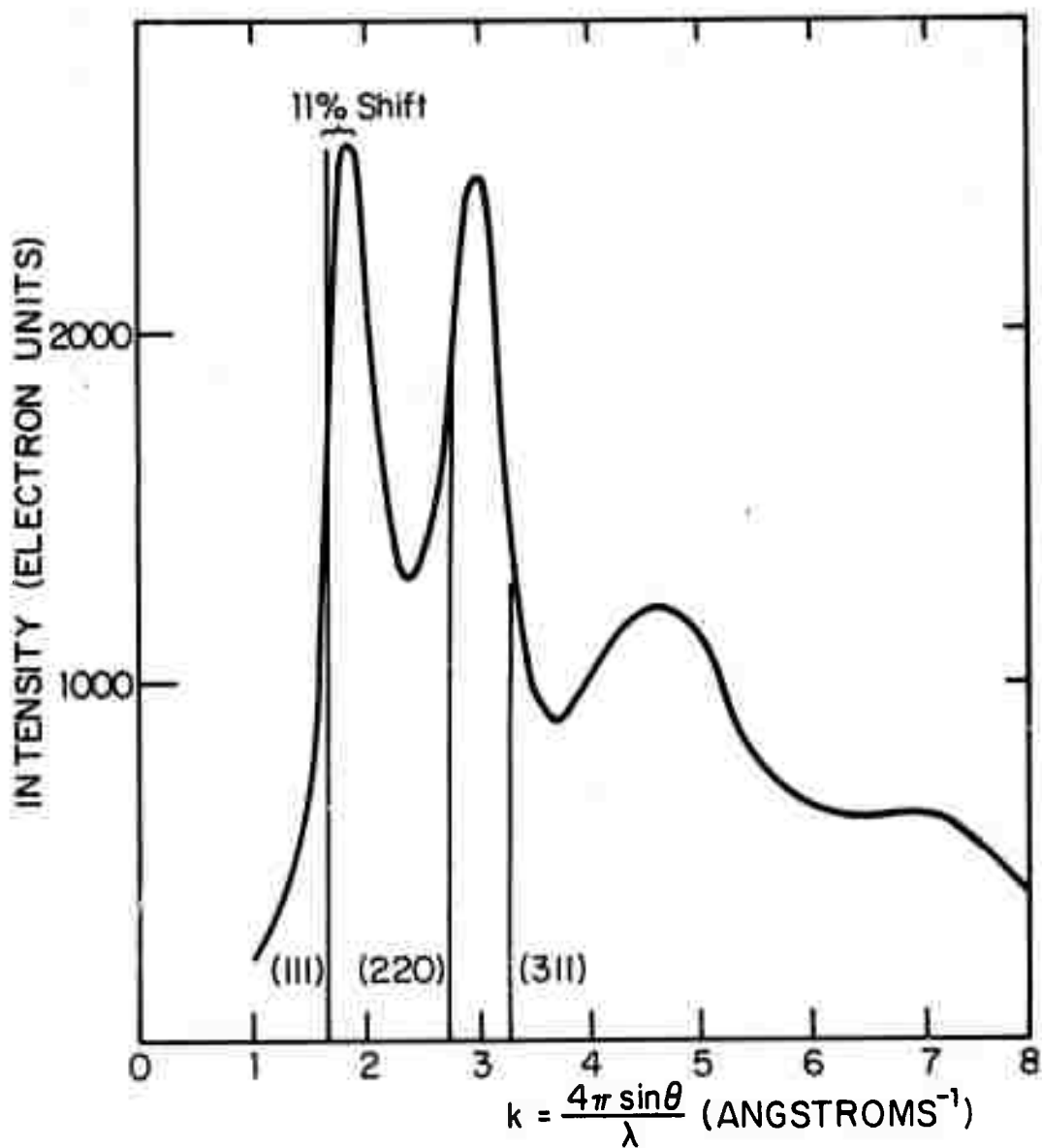
FIG. 5-6 COHERENTLY SCATTERED INTENSITY OF AMORPHOUS SPUTTERED InSb.
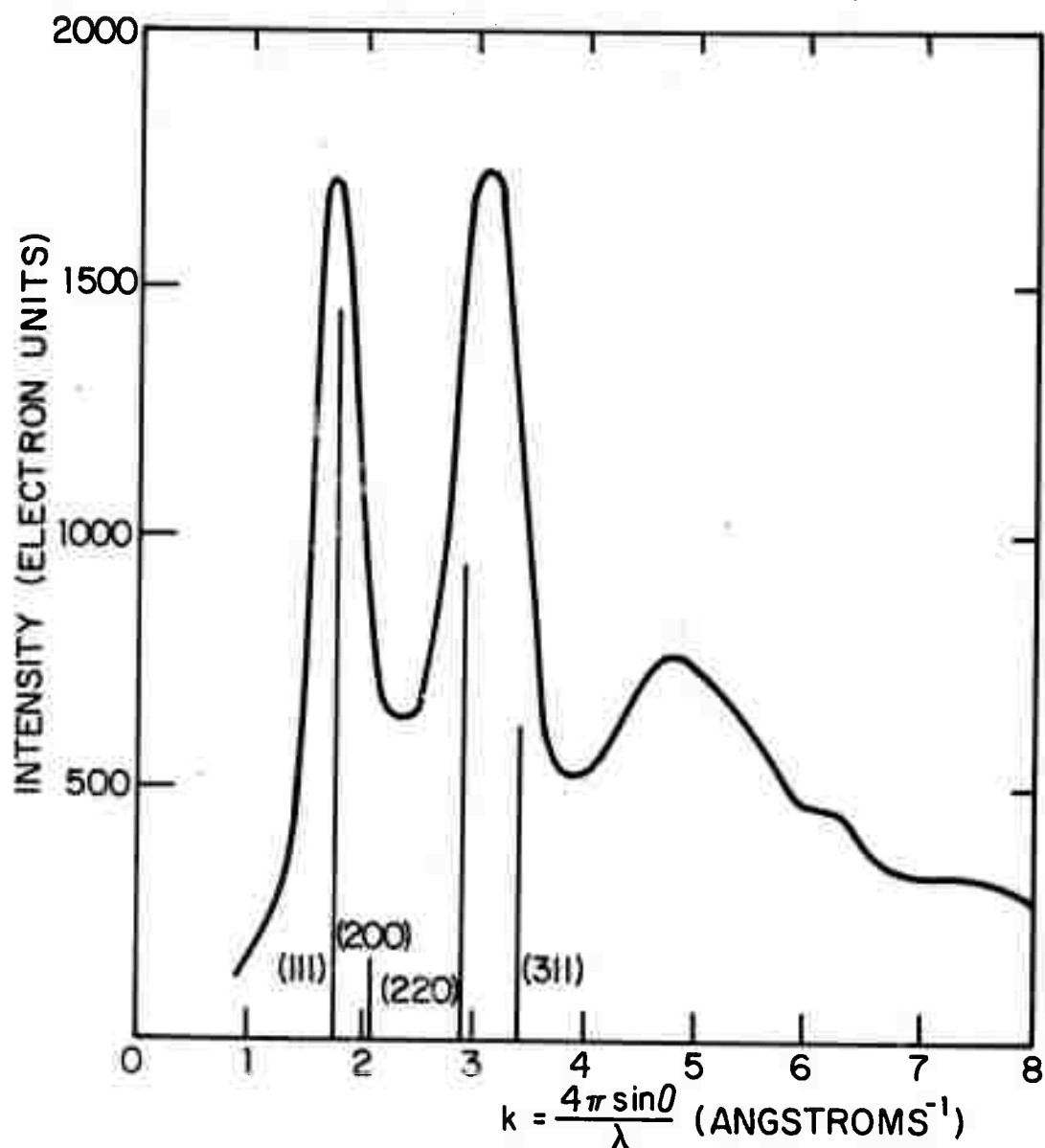
FIG. 5-7 COHERENTLY SCATTERED INTENSITY OF
AMORPHOUS SPUTTERED GeSn.

TABLE 5 - 1 : Summary of First Two Diffraction Peak Positions

Material	$k_1{}^a (\mathring{A}^{-1})$	$k_1{}^c (\mathring{A}^{-1})$	$k_2{}^a (\mathring{A}^{-1})$	$k_2{}^c (\mathring{A}^{-1})$
Se	1.91		3.60	
Ge(el)	1.89	1.92	3.38	3.36
Ge(sp)	1.91	1.92	3.38	3.36
GaAs	1.93	1.93	3.43	3.41
GaP	2.02	2.00	3.47	3.52
GaSb	1.87	1.78	3.19	3.12
InSb	1.87	1.68	2.98	2.92
GeSn	1.78	1.78*	3.14	3.12*

*   GaSb crystalline structure assumed

c   denotes crystalline

a   denotes amorphous

For explanation of k_2^c see text

simply smearing their crystalline k-space structures, but it is necessary to take into account the large shifts in k-space. This has not been done by Kramer [5] or by Romerio and Ashcroft; the sensitivity of the pseudopotential to k[24] suggests that to do so would drastically affect their results.

In all cases, including InSb and GaSb , the second peak positions fall near the weighted average of the (220) and (311) peak positions.

Additional difficulties may arise in the application of diffraction theory to amorphous Se, since it can be seen by comparison of Figure 5-1 to Figures 5-2 to 5-7, that the width of the first diffraction peak of amorphous Se is about twice that of the peaks of the tetrahedrally coordinated materials presented here. This indicates that the k-space structure of amorphous Se is about twice as disordered as that in the other materials; in r-space this indicates that the long range order decays about twice as fast as it does for the other materials.

C. Presentation of the F(k)'s and the RDF's

Figures 5-8 to 5-14 show the F(k)'s of amorphous evaporated Se, amorphous electrodeposited and sputtered Ge, and amorphous sputtered GaAs, GaP, GaSb, InSb, and GeSn respectively. The upper limit on k for the F(k)'s of Ge, GaAs, GaP, and GaSb is 15 $\overset{o}{A}{}^{-1}$. The upper limits on k for the F(k)'s of InSb and GeSn are 13 $\overset{o}{A}{}^{-1}$ and 8 $\overset{o}{A}{}^{-1}$ respectively, since the inadequate thicknesses of the films prevented the

data from being extended to higher k values with certainty. For amorphous Se, the data were taken to $k = 12 \text{ Å}^{-1}$ only.

Shown in Figure 5-15 is the preliminary $F(k)$ of amorphous quenched $ZnCl_2$ deduced from the data of Wicks, Drummond and Turnbull[8] with the computer routines used here. Although chemically $ZnCl_2$ is unrelated to the Group IV elements and to the III-V compounds, it is still presented here since, as will be discussed later, it poses a problem for either the proposed structural models of amorphous Ge or for the usefulness of the RDF in determining the structure.

Figure 5-16 shows the RDF of an amorphous evaporated Se sample provided by Dr. Robert Gorin of Xerox. Figures 5-17 to 5-22 show the RDF's of amorphous electrolytic and sputtered Ge, and of amorphous sputtered GaAs, GaP, GaSb, InSb and GeSn respectively. Since beyond the second neighbor shell the RDF becomes particularly sensitive to random errors in the data and since the real structure rapidly decreases with increasing r, the RDF's are plotted to $r = 10 \text{ Å}$ only. Also included in the RDF's at low r are the oscillations due to errors and termination of the inversion integral so that one may judge for himself the accuracy of these RDF's. As one can see, the errors at low r are not too bad for any of the materials investigated; they are worst for GeSn and GaSb.

Listed in Table 5-2 are the density deficits determined both by hydrostatic weighing and by reduction of the data, as outlined in Section 3-D. Also listed are the most probable distances, the spread, and coordination numbers of the

first and second neighbor shells, the ratio of the first and
second neighbor shells most probable distances, and the bond
angle and spread consistent with the second neighbor distri-
bution. In the last two columns in this table are listed
the maximum k values to which the data have been experi-
mentally extended and whether or not the data have been ex-
trapolated in the analysis of the RDF. Also after each num-
ber listed in this table is the error estimated for each
measurement. Note that the errors become the largest for
GeSn and InSb samples since these were of insufficient
thickness to allow the data to be experimentally extended
with certainty to higher k values or to allow the normali-
zation to be accurately achieved.

Note that the densities determined from analysis of the
x-ray data are in good agreement with those found by hydro-
static weighing. We take this agreement as some indication
of the accuracy of the RDF's. Although the hydrostatic
weighings are to be regarded as the more accurate measure-
ments, in the RDF analysis the very similar densities de-
termined from analysis of the x-ray data have been used for
the sake of self-consistency. From our experience, we be-
lieve that the densities deduced from x-ray measurements are
accurate to only ± 5%.

In the evaluation of the RDF's and the density deficits
from x-rays, the only data used have been from the high
angle diffraction experiments. The lower experimental k
value in all cases is $k = 1.0 \text{ Å}^{-1}$, while the upper limit for

each material is as indicated in Table 5-2. The small angle scattering has not been included in evaluation of the RDF's or densities since as will be shown in the discussion of the small angle scattering in Chapter 6, the scattering in this region is small for these materials.

For the samples for which the F(k) has been extrapolated to high k values as discussed in Section 3-D, the value of σ_1 given in Table 5-2, is estimated, by assuming that the high k behavior of F(k) is described by:

$$F(k) = \frac{C_1}{r_1} \ e^{\frac{-(r-r_1)^2}{2\sigma_1^2}} \ \sin(kr_1) \qquad (5-1)$$

where C_1 and r_1 are found from the trial RDF. It has been found that the value of σ_1 found in this way always agrees closely with the resulting peak width in r-space. For the samples for which the extrapolation is unnecessary, the peak width is estimated by direct examination of the first RDF peak.

The coordination number of the 2nd neighbor shell is somewhat more difficult to estimate than the first, since the 2nd peak in the RDF is not comprised of second nearest neighbors only, but contains some distances between 3rd and possibly 4th nearest neighbors. However, the left hand side of this peak appears to be reasonably well defined and we expect it to contain 2nd nearest neighbors only.[2] The coordination of the 2nd neighbor shell is estimated by assuming that the right hand portion of the distribution is a symmetric reflection of the left hand side about the most probable

value; with this assumption, the coordination of the second shell becomes equal to twice the area of the left hand side of this distribution. The accuracy of the coordination of the second coordination sphere found in this way is estimated to be ±2 atoms.

The spread of the second neighbor shell is found by examination of the left hand portion of the second neighbor distribution as found in the experimental RDF. The gaussian spread of the peak is related to its half width, $x_{\frac{1}{2}}$, by the relation:

$$\sigma_2 = \frac{x_{1/2}}{2.30} \qquad (5\text{-}2)$$

The bonding angle is found by assuming that the second neighbor distribution represents distances between two atoms bonded to the same atom, each with a bond length equal to the first neighbor's most probable distance, r_1. In such a case the bonding angle is given by:

$$\theta(r) = 2 \times \sin^{-1}\left(\frac{r}{2r_1}\right) \qquad (5\text{-}3)$$

where r is the distance to the second nearest neighbor. The most probable bonding angle θ_{mp} is then given by:

$$\theta_{mp} = 2 \times \sin^{-1}\left(\frac{r_2}{2r_1}\right) \qquad (5\text{-}4)$$

where r_2 is the most probable value of the second neighbor distribution. The spread in the bonding angle is approximately related to the spread in the second neighbor distri-

bution σ_2 by the relation

$$\Delta\Theta = \Theta_{mp} - 2 \times \sin^{-1} \frac{1}{2} (\frac{r_2 - \sigma_2}{r_1}) \qquad (5-5)$$

In addition to the Debye temperatures and average atomic weights, listed in Table 5-3 are the thermal spreads calculated with the Debye theory outlined in Appendix III.

The application of this simple Debye theory is less exact for GeSn, GaSb and GaP, where the masses of the two constituent atoms are very different and the phonon spectrum more complicated. For the binary-compounds, the average mass has been used in the calculation of the thermal spreading.

D. Discussion of the F(k)' and the RDF's

We note that all the F(k)'s in Figures 5-8 to 5-15 oscillate about O, as they must. All the F(k)'s are similar and quantitative differences among them are at first difficult to see. First inspection of the RDF's shows that they too are very similar, all exhibiting well separated first neighbor peaks and broader, but still distinct peaks occurring at high r values. Inspection of Table 5-2 shows that all the structures have nearest neighbor distances and densities which are very close to their crystalline values. For now we postpone further comparison of these curves until we have discussed each material in greater detail.
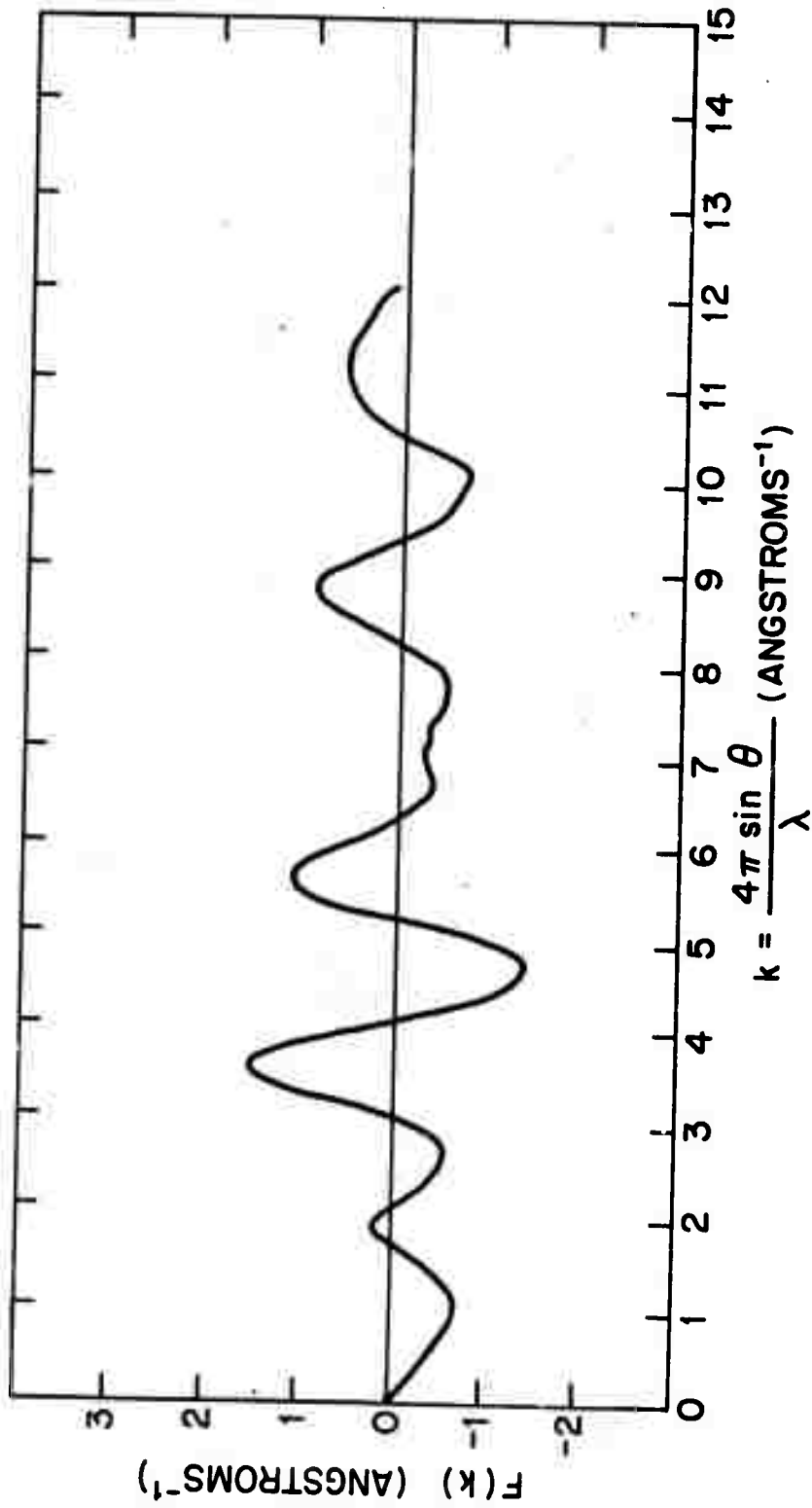
FIG. 5-8   F(k) OF AMORPHOUS EVAPORATED Se.
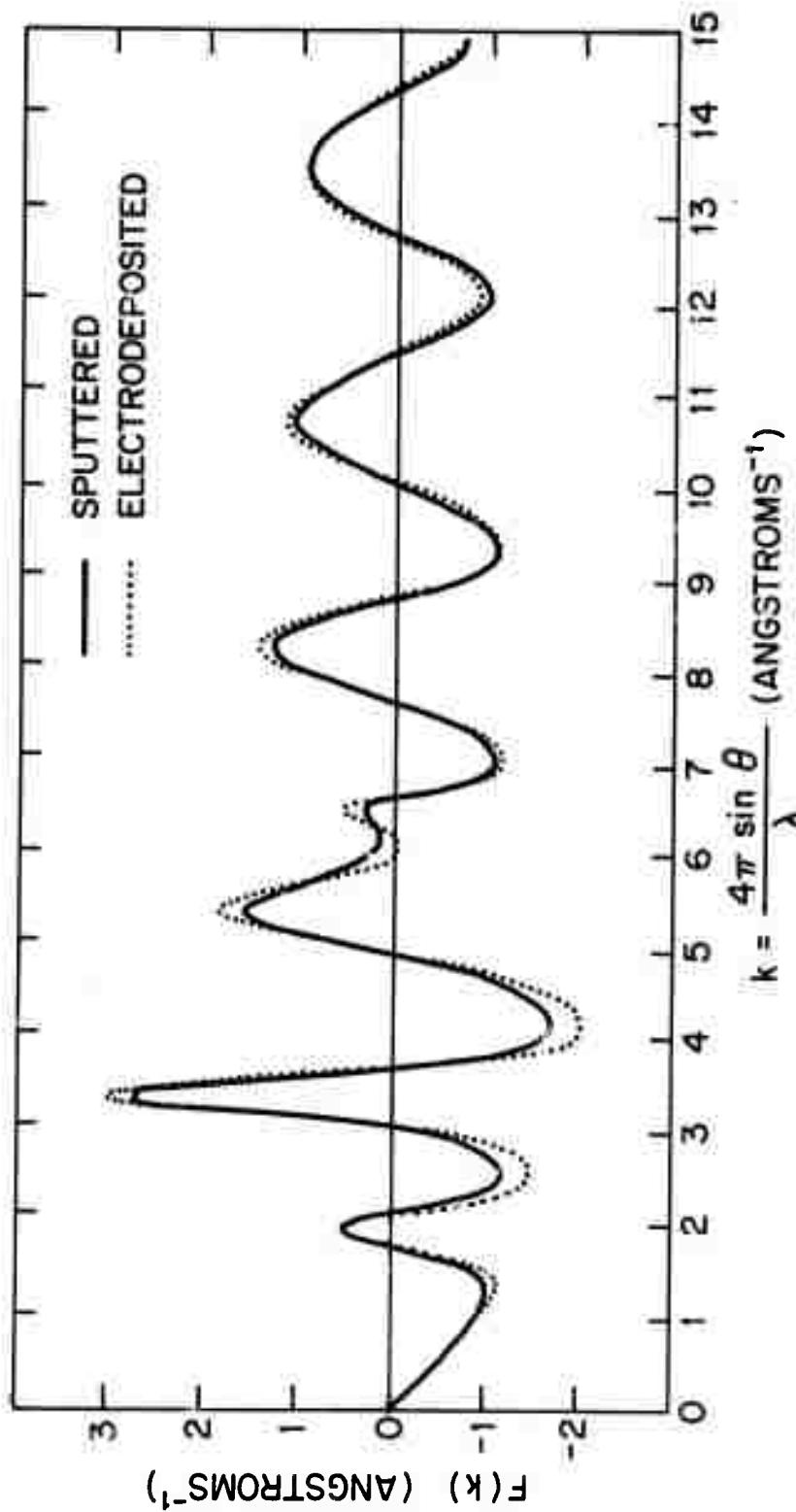
FIG. 5-9   F(k)'S OF AMORPHOUS SPUTTERED AND ELECTRODEPOSITED Ge.
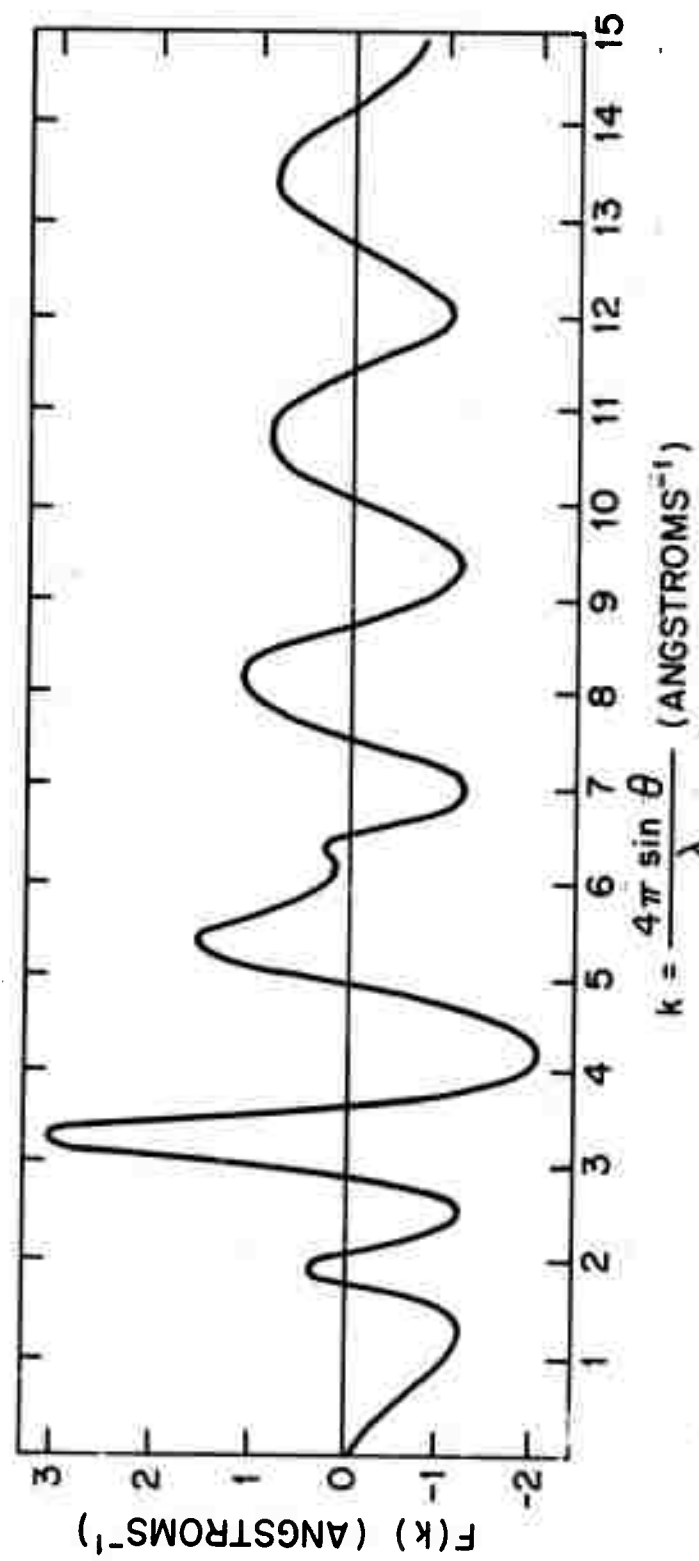
FIG. 5-10   F(k) OF AMORPHOUS SPUTTERED Ga As.
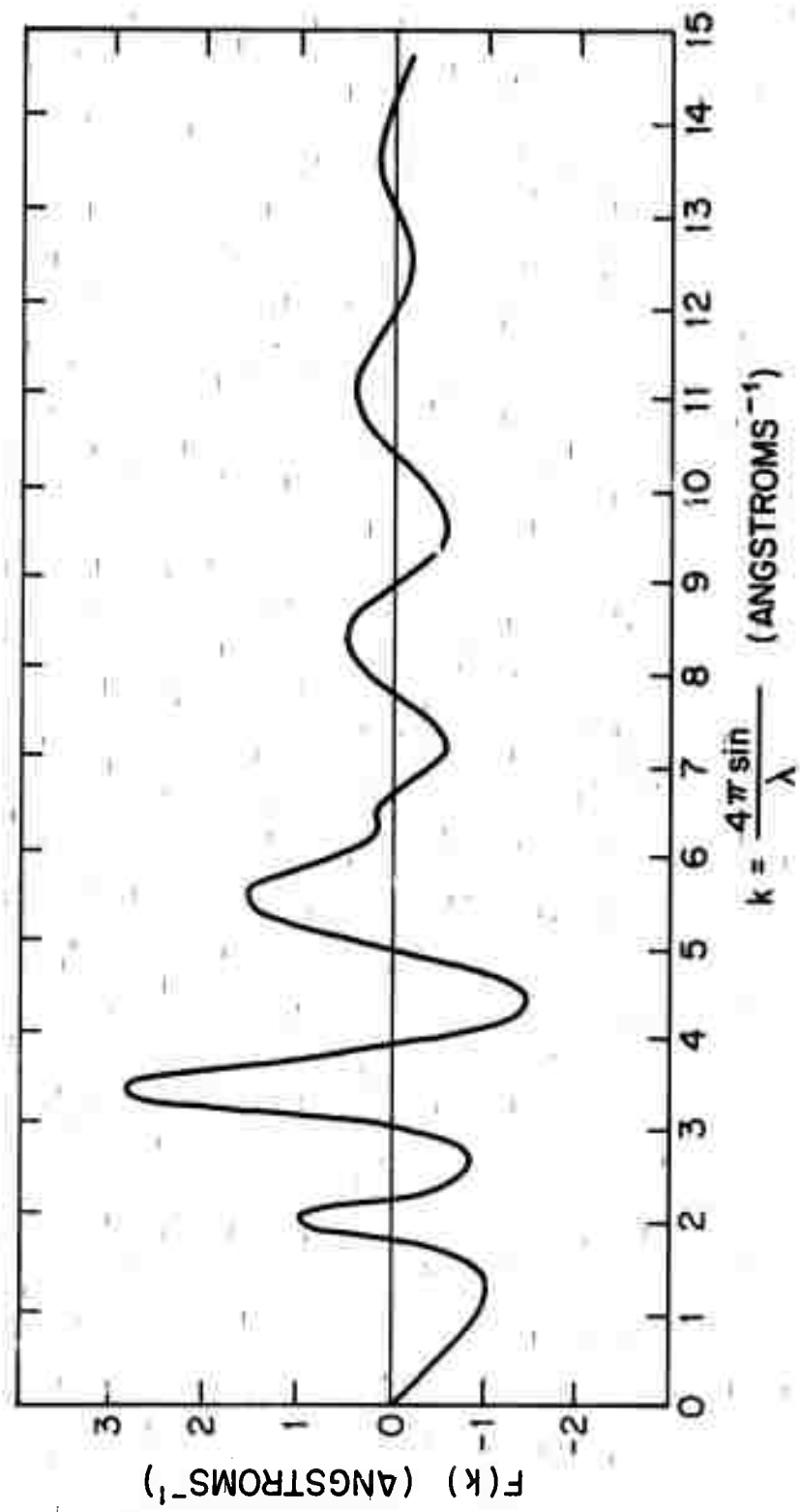
FIG. 5-11   F(k) OF AMORPHOUS SPUTTERED GaP.
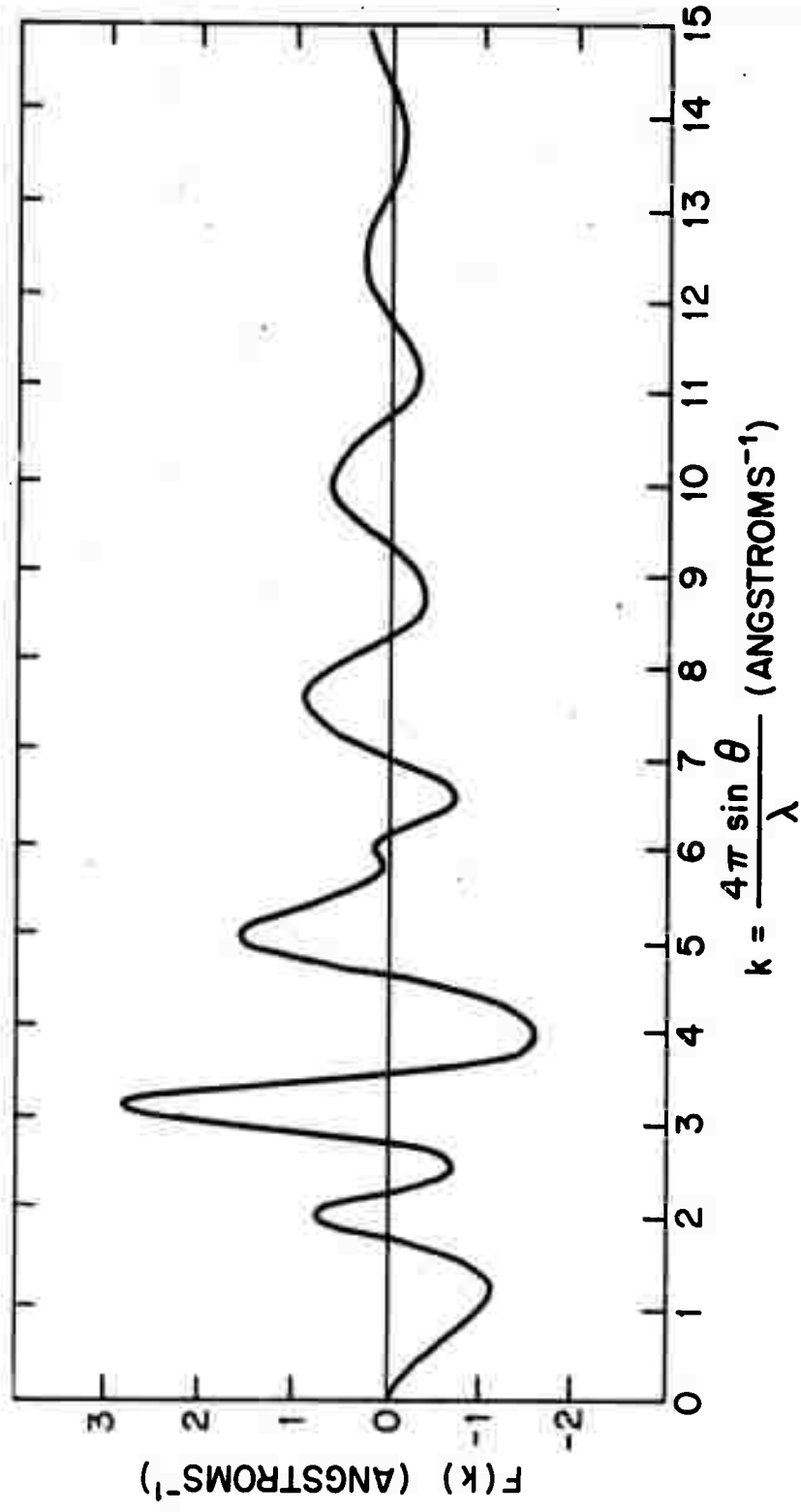
FIG. 5-12   F(k) OF AMORPHOUS SPUTTERED GaSb.
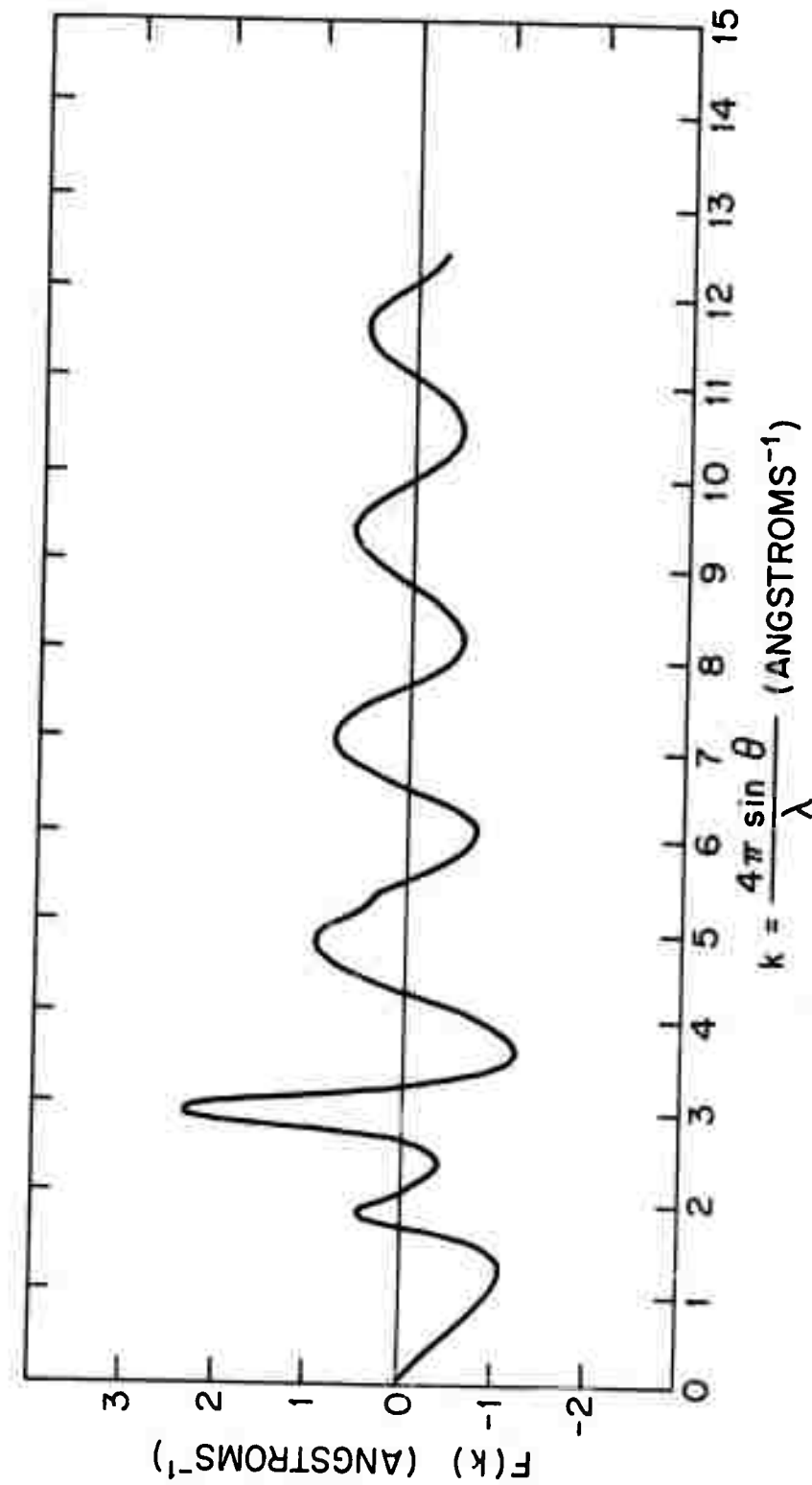
FIG. 5-13   F(k) OF AMORPHOUS SPUTTERED InSb.
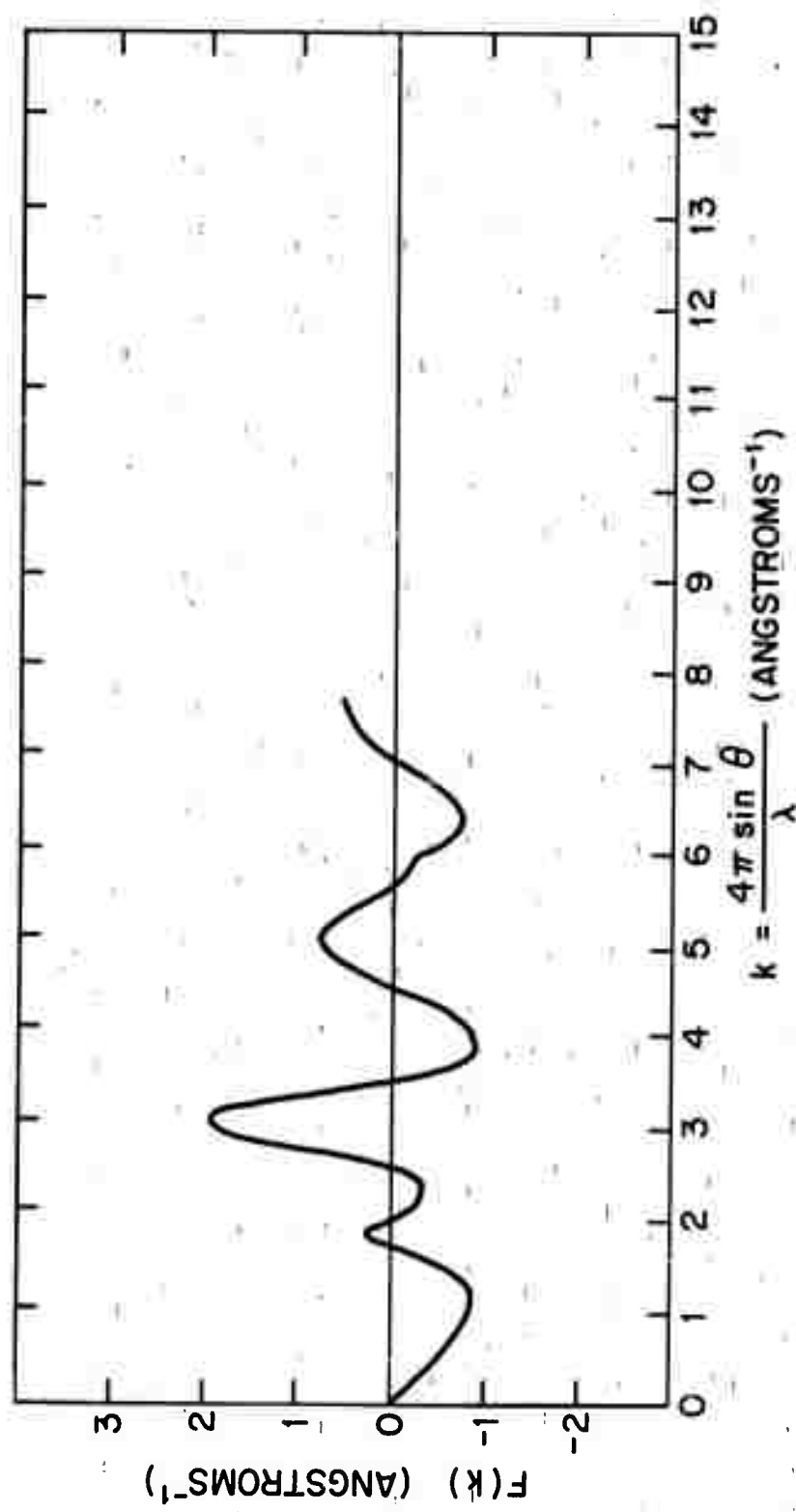
FIG. 5-14 — F(k) OF AMORPHOUS SPUTTERED GeSn.
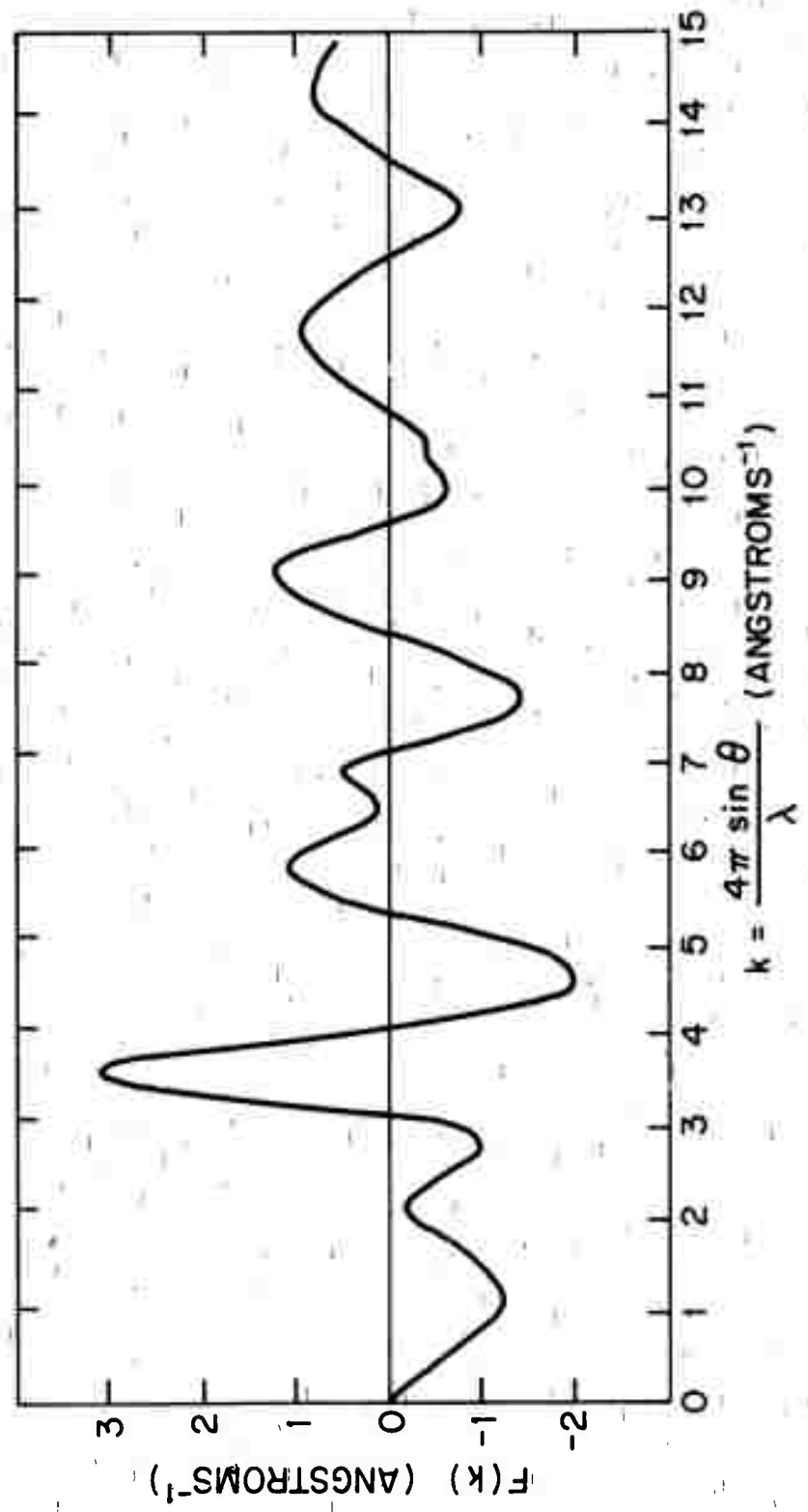
FIG. 5-15. F(k) OF AMORPHOUS QUENCHED $ZnCl_2$. (DATA OF G. WICKS, C. DRUMMOND AND D. TURNBULL.)

Axis labels:
- Horizontal: $k = \dfrac{4\pi \sin\theta}{\lambda}$ (ANGSTROMS^{-1})
- Vertical: F(k) (ANGSTROMS^{-1})
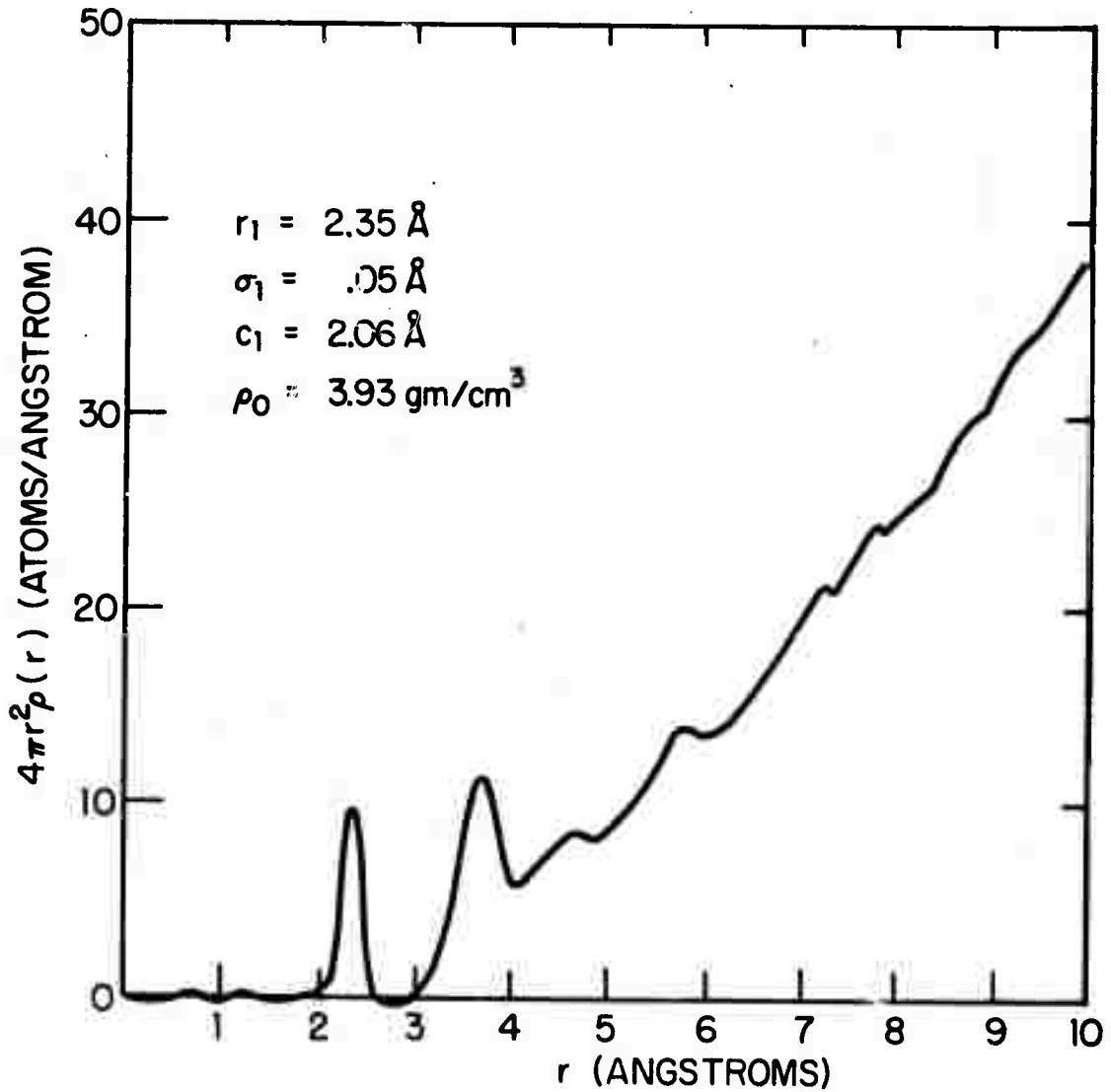
FIG. 5-16   RADIAL DISTRIBUTION OF AMORPHOUS
EVAPORATED Se
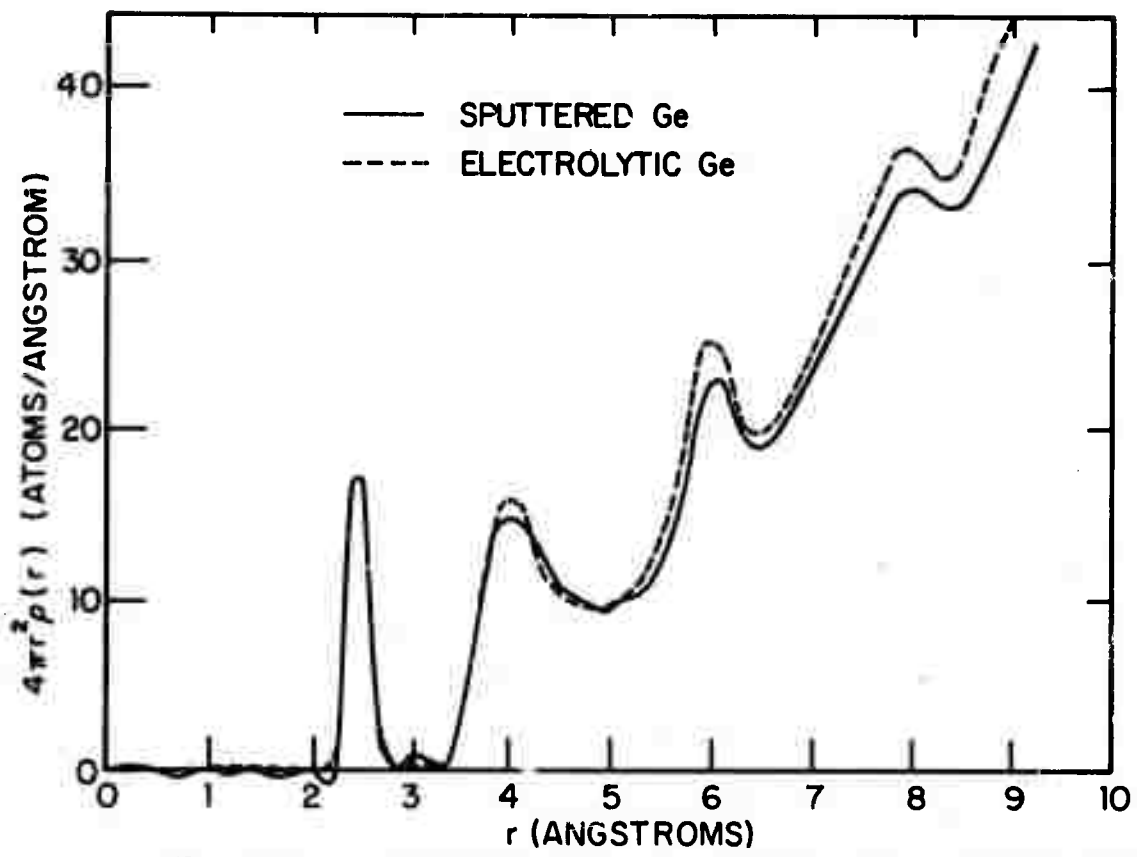
FIG. 5-17 RADIAL DISTRIBUTION FUNCTION OF AMORPHOUS SPUTTERED AND ELECTROLYTIC Ge.
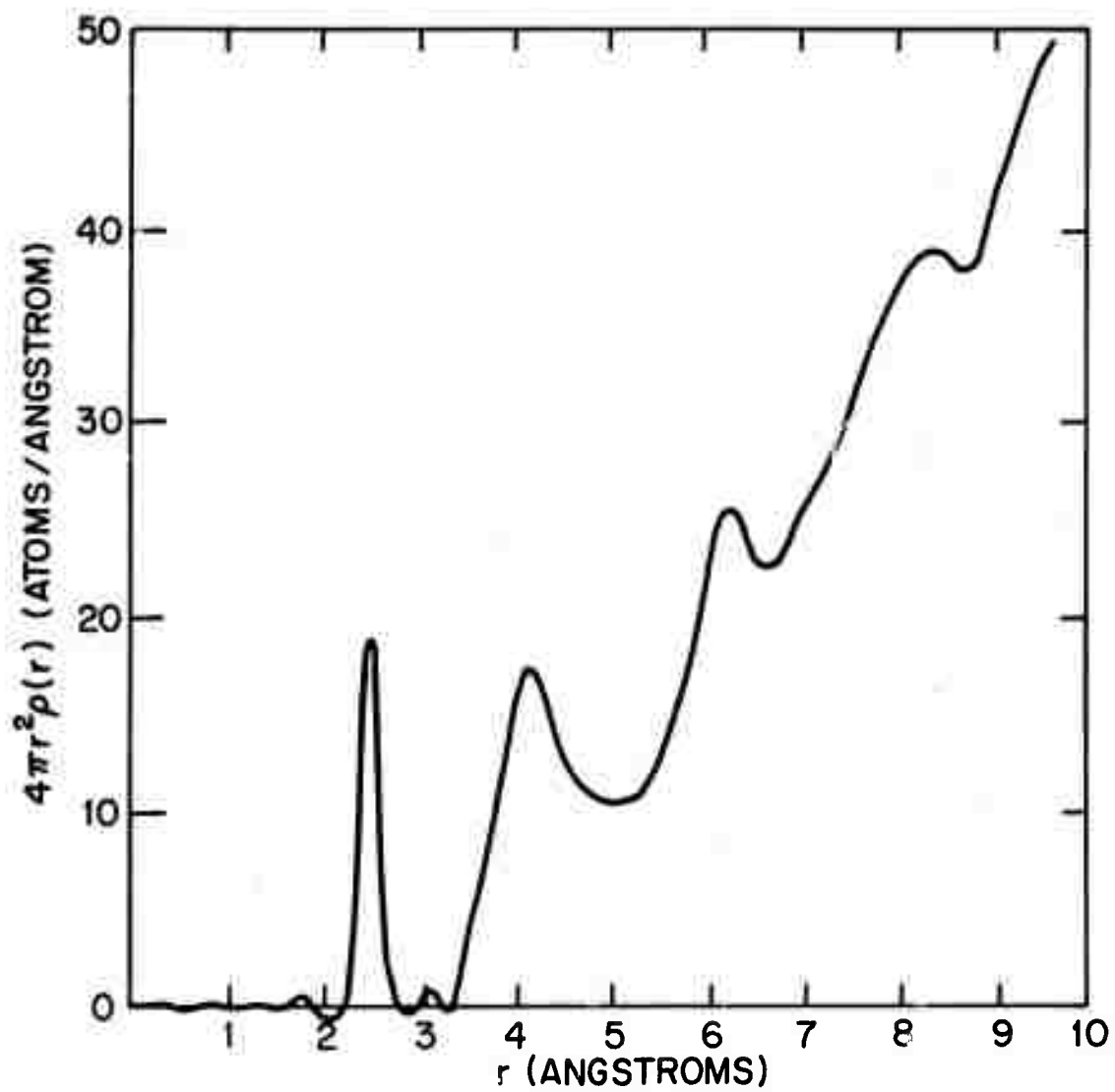
FIG. 5-18 RADIAL DISTRIBUTION FUNCTION OF
AMORPHOUS SPUTTERED GaAs.
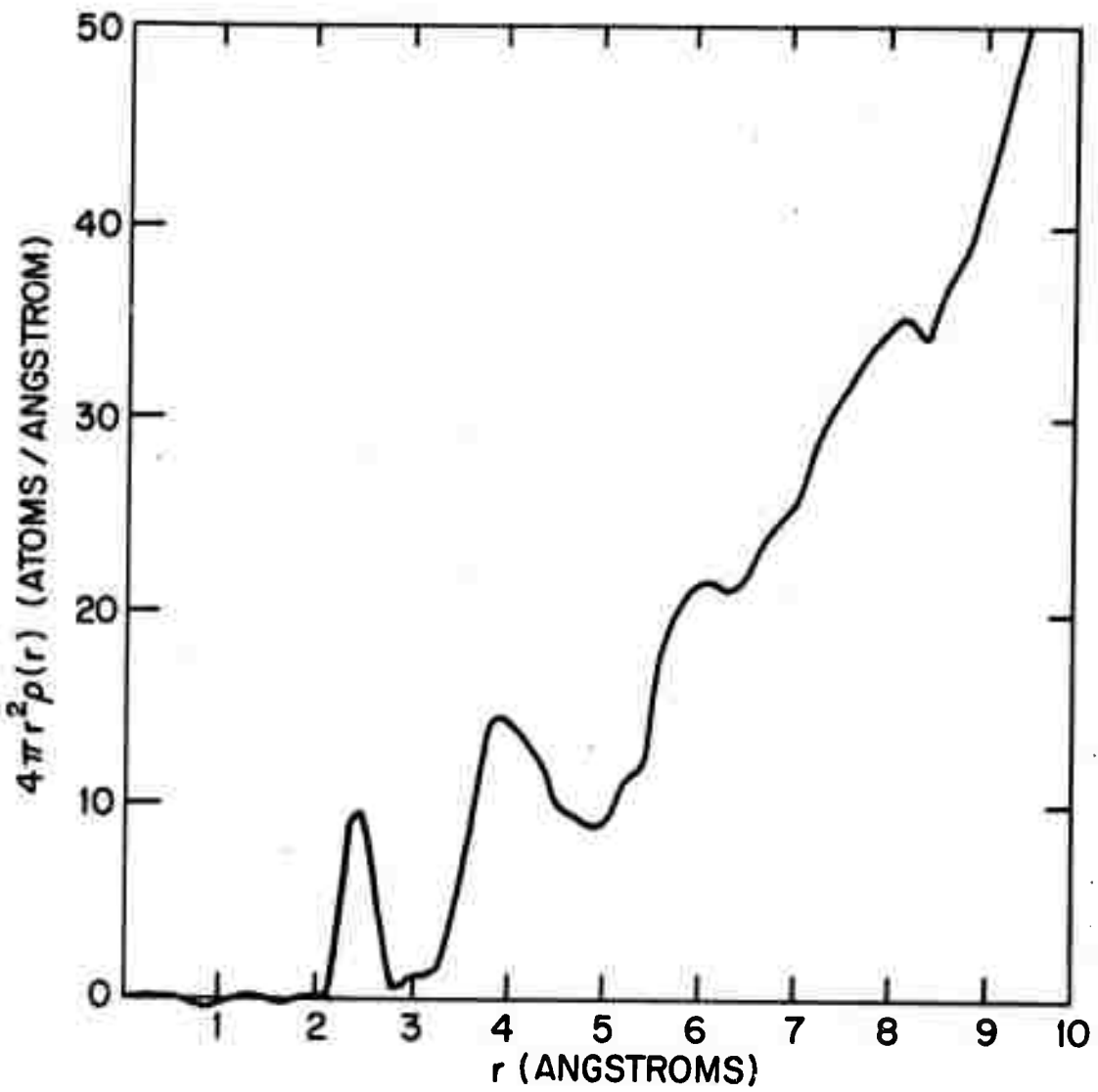
FIG. 5-19 RADIAL DISTRIBUTION FUNCTION OF
AMORPHOUS SPUTTERED GaP.
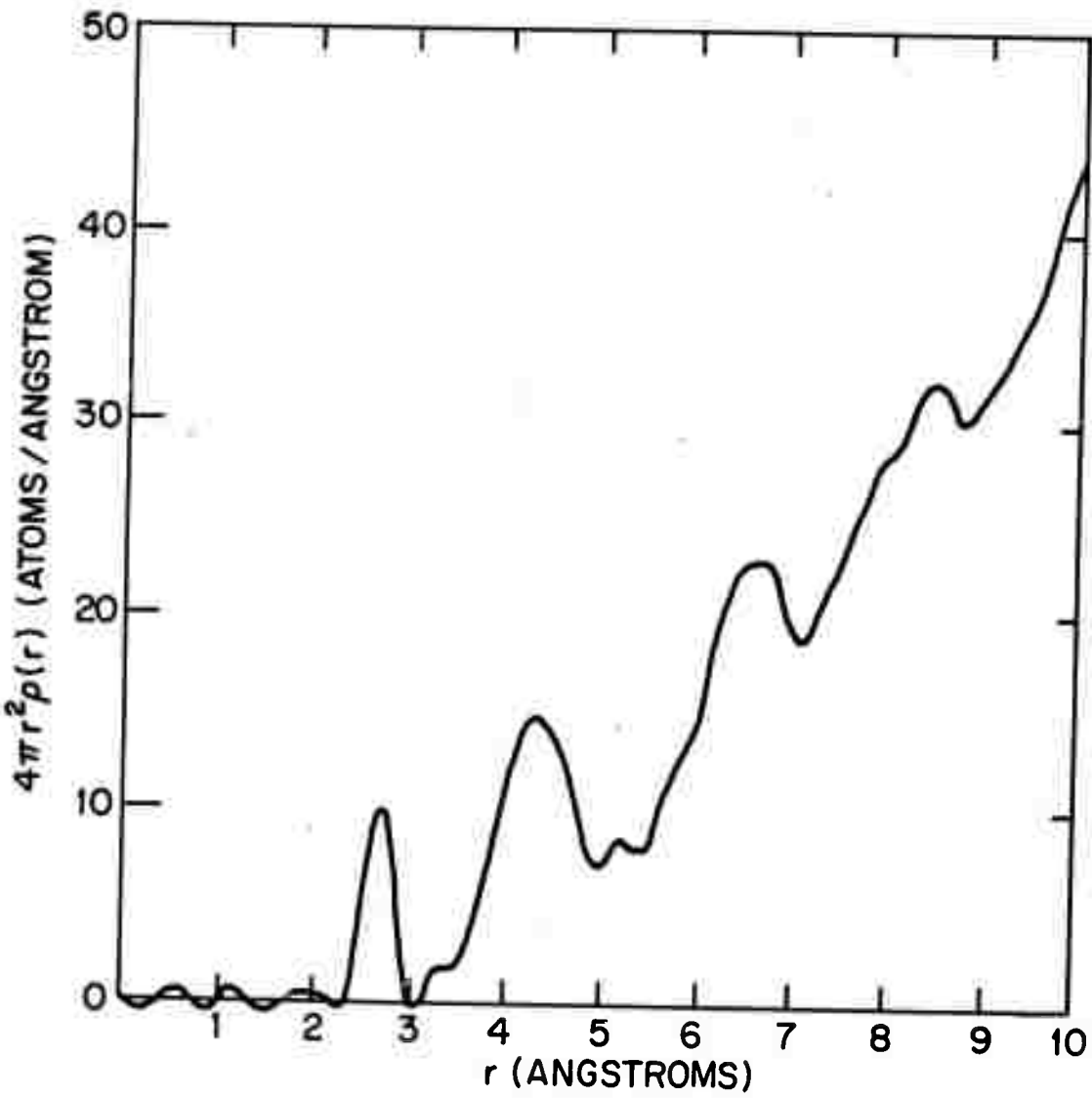
FIG. 5-20 RADIAL DISTRIBUTION FUNCTION OF
AMORPHOUS SPUTTERED Ga Sb.
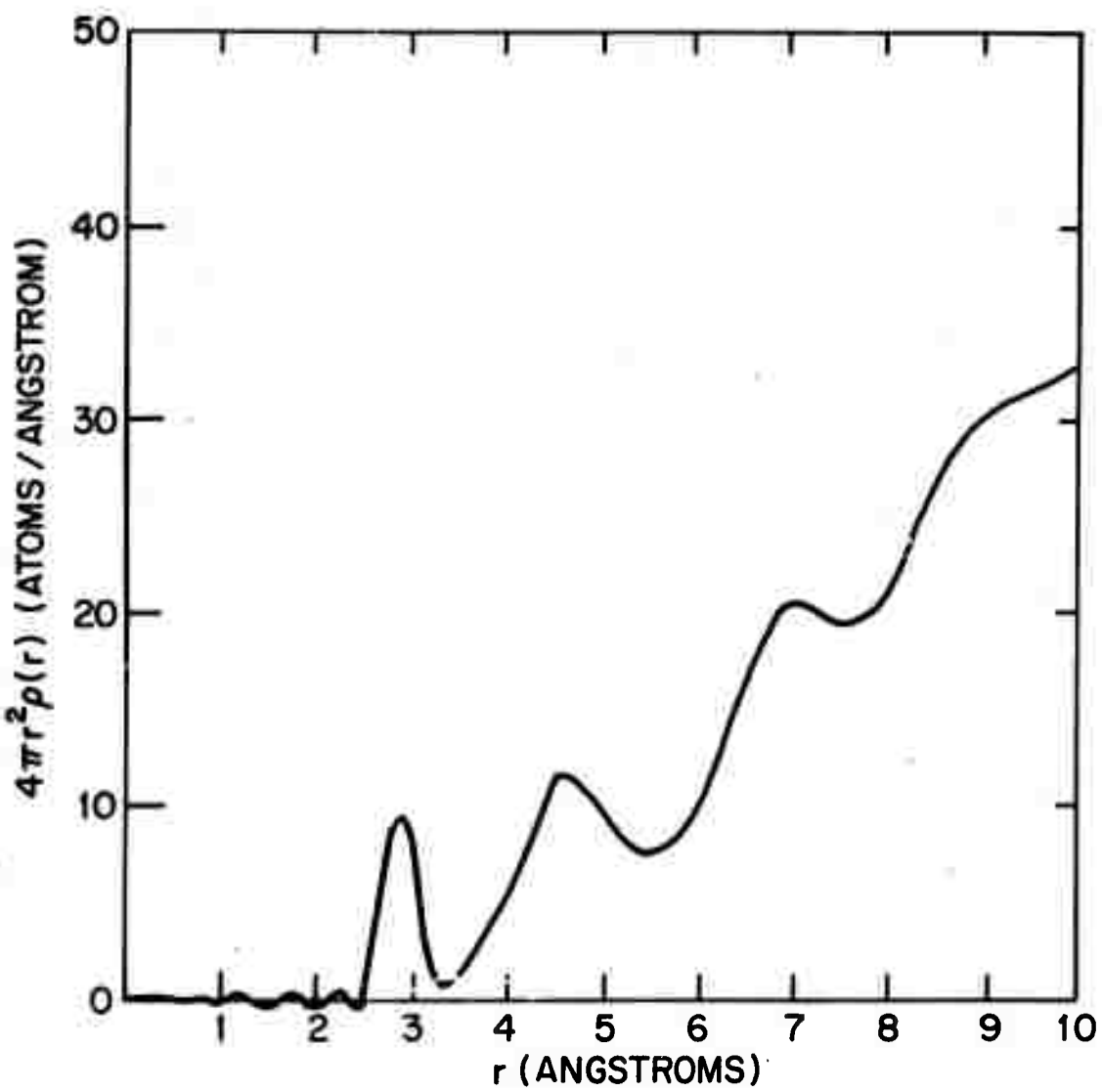
FIG. 5-21 RADIAL DISTRIBUTION FUNCTION OF
AMORPHOUS SPUTTERED In Sb.
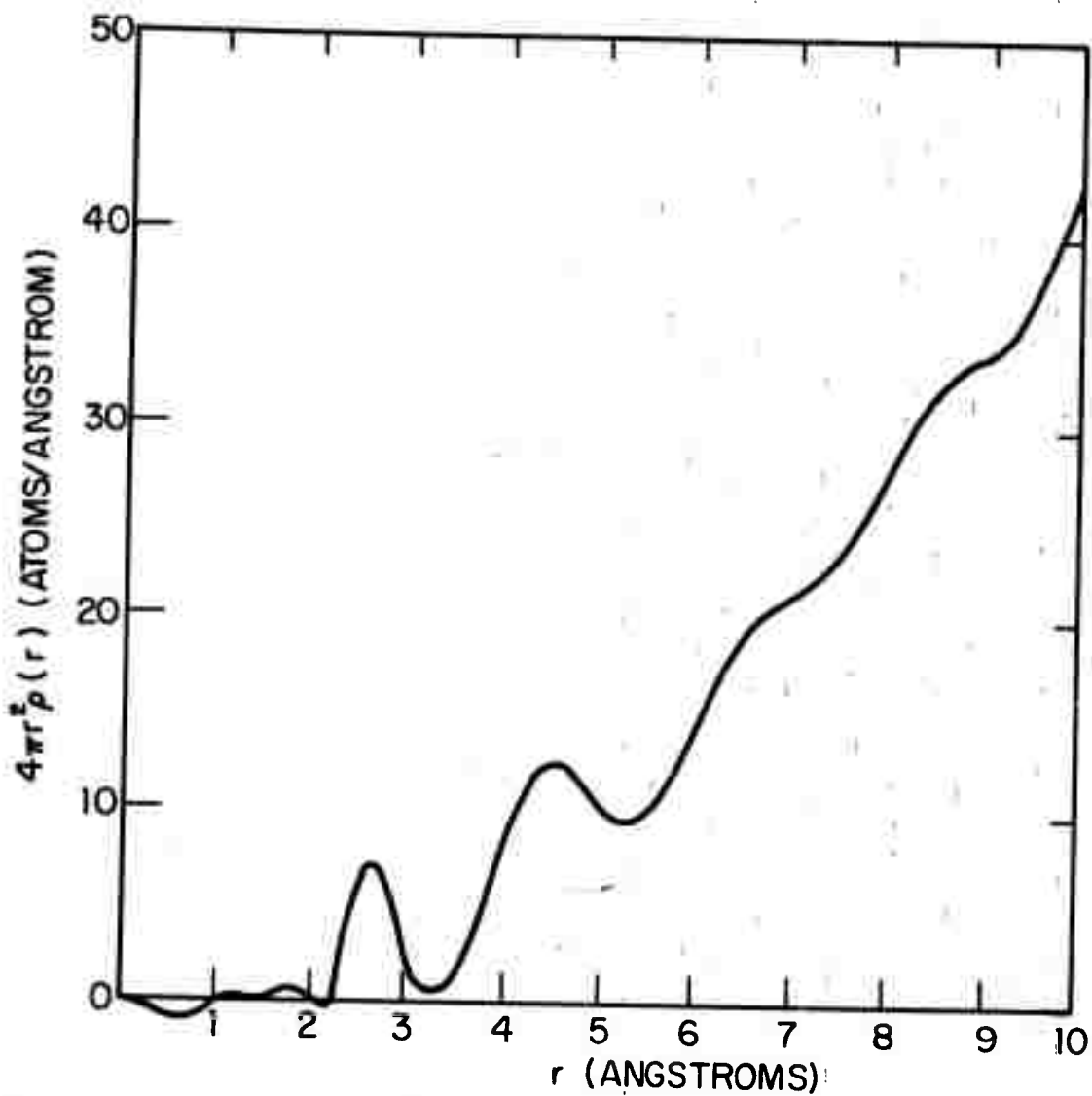
FIG. 5-22 RADIAL DISTRIBUTION FUNCTION OF AMORPHOUS
SPUTTERED GeSn

TABLE 5-2a. Summary of Structural Data

Material	r_1^a(Å)	r_1^c(Å)	σ_1(Å)	c_1^a	r_2^a(Å)	σ_2^a(Å)	c_2^a
Se	2.35±.02		.075±.01	2.06 ±.1	3.74±.05	.3±.05	6.2
Ge (el)	2.46±.03	2.45	.085±.01	3.93 ±.1	4.0 ±.05	.3±.05	11.2
Ge (sp)	2.46±.03	2.45	.085±.01	3.85 ±.1	4.0 ±.05	.3±.05	10.0
GaAs	2.48±.03	2.45	.085±.01	3.93 ±.1	4.1 ±.05	.3±.05	12.8
GaP	2.44±.1^a	2.36	.18 ±.01	3.47 ±.2 (4.0 .2)	3.90±.05	.35±.05	12.0
GaSb	2.67±.03	2.65	.14 ±.01	3.50 ±.2 (3.78 .2)	4.30±.05	.4±.05	13.2
InSb	2.86±.03	2.81	.14 ±.02	3.82 ±.3	4.5 ±.05	.45±.05	12.8
GeSn	2.74±.06	2.65	.22 ±.03	4.0 ±.4	4.5 ±.1	.55±.1	14.8
ZnCl$_2$	2.29±.3	2.29	.075±.01				

a The larger uncertainty in this nearest neighbor position is caused by the difficulty of correcting for a variation with k of the ratio of the atomic scattering factors of Ga and P.

TABLE 5-2b, Summary of Structural Data

Material	r_2^a/r_1^a	θ_{mp}	$\Delta\theta$	%Density Deficit a	%Density Deficit b	k_{max}(Å)	Extra-polated?
Se	1.59	105 ±2	11	20	-	12	Yes
Ge (el)	1.63	109 ±2	10	5	5	15	Yes
Ge (sp)	1.63	109 ±2	10	10	10	15	Yes
GaAs	1.63	109 ±2	10	5	6	15	Yes
GaP	1.61	107 ±2	12	5	-1	15	No
GaSb	1.63	109 ±2	14	2	-1	15	No
InSb	1.60	106 ±2	15	2	2	13	No
GeSn	1.65	111 ±2	17	5	-	8	No

a Density deficit determined by reduction of the x-ray data.

b Density deficit determined by hydrostatic weighing.

TABLE 5-3 Estimates of the Thermal Spreading of the RDF Peaks

Compound	Atomic Weight	$\theta_m (K^o)$	$2U_o^2 (Å^2)$	σ_o (Å)	σ_1^τ (Å)	σ_2^τ (Å)
Se	79	151	.047	.238	.17	.184
Ge	73	290[a]	.0134	.094	.066	.072
GaAs	73	247[b]	.0157	.10	.071	.077
GaP	–					
GaSb	96	235[b]	.019	.14	.079	.109
InSb	118	175[b]	.027	.165	.093	.127

1. **Se**

Although amorphous Se has been investigated by several authors,[9,10] it has been investigated here also to see how well our results agree with those reported earlier.

The $F(k)$ of amorphous evaporated Se, shown in Figure 5-8, is in very good agreement with those found by Kaplow et al.[9] Inversion of this $F(k)$ along with its extrapolated portion gives the RDF in Figure 5-16. The nearest neighbor distribution peaks at $r_1 = 2.35$ Å and has an area which indicates $C_1 = 2.06$ nearest neighbors, and the second neighbor distribution peaks at $r_2 = 3.74$ Å and has an area which indicates $C_2 = 6.2$ second neighbors. These compare well with the values $r_1 = 2.34$ Å, $C_1 = 2.0$, $r_2 = 3.75$ Å, and $C_2 = 6.3$ found by Kaplow et al.[9], and the values $r_1 = 2.36$ Å, $C_1 = 2.1$, $r_2 = 3.72$ Å and $C_2 = 6.0$ found by Krebs and Steffen.[10] The value of σ_1 is estimated to be 0.075 ± 0.01 Å, while the value found by Kaplow et al. is 0.085 Å.[9]

The observed spread of the first peak is much less than the value $\sigma_2^T = 0.215$ Å calculated from the simple Debye theory in Appendix III. It is believed that the difference occurs because of the existence of two types of bonding mechanisms in Se. Atoms lying within the same ring or chain interact with strong covalent forces while atoms in different chains or rings interact with much weaker Van der Waals forces. Therefore, the relative displacement of atoms lying in different rings or chains is expected to be much greater

than the relative displacement between atoms in the same ring or chain. Thus the Debye temperature used is believed to represent the weaker bonding mechanism, and does not correctly represent the interatomic forces between nearest neighbors.

The second neighbor distribution peaking at 3.74 Å with a width of 0.3 Å indicates that the average bonding angle is 105°, as it is in its hexagonal form, but has a spread of about $\pm 11^O$. Since there are no distances occurring in the range 2.6 - 3.0 Å, there appears to be a cut off in the bond angle distortion of about 25°.

2. Ge

The F(k)'s of electrodeposited and sputtered Ge shown in Figure 5-9 are similar to the F(k) of amorphous Si found by Moss and Grazcyk,[4] except that the oscillations at high k do not die away with increasing k as they do in the F(k) of amorphous Si. The faster rate of decrease of the F(k) of amorphous Si may be attributable to instrumental or multiple scattering effects which can be large with the electron diffraction technique they used. Also the rate of oscillation with k in the F(k) of the Ge samples at high k indicates that the first neighbor separation is at a higher r value than in Si.

The RDF's of amorphous electrodeposited and sputtered Ge, as is shown in Figure 5-17, are remarkably similar not only to one another, but also/to the RDF's of amorphous eva-

porated Ge reported by others.[1,12,13] The principal difference between the RDF's presented here and those reported earlier is the sharpness of the first neighbor distribution, which is attributable to higher experimental k values and to the extrapolation procedure outlined in Chapter 3.

The density deficits of 6 and 11% for the electrodeposited and sputtered Ge, are in excellent agreement with those found by hydrostatic weighing. The difference in density of the two accounts for the more rapid rise of the RDF of electrodeposited Ge over the RDF of the sputtered Ge.

The nearest neighbor distributions peak at 2.46 ± 0.025 $\mathring{A}$, which is, within experimental error, equal to the crystalline separation of 2.45 $\mathring{A}$. This is in agreement with the observations of Sayers et al.[14] who have found that the nearest neighbor separation in evaporated Ge is within 1% of the crystalline value. However, Richter and Breitling,[9] who have systematically studied the annealing dependence of the RDF's of evaporated Ge, have found that the nearest neighbor separation varies from 2.54 to 2.43 $\mathring{A}$ with increasing temperature of anneal.

The nearest neighbor distribution is very sharp with a gaussian spread of $\sigma_1 = 0.085$ $\mathring{A}$. The observed spread is just a little more than the spread of 0.066 $\mathring{A}$ calculated with the simple Debye theory; hence little, if any, spread can be attributed to static disorder.

The coordination numbers of the electrodeposited and sputtered Ge are 3.93 ± 0.1 and 3.85 ± 0.1 respectively. Although this reduction in the nearest neighbor coordination

in the sputtered over the electrodeposited Ge is admittedly
hovering in the experimental error, it is partially sub-
stantiated by its lower density, higher ESR signal, and its
greater small angle scattering, which will be presented in
the next Chapter. Also, Wihl et al.[13] find a 5% softer
Raman spectrum for the sputtered Ge, which is consistent
with a higher number of broken bonds.

The second neighbor distribution peaks at 4.0 $\overset{o}{A}$, indi-
cating a most probable bonding angle of 109°, as is found
in the crystalline Ge. The spreading of the second neighbor
peak, $\sigma_2 = .3 \overset{o}{A}$ indicates an RMS spreading of the bond angles
of $\pm 10^\circ$. Since the second neighbor distribution goes to 0
at about 3.4 $\overset{o}{A}$, there must be a cut off in the bond angle
distortions at about 20°, which precludes the existence of
significant numbers of four membered rings.

A four membered ring, assuming that the atoms partici-
pating in it retain the observed bond length, has an aver-
age bonding angle 19.5° less than the tetrahedral bond. The
presence of large numbers of four membered rings would then
show as a peak centered about 3.45 $\overset{o}{A}$, but since no such peak
is observed, there cannot be many four membered rings.

It is important to establish whether the spreading in
the bond angles, or equivalently, the spreading of the
second neighbor distribution is real. Two mechanisms which
can contribute to the spread are thermal and Fourier broaden-
ing.[23] The thermal spread of the second neighbor distri
bution is estimated to be $\sigma_2^T = 0.093 \overset{o}{A}$, and the Fourier
broadening is estimated to be 0.1 $\overset{o}{A}$. Subtracting these two

+The small bump between the first and second neighbor distributions
we believe to be a residual termination error and should therefore
not be considered as significant.

components from the observed spreading still leaves a spread of $\sigma_2 = 0.26$ Å. This indicates that neither thermal broadening nor Fourier broadening can account for the spread of this peak; hence, it must be attributed to real static distortions.

The numbers of second neighbors for the electrolytic and the sputtered Ge are estimated to be 11.2 ± 2 and 10.0 ± 2 respectively. The reduction in the sputtered value over the crystalline value of 12 is partly substantiated by its lower density. Since, as will be shown in Chapter 6, the voids with sizes 6-60 Å cannot account for the deficit, the deficit may be uniformly distributed throughout the network. Hence, we must find a reduction in the numbers of atoms in the higher order shells.

In order to explain the flat region between 4.5 and 5.5Å, and the lack of a peak at the third crystalline peak, the rotations of the tetrahedra about their common bonds must be somewhat random, and certainly they are neither just staggered nor eclipsed. In Chapter 7, it will be shown that the best fit to the RDF occurs when the bonds are completely random and that no combinations of just the staggered and eclipsed configurations can fit the RDF.

However, it is difficult to reconcile the random distribution with the persistence of the peaks at 6.1 Å and 8.1 Å. Richter and Breitling[12] have noted that these are the distances associated with the zig-zag chains of Ge atoms. It is likely that the zig-zag chain is one of the common

structural units found in the amorphous structure, but this observation is far from specification of the structure since one must know how these chains are connected to one another.

3. GaAs

Figure 5-10 shows that the F(k) of amorphous GaAs is very similar to the F(k) of amorphous Ge shown in Figure 5-8. These two curves are directly comparable for structural differences since the scattering factors of Ga and As are nearly the same as the scattering factor of Ge. Both the magnitude and the phase of the F(k) of GaAs is nearly the same at high k as in amorphous Ge, indicating that amorphous GaAs has a nearest neighbor distribution with nearly the same average position and the same width as found in the RDF of amorphous Ge.

Inversion of the F(k) shows that the resulting RDF of GaAs (See Figure 5-18) is similar to the RDF of amorphous Ge, even in detail. Not only are the peak positions in close agreement, but so is the spread of the first peak, as has already been deduced from examination of the F(k) functions. The density deficit found by reduction of the x-ray data is 5%, compared to the deficit of 6% found by hydrostatic weighing.

The nearest neighbor distribution peaks at 2.48 Å compared with the crystalline value of 2.45 Å. This slight expansion may be an artifact caused by the slight difference in the scattering factors of Ga and As. The coordination number of the first neighbor distribution is 3.93 ± 0.1 atoms.

The nearest neighbor distribution is about as sharp as that found for amorphous Ge, and the calculated thermal broadening of this peak, $\sigma_1^T = 0.067$ Å, almost entirely accounts for the observed spread of .085 Å. Since the covalent radii of Ga and As are the same,[15] the occurrence of wrong bonds, i.e., bonds between like atoms, may not necessarily cause a spreading in the nearest neighbor distribution. Hence the observed sharpness of this peak cannot be taken as evidence for the absence of wrong bonds.

The second neighbor distribution peaks at 4.1 Å, with a spread of ± 0.3 Å, indicating a bond angle of $109°±10°$. Since the second neighbour distribution goes to 0 at about 3.5 Å there appears to be a cut off in the rms bond angle distortions at about $20°$, as is found in amorphous Ge. The number of second neighbors is estimated to be 12.8 ±2, which is nearly the same value found in the crystal.

We feel that the greatest significance of this RDF is its similarity to that of amorphous Ge, since it indicates that the ionic difference between Ga and As, at least for the conditions of deposiion investigated, has little effect in changing the resulting RDF, and hence, probably the resulting structure.

4. GaP

Despite the large difference in the scattering factors of Ga and P, Figure 5-11 shows that the F(k) of GaP retains the same basic shape as the F(k) function of amorphous Ge, and hence, we expect the two RDF's to be similar also.

The only notable differences in the F(k)'s of GaP and Ge are that for GaP the first peak is higher and the oscillations at high k die away faster, indicating that the nearest neighbor distribution is wider than in Ge.

Inversion of these data gives the RDF shown in Figure 5-19. Since the scattering factors of Ga and P are significantly different, the observed RDF does not equal the true average RDF, and hence, interpretation of Figure 5-19 must be made accordingly. (see Section 3-C) The density deficit, as found from the reduction of the x-ray data, is 5% which is in reasonable agreement for this method with the deficit of -1% found by hydrostatic weighing.

The observed nearest neighbor peak position at 2.44 Å and the observed spread of 0.14 Å are much different from that which we would expect for crystalline GaP. This observed .08 Å expansion in the interatomic spacing is rather difficult to reconcile with the high density. The observed spread is about twice that expected from thermal broadening. Although a Debye T has not been available for GaP, we do not expect the thermal spreading to be much different from that of Ge.

The fact that the ratio of the scattering factors is not a constant, but weakly modulates about a constant value, may have caused the differences in the position and spread of the nearest neighbor distribution. The rate at which the F(k) damps at high k values, which is a more sensitive indication of the width of the nearest neighbor distribution,

cannot possibly be caused by the scattering factors. Hence, we believe the spread in the nearest neighbor distribution to be real.

It is tempting to ascribe the shift and spread to the existence of wrong bonds. Assuming that the covalent radii of 1.225 Å and 1.13 Å for Ga and P respectively remain valid in all bonding configurations that might be found in amorphous GaP, we find using Equation 3-13 that 50% of the bonds must be wrong to explain both the shift and additional spread in the nearest neighbor distribution. However, we realize that the shift and spread may be caused by other mechanisms which distort the covalent radii away from those given.

The observed coordination of GaP is 3.47 ± 0.2, which is, according to Equation 3-10, equal to the true coordination number provided that 50% of the bonds are wrong. Assuming that the bonding is ionic, that is, each Ga atom is surrounded by P atoms and each P atoms is surrounded by Ga atoms, using Equation 3-10 the corrected coordination number is 4.0 ± 0.3. The observation by Connell and Paul[16] of an optical gap in a sample prepared under identical conditions is evidence against metallic phase separation. This gap would not be expected if several metallic regions of Ga existed. In Chapter 6, we will present a small angle scattering curve which suggests very little, if any, phase separation exists in this sample.

The second neighbor distribution peaks at 3.9 Å with a

spread of 0.35 Å, which indicates a bond angle of 107° with a rms spread of 12°. The number of second neighbors is estimated to be 12.0, but assuming that the ionic bonding prevails, then the second neighbor distribution involves distances between like atoms. Correcting for the effects of scattering factors, as has been discussed in Section 3-C, gives a 2nd neighbor coordination of 10.8 ± 2 atoms.

Again it is significant that the effects of ionicity between the consituent atoms does not significantly alter the RDF from the shape observed for amorphous Ge.

5. GaSb

Despite the large difference in the scattering factors of Ga and Sb, the F(k) of amorphous GaSb, as is shown in Figure 5-12, has the same shape as the F(k) of amorphous Ge, and hence, we expect the RDF to be similar to that of amorphous Ge. However, we note that the rate at which the F(k) decays at high k values indicates that the nearest neighbor distribution is broader than it is in amorphous Ge.

Inversion of the data shows that the RDF of GaSb (see Figure 5-20) is indeed similar in shape to that of amorphous Ge, except that the peaks occur at higher r values. However since the scattering factors of Ga and Sb are different, this RDF does not represent the average true RDF, and interpretation of this RDF must be made with this in mind. (See Chapter 3). The density deficit, as found by reduction of the data, is 2% which is in agreement with the density deficit

of -1% found by hydrostatic weighing. This is consistent with the low intensity of small angle scattering which will be presented in Chapter 6.

The nearest neighbor distribution peaks at 2.67 $\overset{\circ}{A}$, compared to the crystalline value of 2.65 $\overset{\circ}{A}$. This we expect since the density is so close to that of the crystal. The spread of the first neighbor distribution is $\sigma_1 = 0.14$ $\overset{\circ}{A}$ while the calculated thermal spreading is $\sigma_1^T = 0.09$ $\overset{\circ}{A}$. As has been discussed in Section 3-C, both the slight expansion and the discrepancy in the spread may be attributed to wrong bonds. If there were 1/10 wrong bonds, the minimum/fraction found by Drummond[17] in his investigation of the Polk[2] model for amorphous Ge and Si, then using the covalent radii of Ga and Sb of 1.225 $\overset{\circ}{A}$ and 1.41 $\overset{\circ}{A}$ respectively,[15] the additional spread would be 0.03 $\overset{\circ}{A}$, and the shift of the average separation to higher r values would be 0.02 $\overset{\circ}{A}$. Both of these estimates are in agreement with the experimental RDF, but this cannot be taken as conclusive evidence of wrong bonds because of the experimental uncertainties in the peak positions and widths.

However, from Raman scattering studies, Wihl et al.[18] have suggested the presence of several Sb-Sb bonds in a film prepared from the same run as the sample from which this RDF is deduced, even though x-ray fluorescence measurements show that the macroscopic stoichiometry is maintained to within 2%. Since the experimental Raman scattering cross sections of each vibrational mode can vary by several orders

of magnitude and no theory exists for their estimation, the numbers of wrong bonds cannot be deduced accurately from the Raman spectra.

How are the Sb-Sb bonds, if any, distributed? If more than 10% of the bonds were Sb-Sb bonds with the interatomic spacing of amorphous Sb,[7] then we would expect to detect a peak in the RDF at 2.90 Å, but clearly we do not. However, we must realize that the Sb-Sb bond length may differ from the amorphous bond length since this length must depend upon the other types of bonds the Sb atoms are making with their surroundings. Also the small angle scattering results which will be presented in the next Chapter indicate that there are no detectable phase separated regions with diameters in the range 6-60 Å. The combined evidence of the small angle scattering and the RDF suggests that the wrong bonds are homogeneously distributed throughout the structure.

Since the density and the nearest neighbor separation are close to their crystalline values, we expect the true coordination number to be close to the crystalline value. The observed coordination of 3.5 ± 0.2 indicates that it is unlikely that the Ga and Sb atoms are randomly mixed. However, if there were Ga-Sb bonds only, the true coordination number would be 3.78 ± .3. These facts, along with the observation of the spreading of the peak suggests that the density of wrong bonds is finite, but small.

The second neighbor distributuon peaks at 4.3 Å with a spread of about 0.4 Å. This indicates an average bonding angle angle of 109° with an rms spreading of 14°. The observed number of second neighbors is 13.2, but assuming that the

second neighbor peak consists mainly of distances between like atoms, the number of second neighbors becomes 12.3, which is in close agreement with the value of 12.0 observed in the crystal.

This RDF is in fair agreement with the RDF of thin evaporated films of GaSb found by Mikolaichuk and Dutchak.[19] They find that in their as-deposited films, the nearest neighbor distribution peaks at 2.65 Å, with a coordination of 4.0 and the second neighbor distribution peaks at 4.35 Å with a coordination of 10.0. Their experimental maximum k value is 9 Å^{-1}, and their data consist of densitometer tracings of electron diffraction patterns, so the resolution and accuracy of their RDF is believed to be less than the one presented here.

6. InSb

The F(k) of sputtered amorphous InSb is also very similar to that of amorphous Ge, except that the first two peaks are smaller and the curve oscillates more quickly with increasing k, indicating a larger average interatomic spacing. The oscillations at high k are also damped at a faster rate than those in the F(k) of amorphous Ge suggesting that the width of the nearest neighbor distribution is wider than that of amorphous Ge.

Since the scattering factors are essentially equal for In and Sb, the RDF shown in Figure 5-21 is essentially equal to the true RDF. Despite the fact that the first diffrac-

tion peak in the experimental intensity has shifted by 10% to higher k values, the RDF still looks much like that of amorphous Ge. The nearest neighbor distribution peaks at 2.86 Å compared to the crystalline value of 2.81 Å. If the first diffraction peak in the experimental intensity were directly related to the interatomic spacing, then it would mean that the interatomic spacing had contracted by 10%. But this size of shift has not taken place; in fact, the observed most probable value is at 1.8% greater value than the crystalline separation. Further examination of the RDF shows that all the peak positions occur in about the same ratios to the experimental 1st neighbor distance as do the peaks in the amorphous Ge RDF. However, there is a hint of a shoulder on the left side of the 2nd neighbor distribution, which may partly account for the shift in the diffraction peak. That the shift in the first peak position should have little effect on the RDF can be understood since this peak is divided by the large form factor and is multiplied by a small value of k, and hence, eventually makes a minor contribution to the F(k), as can be seen by comparing Figures 5-6 and 5-13.

The density deficit of 1.5% deduced from the hydrostatic weighing is in good agreement with the density deficit of 2% deduced from reduction of the x-ray data. However, in the next section it will be shown that the small angle scattering that has been neglected from the analysis of the RDF makes about an additional 2% contribution to the density

deficit, so the x-ray density deficit corrected for the omission of SAS should be 4%.

The observed spread of the nearest neighbor distribution is estimated to be 0.14 $\overset{o}{A}$, which is just a little more than the calculated thermal spreading of .095 $\overset{o}{A}$. Thus the spread due to disorder is very small. Since the covalent radii of In and Sb are nearly the same, the presence of wrong bonds will not cause an additional spread in the RDF.

The coordination number of the first peak is estimated to be 3.82 ± 0.3. However, since the density deficit is about 2% and the interatomic spacing peaks near the crystalline value, it is more likely that the coordination number is closer to 4.0.

The second neighbor distribution peaks at 4.5 $\overset{o}{A}$ with an rms spread of ±0.45 $\overset{o}{A}$. This indicates an average bonding angle of 106° with an rms spread of ±15°. The coordination of the second peak is measured to be 12.8 ±2 atoms.

7. GeSn

The experimental F(k) of GeSn, as far as it is experimentally extended and except for the size and positions of the peaks, has the same general shape as the F(k) of amorphous Ge. Unfortunately the insufficient thickness of this sample did not allow the data to be extended past k=8.o $\overset{o}{A}^{-1}$ with any certainty. However, a densitometer trace of an x-ray pattern of this sample shows that the oscillations in the intensity decay faster than they do for InSb.

Inverting this F(k) gives the RDF in Figure 5-22.
First inspection of this RDF shows that it is very similar
in shape to that of amorphous Ge, except that its peaks are
broader and occur at higher r values, suggesting that per-
haps the structure of this sample of GeSn is a completely
random mixing of Ge and Sn in an amorphous Ge type struc-
ture. Small angle scattering results, which will be pre-
sented in the next section, suggest that the mixing of Ge
and Sn is random and that little phase separation has taken
place. The density found by reduction of the x-ray data
is 5.20 gm/cm^3. There is no crystalline form consisting of
a 50-50 mix of Ge and Sn, so no direct estimate of the den-
sity deficit is possible. However, GaSb is the material
which is expected to resemble GeSn the most, since the
atomic radii and atomic weights of Ge and Ga, and of Sn and
Sb are nearly the same. Compared to the density of cry-
stalline GaSb, the deficit is 10%.

The first neighbor distribution peaks at 2.74 Å.
Assuming that the mixing is completely random so that Ge-Ge,
Ge-Sn, and Sn-Sn bonds are all equally likely, and assuming
the covalent diameters for Ge and Sn are 2.45 Å and 2.81 Å
respectively, gives for the calculated observed nearest
neighbor separation r_1 = 2.67 Å. However, these same cova-
lent diameters predict a nearest neighbor separation in cry-
stalline GaSb, which is 0.02 Å too small. Accounting for
this gives a predicted average neighbor separation of 2.69Å,
which is in fair agreement with that observed. If the dis-

crepancy is not experimental then there is a slight expansion of the distances or there is a preference for Ge-Ge and Sn-Sn bonds over GeSn bonds.

The spread of the first neighbor shell is measured to be $\sigma_1 = 0.22$ Å. Uncertainties arise in all peak widths, particularly the first, since the experimental data have been extended to a k value of only 8.0 Å^{-1}, and hence, part of the broadening may be attributed to Fourier broadening. However, since the densitometer traces show that the oscillations in k space die away faster than for InSb, the true peak height must be somewhere between that observed and that of amorphous InSb. Assuming the random mixing of Ge and Sn, the predicted observed spread using Equation 3-13 is $\sigma_1 = 0.13$ Å, which is less than the observed spread of $\sigma = .22$. Including thermal broadening, assuming it to be the same as that expected in GaSb, which is probably an underestimate, the peak width is predicted to be $\sigma_1 = .155$.

The observed coordination number of the first neighbor shell is $4.0 \pm .4$, which suggests by arguments outlined in Section 3-C that the mixing is totally random. However, the effects due to the correlations between Ge and Sn can change the coordination away from its true value by no more than 7%, which is within the experimental error.

The second neighbor distribution peaks at 4.52 Å with a spread of $\sigma_2 = 0.55$ Å, which indicates an average bonding angle of 111°, with a spread of $\pm 17^\circ$. However, part of this spread includes bond length fluctuations. Accounting for

this gives an approximate rms bond angle uncertainty of $\pm15^\circ$.

If the mixing is totally random, one may expect to find some distances in this RDF which occur in the RDF of amorphous Ge, particularly in the regions of the first and second neighbor shells. We do not see such peaks since they are weighted by the term

$$\frac{f_{Ge}^2}{(f_{Ge} + f_{Sn})^2} \sim 16$$

so the observed RDF is influenced very little by the Ge-Ge distances and is mostly determined by Ge-Sn and Sn-Sn distances.

Since Ge and Ga, and Sn and Sb have the same covalent radii, it is of interest to compare the RDF's of GeSn and GaSb. The ionicity difference between Ga and Sb tends to favor the formation of Ga-Sb bonds; however, since there is little ionicity difference between Ge and Sn, we expect there to be very little discrimination between the three types of possible bonds: Ge-Ge, Ge-Sn, and Sn-Sn. As has already been discussed, the differences observed between the amorphous and crystalline interatomic spacings can be attributed to differences in the correlations between the two components of each material. For GeSn the nearest neighbor position suggests that Ge-Ge, GeSn and Sn-Sn bonds occur in about equal portions and for GaSb, the nearest neighbor position indicates that Ga-Sb bonds dominate the structure. The

observed structure in the RDF of GaSb is much stronger than it is in the RDF of GeSn suggesting that a single bond length dominates the GaSb RDF, whereas the greater amount of disorder in the GeSn suggests that the three types of bonds have occurred.

It is interesting to find that the 50-50 mixture of Ge and Sn can be produced by sputtering/in these proportions, since the most Sn that can be put into crystalline Ge under thermodynamic equilibrium conditions is 1%. This system is also of interest since the mixing of Ge and Sn appears to introduce bond length fluctuations, which do not occur in the other amorphous III-V's studied here.

Since nothing has ever been reported concerning the electronic properties of a GeSn amorphous alloy, we feel that it is worthwhile to include here a discussion on some of the preliminary results for this sample. Connell has been unable to measure any optical transmission out to 16 microns through a 10 micron thick film prepared on a BaF_2 substrate.

Preliminary four terminal measurements on a sample wired with silver epoxy contacts, gives a conductivity at $300^{\circ}K$ of $1.1 \times 10^3 ohm^{-1}cm^{-1}$ which changes very little down to $4^{\circ}K$. The magnitude of the conductivity at $300^{\circ}K$ is typical of several amorphous semiconductors, but it would be premature to draw further conclusions on any detailed conduction mechanism.

8. <u>$ZnCl_2$</u>

Although the data are preliminary and normalized to an

accuracy of only about ±10%, the observed shape of the F(k) of quenched amorphous $ZnCl_2$, shown in Figure 5-15, bears a very strong resemblance to those of the amorphous Ge family of structures. The great similarity in the F(k) of $ZnCl_2$ to that of amorphous Ge indicates that the RDF's must be very similar at least in shape. The persistence of very strong oscillations at high k indicates that the first neighbor distribution is very sharp.

If the structure contained 50% wrong bonds, then we should expect to find, as has been discussed in Chapter 3, a nearest neighbor distribution which is both significantly broadened and shifted to higher r values since the Zn-Zn and the Cl-Cl bond lengths are both larger than the Zn-Cl bond length. However, since the nearest neighbor distribution is sharp and has the crystalline Zn-Cl bond length, it is very unlikely that this number of wrong bonds exists, but is more likely that most of the bonds are ZnCl bonds.

The preliminary RDF of $ZnCl_2$ of Wicks, Drummond and Turnbull[8] as expected from the F(k), has the basic similarities in shape to the RDF of the amorphous Ge structure. Yet we know that the structure must differ from that of Ge since the chemical formula $ZnCl_2$ demands that, as long as only Zn-Cl bonds exist, every Zn atom has twice as many nearest neighbors as does every Cl atom. In the $ZnCl_2$ crystal structure every Zn atom is surrounded by 4 Cl atoms and every Cl atom is surrounded by 2 Zn atoms. We may expect the atoms in the amorphous form to be similarly coordinated.

Turnbull[8] has suggested that since $ZnCl_2$ is chemically similar to SiO_2, amorphous $ZnCl_2$ may have a structure similar to that of vitreous SiO_2. If this were so, we should then expect the $F(k)$ function to be similar to the $F(k)$ of vitreous SiO_2[10] since the ratio of the scattering factors of Zn to Cl is about the same as that of Si to O.

An alternative structure suggested by Polk[21] is that the Cl ions are packed in a dense random structure, such as those built by Finney,[22] and the Zn^{+2} ions sit in the tetrahedral holes produced by the Cl^- ions. However, it has not yet been shown that such a structure has an $F(k)$ function similar to the one observed.

If there were a loss of Cl during the preparation of the sample, so that the effective chemical composition is ZnCl, then we can expect the resulting structure to be similar to that of amorphous Ge and the III-V's. However, since the first neighbor distribution peaks at 2.29 Å, the value of crystalline $ZnCl_2$, it is likely that the material is $ZnCl_2$ since we expect the nearest neighbor distance to be different for a structure based on ZnCl.

These results, we believe, present difficulties for the continuous random network models as they are believed to be today. For amorphous Ge, we have postulated the existence of 5 membered rings; however, it is difficult to imagine the existence of 5 membered rings in amorphous $ZnCl_2$ because of the large ionic difference between Zn and Cl. The RDF of $ZnCl_2$ may be an indication that it is possible to

fit the RDF of amorphous Ge entirely with even membered rings having 6 or more members. If the structures are significantly different, then this indicates the inadequacies of the RDF in determining the structure.

E. Microcrystalline models
1. Introduction

Rudee,[3] on the basis of his observations with dark field electron microscopy, has concluded that amorphous Si and Ge are entirely composed of microcrystallites 14$\overset{o}{A}$ in diameter. Figures 5-23 and 5-24 show a dark field micrograph and the corresponding diffraction pattern taken by Rudee[3] of a 200 $\overset{o}{A}$ thick thin film of Ge sputtered in this laboratory. We note that the diffraction pattern exhibits diffuse rings, which, by the criterion used in the past, operationally classifies the sample as amorphous, but the micrograph does indeed show spots on the order of 15 $\overset{o}{A}$.

Rudee[3] bases his conclusions on two assumptions. First, he assumes that all experimental RDF's are so inaccurate that they are unable to distinguish among the various proposed structural models for the short range order. Second, he assumes that the observed diffraction effects can not be observed from a random network structure, in which the bond angles are distorted 10°. It has been shown earlier in this Chapter that, in a film prepared in the same way as Rudee's film, the 10° bond angle distortion is real, and not an artifact of thermal vibration or Fourier broadening.

Moss and Graczyk have found that the F(k)'s calculated

FIG. 5-23a ELECTRON DIFFRACTION PATTERN OF
AN AMORPHOUS SPUTTERED Ge FILM
200Å THICK. (COURTESY OF M.L. RUDEE)
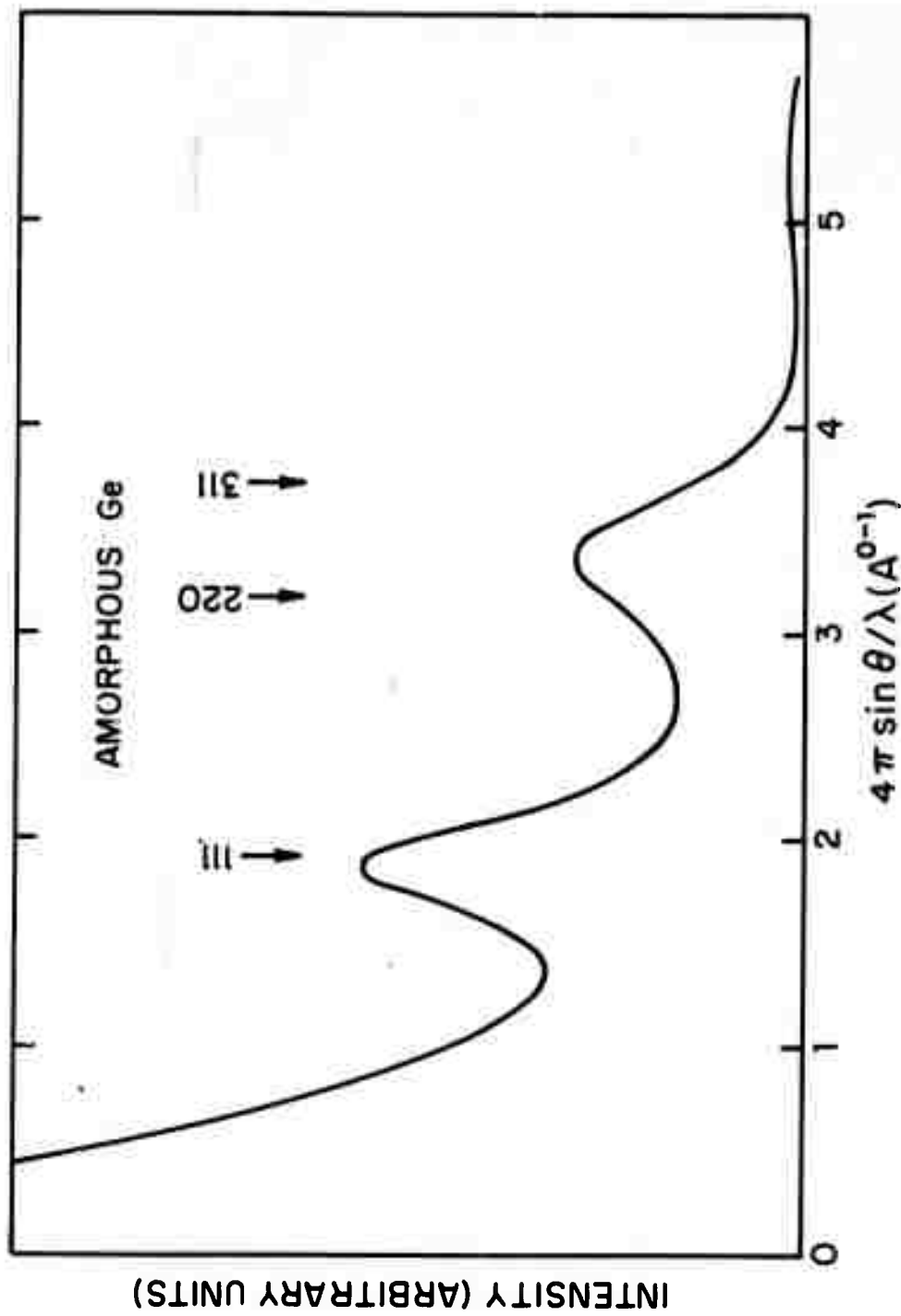
FIG. 5-23b DENSITOMETER TRACE OF ELECTRON DIFFRACTION
PATTERN OF AMORPHOUS SPUTTERED Ge
(COURTESY OF M. L. RUDEE)

100Å
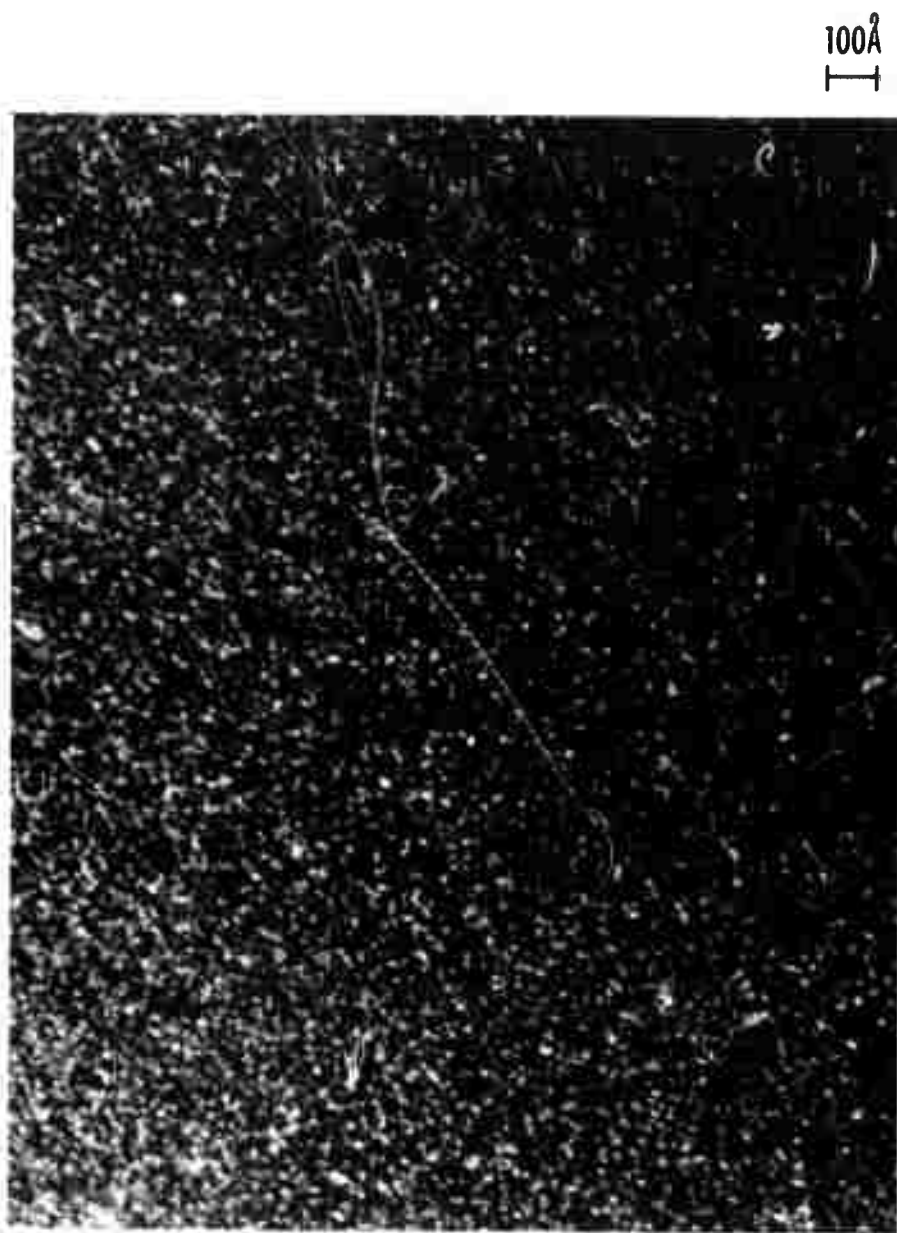
FIG. 5-24 DARK FIELD MICROGRAPH OF AN AMORPHOUS
SPUTTERED Ge FILM 200Å THICK.
(COURTESY OF M.L. RUDEE)

for a single isolated microcrystallite of Si do not agree with their experimental $F(k)$.[4] The real solid, of course, if it were microcrystalline would have to consist of a very large number of microcrystallites packed closely together to maintain a bulk density within 10% of the crystalline value.

However, their calculations are not entirely conclusive since they have not included interference effects between microcrystals, which are expected to be large when the sizes of the crystallites become small.

Upon inverting their experimental $F(k)$, Moss and Graczyk have obtained an RDF which conspicuously lacks the 3rd crystalline nearest neighbor peak, indicating that the short range order is not microcrystalline. They have interpreted their RDF in terms of a continuous random network model constructed by Polk, which not only lacks this peak but also has a 10° bond angle distortion.

Here our objectives are two fold; first we show that the inclusion of the interference effects for the assumed correlations between microcrystals does not significantly alter Moss and Graczyk's results; and second, we show that the experimentalist can obtain an RDF which resolves the third neighbor peak in the microcrystalline structure even for crystallite sizes smaller than are consistent with the diffraction pattern.

2. Specification of the microcrystalline model

The primary difficulty facing those advocating the microcrystalline model has been the specification of the correlations existing between the microcrystals. In a structure consisting of microcrystals, it is expected that regions of mismatch between the microcrystals lead to the formation of many voids. However, the weak small angle scattering in most amorphous semiconductors (see the next chapter) indicates that the packing efficiency of their structure is very high, with no more than 1% of the sample volume occupied by voids with radii between 3 and 30 Å. Either the microcrystals have a shape that allows all space to be filled with little excess volume or there must be some connective tissue with an electron density comparable to the bulk filling the regions of mismatch. Neither of these difficulties, that is, specification of the microcrystal shape that fills all space or the nature of the connective tissue, has been adequately explained, and we make no pretense of doing this here. However, it is necessary for us to make some assumptions concerning the correlations between the microcrystals, thus our results are limited to only those structures that are consistent with these assumptions.

We assume that the microcrystals are polygons, all of the same size, but not necessarily the same shape, and are packed in such a way that there are no large regions of mismatch between them. We must however, assume that the micro-

crystals are approximately spherical in order to simplify the calculations. We further assume that on the ensemble average, the correlations between the atoms lying in different microcrystals are such that the model becomes statistically equivalent to calculating the properties of a single isolated microcrystal lying in a uniform spatial distribution of atoms. We also impose the condition that no two atoms can approach within an interatomic spacing of one another.

3. Calculation of the RDF

The radial distribution function for any ensemble of N atoms is given by

$$4\pi r^2 \rho(r) = \frac{1}{N} \sum_{i,j} \delta(r - r_i - r_j) = \Sigma_1 + \Sigma_2 \quad (5-6)$$

where i and j extend over all atoms within the solid. The RDF can be broken into two classes of terms: summations which are between atoms lying within the same microcrystal, Σ_1, and those between atoms lying in different microcrystals, Σ_2.

To calculate the RDF, we consider the environment seen by the average atom. For an arbitrary vector of radius r drawn from any atom in the solid, the probability that this vector lies in the microcrystal containing this atom is:

$$\gamma(r) = 1 - \frac{3}{2}\frac{r}{a} + \frac{1}{2}\left(\frac{r}{a}\right)^3 \quad \text{for} \quad r < a \quad (5-7)$$
$$0 \quad \text{for} \quad r > a$$

where a is the diameter of the crystallite, and the probability that it does not is:

$$1 - \gamma(r)$$

This suggests that we take for the intraparticle summations:

$$\Sigma_1 = \gamma(r) \times RDF(r)_{cryst} \qquad (5-8)$$

and for the interparticle summation:

$$\Sigma_2 = \begin{array}{ll} 4\pi r^2 \rho_o (1 - \gamma(r)) & r > r_1 \\ 0 & r < r_1 \end{array} \qquad (5-9)$$

where ρ_o is the average atomic density, and r_1 is the nearest neighbor separation. Σ_2 has been taken to be 0 for $r < r_1$ to ensure that no two atoms can approach within an interatomic distance of one another.

4. Calculation of the F(k) and observed RDF

With the RDF computed as above, the F(k) is computed by:

$$F(k) = e^{-\frac{\sigma^2 k^2}{2}} \int_0^a 4\pi r^2 (\rho(r) - \rho_o) \frac{\sin(kr)}{r} dr \qquad (5-10)$$

Note that the upper limit of the integral is a, since for $r > a$, $\rho(r) = 0$. The purpose of the exponential damping factor is to artificially include thermal and instrumental broadening effects. The value of σ is taken to be equal to

.17 Å which is larger than most found experimentally in this investigation, and corresponds to an effective temperature near the melting point of Ge. This F(k) is then inverted via:

$$4\pi r^2 \rho(r) = 4\pi r^2 \rho_o + \frac{2r}{\pi} \int_0^{15} F(k)\sin(kr)\,dk \quad (5\text{-}11)$$

to give a RDF similar to that/the which experimentalist using a similar amount of Fourier information would observe. By examining the RDF found in this way, we can determine whether the experimental RDF has the resolution to resolve the microcrystalline model.

5. Results and Discussion

The F(k)'s are reasonably well behaved, that is, do not have a large peak near k=0. This indicates that our inclusion of the interparticle interference terms is physically reasonable and that the model **agrees** with the observation of a weak SAS intensity. Comparison of these curves to those of Moss and Graczyk[7] shows that they are very similar; hence, according/these to calculations the conclusions of Moss and Graczyk[7] still stand. Figure 5-25 shows that for a 14 Å microcrystal, the 2nd and 3rd peaks start to split, and clearly this is not observed experimentally, not even by Rudee. For the 8 Å crystallite size, the 2nd and 3rd peaks are not split, but the width of the 2nd peak is too great, as has been noted by Moss and Graczyk. The F(k)'s for all
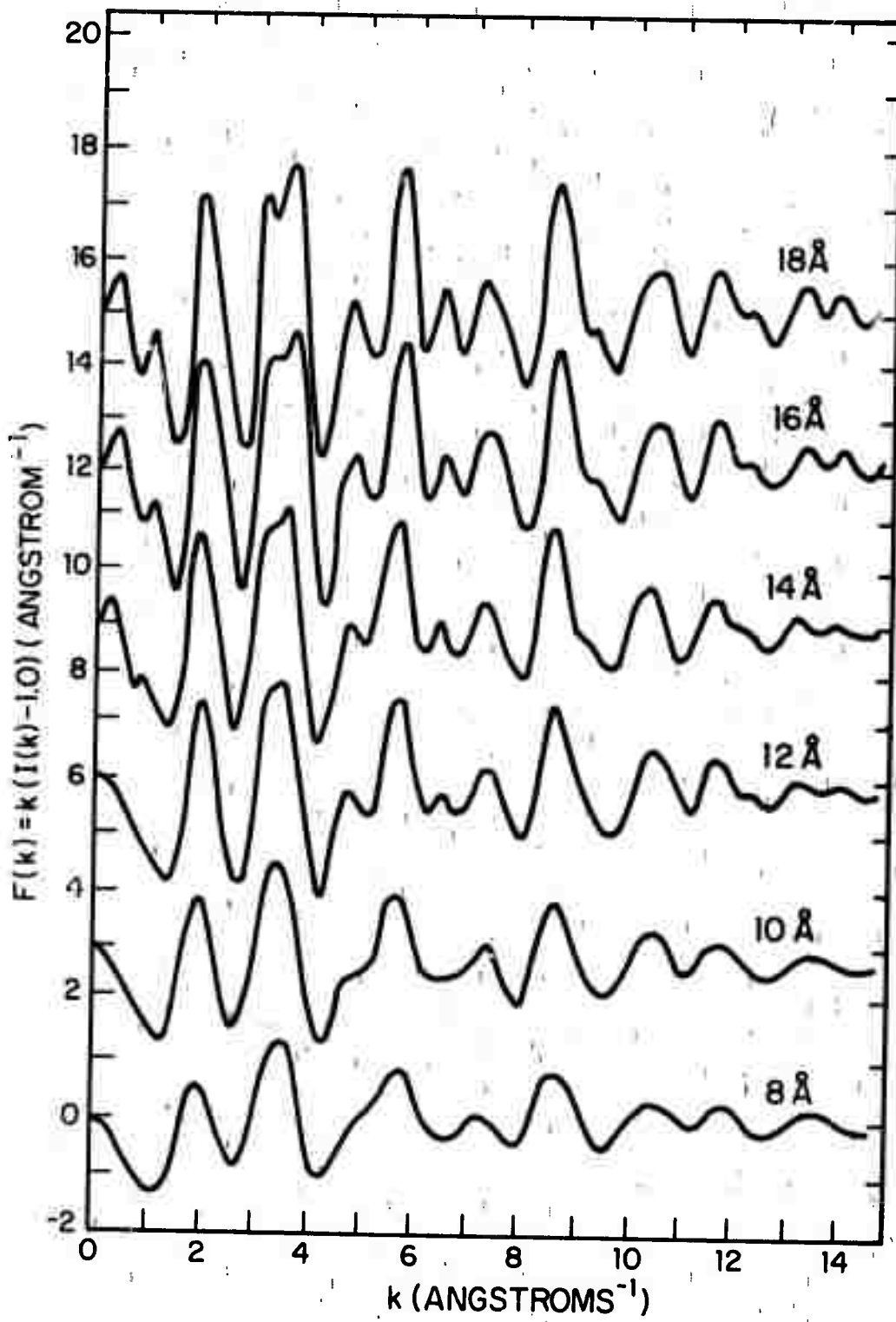
FIG. 5-25 F(k) FOR MICROCRYSTALS OF VARIOUS DIAMETERS

the crystallite sizes do not agree well with experiment, particularly in matching the relative heights and sharpnesses of the first and second peaks, and the oscillations at high k in the calculated F(k)'s never agree with those observed experimentally.

The inadequacies of the microcrystalline model are more dramatically exposed by comparing their RDF's as are shown in Figure 5-26. Note that even for a crystallite smaller than is consistent with line broadening, the third peak in the crystalline RDF is resolved, and for the 14 Å particle size, the structure is entirely different from the experimental RDF.

In particular, we note that for the sizes of crystallites investigated, the RDF does not go to zero between the first and second neighbor distributions as it has been found to experimentally. In this model this arises because the atoms at the surface of each microcrystallite have some neighbors at distances between the crystalline first and second neighbor distances. We note that for the 8 Å crystallite model, the first and second nearest neighbors comprise essentially all the structure observed in the RDF, and that the F(k) still exhibits the general behavior of all those observed experimentally in this investigation. This indicates that for many amorphous materials perhaps the first and second neighbor distributions determine most of the behavior of the F(k); thus the similarity of the F(k) of amorphous Se to those of amorphous Ge may not be so surprising
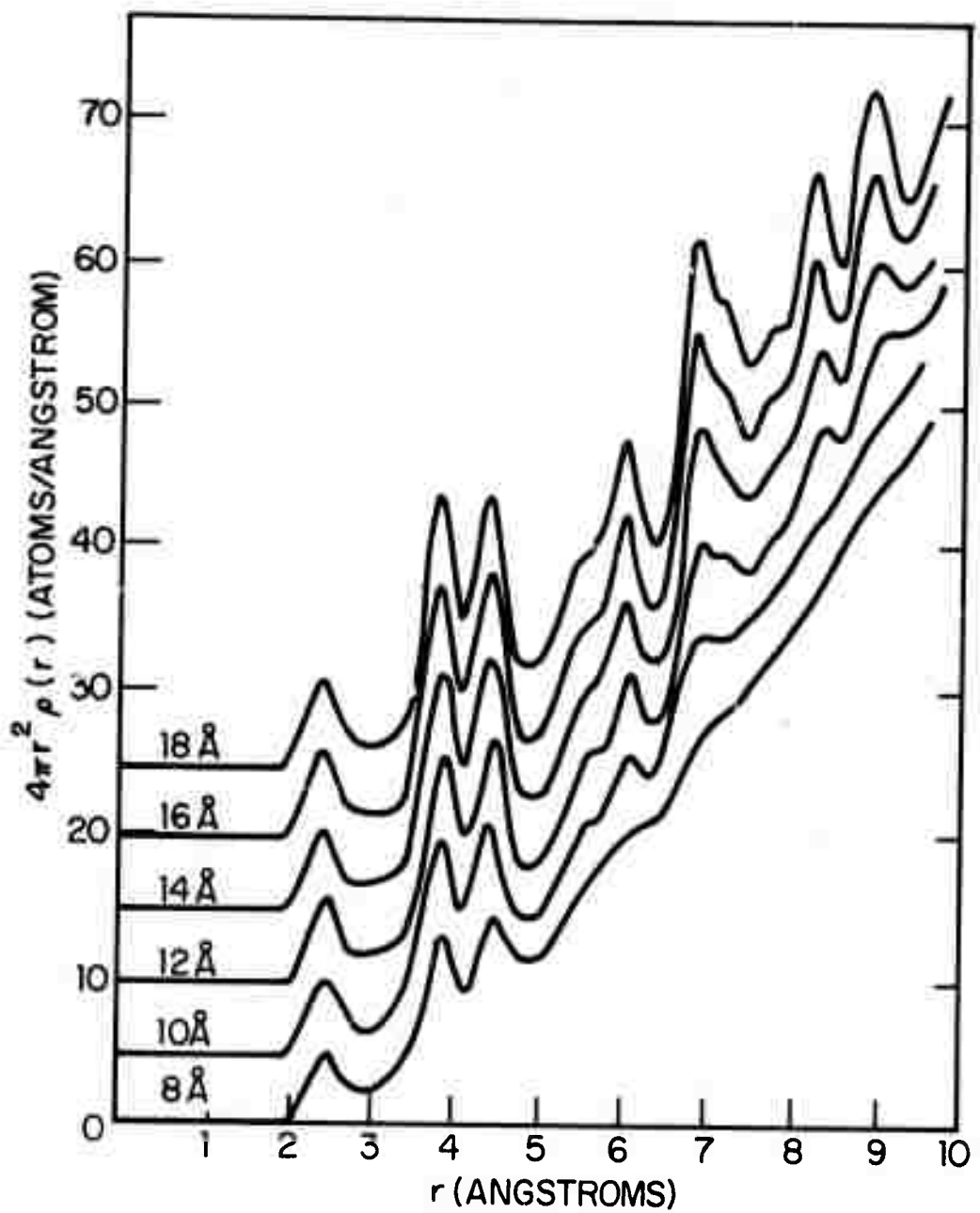
FIG. 5-26   RDF's FOR MICROCRYSTALS OF VARIOUS DIAMETERS

since the first two peaks in the RDF are similar in shape.

However, we must admit that we have not totally eliminated other microcrystalline models by this calculation. It is possible that different correlations between the microcrystals may lead to results which are in better agreement with experiment. Also, one may specify a connective tissue between the crystallites, but the specification of the structure of the connective tissue and how it connects to the microcrystals becomes a complex, if not intractable, problem.

Nevertheless, we can use the results presented here to get an idea of what these correlations must be in order to explain the experimental RDF. The intraparticle summations, Σ_1, as given by Equation 5-8 should be correct since they are independent of the correlations between the microcrystals and depend upon the internal structure of the microcrystal only. To bring any microcrystal model into agreement with the experimental RDF, the interparticle summations, Σ_2, must be given by:

$$\Sigma_2 = 4\pi r^2 \rho(r)_{exp} - \gamma(r) 4\pi r^2 \rho(r)_{cryst.}$$

In computing the RDF's in Figure 5-26, Σ_2 has been assumed to be almost structureless, and hence most of the structure in these curves is from the intraparticle summations. Comparing these curves to Figure 5-16, we see that Σ_2 would need to have a considerable amount of structure to bring the microcrystalline model into agreement with experiment.

Since the correlations between atoms within different micro-crystals must be equal in strength to the correlations between the atoms within the same microcrystal , we find it difficult to believe that the amorphous Ge consists of small crystallites having the diamond structure. However, other microcrystal structures may fit the experimental results better than the diamond structure.

We conclude that if the structure were microcrystalline with the type of correlations specified between the micro-crystal, the experimentalist could resolve the 3rd nearest neighbor peak in the RDF, but since this peak has not been observed experimentally, the structure cannot be of this form. The calculated F(k)'s have also been found to be in-consistent with the experimental F(k)'s. Interparticle interference, as it has been included here, does not significantly alter the behavior of those curves calculated by Moss and Graczyk.[4]

F. Summary and Conclusions

The F(k)'s of Ge, GaAs, GaP, GaSb, InSb and GeSn are all remarkably similar in shape. At high k all behave as a single sinusoidal function indicating that in all these structures the first coordination sphere is well defined.

Inversion of these F(k)'s shows that the RDF's of these materials are very similar in shape, suggesting that these materials all have the same basic structure. This struc-ture is characterized by a first neighbor distribution which

is well separated from the second neighbor distribution.
In all cases the nearest neighbor distribution peaks near
the corresponding crystalline value. For Ge, GaAs and
InSb the spread in the first neighbor distribution is very
close to that calculated for thermal spreading. For GaSb,
GaP and GeSn, there appears to be a spread which is due to
static disorder.

The second neighbor distribution peaks near that ex-
pected for the second neighbor in the corresponding crys-
talline form. The number of second neighbors is found to
be very close to 12, as is found in the crystal. To ac-
count for the spreading of the second neighbor distribution,
the bond angles must be distorted from 10-17°.

Absent in all of these RDF's is the peak corresponding
to the 3rd crystalline neighbor. It has been shown that if
the SRO were microcrystalline, then the third crystalline
neighbor would have been resolved very easily experimentally.
To account for the absence of the 3rd crystalline neighbor
rotations of the atoms about their common bonds must be to
first order random.

The only structural model that appears to be consistent
with these observations is the continuous random network.
Moreover, since these RDF's are similar, it is likely that
they have similar structures. If we accept the continuous
random network model in its present form, and hence, the
presence of five membered rings in Ge, then we must also

accept the presence of large numbers of wrong bonds in the amorphous III-V materials.

A difficulty is produced by the fact that the F(k) of $ZnCl_2$ is strikingly similar to that of Ge, and it is hard to believe that there are five membered rings in a material as ionic as $ZnCl_2$. If we were to conclude that there are no five membered rings in any of the other materials, then the CRN would have to be considerably modified. At present the reconciliation of the similarities in the F(k) functions of Ge and $ZnCl_2$ either poses a serious problem for the CRN model, or it demonstrates the inadequacies of RDF's in specifying the structure.

REFERENCES

1. R. Grigorovici and R. Manaila, J. Non-Cryst. Solids, 1, 371 (1969)

2. D.E. Polk, J. Non-Cryst. Solids, 5, 365 (1971)

3. M.L. Rudee, Phys. Stat. Solidi 46b, K1 (1971) (1971)

4. S.C. Moss and J.F. Graczyk, Phys. Rev. Lett. 23, 1167 (1969) and Proc. Tenth International Conf. on the Phys. of Semiconductors, Cambridge, Mass. (1970)

5. B. Kramer, Phys. Stat. Solidi 41, 725 (1970) and J. Non-Cryst. Solids, in press

6. M.V. Romerio and N.W. Ashcroft, J. Non-Cryst. Solids, 5, 264 (1971)

7. W. Eckenbach, W. Fuhs, and J. Stuke, J. Non-Cryst. Solids, 5, 264 (1971)

8. G. Wicks, C. Drummond, and D. Turnbull, private communication and to be published.

9. R. Kaplow and T.A. Rowe and B.L. Averbach, Phys. Rev. 168, 1068 (1968)

10. H. Krebs and R. Steffen, Z. für Ang. und Allg. Chem. 327, 224 (1964)

11. J.F. Graczyk and S.C. Moss, private communication

12. H. Richter and G. Breitling, Z. Naturforschg. 13a, 988 (1958)

13. T.B. Light and C.N.J. Wagner, J. Appl. Cryst. 1, 199 (1968)

14. D.E. Sayers, F.W. Lytle, and E.A. Stern, Bull. Amer. Phys. Soc. Ser II 16, 302 (1971) and to be published

15. J.A. Van Vechten and J.C. Phillips, Phys. Rev. 32, 2160 (1970)

16. G.A.N. Connell and W. Paul, J. Non-Cryst. Solids, in press

17. C.H. Drummond, private communication

18. M. Wihl, J. Tauc, M. Cardona, J. Non-Cryst. Solids, in press

19. A.G. Mikolaichuk and Y.I. Dutchak, Kristollografiya 9, 106 (1964)

20. R.L. Mozzi and B.E. Warren, J. Appl. Cryst. 2, 164 (1969)

21. D.E. Polk, private communication

22. J.L. Finney. Ph.D. Thesis, University of London (1967)

23. B.E. Warren, X-ray Diffraction, Addison Wesley, Reading Mass., 1971, Chapter 10

24. See tables of pseudopotential values in Pseudopential Theory in the Theory of Metals. W.A. Harrison, W.A. Benjamin, New York, 1966

CHAPTER 6

SMALL ANGLE SCATTERING IN SOME AMORPHOUS SEMICONDUCTORS

A. Introduction

It is believed that the presence of voids can change the electronic properties of amorphous semiconductors to such an extent that the properties intrinsic to the ideal void free material can be obscured. Therefore, it is important to establish the concentration and sizes of voids in amorphous materials before their electronic properties can be thoroughly understood. Also, for compound materials, it is necessary to establish whether or not the material has separated into its constituent phases. Unfortunately, in comparison to the numbers of papers reporting the electronic properties, very few papers have been devoted to an investigation of the occurrence of voids or phase separation in amorphous semiconductors.

In this chapter, the results of small angle x-ray scattering, (SAS), on amorphous films of Ge, Si, Se, GeSn, GaAs, GaP, GaSb, and InSb will be presented. Small angle scattering, which is sensitive to electron density fluctuations, provides a means to detect voids and/or phase separated regions. Our objective has been to employ SAS techniques, which have not been widely applied to amorphous semiconductors. In particular, efforts have been made to scale the small angle scattered intensity to electron units so that estimates of the concentrations of voids can be made. Also, an attempt has been made for some of the materials investigated here to find the total density deficit and internal surface attributable to voids.

The total internal surfaces as deduced from small angle scattering for Ge and Si have been compared with the observed electron spin resonance signals.

Although Moss and Graczyk[1] have observed small angle scattering in very thin films of amorphous Si, surface roughness has not entirely been eliminated as the source of this scattering. Nor has it been established that voids occur in very thick films. The results to be presented here conclusively demonstrate the existence of voids distributed throughout the bulk in thick, amorphous films of Ge and Si.

The results for amorphous Ge have been determined on a number of samples, so that we believe them to be representative of what would be found by others for the deposition parameters used. Nevertheless, qualitatively different behavior might be found for other deposition conditions. By comparison, the results presented here for the other materials are preliminary, since only one sample of each has been measured. Their overall similarity gives an idea of what is generally to be expected, and examined in toto, they do place limits on void densities which should be incorporated in speculative models. However, small differences between them are probably meaningless at this exploratory stage.

B. Presentation of the small angle scattering results

In the SAS curves to be presented, the experimental data have been collected over the range from $k=0.04 \text{ Å}^{-1}$ to 1.96 Å^{-1}. Below a k value of 0.04 Å^{-1}, the data, as has been

discussed in Chapter 4, have been extrapolated to $k=0$ $\mathring{A}^{-1}$.
The experimental points have been included on all figures,
except where to do so would lead to confusion because of the
overlapping of several curves. Since the data have been col-
lected at constant time intervals between steps, the statis-
tical error is the worst at the smallest intensities.

The SAS of a polycrystalline sputtered Ge film shown in
Figure 6-1 is presented first so that it can be compared with
the SAS of the amorphous materials. This film has been ob-
tained by removing it from the inside of the bell jar wall af-
ter the end of a run intended to make amorphous Ge. This film
is most likely crystalline because the inside of the
bell jar was not cooled.[2] Whatever caused the film to be
crystalline does not concern us here; what matters is that
the film is crystalline. This curve is typical of what is
found for three films obtained in this way.

The .15 $\mathring{A}^{-1}$ half width at the (111) peak indicates that
the experimental resolution in this region is good. However,
as will be shown later, at smaller k values the resolution
becomes much worse and some of the experimental curves require
large corrections. In the region $k=0.5$ to 1.5 $\mathring{A}^{-1}$, the in-
tensity is very low, as is expected for a polycrystalline
material with few small internal defects. Although not con-
clusive, this low intensity is assurance that the procedure
used to subtract the background is correct. This curve has
been normalized to electron units by assuming that the area
under the (111) diffraction peak in polycrystalline Ge is equal

to the area under the first diffraction peak in amorphous Ge. Since the right side of this peak has not been experimentally determined, the total area of the peak has been assumed to be equal to twice the area of the left hand side of the peak, which has been experimentally determined.

Note the rapid rise in the intensity at the origin. This indicates that in this sample there are inhomogeneities; the magnitude of this scattering suggests that they are most likely voids. The SAS of a single crystal does not give this large intensity at the origin, but remains very small at the lowest angles. Only when voids are present is the SAS appreciable. In a microcrystalline structure voids presumably result as large regions of mismatch between the crystallites. We discuss this problem later in the chapter.

Figure 6-2 shows the SAS of amorphous Ge prepared by evaporation, electrodeposition, and sputtering. Three, six and three samples prepared by evaporation, electrodeposition, and sputtering respectively have been investigated. The electrodeposited Ge samples exhibit no peaks in the SAS down to the lowest angles detectable; on the other hand, the evaporated and sputtered Ge samples exhibit peaks near the origin that vary by about a factor of two in intensity at the lowest angles.

The SAS of the sputtered and electrolytic Ge samples has been normalized by using the high angle diffraction curves obtained in this investigation. High angle diffraction experiments on the evaporated Ge samples have not been possible with

the techniques used here since the samples are of inadequate thickness and surface area. Since no high angle diffraction experiments have been conducted on the evaporated Ge samples, the average high angle scattering curves of Richter and Breitling,[3] and Grigorovic and Manaila[4] have been used to normalize the SAS curve for evaporated Ge. Since the height of the peak at k=1.9 $\overset{o}{A}^{-1}$ of the evaporated Ge has been found to be very close to that of sputtered and electrodeposited, all three peak heights have been taken to be the same. The error in doing this is estimated to be no more than 5%, which is also about equal to the experimental error in this region.

Plotted in Figure 5-3 is the SAS curve for evaporated Ge for k < .5 $\overset{o}{A}^{-1}$ along with the same curve corrected for collimation effects. Plotted logarithmically as a function of k,[2] in Figure 6-4 are the uncorrected SAS curves for two evaporated Ge samples, one prepared by A.P. Barna and the other prepared in this laboratory.

Figure 6-5 shows the SAS of an evaporated amorphous Si sample, provided by M.H. Brodsky of IBM. Plotted on a logarithmic scale for k < 0.5 $\overset{o}{A}^{-1}$ in Figure 6-6 are raw experimental SAS data for this sample and the same data corrected for the effects of collimation. The SAS curves for amorphous evaporated Si have been normalized by matching them onto the high angle scattering curves for amorphous Si obtained by Richter and Breitling.

Figure 6-7 shows the SAS curve for an amorphous evaporated Se sample, provided by Dr. R. Gorin of Xerox. Figures 6-8 to

6-12 show the SAS curves for amorphous sputtered films of
GaAs, GaP, GaSb, InSn, and GeSn. All of these curves have
been normalized by matching them onto the high angle scat-
tering curves that have been presented in Chapter 5.

Since the SAS curves for sputtered InSb, GeSn and eva-
porated Ge and Si exhibit rapidly varying intensities near
the origin, it has been necessary to apply to each of these
curves the collimation corrections that have been discussed
in Chapter 4. The corrected and uncorrected curves for these
materials are shown in Figures 6-3, 6-6, 6-11, 6-12. For
these curves the corrections are large; for GeSn and InSb,
they are about a factor of two at the origin; for evaporated
Ge and Si, they are about a factor of ten at the origin. At
higher k, where the instrumental resolution increases and the
curves vary less rapidly, the corrections are less than 2%.

Since the SAS curves for electrolytic and sputtered Ge,
for sputtered GaAs, GaP, GaSb and for evaporated Se display
no rapidly rising peaks as k decreases to 0, no collimation
corrections have been made for them.

Summarized in Table 6-1 for most of the materials are the
total density deficits attributed to the complementary parti-
cles producing the SAS by assuming that the complementary
particles have the same electron density as a void. For eva-
porated Ge and Si and for sputtered GeSn and InSb, where the
SAS intensities are large, the density deficits have been
found by the evaluation of Equation 4.22. For GaP, GaAs, and
sputtered Ge, the density deficits have been estimated by

comparison of their SAS curves to the curves in Figure 4-1. Since the curves for Se, GaSb, and electrodeposited Ge display no peaks near the origin that are obviously identifiable as scattering from inhomogeneities, no estimates have been made for their density deficits. In a column adjacent to the estimated SAS density deficits, are listed the density deficits determined from hydrostatic weighing.

Figure 6-13 shows the $\gamma(r)$ functions for the four materials exhibiting the large SAS peaks. All the $\gamma(r)$ functions have been normalized so that $\gamma(0) = 1$. As discussed in Section 4-B, the value at which this function goes to 0 gives the largest diameter for which the term $N(r)$ $V(r)$ makes a significant contribution to the intensity. These values we take as representing the largest void size detected. For the other samples with little SAS, the largest detected void size has been estimated by comparison of their SAS curves to the curves plotted in Figure 4-1. The radius of the largest particle size detected in each material is listed in the last column in Table 6-1.

Figures 6-14 and 6-14b show the void radius distributions, $N(r)$, for evaporated Ge and Si and for sputtered InSb and GeSn, normalized to give the number of voids per cubic centimeter per angstrom. As expected from the similarities in their experimental intensity curves, the particle distributions for evaporated Ge and Si and for sputtered GeSn and InSb are similar in shape.

Note that the void radius distributions fall off very ra-

pidly with increasing void radius. It has been found that in the regions above the point where the $Y(r)$ function goes to zero, the distributions become negative and oscillatory. This is believed to be caused by termination errors arising from the inversion of Equations 4-16. It is easy to show with Equation 4-16 that a constant error in the SAS intensity leads to a termination error in $N(r)$ that decreases as $1/r^3$, whereas the true void distribution must decrease faster than $1/r^4$ in order that the integral $\int_0^\infty N(r) \, V(r) \, dr$ converge. Hence, as r increases a point is reached where the calculated distribution is obscured by termination errors. However, as long as the void distribution appears to be well behaved (that is, does not go negative or wildly oscillate) below the r value at which $\gamma(r)$ becomes equal to zero, then the void distribution is probably not obscured in this range. Such has been found to be the case here; only for high r values, beyond the largest void diameter detected, do the distributions behave unphysically.

Figures 6-15 and 6-17 show the void volume distributions, $V(r) \, N(r)$, as a function of r for these four materials. In Figure 6-16 is plotted the surface area distribution, $4\pi r^2 N(r)$, for the voids in evaporated Ge. In calculating these distributions, it has been assumed that the voids are spherical so that the volume and surface area of a void of radius r are given by $\frac{4\pi}{3} r^3$ and $4\pi r^2$ respectively. The volume distributions have been normalized so that their integrals over r give the total void volume in $\overset{\circ}{A}{}^3$ per cm^3. The surface area

distribution has been normalized so that its integral over r gives the total void surface area in $\overset{\circ}{A}{}^2$ per cm^3.

The void volume distributions for GeSn and InSb become equal to zero before the upper limit of detectability of 30 $\overset{\circ}{A}$ is exceeded. Unfortunately, this is not true for the distributions for evaporated Ge and Si. Because of the uncertainties in the deconvolution of the data from the effects of collimation and in the extrapolation of the data to k=0, we cannot be certain whether these distributions are correct for r>30 $\overset{\circ}{A}$. Also, since the separation of the SAS from the background and from the scattering from the ideal material is uncertain, we cannot be sure that the distributions for r < 3 $\overset{\circ}{A}$ are correct either.

Figures 6-18 and 6-19 show the SAS of amorphous Ge prepared by electrodeposition and sputtering for various annealing conditions.

Finally, Figures 6-20 and 6-21 show respectively the SAS of a partially crystallized InSb film and of a film that has been deliberately made off stoichiometry.

C. Discussion of the small angle scattering results.

1. Ge

Evaluation of the volume integral for the evaporated amorphous Ge sample gives a density deficit due to the large observable voids of 3% . However, for the same reasons that the void distributions may be in error, this estimate of the void volume may be in error by as much as 100%. Nevertheless it is believed that this number is a reasonable lower bound

on the density deficit attributable to voids.

It has been suggested by Richter and Breitling[3] that the structure of amorphous Ge may consist of microcrystallites immersed in a completely random medium, the details of which have remained unspecified. Since such a system is inhomogeneous, it is expected to produce SAS. Assuming that the electron density difference between the crystallites and the disordered medium is .1 ρ_c , which is the upper bound established by the most recent investigations,[1,5] evaluation of Equation 4-22 gives a microcrystal volume of 500% of the total sample volume, which is physically unrealistic. Only voids can account for the magnitude of the observed scattering. We cannot, however, rule out the possibility that the structure is microcrystalline. This calculation merely establishes the presence of voids.

The question may arise as to whether the SAS observed in these films is representative of the SAS of films produced in other laboratories. The SAS curves shown in Figure 6-4 for two evaporated Ge samples, one prepared by A.P. Barna, and the other by ourselves, are similar. Although the comparison with one other film made elsewhere is insufficient to prove that this SAS is typical of evaporated amorphous Ge, it does at least suggest that this is a possibility. Cargill's recent SAS measurements on evaporated amorphous Ge films of several microns in thickness are in qualitative agreement with the SAS observed here.[6]

However, the measurements by Cargill[5] on his evaporated

Ge samples show that the SAS intensity is not isotropic, but is a function of the angle between the normal to the sample's surface and the incident beam direction. This indicates that in his samples neither are the shapes of the voids spherical nor are their orientations in space random. Cargill[6] interprets his SAS curves in terms of scattering from ellipsoids or pinholes having their longest dimensions about 2000 $\overset{\circ}{A}$ in the direction normal to the plane of the samples. Similar conclusions have been reached by Donovan and Heineman,[7] who, using high resolution electron microscopy, have found what appears to be a crack network in very thin films of 100 $\overset{\circ}{A}$ thickness. The impetus for these investigations was the prior deduction of Galeener[8] that voids of this shape can explain the behavior of the ϵ_2 of amorphous Ge at photon energies ~ 5 eV.

This anisotropic SAS, if it exists in our samples, introduces further uncertainty to all the results deduced from the SAS curves. However we believe this anisotropic SAS to be unlikely in our films, for if the voids were the shape that Cargill finds, and if they were to account for a few percent of the density deficit, then the observed scattering should be 10-100 more intense than is observed here. The presence of voids of elongated shape would reduce the accuracy of the deduced void distributions. The extraction of particle size distributions for particles of shape other than spherical from the SAS data has not, to the author's knowledge, been treated. Nevertheless, distributions derived with

the use of Equation 4-16 are still of qualitative importance in telling us how the complementary volume is distributed.

Figure 6-15 shows that the corresponding volume distribution for evaporated Ge peaks at 16 $\overset{o}{A}$ and begins to diminish rapidly near the upper limit (30 $\overset{o}{A}$) of reliable detection but does not go to zero until r = 40 $\overset{o}{A}$. The decreasing slope of this curve for r > 16 $\overset{o}{A}$ suggests that most of the voids lie in the range r = 0 to r = 40, but then again, since the upper limit of reliable detection is about 30 $\overset{o}{A}$, and what lies beyond this range is sensitive to the extrapolation of the data to k = 0, we cannot be sure of the shape of the curve beyond this point. However, since the volume sum rule has shown that at least half of the volume deficit is attributable to the detectable voids, the other half may be due to monoatomic vacancies or possibly to voids with r > 40 $\overset{o}{A}$.

Since the SAS of the sputtered Ge film is weak and slowly varying near k = 0, collimation corrections and computer reductions of the data have not been attempted. The bump near the origin can be adequately fitted with a function of form:

$$I(k) = \frac{1}{(1 + (kr_o/5)^2)^2} \quad , \text{ with } r_o = 4 \ \overset{o}{A},$$

which, as has been discussed in Section 4-B corresponds to a void distribution having the form:

$$N(r) = A e^{-\left(\frac{r}{r_o}\right)^2}$$

The density deficit attributable to the SAS of sputtered Ge
is only 0.5%, which is only a small fraction of the 10%
deficit found by hydrostatic weighings. If there is no SAS
below the minimum k value detectable, then the remainder of
the density deficit must be uniformly distributed throughout
the network in small voids or it is intrinsic to the network
structure.

The SAS curve for the electrodeposited Ge film remains
flat down to k = 1.0 $\overset{o}{A}^{-1}$ and does not go to zero at the
smallest experimental k values. However, since uncertaintiss
in the background make it difficilt to estimate the height
of the flat portion of this curve, no reliable estimates of
the density deficit could be made. Nevertheless, the con-
tribution to the density deficit is certainly no greater
than the 0.5% estimated for sputtered Ge, which implies that
again the remainder of the deficit must be unifromly distri-
buted in atomic sized voids or it is intrinsic to the network
structure.

The numbers of surface bonds determined from the SAS
curves for the amorphous Ge prepared by the three methods
are in qualitative agreement with those determined from the
electron spin resonance (ESR) measurements conducted in this
laboratory and with ESR measurements conducted at IBM by
D. C. Kaplan and R.S. Title.[9] As is expected from the SAS
curves, the evaporated Ge has the largest ESR signal with an
observed spin density of 2 X 10^{20} /cm^3.[6] The sputtered Ge,

as found in our laboratory, has a spin density about $7 \times 10^{19}/cm^3$, which is 1/3 that of the evaporated. As is suggested by its SAS curve, the electrodeposited Ge has the fewest spins with $2 \times 10^{19} /cm^3$.[5]

Drummond[10] has found that there are 256 broken bonds on the surface of the Polk model for amorphous Ge and Si,[5] which, scaled to the Ge atom, is equivalent to a sphere 15 Å in radius. This gives a broken bond surface density of $.11 / Å^2$. Using this number, along with the total surface area as deduced from the surface area distribution in Figure 6-16, the number of surface bonds in this sample of evaporated Ge is $3.50 \times 10^{20} / cm^3$, while the spin density of evaporated Ge has been found to be typically $2 \times 10^{20} / cm^3$.[9,11,12] The number of surface bonds accounted for by the SAS of the sputtered Ge is about $2 \times 10^{20} / cm^3$ while the observed spin density is $7 \times 10^{19} / cm^3$.

It has been assumed by Title et al.[12] on the basis of the experimental results of Haneman[13] that only 1/10 of the surface bonds produce a spin signal; thus if this fraction is correct, the number of surface bonds must be 10 times greater than the observed ESR spins. It has been found that the number of surface bonds accounted for by the SAS of evaporated and sputtered Ge is only about a factor 2 greater than the spin density. Better agreement with the ESR measurements, accepting the assumption that only 1/10 of the surface bonds produces a spin, might be found if the large voids and the smaller voids can be more accurately extracted from the SAS.

Nevertheless, the order of magnitude agreement between the number of surface bonds predicted by the two methods does make the connection between the ESR signal and the internal surface more convincing.

It is interesting that the optical absorption edges of amorphous Ge prepared by the three methods may also correlate with differences in their SAS curves. The evaporated Ge has a flat edge with a high absorption coefficient, the sputtered Ge has a steeper edge with a lower absorption coefficient, and the electrodeposited Ge has an even steeper edge and lower absorption coefficient.[14] When the materials are annealed, the absorption is reduced and the edges shift to a common asymptote at an energy near 1 ev. Connell and Paul,[14] by applying the optical oscillator sum rule to the reduction in the integrated absorption, have found that the number of electronic transitions removed by annealing agree with the numbers of surface bonds deduced from the SAS and ESR. This suggests that in the as-deposited films the optical absorption edge may come from electronic states associated with the voids.

However, as will be discussed later, the observed changes in the SAS with anneal do not account for the changes in the optical absorption edge. It has been speculated that the annealing causes the total surface area of the voids to decrease with annealing, thereby reducing the number of broken bonds.[12] The discrepancy indicates that some other mechanism may be responsible for the reductions in the

ESR and the absorption edge.

We suggest that if oxygen and/or other gases reside in voids, annealing can initiate the oxidation of any dangling bonds, which may cause the large changes in the ESR and the optical edge, while causing no changes in the SAS. Another possibility is that since the Ge atoms on the surface of the void are not as constrained as those in the bulk, annealing allows those atoms on the surface of the void to rearrange themselves so as to reduce the total number of broken bonds, while the void essentially remains unchanged.

The large differences between the SAS curves for the Ge prepared by the three methods clearly demonstrates that the presence of voids is not intrinsic to the material, but depends on the deposition process.

2. Si

Figures 6-5 and 6-6 show that the SAS of amorphous evaporated Si is very similar to that of amorphous evaporated Ge. Evaluation of the volume integral gives a deficit volume of 4%, which is to be attributed to the voids larger than 3 Å and smaller than 60 Å. If the SAS were due to microcrystallites in an amorphous matrix, the volume of the complementary particles would be 400% of the total sample volume, which is again too large to be physically meaningful.

On the other hand, the hydrostatic weighings give a density deficit of 10%, which is greater than the deficit attributed to the larger voids. Therefore, the remainder of the deficit

is either in larger or smaller voids than were detectable, or it is intrinsic to the network structure.

The SAS of this Si sample is qualitatively the same as that obtained in thin evaporated films with electron diffraction by Moss and Graczyk.[1] The curve presented here demonstrates that the presence of voids in Si is not just an artifact of thin films, but that it occurs in thick films as well.

Figure 6-15 shows that the void volume distribution for this Si sample peaks at a particle radius of about 15 $\overset{o}{A}$ and rapidly decays near $r = 40$ $\overset{o}{A}$ which is a little above the estimated upper limit of reliable detectability. Although the volume sum rule accounts for 40% of the 10% deficit, 60% of the volume deficit may lie in voids with $r > 30$ $\overset{o}{A}$. As discussed previously, the distributions for values of r less than 3 $\overset{o}{A}$ and greater than 30 $\overset{o}{A}$ may be in considerable error.

Since the void distributions for evaporated Si and Ge are similar in shape and magnitude, it is expected that the ESR signals observed in the evaporated Si and Ge samples would be similar. Indeed this has been found to be so by Brodsky and Title[11] in experiments conducted on other Si and Ge films prepared by evaporation.

3. Se

The SAS of amorphous evaporated Se, shown in Figure 6-1, is very small at the lowest detectable k values. This indicates that there are no appreciable numbers of voids in

the range r= 3-30 Å. If there is little scattering re-
maining at smaller k values than have been detected, the
density deficit of amorphous Se may be attributed to the
presence of voids smaller than 3 Å in radius, or it may be
intrinsic to the network structure. To the author's know-
ledge, there have been no other experiments performed that
give information concerning voids in amorphous Se. However,
we again caution the reader that this is a measurement on
one sample and that one cannot infer from this that voids
do not occur in films prepared under different deposition
conditions.

We note also that the width of the diffraction peak in
this sample of Se is about twice as wide as that for any
other material investigated here. This observation has been
discussed at length in Chapter 5.

4. GaP, GaAs, and GaSb

All of the amorphous gallium compounds, GaP, GaAs, and
GaSb exhibit weak SAS, as is shown in Figures 6-8, 6-9 and
6-10 respectively. The SAS curves for GaAs and GaP show a
slight increase in the intensity for k values approaching
the origin, which is consistent with voids having radii of
about 4 - 5 Å, and a total volume of about 1/2 - 1% of the
total sample volume. The SAS curve for GaSb remains es-
sentially flat at the smallest angles. The significance of
these curves is that since the SAS in all three is rela-
tively weak, no appreciable, if any, phase separation has

taken place in particles of less than 30 $\overset{o}{A}$ radius. This suggests that to a very high degree, the atoms are homogeneously distributed in space.

That is, it is unlikely that many regions exist that contain an excess of one type of atom over the other; the atoms of each kind must be well mixed at least on a scale less than 60 $\overset{o}{A}$ with those of the other kind. The details of the correlations between the two types of constituent atoms cannot be determined from this measurement alone, but combined with the RDF analysis presented in Chapter 5, it appears that each Group III atom is surrounded by four Group V atoms and each Group V atom is surrounded by four Group III atoms. The low optical absorption in the infrared observed by Connell and Paul[14] is additional evidence that the atoms are arranged in this way. An appreciable amount of separation of the constituents into their metallic phases is expected to cause a large infrared absorption.

5. <u>InSb</u>

The SAS curve for InSb shown in Figure 6-11, displays a peak at the origin which, although not nearly as intense as the peak for evaporated Ge and Si, is easily separable from the intensity of the first diffraction peak near 1.9 $\overset{o}{A}{}^{-1}$ and the background. The void volume distribution in Figure 6-17 shows that most of the density deficit is in 5 $\overset{o}{A}$ radius voids, and suggests that nothing lies in regions of r larger than 10 $\overset{o}{A}$. Evaluation of the volume integral gives a density deficit of 2%, which is in agreement with the deficit

found by hydrostatic weighing. If this scattering were pro-
duced by phase separated amorphous Sb, which has a density
of $5.57 gm/cm^3$ [15], the volume of amorphous Sb would be 1000%
of the total sample volume, which is impossible. If the
scattering were produced by phase separated particles of
crystalline Sb or In, with densities of 6.69 and $7.29 gm/cm^3$
respectively, the total volumes of these particles would be
64 and 100% respectively. If phase separation were this
extensive, then such a system would be expected to behave
like metallic In or Sb and would have a high absorption co-
efficient in the infrared. However, Connell[16] has measured
a small absorption coefficient in the infrared. These re-
sults taken together suggest that there has been no phase
separation.

Hence, it is concluded that the SAS from this sample of
amorphous InSb is most likely from voids, and that very
little separation of the constituents into their crystalline
or amorphous phases has taken place.

6. GeSn

The SAS curve for GeSn shown in Figure 6-12 has a peak
at the origin which has nearly the same shape as the peak
for InSb, but is twice as intense. It is not surprising then
that the void volume distribution for GeSn shown in Figure
6-17 has the same shape as the distribution for InSb. Since
the void volume distribution is rapidly falling before a
radius of 30 $\overset{o}{A}$, the approximate upper limit of detectability,
it is likely that all the larger voids are accounted for in

this distribution.

Application of the volume sum rule to these SAS data gives a density deficit of 4%. If the scattering were from either phase separated Ge or Sn immersed in a matrix of GeSn, the complementary volume would be 50% of the total sample volume, which seems unlikely, but cannot be eliminated as a possibility. Preliminary optical measurements by Connell[16] have shown that GeSn prepared on BaF_2 substrates is opaque in the infrared. However, this does not prove the existence of phase separation, since a random mixing of Ge and Sn may produce significant absorption in the IR.

The degree of homogeneity of this sample is significant to the deposition process, since the target used in the sputtering process consisted of a mixture of Ge and Sn powders and the resulting film seems to be well mixed on an atomic scale.

D. <u>SAS of amorphous Ge as a function of annealing temperature</u>

Figure 6-18a shows typical changes in the SAS of electrodeposited samples as a function of one-hour isochronal anneals at several temperatures. For annealing T greater than 225° C, the high angle diffraction curve begins to show signs of crystallinity. It has been found that usually the intensity at the smallest angles tends to increase slightly with increasing temperature of anneal, and that there is a smaller, and just detectable decrease in the SAS at inter-

mediate k values. This behavior is shown in Figure -18b,
in which is plotted the change in the SAS intensity of an
electrodeposited Ge film that has been annealed at 120° and
at 150° C until the change in the resistance at each tempe-
rature becomes negligible (a"terminal" anneal) This behavior
of the SAS with annealing is consistent with the condensa-
tion of the smaller voids into larger voids. Also, in
Figure -18b there appears to be a slight increase of the
first diffraction peak at k = 1.92 $\overset{O}{A}^{-1}$ of about 2 per cent,
although this is not as pronounced as the changes occurring
at smaller angles in Figure 18a.

Figure 6-19 shows the annealing behavior of the SAS of
sputtered amorphous Ge. Here, the terminal anneals were
continued for several days at each temperature until the
change in the resistance with time became negligible. The
same behavior is observed as in the electrodeposited films
but the changes do not occur until higher temperatures are
reached. The normalization of the data for the 307° C an-
neal is uncertain since the sample broke during the annealing
run. The curve has been normalized by assuming that the
peak at k = 1.92 $\overset{O}{A}^{-1}$ has the same height as for the earlier
anneals. Since little change of this peak height has been
found in the annealing of the electrodeposited films, it is
believed that the error introduced by normalizing in this
way is about 5% at worst. At intermediate k values the re-
duction in the SAS is the same order as the possible error
in the normalization, and so it has not been shown. The

change observed at small angles is, however, much larger than any normalization error, and implies an increase in the number of larger voids.

E.   SAS of crystallized and offstoichiometric InSb

Figure 6-20 shows the uncorrected SAS of an amorphous InSb film that has been annealed at 150° C for three hours. Although the film has been partially crystallized with the annealing there is not a significant difference between the scattering at small angles in Figures 6-20 and 6-11. We note, however, that at higher angles, not only has the diffraction peak sharpened, but it has also shifted to smaller k values, to about the same position, k = 1.78 $\overset{O}{A}^{-1}$, that is expected for crystalline InSb. This is additional evidence that the first diffraction peaks in amorphous and crystal- line InSb do not occur at the same k value.

Figure 6-21 shows the SAS from a sample sputtered onto a substrate held at 0° C. The target used in sputtering this sample consisted of a pressed powder comprised of 55 atomic percent   In powder and 45 atomic percent Sb powder. The position of the first diffraction peak is, within the 2% experimental accuracy, the same as that of crystalline InSb; this suggests that although the In and the Sb were not in chemical combination in the target, they are in chemical combination in the resulting film.

It is interesting to note that, since this curve does not exhibit any large peaks near the origin, there are few,

if any, phase separated particles 3 to 30 Å in radius. One would expect the excess In to separate from the InSb; however, the flat continuous part of the intensity below the first diffraction peak suggests that the excess In is randomly dispersed throughout the structure, perhaps in the large interstitial holes available in the diamond structure.

F. Surface roughness

Surface roughness is also expected to produce some SAS. It can be easily demonstrated, however, that surface roughness cannot account for the magnitude of the scattering found in the materials presented here. If the scattering were from a surface having a roughness that varies with a scale R_o, then the shape of the small angle scattering curve would reflect this scale in about the same way as it does for a void of radius R_o. The maximum radius of the detected void sizes listed in Table 1 also represents the maximum scale of the surface roughness, if the scattering were produced by surface roughness. Since the surface is only R_o thick then the maximum volume deficit percent for which it can account is $2R_o/t$, where t is the thickness of the film.

We consider the worst two cases, the evaporated Ge and Si films, where the SAS intensities are the largest. For the Ge and Si films, the thicknesses are 100,000 Å while the maximum R_o is 40 Å; hence, the maximum volume deficit that can be attributed to this roughness is:

$$\frac{2R_o}{t} = 2 \times 40/10^5 = 8.0 \times 10^{-4} = .08 \text{ \%}$$

which is far smaller than is observed; hence, we must rule out surface scattering as the dominant SAS mechanism. Since the films investigated by Moss and Grazcyk[1] were only 100 Å thick, surface roughness could have easily produced the SAS of these films.

G. SAS and the microdomained structures

The low SAS intensities for Se, GaP, GaAs, GaSb and sputtered and electrodeposited Ge indicate that these materials most likely do not consist of domains of size less than 60Å. In materials consisting of domains, voids are expected to arise because of a mis-match between the boundaries of the domains. The sizes of the voids resulting in this way are expected to be from a few angstroms to about the size of the domains.

The volume deficit found from the SAS also tells us how efficiently any domains in these materials must be packed. The maximum volume deficit that can be attributed to mismatch regions of size less than 60 Å across has been found to be, at most, 1% of the total sample volume for these materials. Hence, either the packing efficiency of the domains must be very high or there is some connective tissue having an electron density comparable to that of the domains filling the regions of mismatch.[17]

The domains can have internal configurations which are either ordered or disordered. However, if they are internally

ordered, they must be no larger than 10-15 Å and must be positioned incoherently relative to one another to be consistent with the experimentally observed diffraction patterns. For a material consisting of ordered domains having a high packing efficiency, it is difficult to understand how in such a structure the domains can be arranged so as to produce incoherent diffraction between themselves.

On the otherhand, if the domains are internally disordered they can be larger than 15 Å and still be consistent with the diffraction patterns. However, for a structure consisting of internally disordered domains, it is still difficult to believe that few regions of mismatch occur with sizes less than 60 Å. We cannot rule out the possibility that the structure consists of domains with internal disorder of size greater than 60 Å.

For amorphous evaporated Ge and Si, and sputtered InSb and GeSn, where the deficit volumes are much larger, the arguments against their having domained structures are less strong.

H. Summary and conclusions

This investigation must be considered as preliminary since the number of samples investigated for each material is small and the range of deposition conditions limited. However, because of the similarities observed among a variety of amorphous semiconductors, we believe that these results are typical of what one should expect to find under similar deposition conditions. Nevertheless, some definite

conclusions may be drawn.

The SAS of the amorphous Ge prepared by three different methods has shown that the small angle scattering is certainly not intrinsic to the materials, but is dependent on the method of preparation. The accumulated SAS results seem to indicate that large voids are more likely to occur in evaporated films. For evaporated Si and Ge it has been established that voids are present through the bulk, that at least half of the density deficit can be attributed to voids, and that the internal surface area attributed to voids as deduced from the small angle scattering and the ESR signals is in good agreement.

The dependence of the SAS of Ge on the temperature of anneal shows that, prior to crystallization, there are slight internal rearrangements that cause the SAS to increase at the smallest angles and to decrease at the intermediate angles, which suggests a condensation of small voids into larger ones.

The SAS indicates that there is little, if any phase separation in the compound materials, GaP, GaSb, GaAs, InSb and GeSn.

Moreover, the weak SAS found in Se, GaAs, GaP, GaSb and electrodeposited and sputtered Ge indicates that the packing efficiency of their structure is very high. We have argued that it is unlikely that these materials consist of ordered domains since it is difficult to understand how such a structure can show little SAS and yet sustain incoherent diffrac-

tion between the domains. It is therefore likely that the structure of these materials is that of the continuous random network.

REFERENCES

1. S.C. Moss and J.F. Graczyk, Phys. Rev. Lett. 23, 1167 (1969)

2. A demonstration that acoustical shock waves caused sputtered Ge to crystallize was provided by Rustum Roy at The Third International Conference of Liquid and Amorphous Semiconductors held at Ann Arbor, Michigan, 1971

3. H. Richter and G. Breitling, Z. Naturforsch, 139, 988 (1958)

4. R. Grigorovici and R. Manaila, Thin Solid Films, 1, 343 (1967)

5. D.E. Polk, J. Non-Cryst. Solids, 5, 365 (1971)

6. G.S. Cargill III, Bull. Amer. Phys. Soc. 16, 1424, (1971), also private communication

7. T.M. Donovan and K. Heinemann, Phys. Rev. Lett. 27, 1794 (1971)

8. F.L. Galeener, Phys. Rev. Lett. 27, 1716 (1971)

9. D.C. Kaplan and R.S. Title, private communication

10. C.H. Drummond, private communication

11. M.H. Brodsky and R.S. Title, Phys. Rev. Lett. 23, 581 (1969)

12. R.S. Title, M.A. Brodsky, B.L. Crowder, Tenth International Conference on the Physics of Semiconductors, Cambridge, Mass., 1970

13. D. Haneman, Phys. Rev. 170, 705 (1968)

14. G.A.N. Connell and W. Paul, J Non-Cryst. Solids, in press

15. H. Krebs and R. Steffen, Z. für Anor. und Allg. Chemie, 327, 224 (1964)

16. G.A.N. Connell, private communication

17. D. Turnbull and D.E. Polk, J. Non-Cryst. Solids, in press

TABLE 6-1. Summary of the SAS Data.

Material	Density Deficit determined from SAS data (%)	Density Deficit determined from weighing (%).	Largest Void Radius Detected (Å)
Ge(el.)	-	5	2
Ge(ev.)	5	10	40
Ge(sp.)	.5	10	5
GaP	.5	- 1	4
GaAs	.5	6	4
GaSb	-	-	2
Si	4	10	40
GeSn	4	-	9
InSb	2	1.5	8
Se	-	12	2
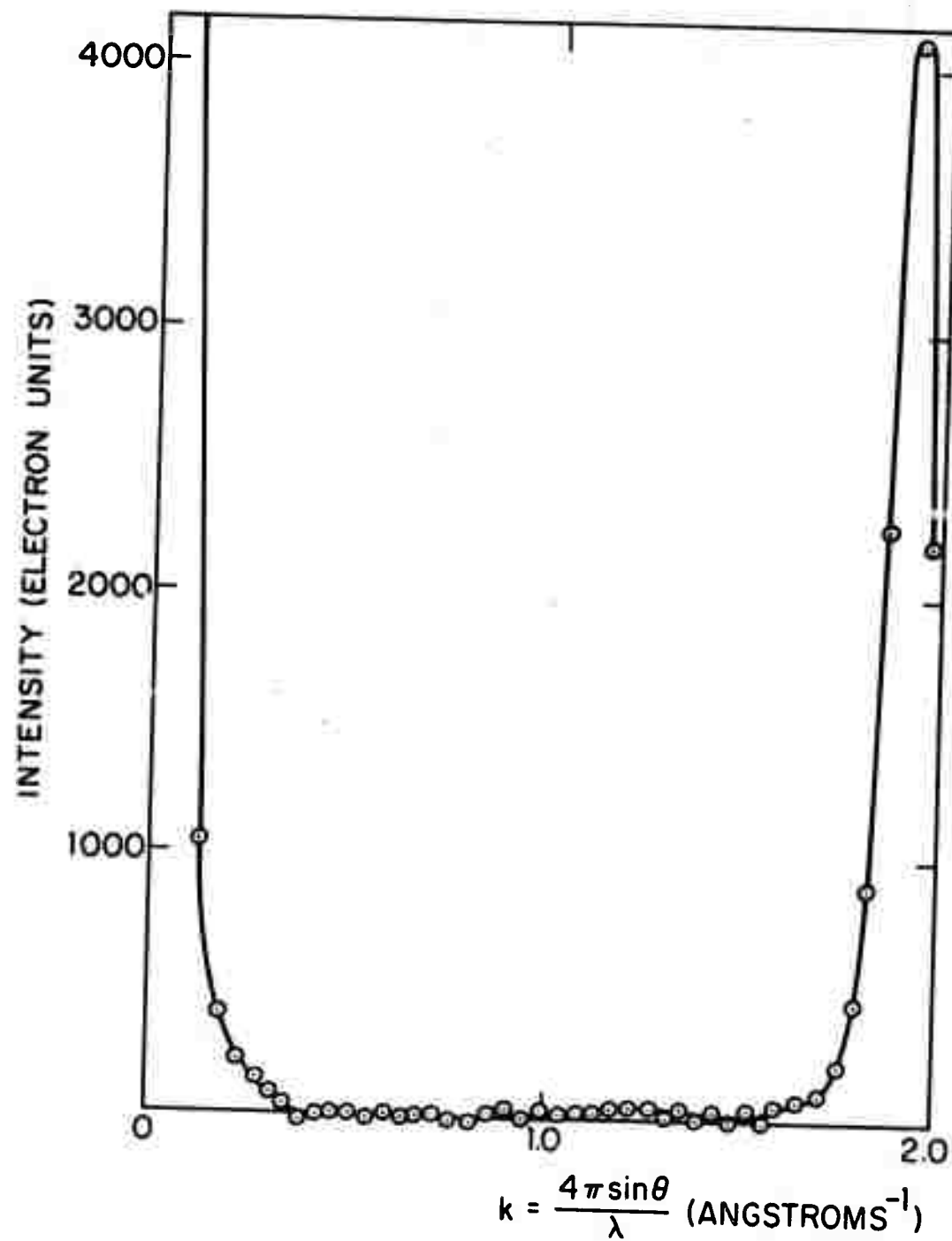
FIG. 6-1   SMALL ANGLE SCATTERING OF
POLYCRYSTALLINE Ge.
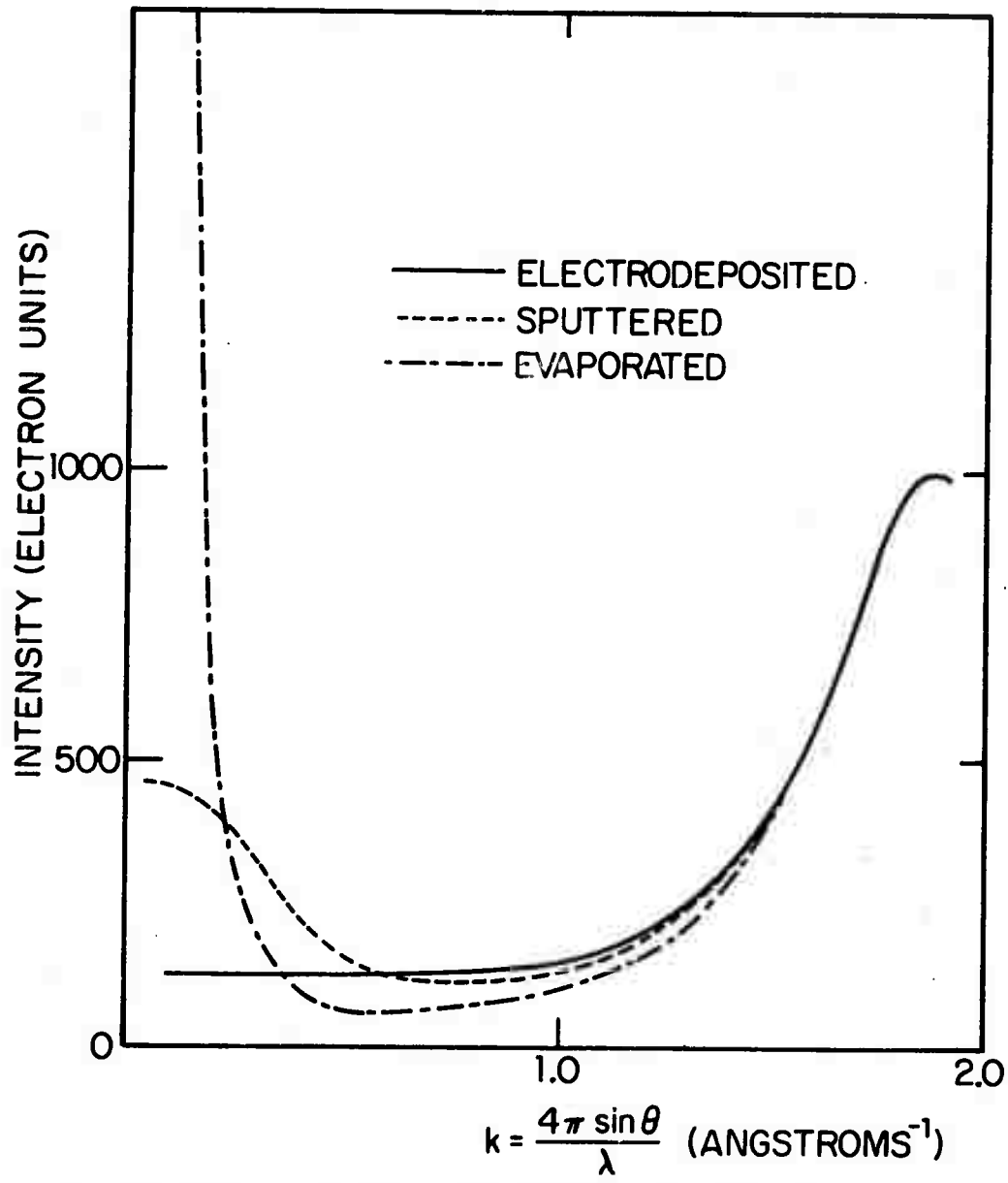
FIG. 6-2 SMALL ANGLE SCATTERING OF AMORPHOUS Ge PREPARED BY ELECTRODEPOSITION, SPUTTERING AND EVAPORATION.
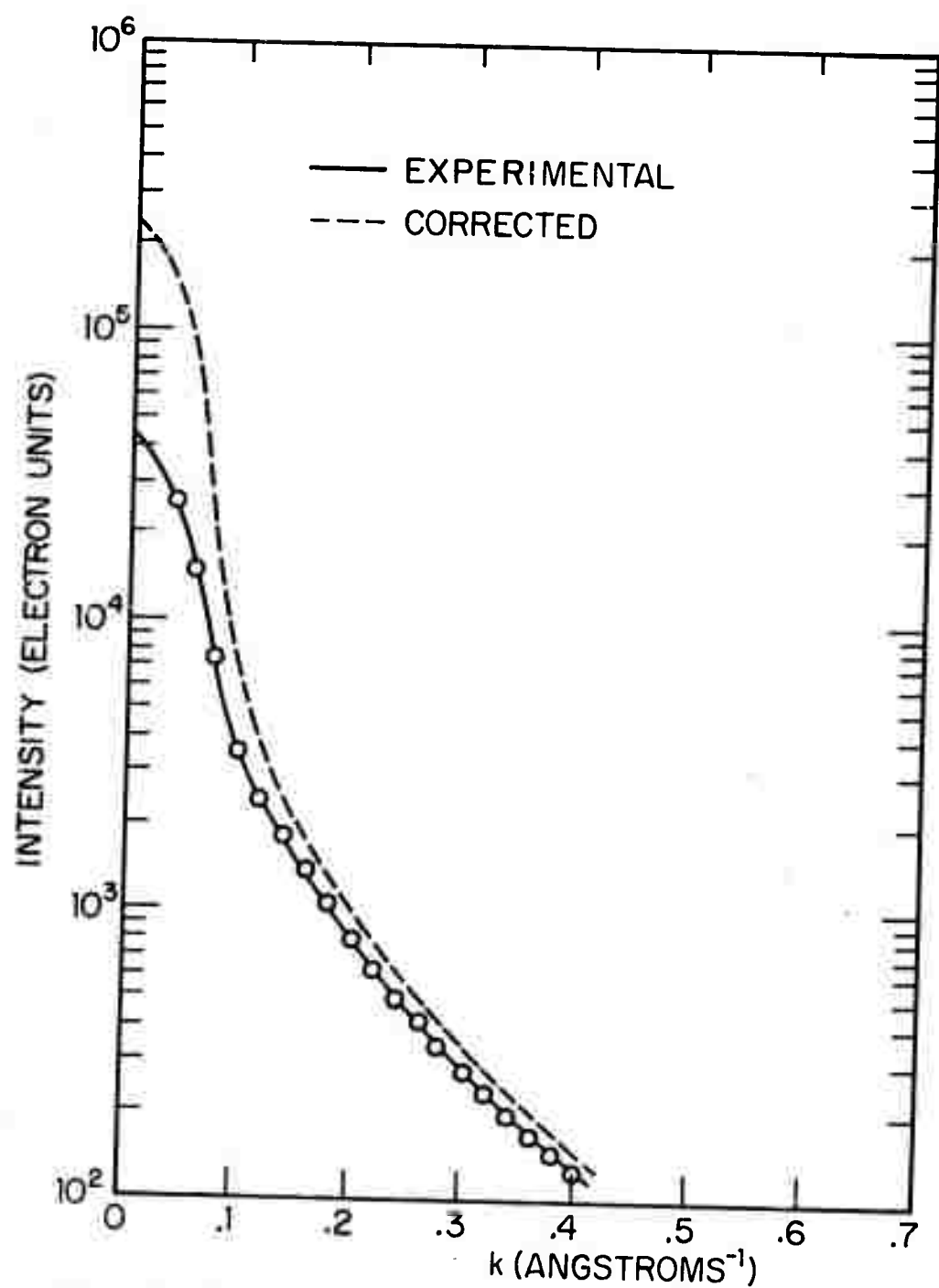
FIG. 6-3 EXPERIMENTAL AND CORRECTED SMALL ANGLE SCATTERING OF AMORPHOUS EVAPORATED Ge.
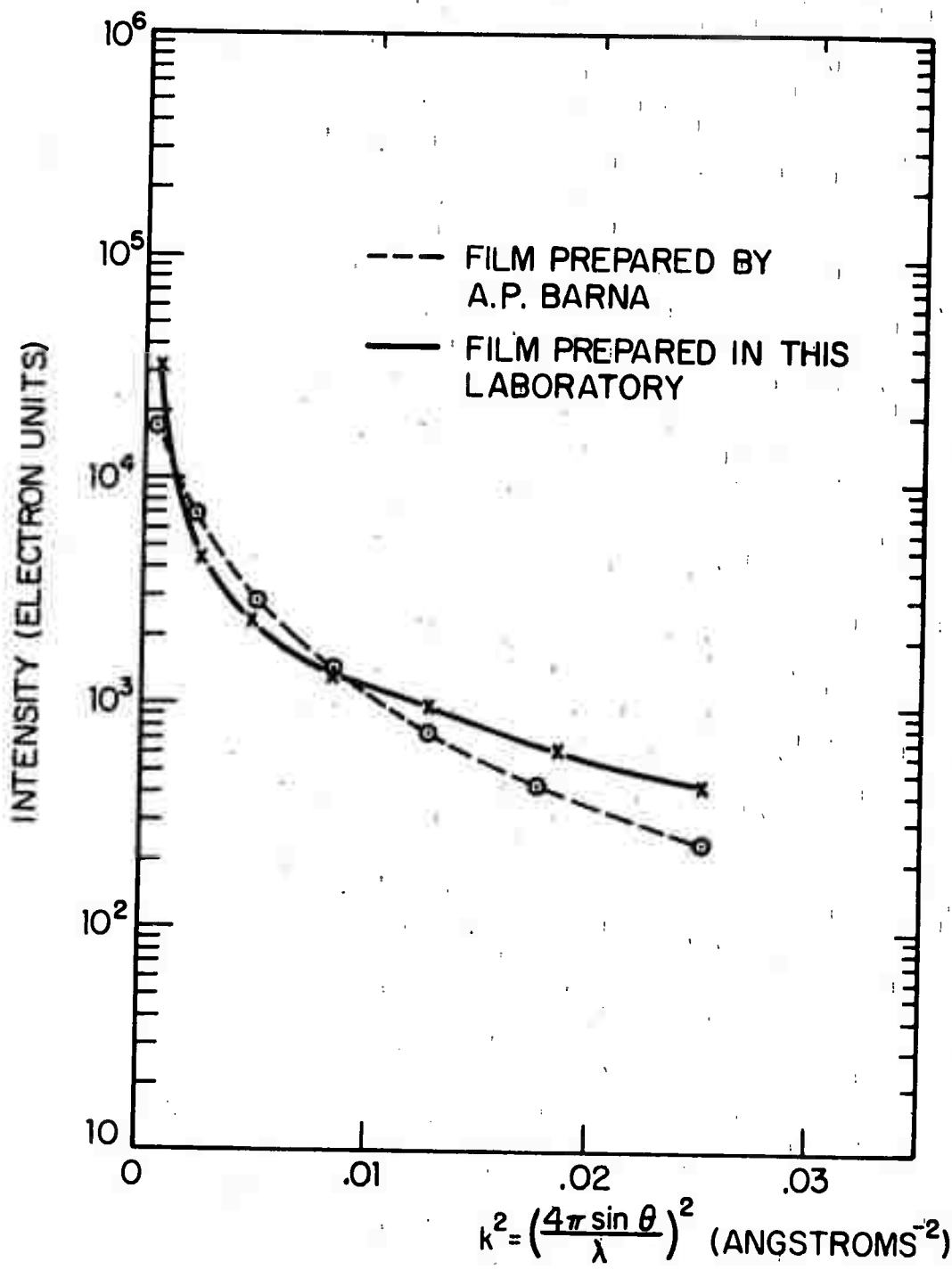
FIG. 6-4 SMALL ANGLE SCATTERING OF EVAPORATED
GE FILMS, ONE PREPARED BY A.P. BARNA
AND THE OTHER BY OURSELVES.

$$k = \frac{4\pi \sin\theta}{\lambda} \text{ (ANGSTROMS}^{-1}\text{)}$$
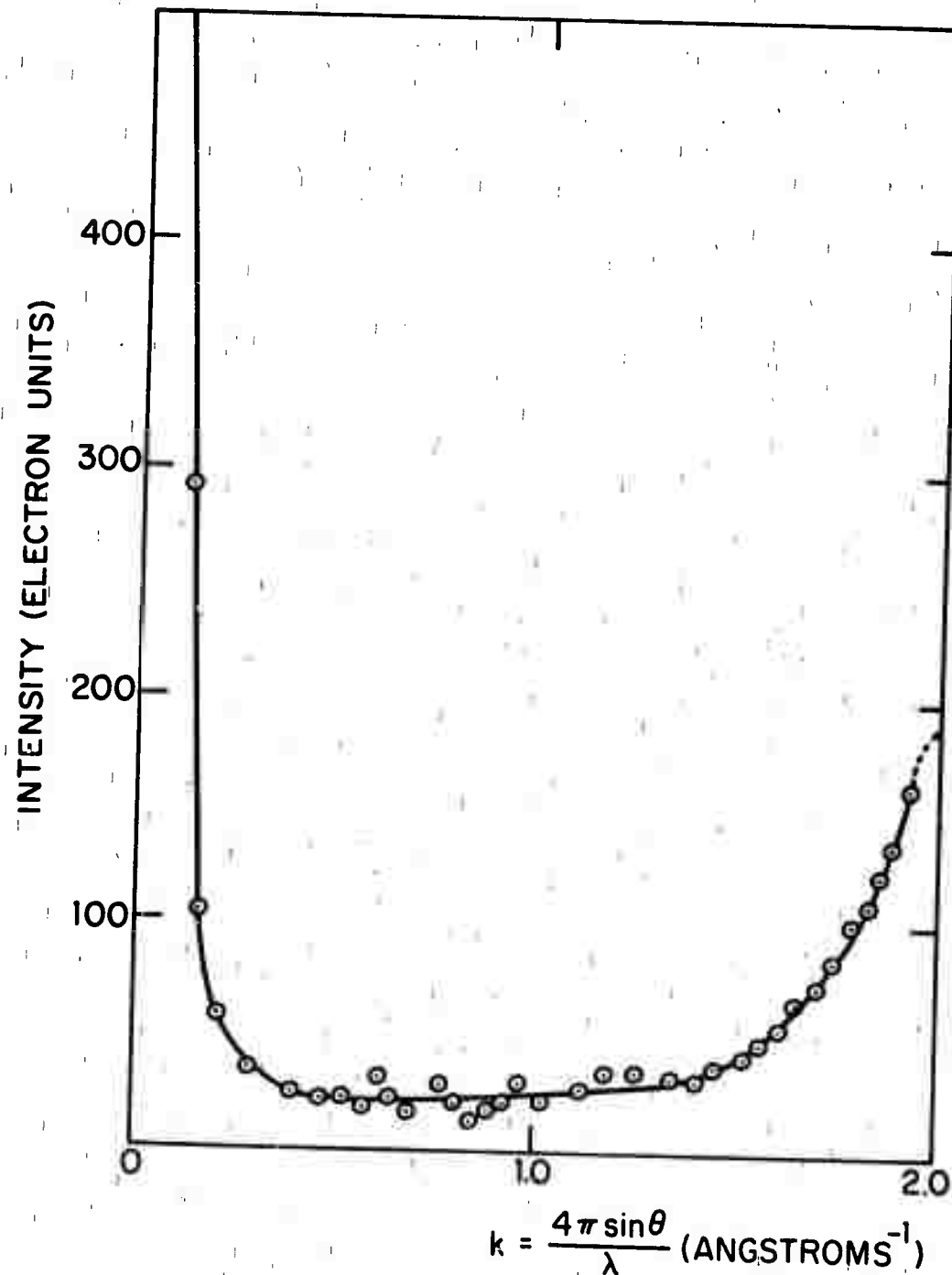
FIG. 6-5   SMALL ANGLE SCATTERING OF
AMORPHOUS EVAPORATED Si.
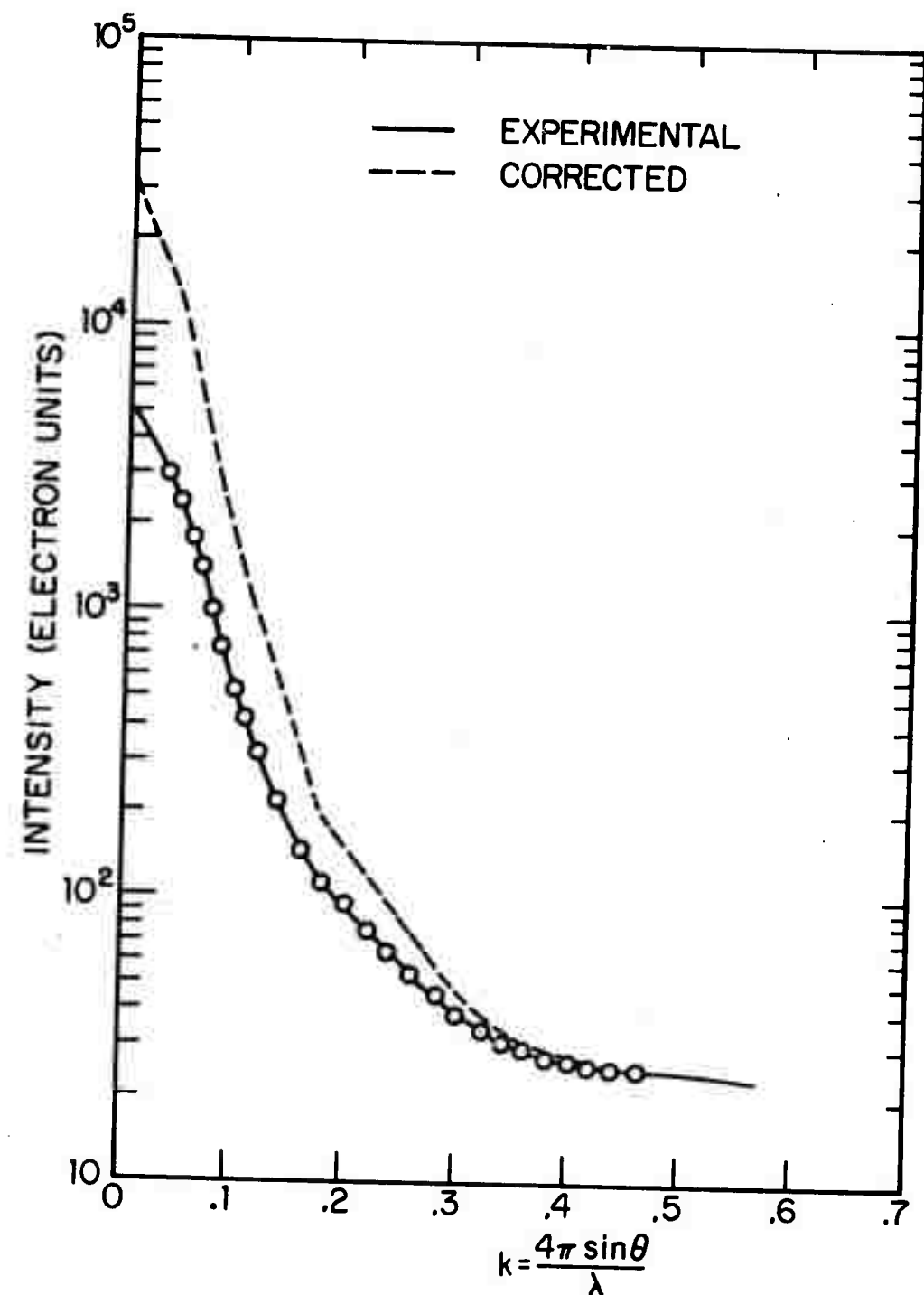
FIG. 6-6 EXPERIMENTAL AND CORRECTED SMALL
ANGLE SCATTERING OF AMORPHOUS
EVAPORATED Si.
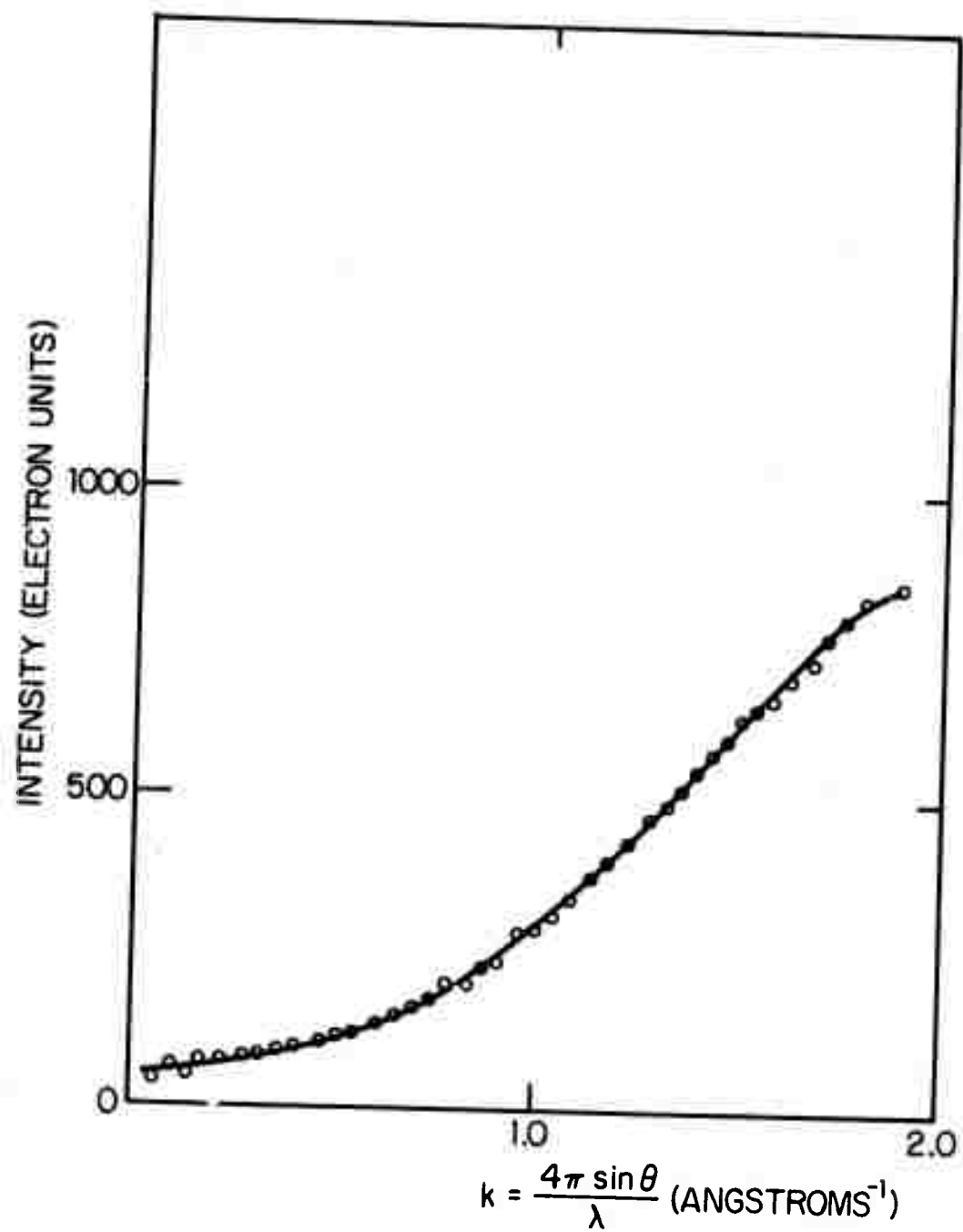
FIG. 6-7 SMALL ANGLE SCATTERING OF AMORPHOUS
EVAPORATED Se
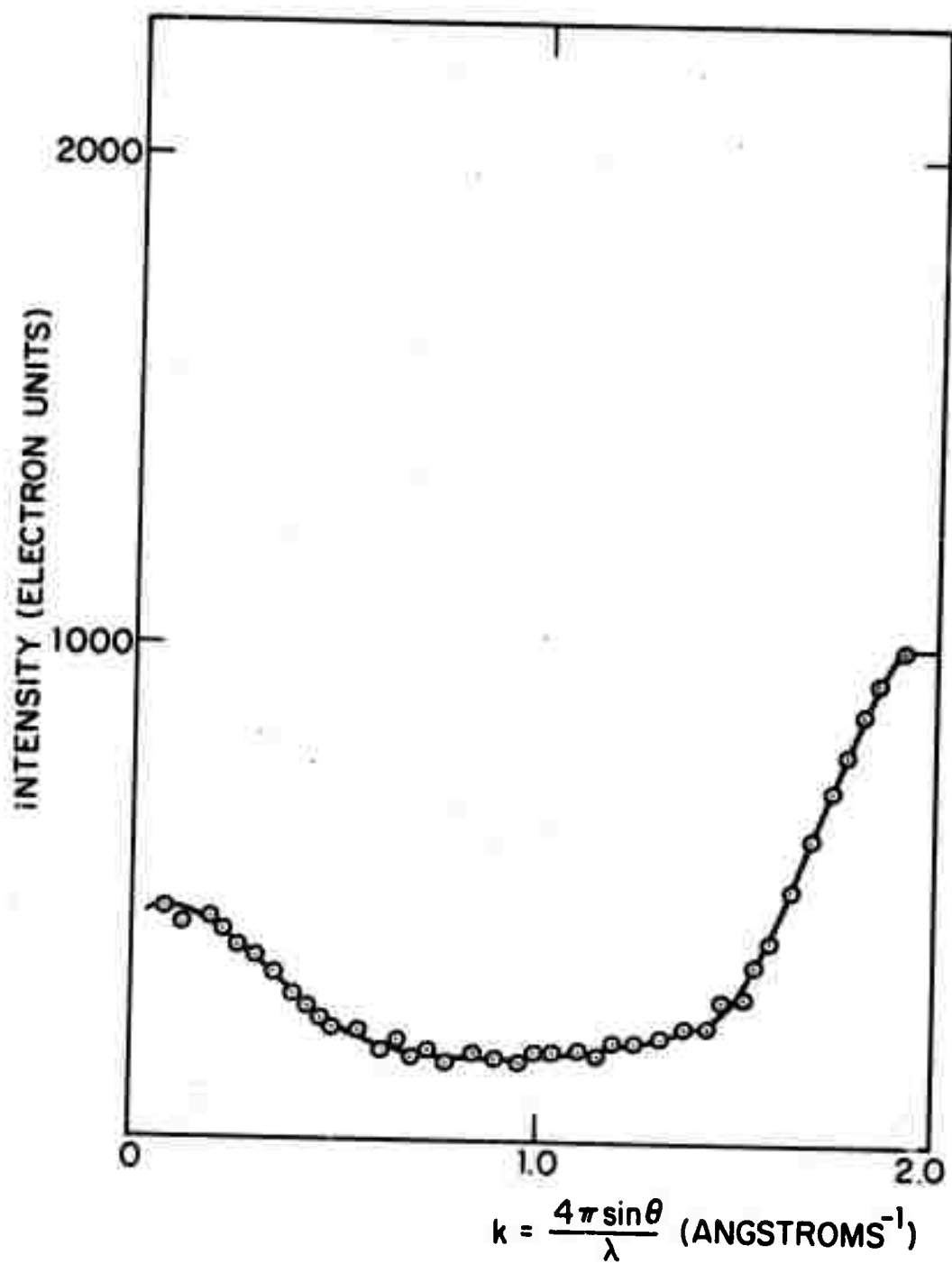
FIG. 6-8   SMALL ANGLE SCATTERING OF
AMORPHOUS SPUTTERED GaAs.
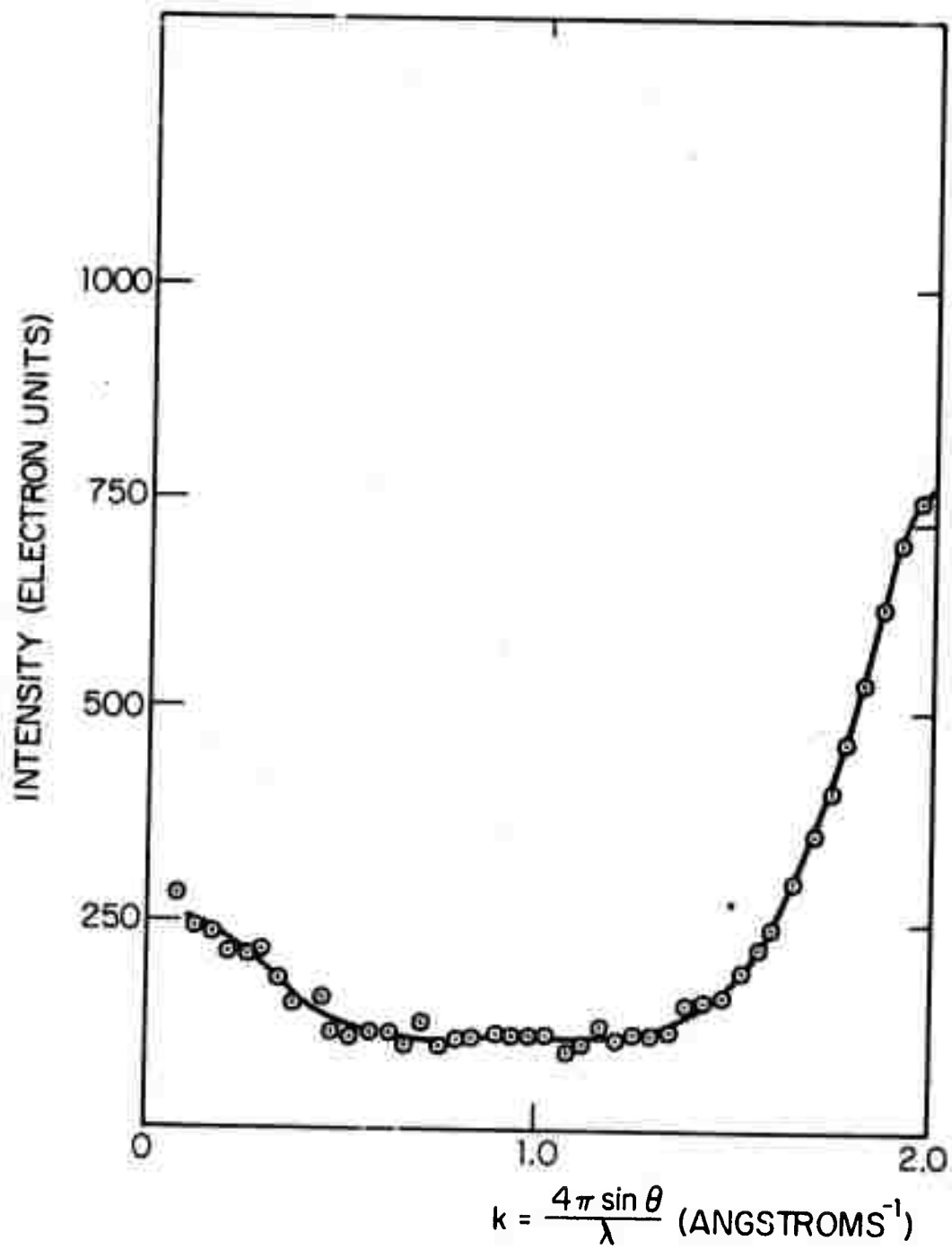
FIG. 6-9   SMALL ANGLE SCATTERING OF AMORPHOUS
SPUTTERED GaP
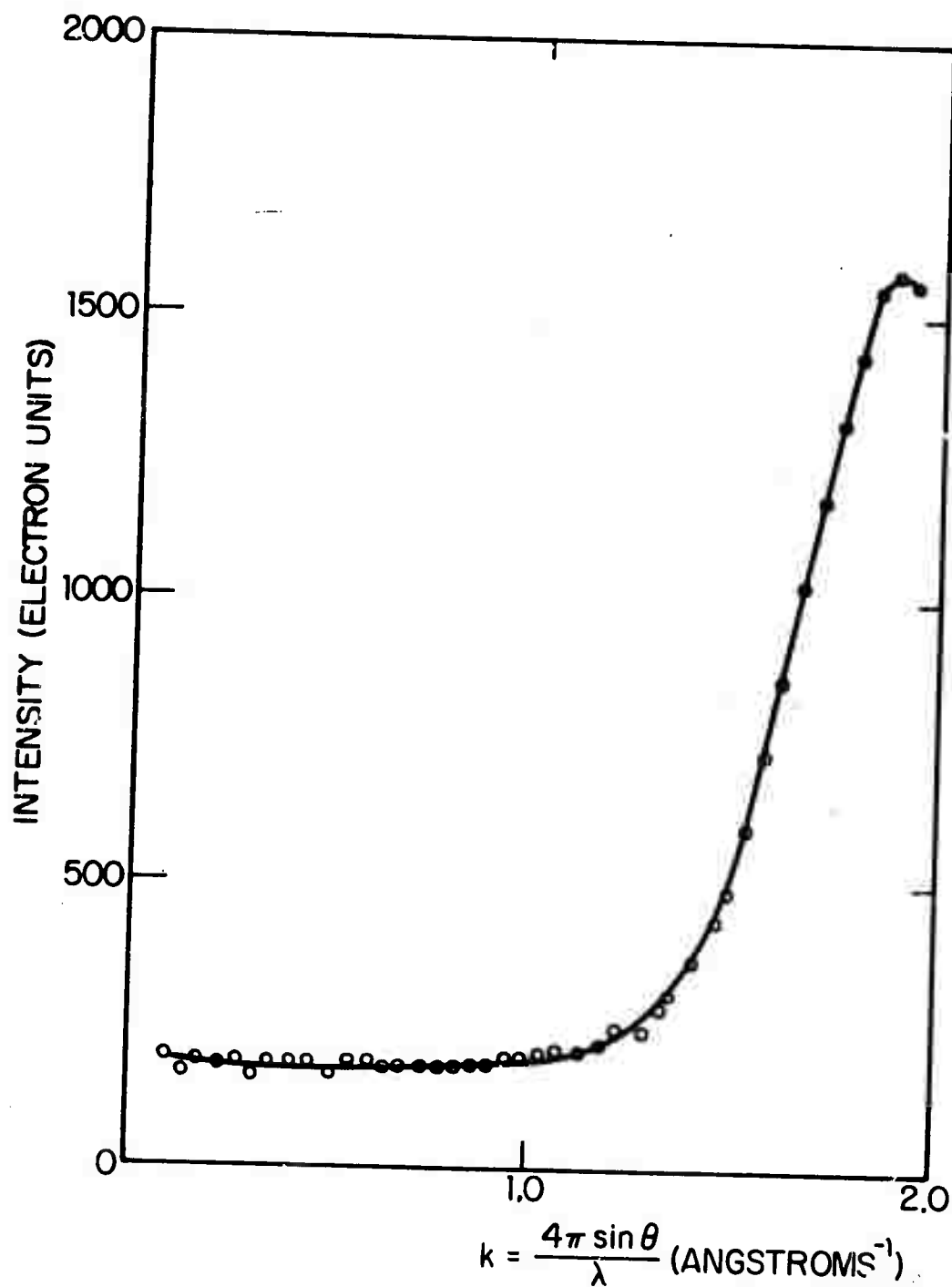
FIG. 6-10   SMALL ANGLE SCATTERING OF AMORPHOUS
SPUTTERED GaSb
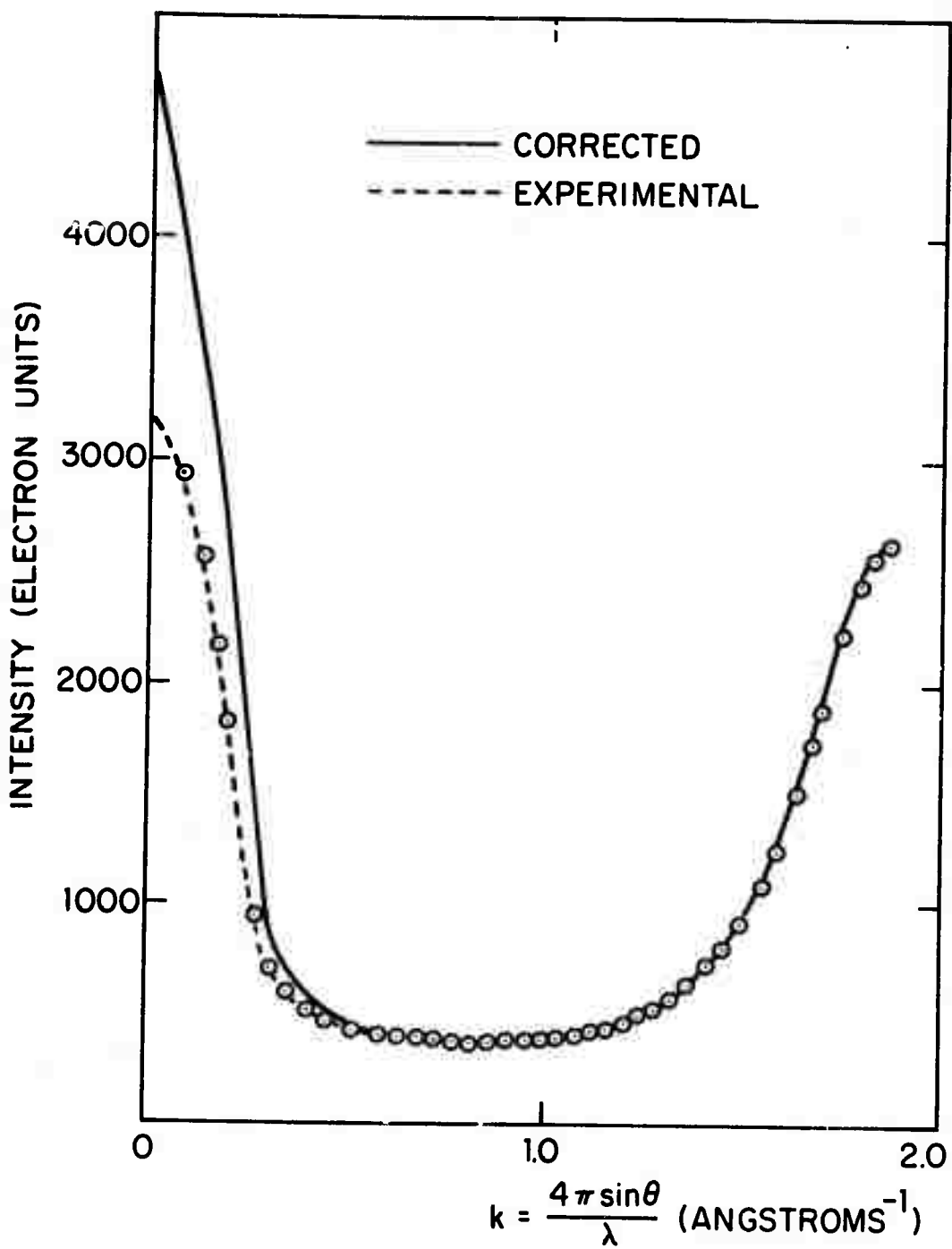
FIG. 6-11   SMALL ANGLE SCATTERING OF
AMORPHOUS SPUTTERED InSb.
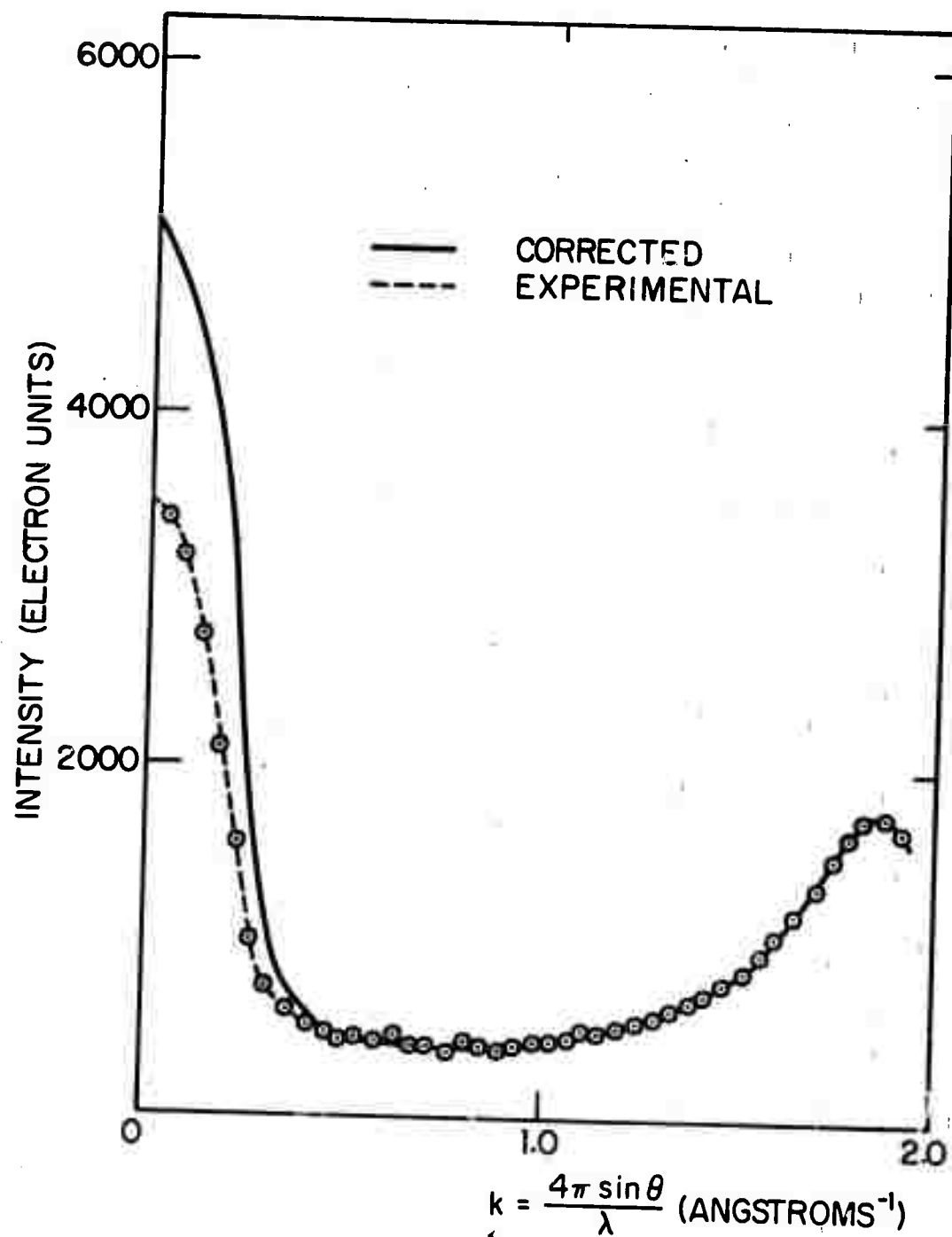
FIG. 6-12 SMALL ANGLE SCATTERING OF AMORPHOUS
SPUTTERED GeSn.
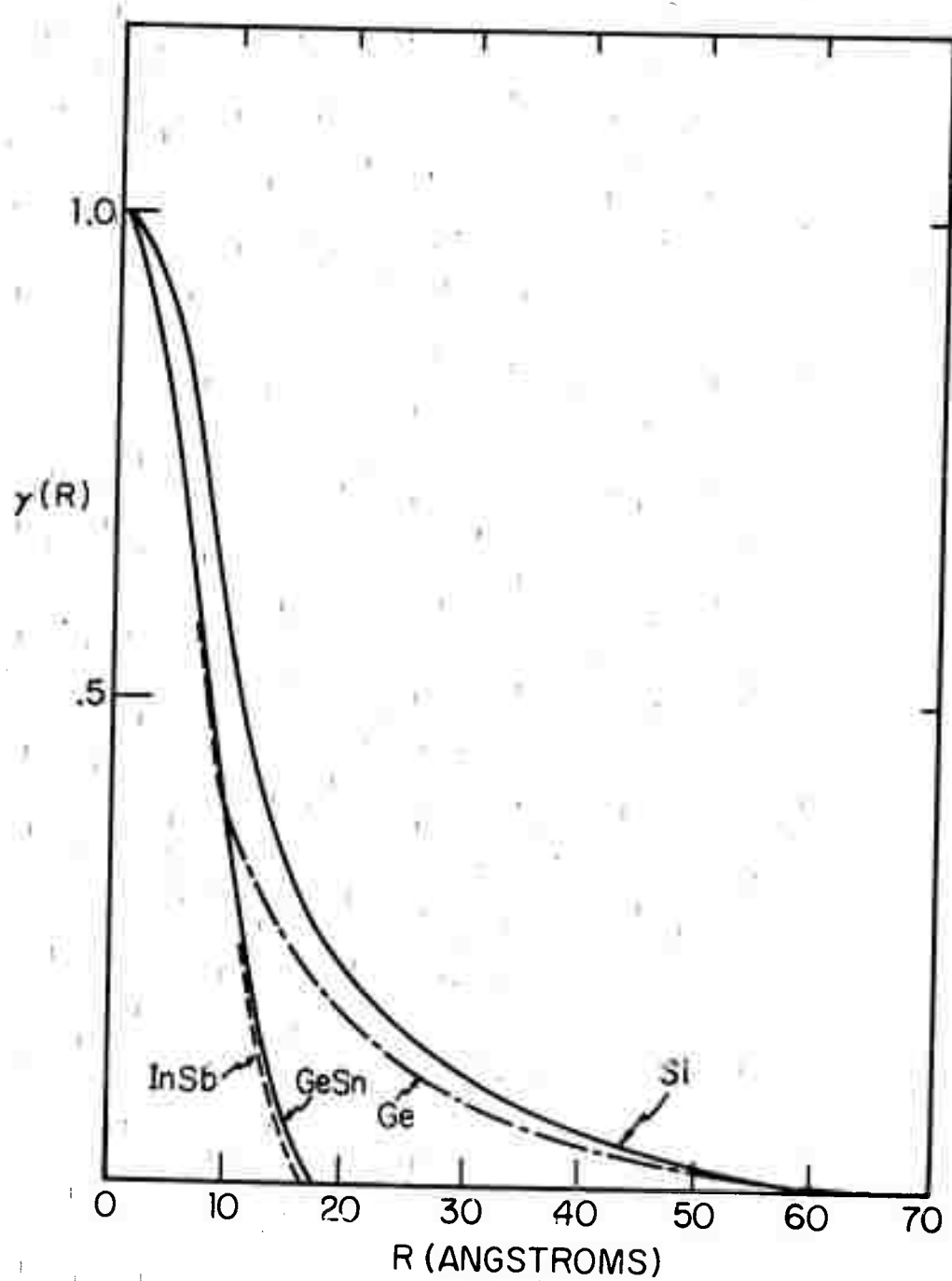
FIG. 6-13 $\gamma(R)$ FOR AMORPHOUS SPUTTERED InSb, GeSn, AND FOR AMORPHOUS EVAPORATED Si AND Ge.
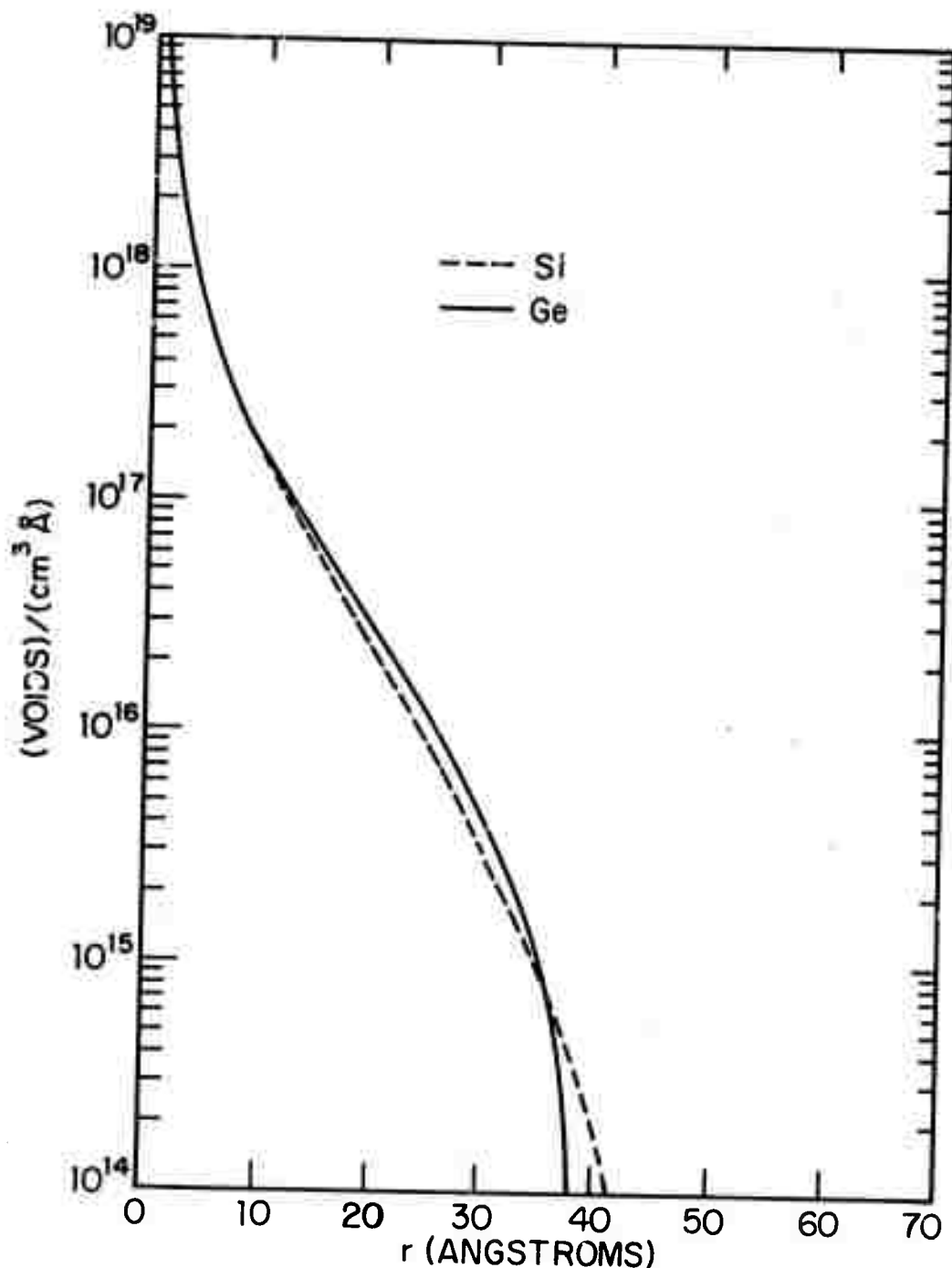
FIG.6-14 VOID RADIUS DISTRIBUTION, N(R), FOR
AMORPHOUS EVAPORATED Ge AND Si.
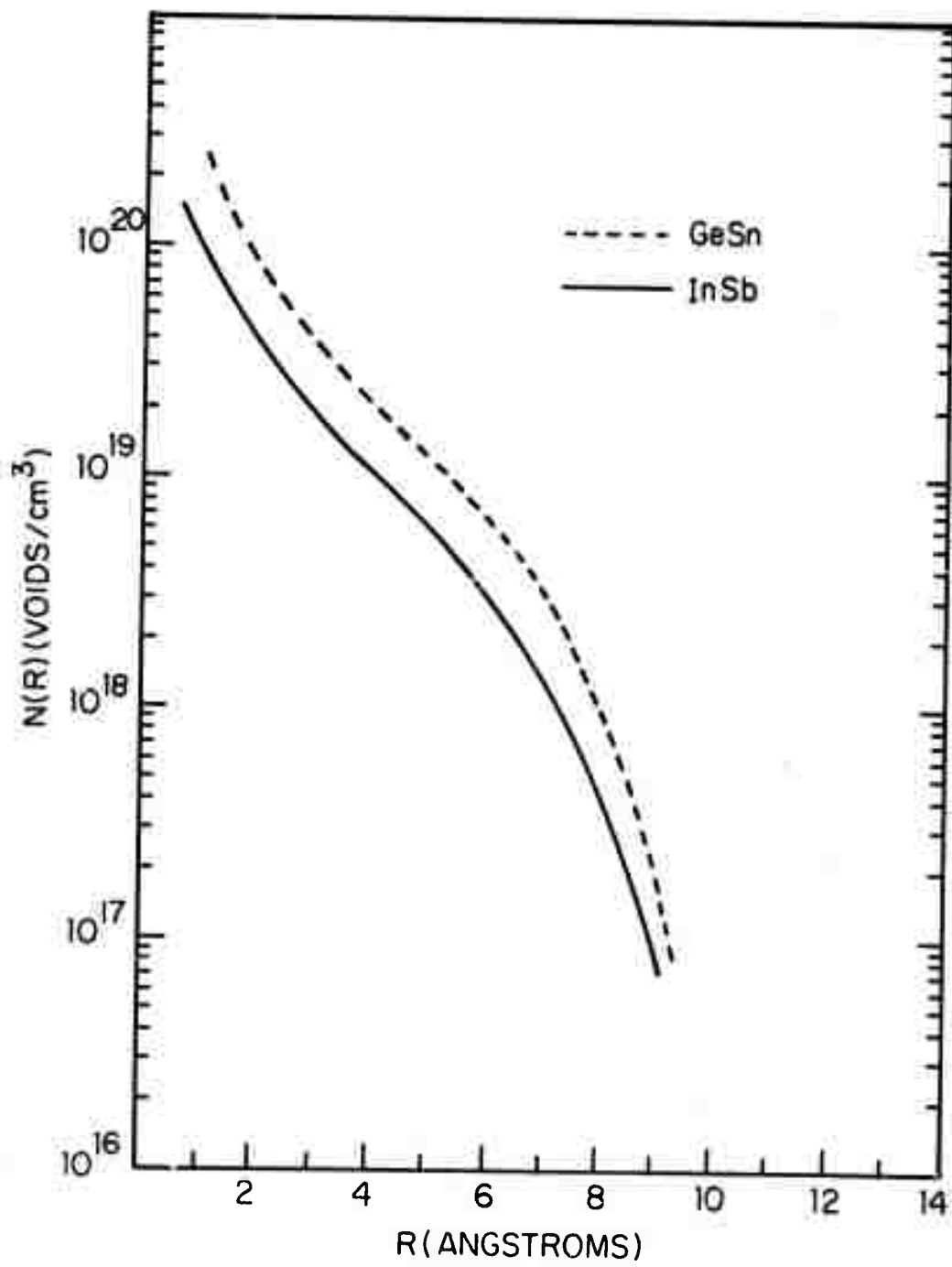
FIG. 6-14b VOID RADIUS DISTRIBUTION, N(R), FOR AMORPHOUS SPUTTERED GeSn AND InSb.
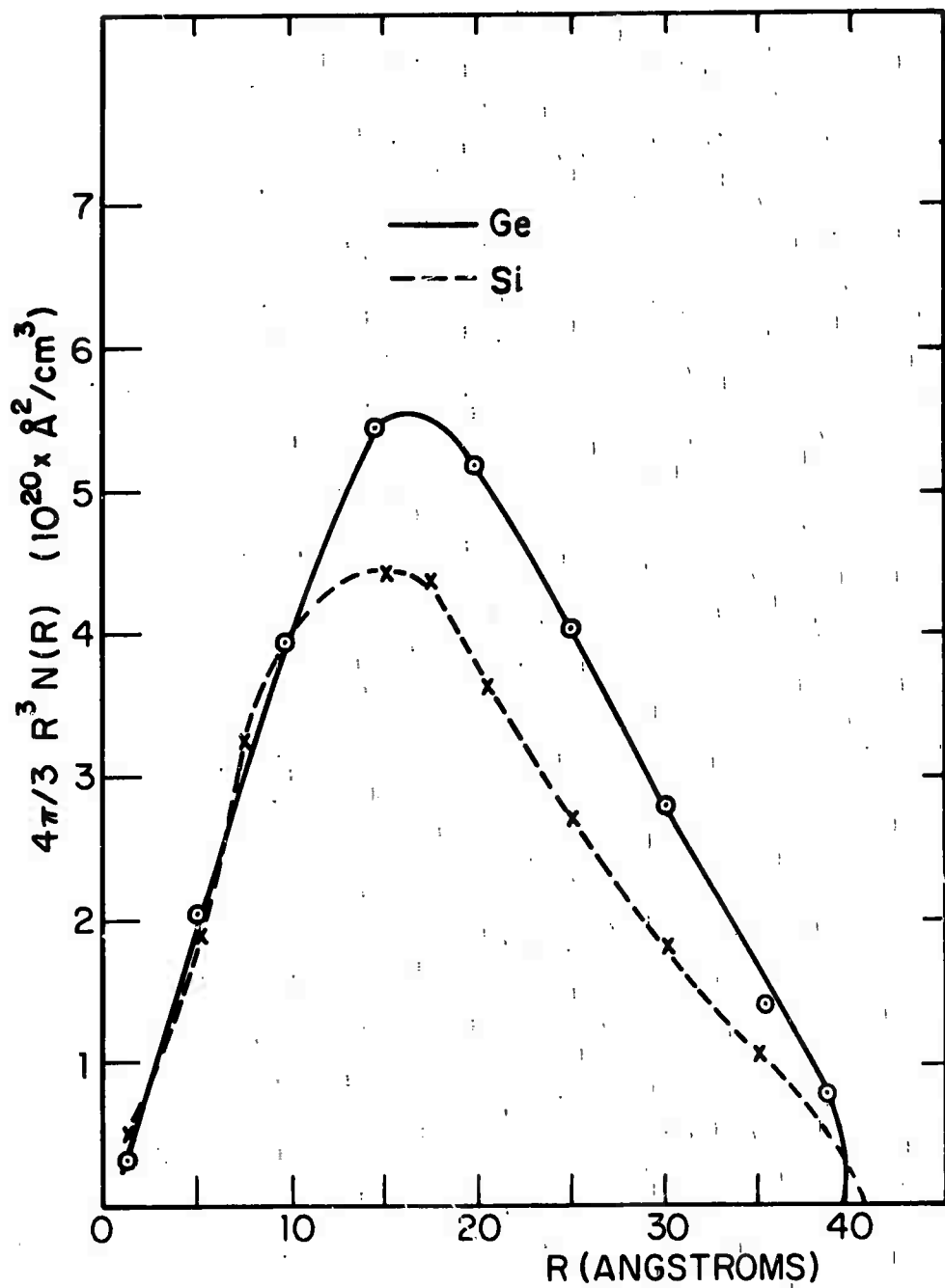
FIG. 6-15 VOLUME DISTRIBUTIONS, $4\pi/3\ R^3 N(R)$, FOR AMORPHOUS EVAPORATED Ge AND Si.
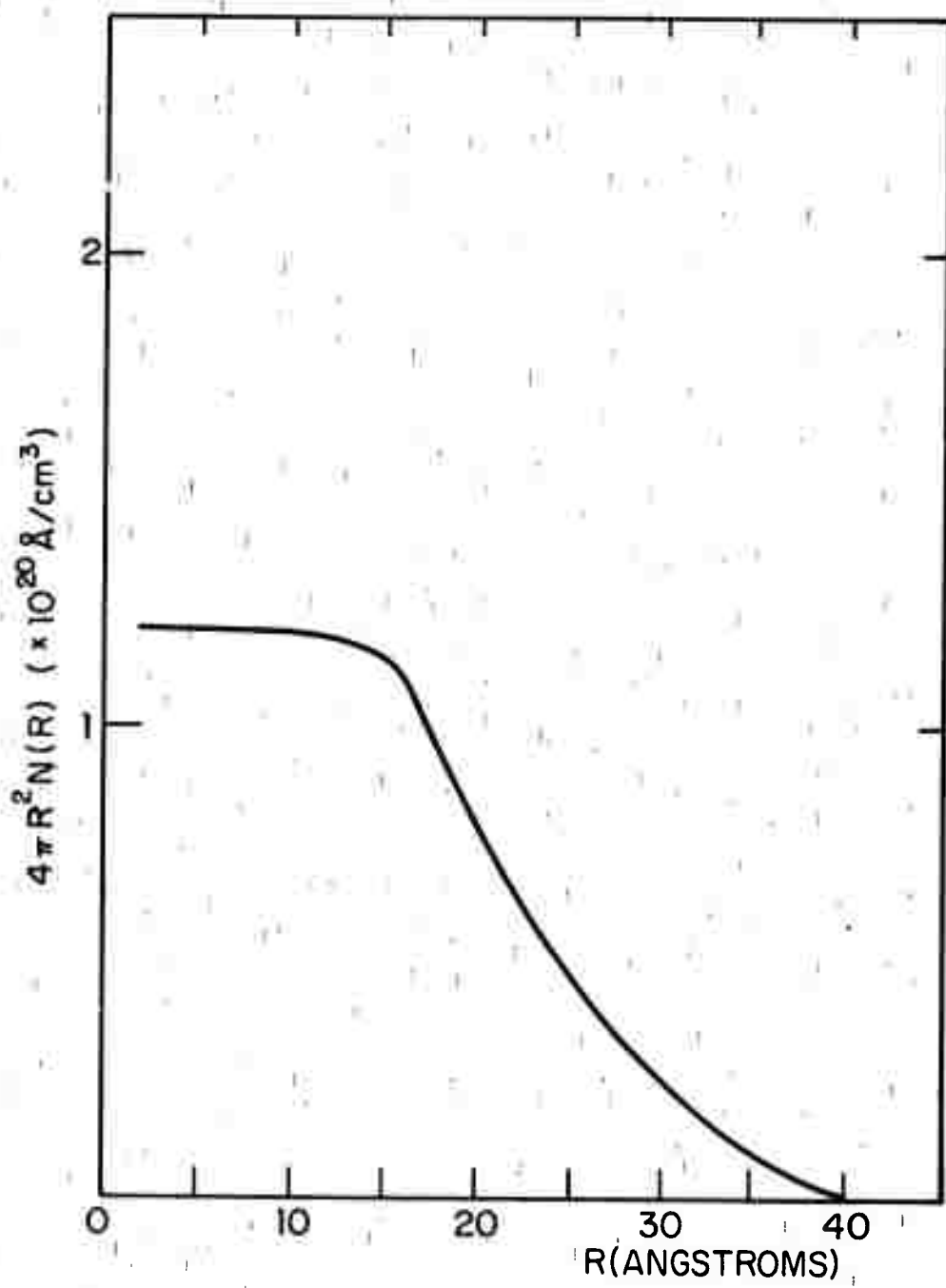
FIG. 6-16 SURFACE AREA DISTRIBUTION, $4\pi R^2 N(R)$, FOR AMORPHOUS EVAPORATED Ge.
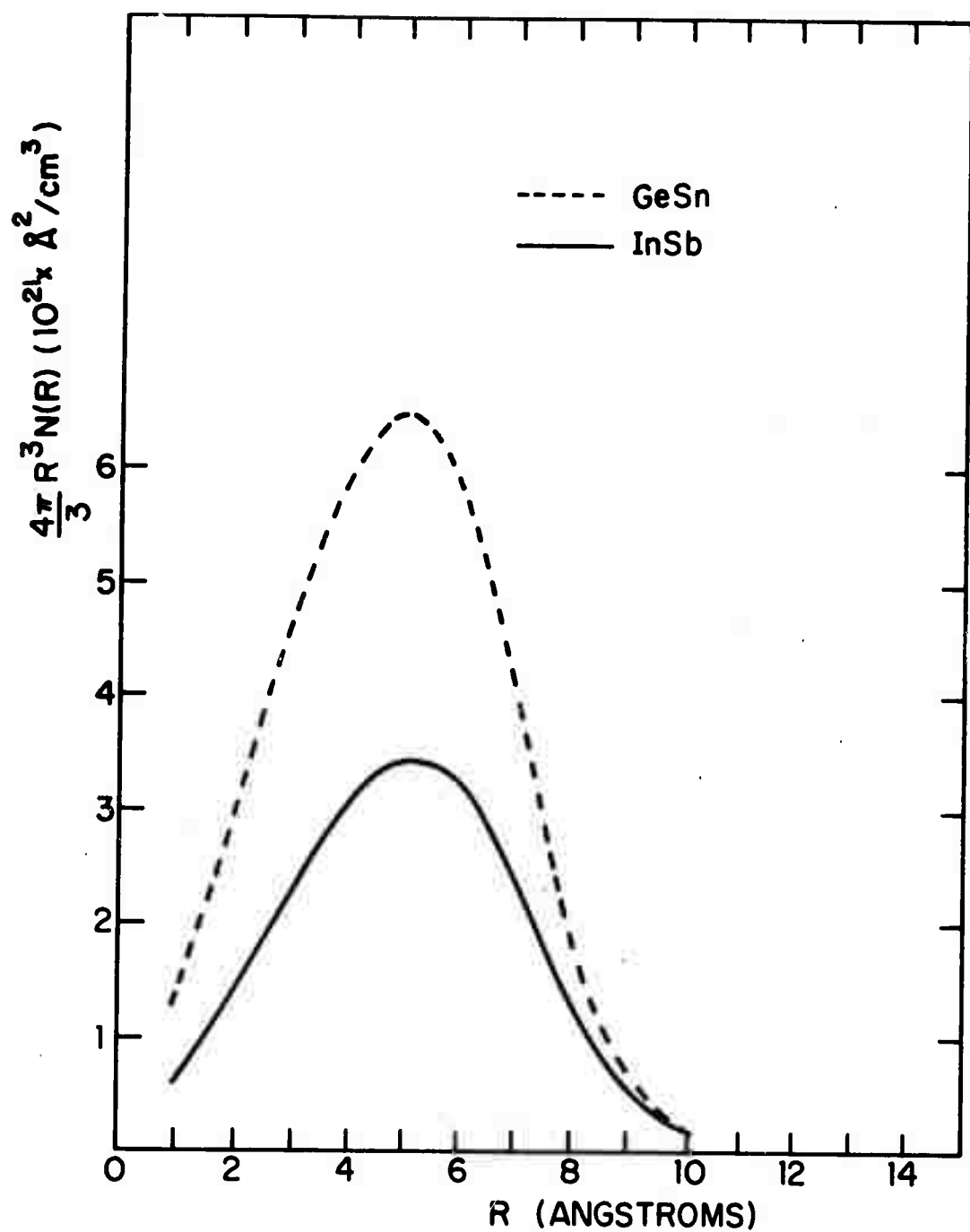
FIG. 6-17 VOLUME DISTRIBUTIONS, $\frac{4\pi}{3}R^3N(R)$, FOR AMORPHOUS SPUTTERED GeSn AND InSb.
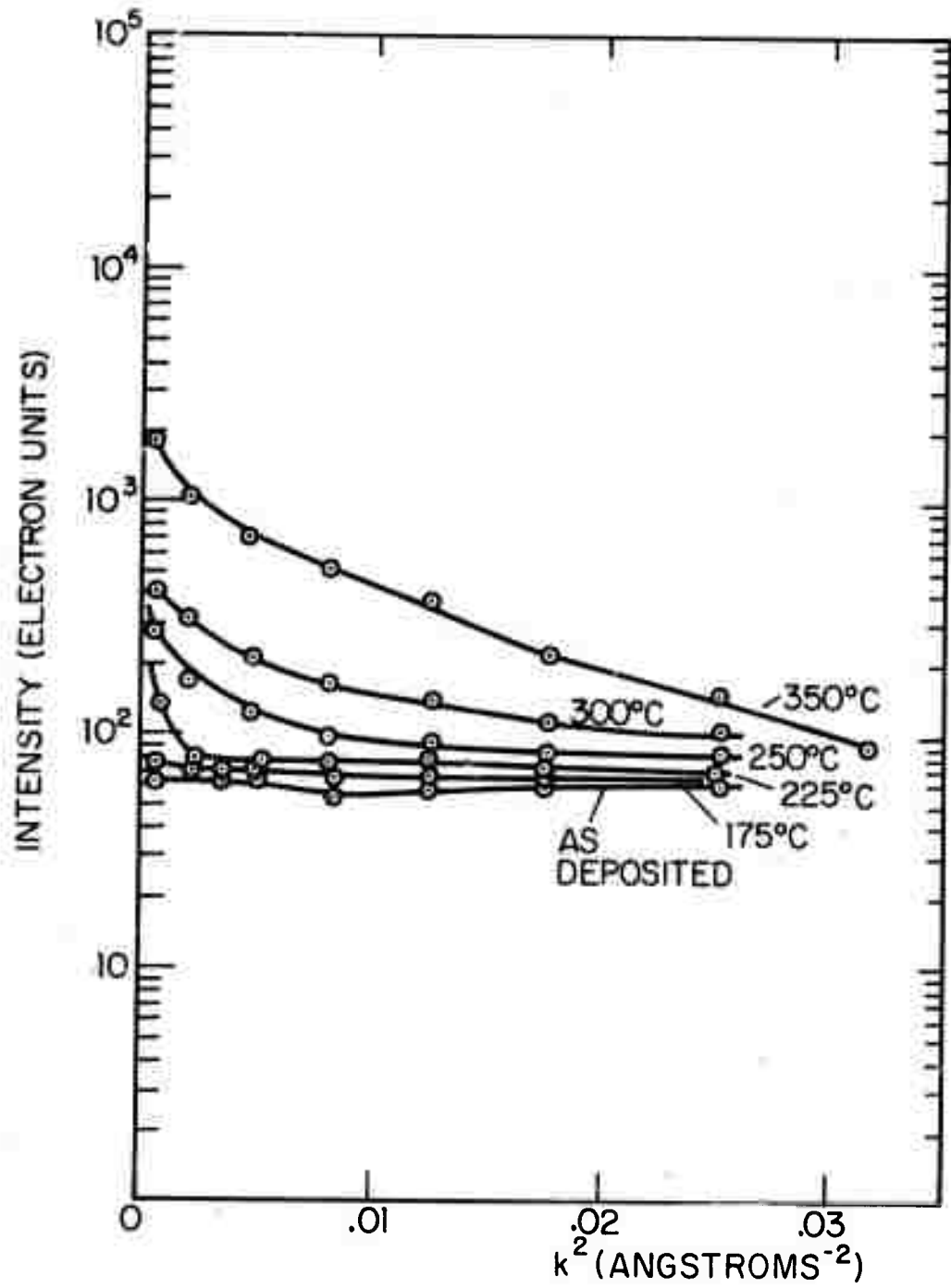
FIG. 6-18a ANNEALING DEPENDENCE OF THE SMALL
ANGLE SCATTERING OF AMORPHOUS
ELECTRODEPOSITED Ge.
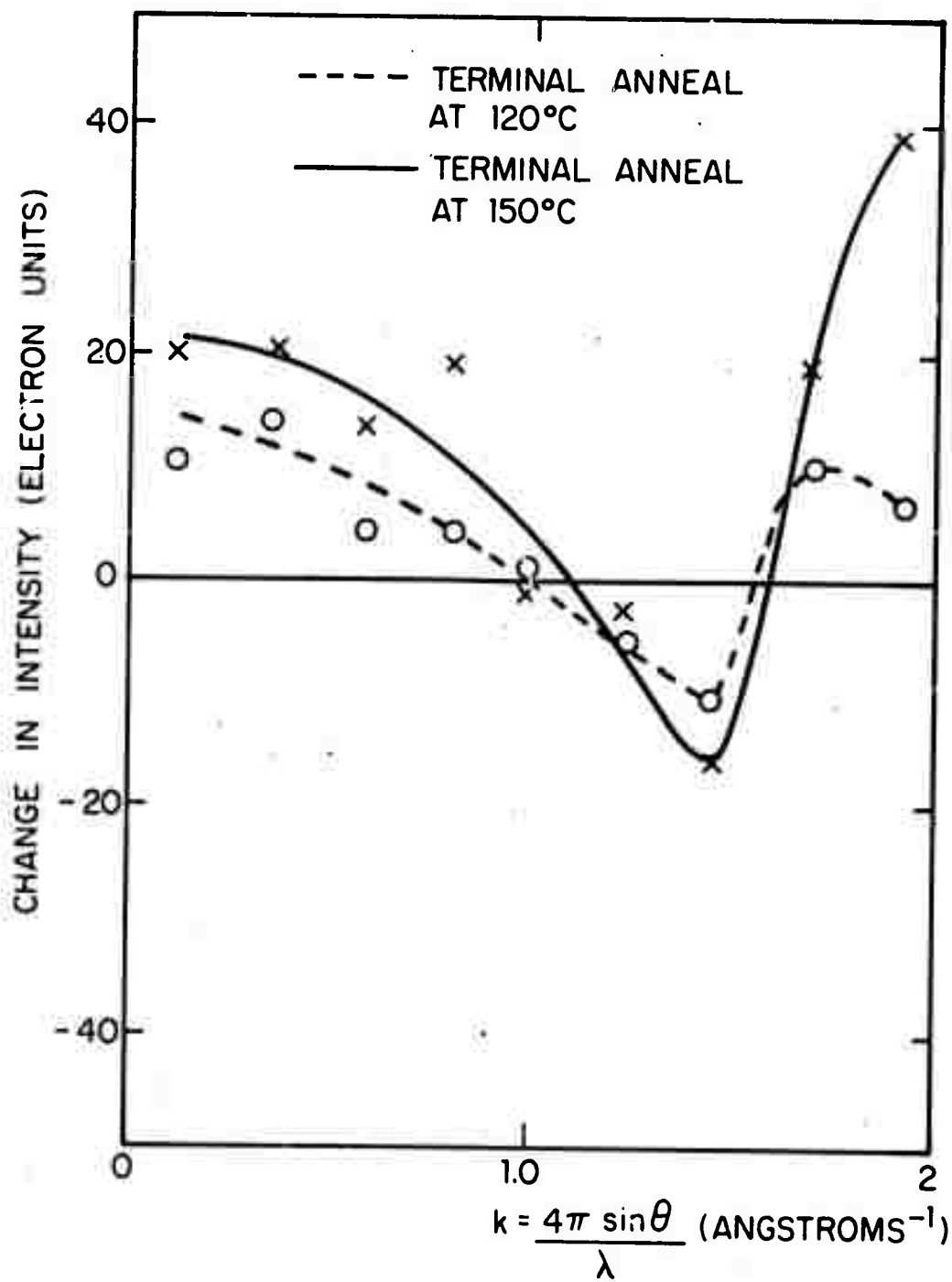
FIG. 6-18b CHANGE IN THE SAS OF ELECTRO-
DEPOSITED GE FOR TERMINAL ANNEALS
AT 120°C AND 150°C.

$$k = \frac{4\pi \sin \theta}{\lambda} \ (ANGSTROMS^{-1})$$
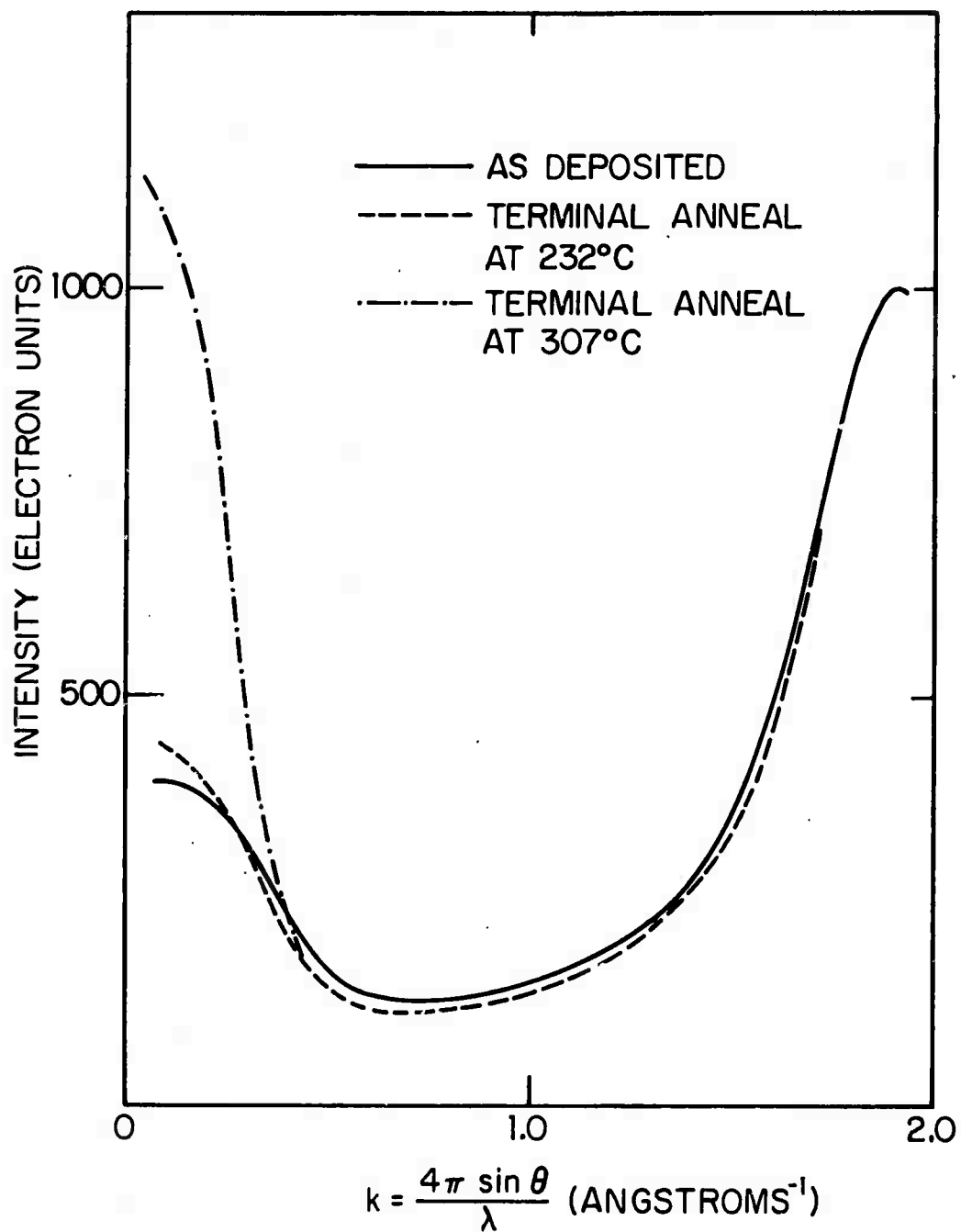
FIG 6-19 SMALL ANGLE SCATTERING OF AMORPHOUS
SPUTTERED Ge As-DEPOSITED AND ANNEALED
TO TERMINATION AT 232°C AND 307°C.
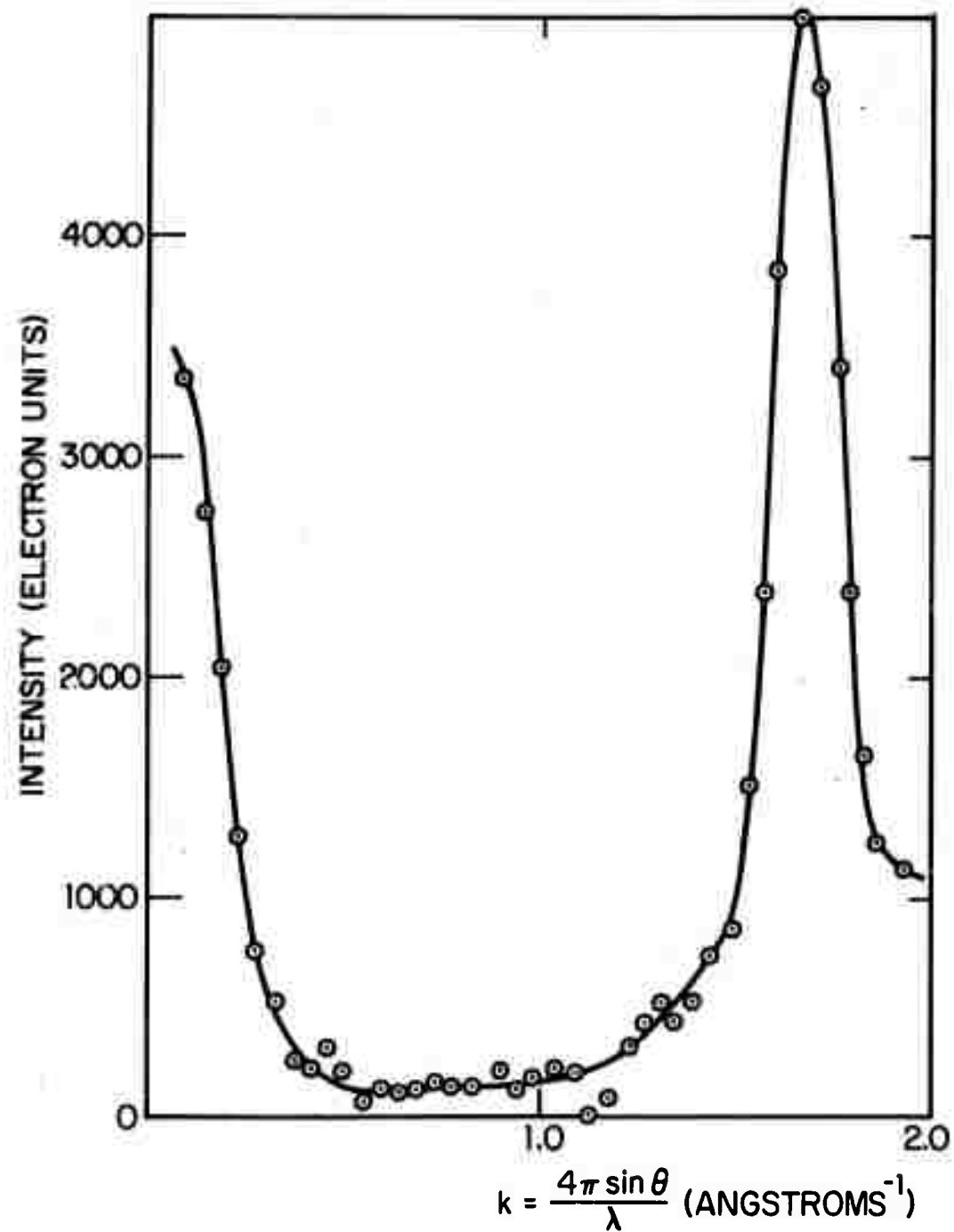
FIG. 6-20 SMALL ANGLE SCATTERING OF AMORPHOUS
SPUTTERED InSb
ANNEALED AT 150°C FOR 3HRS.
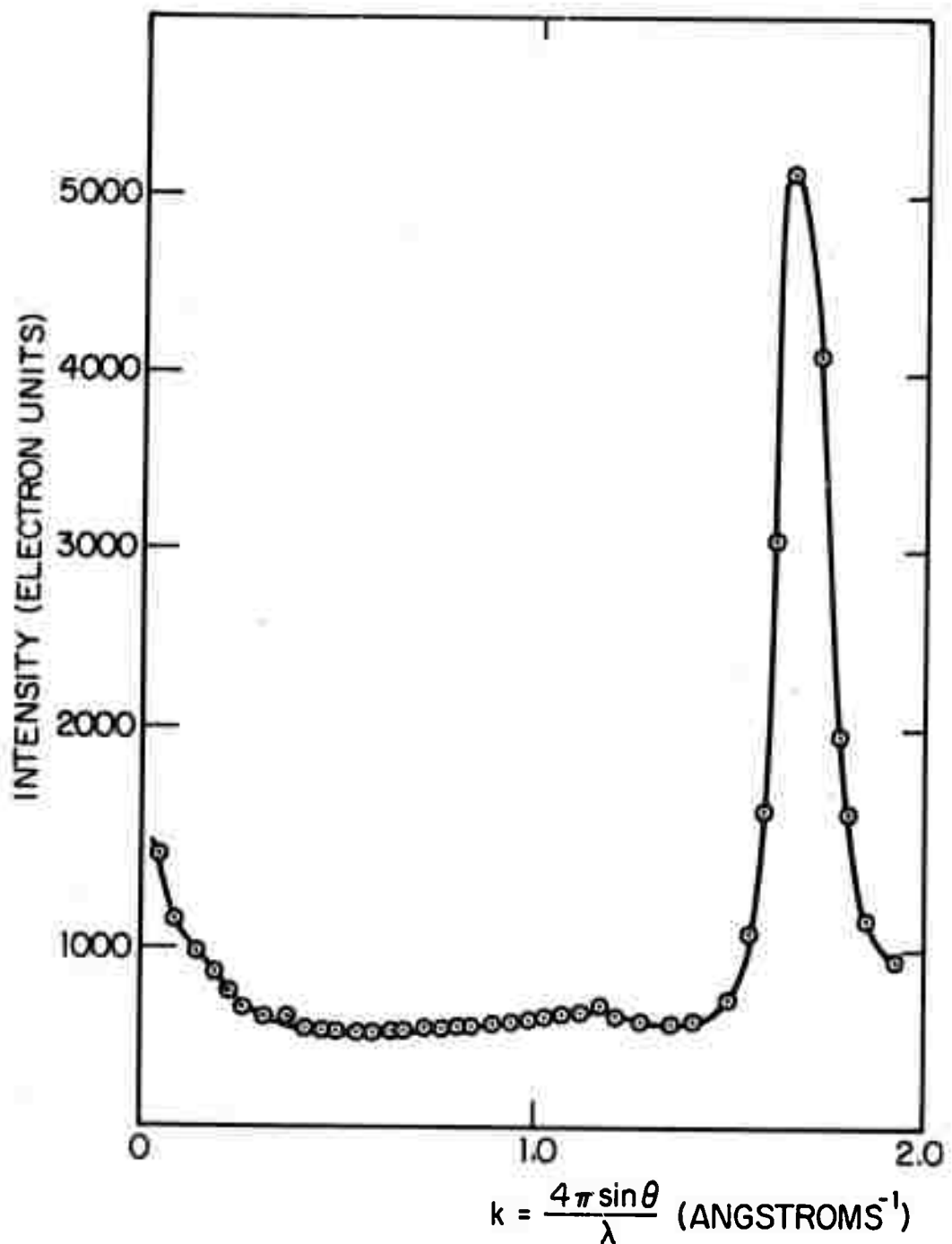
FIG. 6-21 SMALL ANGLE SCATTERING OF A
SPUTTERED FILM MADE FROM A
55% In-45% Sb TARGET.

CHAPTER 7

COMPUTER SIMULATION OF THE DEPOSITION PROCESS

A. Introduction

Structural models are of use in revealing the ring sta-
tistics, dihedral angle distributions, and other short range
correlations which are not revealed directly by the experimental
RDF. The necessary prerequisite of any acceptable structural
model is that its RDF agree with the experimental RDF. There
have been a few attempts to build physical models of amorphous
Ge, but since the accumulation of the statistics necessary to
characterize these models is difficult, none of these models
has been adequately characterized.[1,2]

Since no adequately charaterized model of the structure
of amorphous Ge has yet been presented, this study has been
undertaken to attempt the construction of various models of
amorphous Ge on a digital computer with a procedure that also
to some degree represents the deposition process.

The construction of a structural model on a computer has
significant advantages over the construction with physical
units. For a model constructed on a computer, the atomic
positions lie in the computer's memory so that the statistics
necessary to characterize the structure can be accumulated
with accuracy and little additional effort; however, for a
model constructed with physical units, accumulation of the
same statistics requires considerable additional effort.
Moreover, controlling the parameters governing the construction
of a model is easy on a computer, whereas with a physical

construction, controlling the parameters may be very difficult.

Since several different structures may result for a specific atomic unit, conducting a parameter search with physical building blocks would be a formidable task. The completion of the construction and the characterization of only one structural model may take weeks, whereas with a computer, after the necessary algorithms have been developed, it may take only a few minutes. In all respects we believe the computer constructions to be superior to physical constructions, and out of these computer constructions will come many future results concerning the details of the short range order of amorphous semiconductors. How then do we procede to construct the amorphous Ge structure?

As far as the author knows, the first attempt to build a structure of an amorphous material on a computer was by Kaplow et al..[3] To simulate the structure of amorphous Se, they started with different crystalline clusters of 100 atoms and randomly perturbed the positions of the atoms keeping only those perturbations which improved the fit to the experimental RDF, until an adequate fit was achieved.

There are objections to using this method in building the amorphous Ge structure. This method does not in an way represent the atom by atom build up that actually takes place during the formation of the real amorphous solid. For a cluster containing several hundred atoms, it is virtually impossible to make major adjustments for atoms well inside the cluster without severe bond length distortions. Moreover, the value of

models made with this procedure is diluted since the procedure is essentially a Monte Carlo fitting routine, which is virtually guaranteed success with several disposable atomic positions.

We believe that the structure of amorphous Ge differs considerably from that of crystalline Ge, and hence methods based on perturbations of the crystalline lattice will have difficulties in producing a structure with an RDF that fits the experimental RDF of amorphous Ge in detail. However, Henderson and Herman[4,5] using a similar method have achieved some success in generating a structure on a computer which agrees with the experimental RDF.

Although its peaks are somewhat broader, the RDF generated by Henderson and Herman, as shown in Figure 7-1, does have the rough features of the experimental RDF. In their method, the inital positions of the atoms are taken to be those of the crystal, and each atom is successively displaced randomly by 10% of the interatomic distance about the central position defined by its four nearest neighbors. After each atom has been moved a few hundred times, the structure appears to converge. Unlike the method used by Kaplow et al., all moves are retained, whether or not they improve the fit to the RDF. Physically, the technique simulates the thermal motion found in liquids, and hence, the resulting structure is expected to be much like a frozen tetrahedrally coordinated liquid. In no way can this method represent the deposition process. However, since the basic tetrahedral unit is preserved, it is
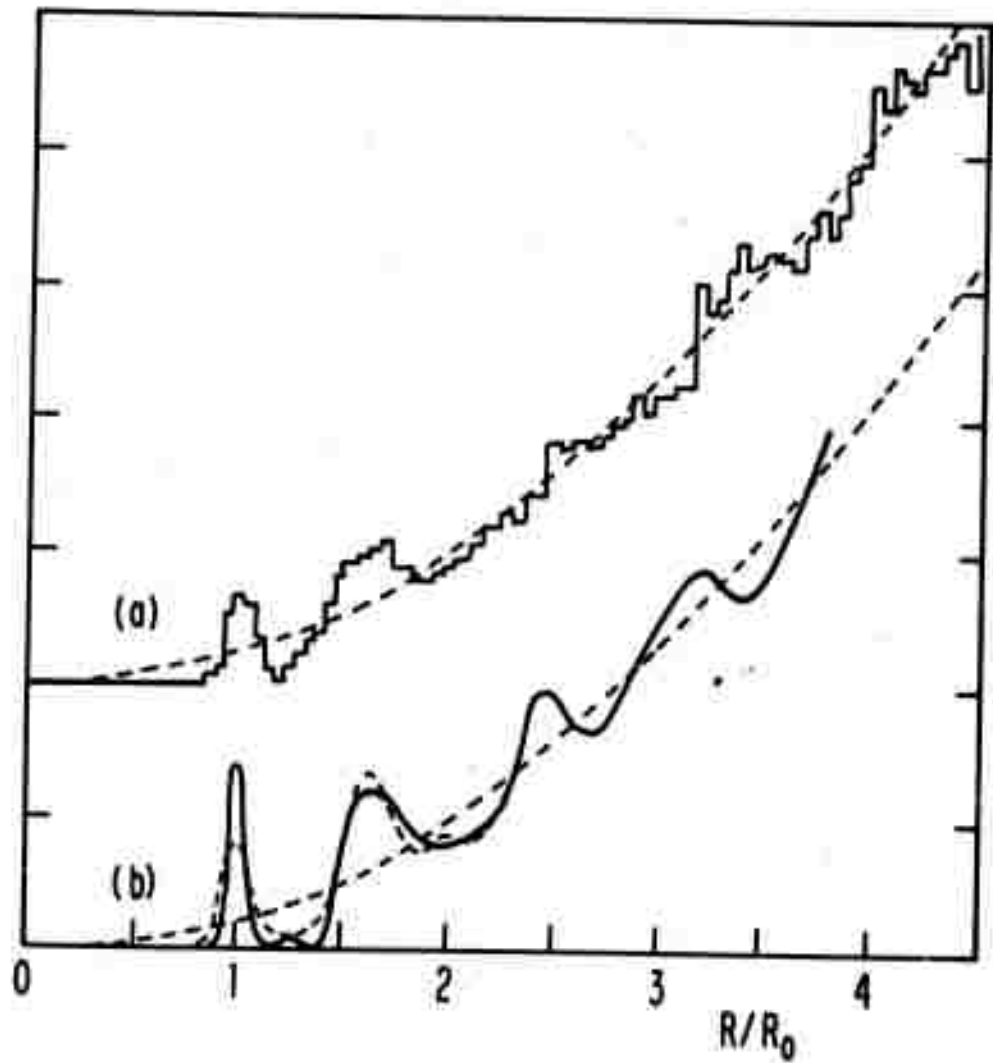
FIG. 7-1 (a) RDF OF COMPUTER GENERATED STRUCTURE BY
              HENDERSON.
          (b) EXPERIMENTAL RDF OF AMORPHOUS Si BY
              MOSS AND GRACZYK AND OF AMORPHOUS Ge
              BY SHEVCHIK AND PAUL

not surprizing that some fit to the experimental RDF has been achieved.

Recently Bennett[6] has successfully generated on a computer structures that are similar to the models of the dense random packed structures built with steel balls by Finney[7]. The RDF of the structure built by Finney has been shown by Cargill[8] to fit accurately the experimental RDF's of amorphous NiP alloys. Bennett[6] has found that such structures are simply generated by sequentially filling the tetrahedral sites available at the surface of the cluster. Since Bennett's method is essentially an atom by atom buildup of the solid, it must to some degree be regarded as representing the actual deposition process at low temperatures for most dense packed amorphous materials.

Another approach that one may suggest is to let an arbitrary initial cluster of atoms relax to an energy minimum via some pairwise interaction potential. However, Weaire[9] has found in his attempts to calculate the shear forces in amorphous alloys having the structures generated by Bennett[6], that the computational time for such a procedure is astronomical, taking about 10 minutes for a cluster of 25 atoms to converge, and even then, the cluster eventually crystallizes. The difficulty with this approach is that for some amorphous solids, the amorphous structure is not the one of lowest energy, and hence methods based on energy minimization of large numbers of atoms will most likely fail.

If it is not the state of lowest energy, what is it that holds the amorphous structure together? We contend that

a strong analogy exists between the amorphous structure and the Roman arch. Obviously, the state of lowest energy for the arch is a pile of rocks lying on the ground; it is the geometry of the arch that locks each building block into its position, thereby stabilizing it to all fluctuations short of earthquake proportions. Similarly, it it the geometry of the amorphous structure that holds it in place, and hence, a method of building the amorphous Ge structure based on geometrical considerations is the most logical procedure to adopt.

B. Description of the deposition simulation

1. Basic assumption and considerations

First we consider the size of the model cluster. Since the experimental RDF exhibits structure out to about 10 $\overset{o}{A}$, a model RDF should extend at least this far. To acquire good statistics for the model cluster, the cluster should be as large as possible. However, since computer time and memory are limited, we must work with a cluster of a rather small size. We choose a cluster of 1000 atoms as the optimum size for this investigation, since we expect this number of atoms to produce a cluster 20 $\overset{o}{A}$ in radius, thus allowing the model RDF to be extended to about r = 10 $\overset{o}{A}$ with fair statistics.

In the remainder of this section we will describe the details of the simulation of the model deposition process. First we specify a set of rules that governs the behavior of an ad-atom on the surface in becoming a part of the cluster, build up the cluster by adding atoms one at a time, calculate the resulting RDF of the cluster, and finally, see how well the

                     with
RDF agrees /the experimental RDF's of amorphous Ge that have
been presented in Chapter 5. Before describing in detail
the method of construction, let us discuss the basic approx-
mation needed to simplify the problem.

     The basic approximation used will henceforth be referred
to as the "one atom approximation". In this approximation,
only the adatom, the atom being placed on the cluster, is
moved and all other atoms in the cluster are held fixed.
Once the adatom is successfully positioned, its position too
becomes final so that it can provide additional sites for on-
coming adatoms. In a real solid, placing an additional atom
on the cluster certainly involves some relaxations of the
neighboring atoms; however, if we were to include these relax-
ations, the computational time would rise enormously making
such an endeavor impracticable. We believe, nevertheless,
that the one atom approximation will serve to allow the gen-
eration of a structure that describes the gross features of
the experimental RDF, and that the incorporation of many atom
relaxations would be just a small refinement on the model.
Besides, the inclusion of too many atom rearrangements would
defeat our purpose of generating an amorphous structure since
it might lead to crystallization. The deposition process of
the real solid can pack a structure more efficiently than can
be done here, thus, we expect our model to give only a reason-
able upper bound on quantities such as the number of broken
bonds, the bond angle distortions, and the density.

     Two schemes have been used in simulating the deposition

process. The first method, which will be referred to as Scheme I, was a preliminary attempt to simulate the deposition process, but it is still presented here because it has produced a rather interesting variety of structures. In Scheme I, both the position of the adatom and the equilibrium direction of the adatom's bonds become fixed as soon as the adatom becomes a part of the cluster. The second method, which will be referred to as Scheme II, is much more sophisticated, has fewer constraints, and more realistically represents the deposition process than does Scheme I. In Scheme II the position of the adatom becomes fixed as soon as it becomes a part of the cluster also, but the directions of the equilibrium bonds of the adatom do not become fully specified until the adatom has completed two bonds. We believe that this Scheme II very closely approximated the logic used by Polk[1] in constructing his model, and hence, should produce a structure similar to that of Polk's model.

2. The surface sites

We expect the adatom to find on the surface single, double, and triple sites in which it is able to satisfy one, two, and three bonds respectively. The act of satisfying the bonding of a single double, or triple site, we shall call a single, double, and triple joining respectively. The numbers of each type of sites on the surface can not be determined a priori, but are among the more important mnumbers to be determined in this simulation.

The criterion that we choose in determining which of the possible sites the adatom will satisfy, is to allow it to first attempt that site which will satisfy the greatest number of bonds, subject to the constraints to be specified in the next section. This is equivalent to allowing the adatom to minimize its energy. In the real deposition process, however, the adatom may not always be able to minimize its energy since kinetic factors may prevent it from finding the state of lowest energy. We believe that energy minimization extended over several atoms may lead to crystallization, but as long as we limit energy minimization to only one atom at a time, we have little possibility that the structure will crystallize.

3. Bonding criteria

It is necessary to establish the criteria which determines whether an adatom is successfully or unsuccessfully positioned on the cluster. But in order to do this, it is first necessary to specify the properties of the model atoms. We take our atom to be a hard sphere having the crystalline diameter of 2.45 $\mathring{R}$ and slightly flexible tetrahedral bonds.

An adatom is successfully positioned if the following criteria are satisfied:

(1) All of its bonds with surface atoms must have length 2.45 $\mathring{R}$.

(2) The adatom can have no other neighbors at a separation from $r = 2.5$ to $r = 3.2$ $\mathring{R}$.

3) All atoms participating in bonds with the adatom must

have upon completion of these bonds 4 or fewer near-
est neighbors.

These three conditions have been made by taking into ac-
count the experimental RDF of amorphous Ge. The observed
sharpness of the first peak in the experimental RDF justifies
the use of the hard sphere approximation (see chapter 5).
The second condition is imposed since there are no atomic
distances observed on the experimental RDF in the region
$r = 2.5$ to $r = 3.2 \text{ Å}$. This condition also automatically
limits all bond angle distortions to a maximum of 30°. The
third condition is imposed since the experimental RDF's show
 that the average coordination number is very close to four.
Although the experimental RDF's have not established that the
coordination number is four for each atom, this is probably
true. However, in some cases we expect the local geometry may
be such that an atom cannot be placed so as to satisfy a bond
without violating the above conditions. In this case, the
bond is left uncompleted, or "dangling". We can therefore
never expect to find in this model a coordination number
greater than 4, but occasionally we may find coordination numbers
less than 4.

4. The initial cluster

To start the atom by atom build up of the cluster, it is first necessary to generate an initial amorphous seed since initially there are insufficient atoms in place to produce double and triple sites. The seed is generated by placing a single atom at the origin. The four bonds of this atom are distorted within a 20° solid angle about their corresponding undistorted bonding directions. Atoms are added to each of these four bonds, and the unsatisfied bonds of these atoms are then likewise distorted. Additional atoms are added to the unfilled bonds of this 5 atom cluster until a seed of 15 atoms is generated. Once the seed is generated, the atoms are then positioned in slightly different ways, in both Schemes I and II.

The seed cluster was deliberately chosen to be small to keep its effect on the structure of the cluster minimal. Early work showed that the resulting structure for Scheme I clusters was insensitive to the details of the initial seed, provided that its bonds were distorted by 20°. When a crystalline seed cluster was used, however, the crystalline structure resulted. No detailed investigation of the amount of distortion in the amorphous seed needed to generate the amorphous structure was made.

5. Scheme I.

In this scheme, the adatom attempts to satisfy double sites (double joining) and to satisfy single sites (single joining) and as soon as the adatom is positioned, the directions of its equilibrium bonds are specified. To do this it is necessary to specify the dihedral angle, ϕ , between the equilibrium bonding directions of the parent atom and of the adatom, as shown in Figure 7-2 for two atoms in the staggered and eclipsed configurations

In Scheme I, the adatom, at first disregarding the bonding criteria, joins to an unsatisfied bond belonging to an atom on the surface of the cluster. The surface atom to which it initially bonds will henceforth be referred to as the parent atom. The adatom, after finding the nearest atom that is not attached to the parent atom, attempts to bond with this nearest neighbor atom also, by bending both the bond that it makes with the parent atom and the nearest neighbor atom.

If the adatom cannot successfully bond with a neighboring atom, it attempts the position associated with the equilibrium parent bond, and if still unsuccessful, it twice attempts the position associated with parent bonds that have been randomly distorted within a 20° solid angle about their equilibrium directions. Although there may be an adequate single bond configuration existing, the adatom may not find it since the searching routine is incomplete. Also, which of the bonding criteria caused the attempt to fail is not recorded, although such knowledge may have helped improve the efficiency of the
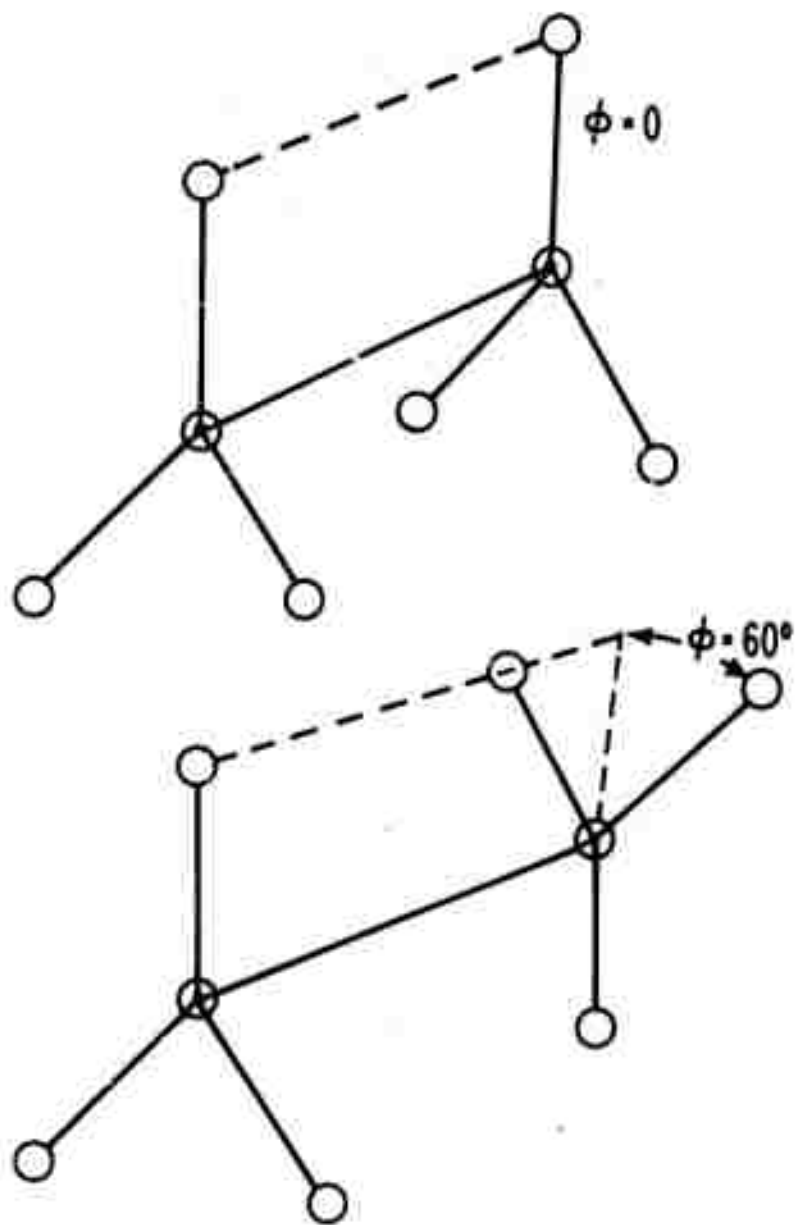
FIG. 7-2   THE ECLIPSED (TOP) AND THE STAGGERED (BOTTOM)
          CONFIGURATIONS.

SCALE |——————| 10Å
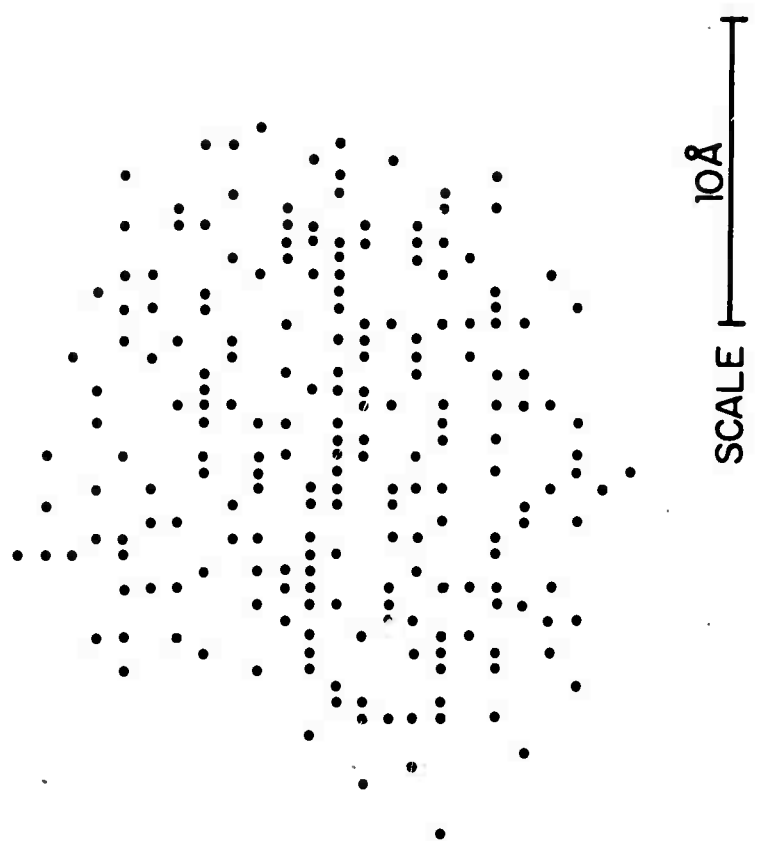
FIG. 7-3(a) CLUSTER OF 250 ATOMS
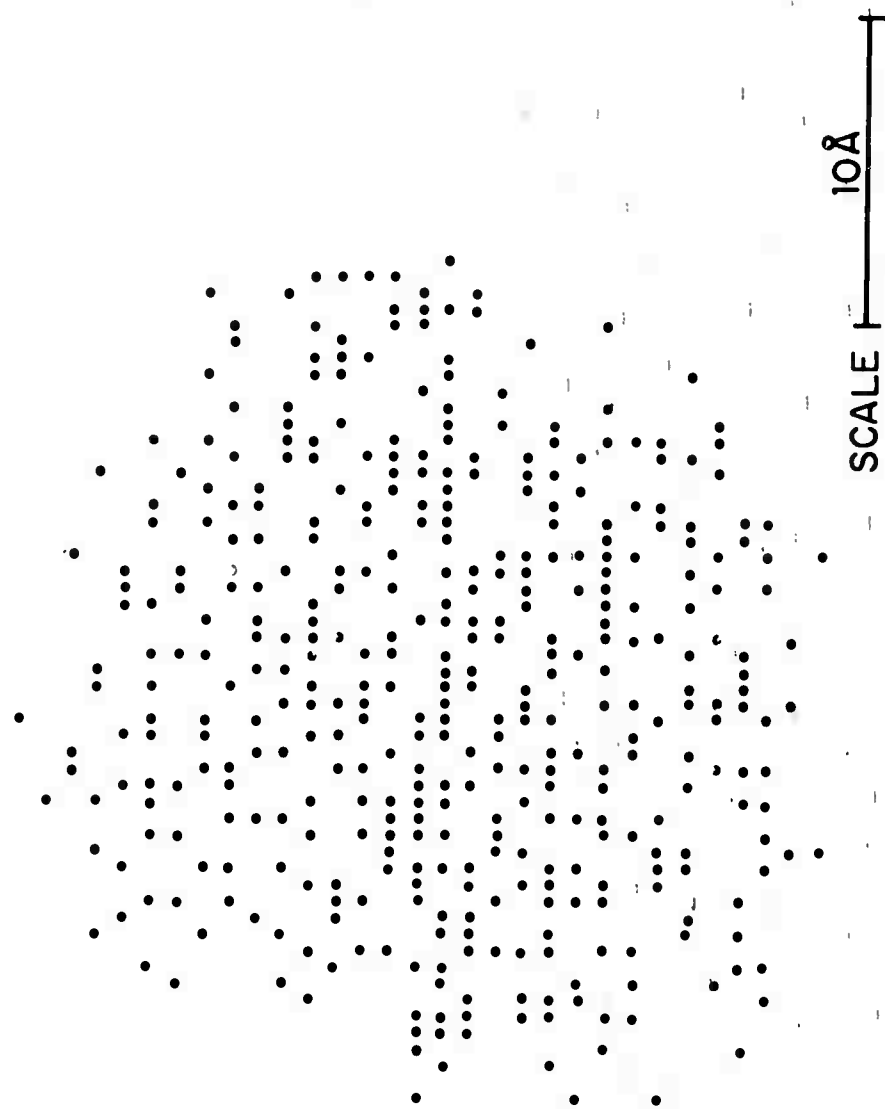
FIG. 7-3 (b) CLUSTER OF 500 ATOMS

SCALE ⊢————⊣ 10 Å
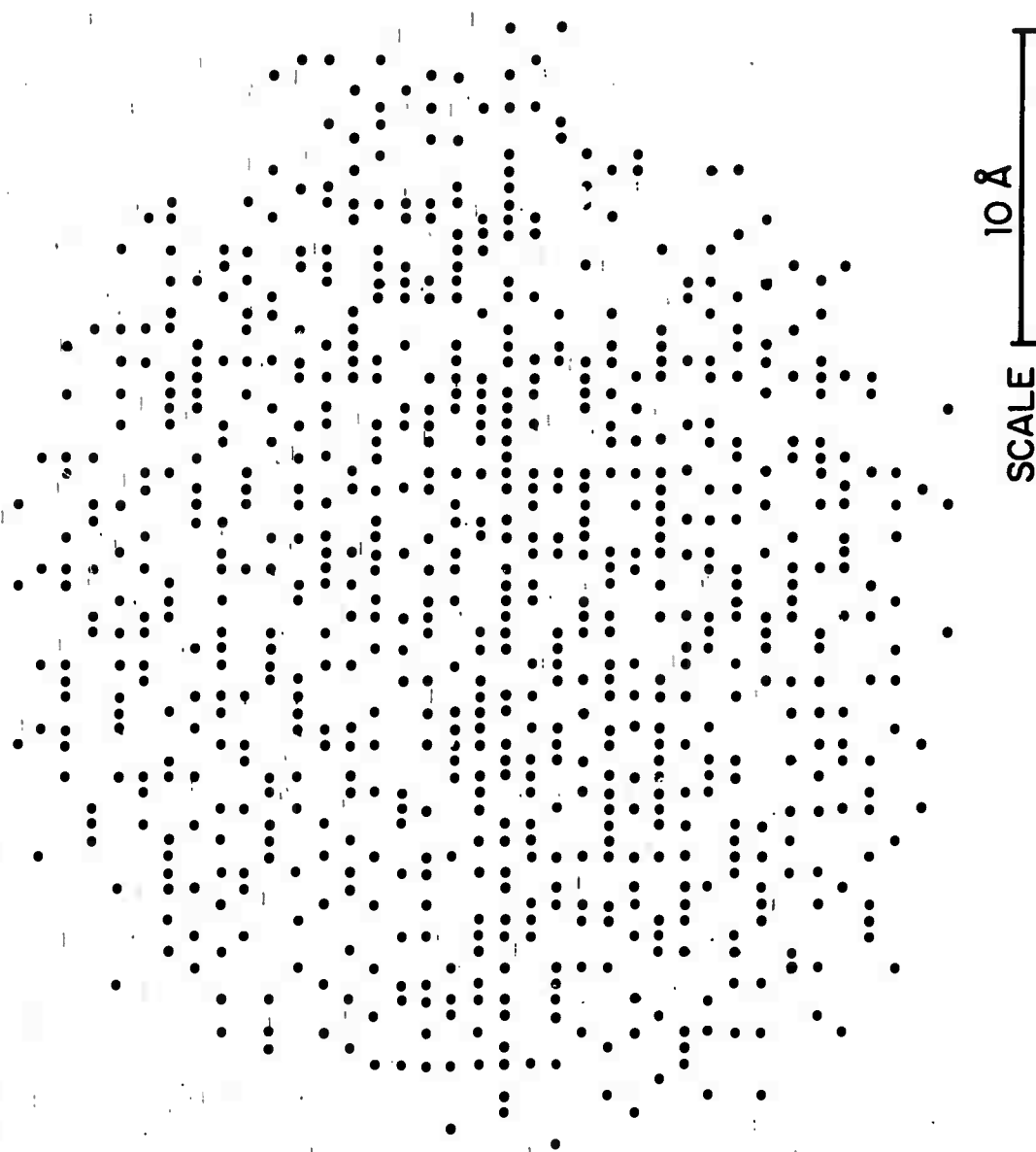
FIG. 7-3(c) CLUSTER OF 1000 ATOMS

the search routine by preventing the adatom from making the same mistake twice. Nevertheless, we feel that this computational difficiency may not drastically affect the results.

If the adatom fails in all of these attempts to satisfy the **parent** bond, the parent bond is left unsatisfied or dangling, and the adatom moves to a new parent bond and likewise attempts to satisfy the new parent bond and any neighboring bonds. However, the bond that has been left dangling may yet be satisfied by serving as a nearest neighbor bond for other adatoms connected to neighboring atoms.

6. Scheme II

As in Scheme I, the adatom initially approaches the cluster and, disregarding the bonding criteria, makes a single bond with the parent atom. However, in Scheme II, the adatom is permitted to search more thoroughly its environment than in Scheme I to see if it can further complete its, and its neighbors bonding requirements. In this scheme, the adatom first attempts to satisfy 3 bonds (the triple site), if unsuccessful, 2 bonds (the double site), and if still unsuccessful, 1 bond (the single site).

The primary difference between this scheme and Scheme I is that the dihedral angles are not specified at the outset. When the parent atom is attached to the cluster by only one bond, the parent atom is free to rotate itself about this bond to provide the adatom with an additional degree of freedom to help satisfy the local bonding. When the adatom suc-

cessfully bonds with neighboring atoms also that have only one cluster bond, these neighboring atoms are rotated so as to reduce the strain of the bonds made with the adatom. If a cluster atom already has two satisfied bonds, it is not permitted to rotate.

To illustrate the logic involved in this simulation, we trace through the decisions that an adatom must make with the aid of the logic flow chart in Figure 7-4. After the seed cluster has been generated, an adatom joins to a bond of an arbitrary surface atom (the parent atom), and then searches its local environment for its first and second nearest neighbors. The adatom does not count any other atoms that are attached to the parent atom as either the first or second nearest neighbors since forming a bond with these atoms results in a three membered ring, which is excluded as a possibility because of its excessive strain energy. The adatom then makes a series of attempts to satisfy the local bonding.

The adatom first attempts to bond with both its first and second nearest neighbors as well as the parent atom, thereby satisfying three bonds. If unsucessful, the adatom attempts to satisfy only one additional bond with first, the first nearest neighbor, and if unsuccessful, the second nearest neighbor. If the adatom is still unsuceessful, it has at this point two options.

If the parent atom has only one bond connecting it to the cluster, the parent atom rotates about this bond by 120°, thereby bringing the adatom into a different environment.
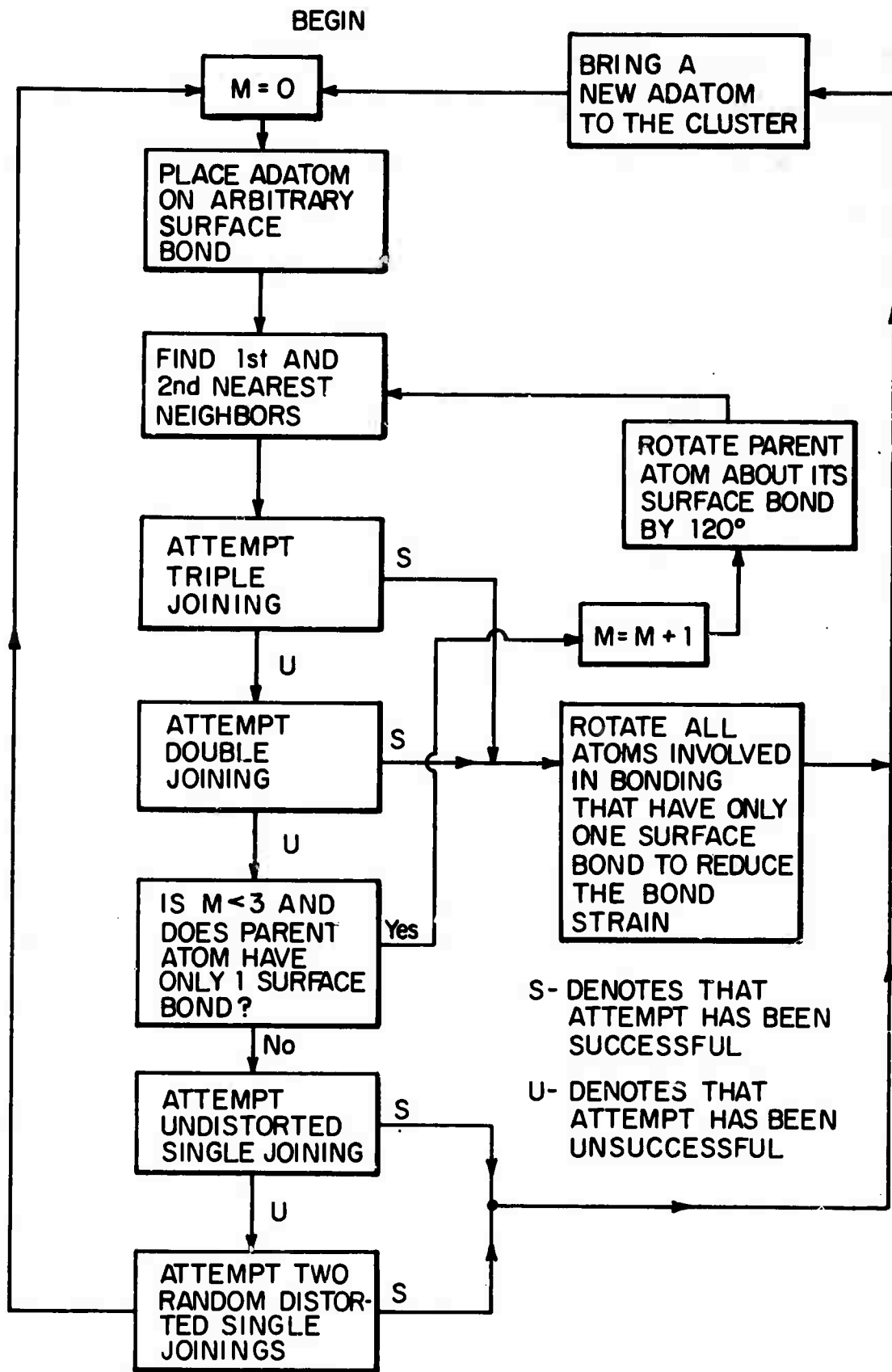
FIG. 7-4 SCHEMATIC OF LOGIC FOR SCHEME II DEPOSITION ROUTINE

The adatom again finds its first and second nearest neighbors and tries to form three, and if unsuccessful, two bonds as described above. If the adatom still is unsuccessful, the parent atom again rotates by 120°, and the adatom attempts to satisfy its bonding requirements as before.

There is nothing special about the 120° dihedral angle rotation increment. We can use different increments, but we feel that the 120° increment allows us to cover the entire dihedral rotation of 360° without losing anything significant that would be given by using a finer increment.

If the adatom still has not satisfied three or two bonds, it returns to its initial position, where it would have been if the parent atom were not originally free to rotate. Then the adatom attempts to satisfy just a single bond with the parent atom. It does this by first attempting the position associated with the undistorted equilibrium bond of the parent atom and if unsuccessful, it twice attempts the positions associated with randomly distorted bonds of the parent atom. If unsuccessful still, the adatom leaves this parent bond and moves to another unsatisfied bond on the cluster and goes through the same series of attempts as described above to satisfy this new bond.

7. The bonding sequence

In both schemes, we sequentially bring an adatom to every site available on the surface at least once, so the atoms are not added in a completely random fashion. In the real deposi-

tion process, where the many atom rearrangements are suppressed and the atoms arrive at the surface completely randomly at any point, there is the possibility that an adatom will not arrive at a bonding site before neighboring atoms have completed their bonds. In such a situation, the completed bonds on the neighboring atoms can make the uncompleted bond inaccessible for completion by oncoming adatoms, thus a void or dangling bond results. In this sense, the model deposition process may produce fewer voids than occur in the real solid.

C. Calculation of the statistical properties of the cluster

After each adatom has been sucessfully positioned on the cluster, the bond angles between the bond connecting the adatom to the parent atom, and the other satisfied bonds on the parent atom are caculated. The bond angles involving the bonds between the adatom and its nearest neighbors are not computed since it has been found that this requires excessive computer time to find the locations of the nearest neighbors of the nearest neighbor atoms, which are necessary to have in order to compute these bond angles. Nevertheless, the bond angles computed, we believe, do give an adequate sampling of the entire bond angle distribution.

For Scheme II, the dihedral angle between two atoms is taken to be equal to the angles defined between the two sets of three equilibrium bond directions on each atom as seen by viewing the two atoms along a common bond as in Figure 7-2 . Thus for each bond, one dihedral angle is calculated.

For Scheme I, no calculations of the dihedral angle distribution were made, however webelieve the resulting dihedral angle distributions to be centered about ϕ.

After the 1000 atomic positions are generated, the statistical properties, the density, RDF, and two dimensional projections of the cluster are computed. The density is computed by finding the number of atoms within a 14 $\overset{o}{A}$ and a 15 $\overset{o}{A}$ radii spheres centered about the origin for Schemes I and II respectively. These radii have been chosen to be somewhat less than the radius of the cluster so as to avoid surface effects. Typically there are 450 -500 atoms in these spheres.

For Scheme I, the RDF is calculated by finding the average of the RDF's calculated from all centers lying within a sphere of 7 $\overset{o}{A}$ radius centered about the origin, which typically contains 60- 70 sites. For Scheme II, the sphere is taken to have a radius of 8 $\overset{o}{A}$ and usually contains about 90 sites. More explicitly, the RDF is given by:

$$RDF(r) = \frac{1}{N} \sum_{i,j} \delta(r - r_i - r_j)$$

where N is the number of atoms in the inner sphere, i extends over only those atoms in the inner sphere, and j extends over all the atoms within the cluster.

For Scheme I the RDF is smoothed as follows. First the F(k) is computed from the formula:

$$F(k) = \int_0^{10} (RDF(r) - 4\pi\rho_0 r^2) \frac{\sin(kr)}{r} dr$$

where ρ_0 is the average atomic density of the cluster computed as described before. The RDF's which are to be presented for Scheme I have been found by invering back the $F(k)$ via the formula:

$$RDF(r) = 4\pi r^2 \rho_0 + \frac{2r}{\pi}\int_0^{15} F(k) \sin(kr) dk$$

The upper limit on the integral has been taken to be 15 $\overset{o}{A}^{-1}$ since this is the same upper limit employed in the collection of the experimental data presented in Chapter 5. We present this transformed RDF rather than the histogram RDF since it is easier to compare with the experimental RDF, which contains both phonon and Fourier broadening. Moreover, this inversion process also tends to average out the statistical fluctuations inherent in a model of this size. Figure 7-5 shows that the inverted RDF faithfully reproduces the essential features of the exact histogram RDF.

D. Results and discussion of Scheme I

The clusters for both Scheme I and Scheme II grow at a rate of 20 atoms per second on a Xerox Sigma Seven Computer. The cluster grows approximately spherically as is shown in Figures 7-3 (a-c) when it consists of 250, 500, and 1000 atoms respectively. These figures are
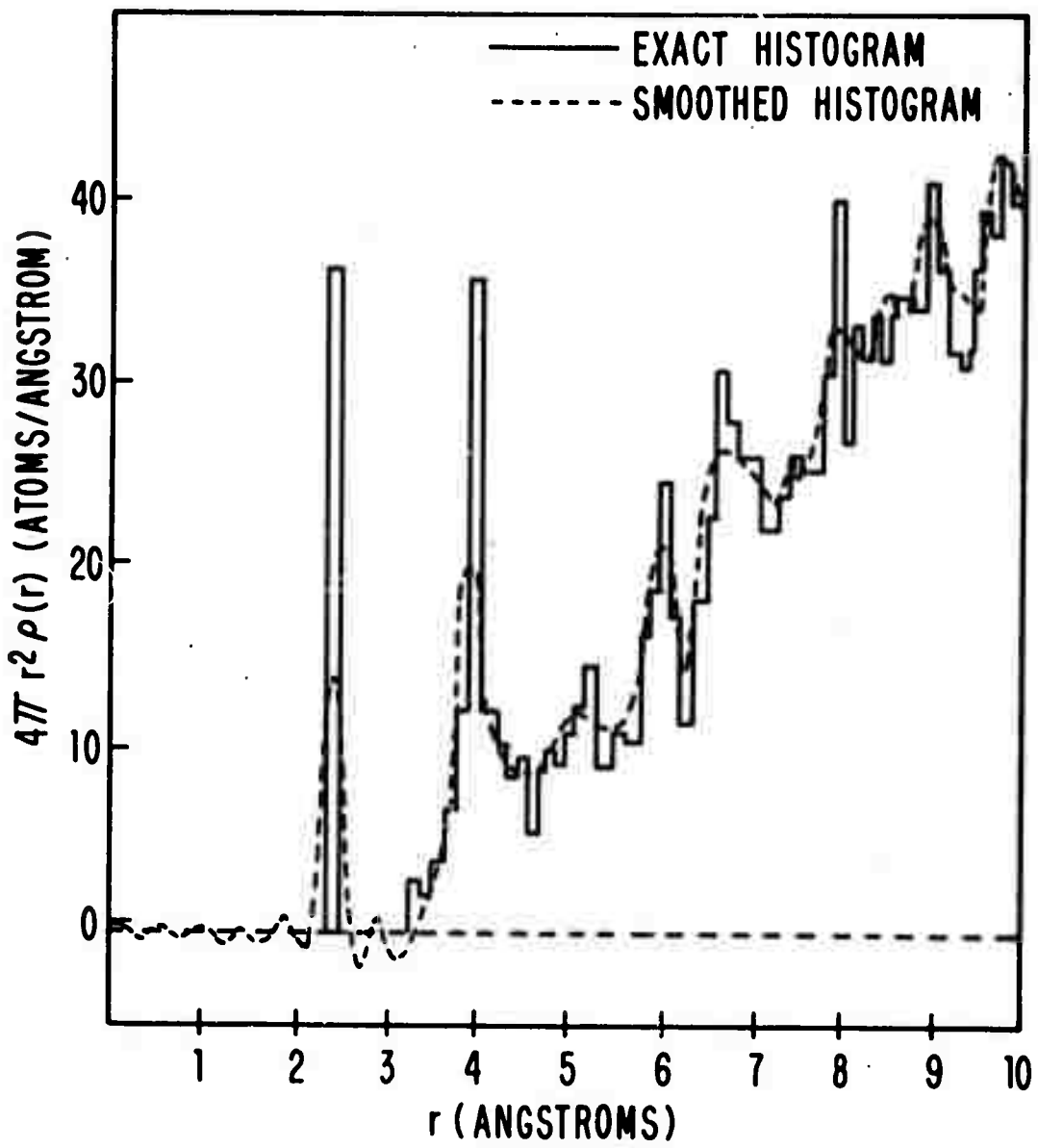
FIG. 7-5 COMPARISON OF HISTOGRAM RDF WITH SMOOTHED HISTOGRAM RDF.

two dimensional projections of the atomic coordinates which have been produced with the computer line printer, so that the accuracy of each point is only 0.5 $\overset{o}{A}$. It has been found that the cluster grows to a radius of about 18 to 19 $\overset{o}{A}$ and the center of mass never deviates by more than 1 $\overset{o}{A}$ from the origin.

With all of the Scheme I RDF's to be presented, the RDF of electrodeposited Ge is also included for sake of comparison .

Shown in Figure 7-6 is the crystalline RDF generated by Scheme I by restricting the bond angle fluctuations to zero and ϕ to the staggered configuration. We again note that the most striking difference between the experimental RDF and the crystalline is the lack of a peak at the third crystalline neighbor distance.   Now we will examine how the RDF changes as ϕ varies from the diamond-like staggered configurations to the amorphon-like eclipsed configurations.

For $\phi = 60^{o}$, corresponding to the staggered configuration, the RDF in Figure 7-7 shows that some of the crystalline peaks do persist (compare with Figure 7-6). The density deficit is 3.2%, the rms bond angle uncertainty is 9.65^{o} and the coordination number is 3.96 atoms; however, the persistence of a peak at the third crystalline neighbor distance rules out this structure from representing the observed form of amorphous Ge.

For ϕ 30° away from the crystalline dihedral angle, midway between the staggered and the eclipsed configurations,
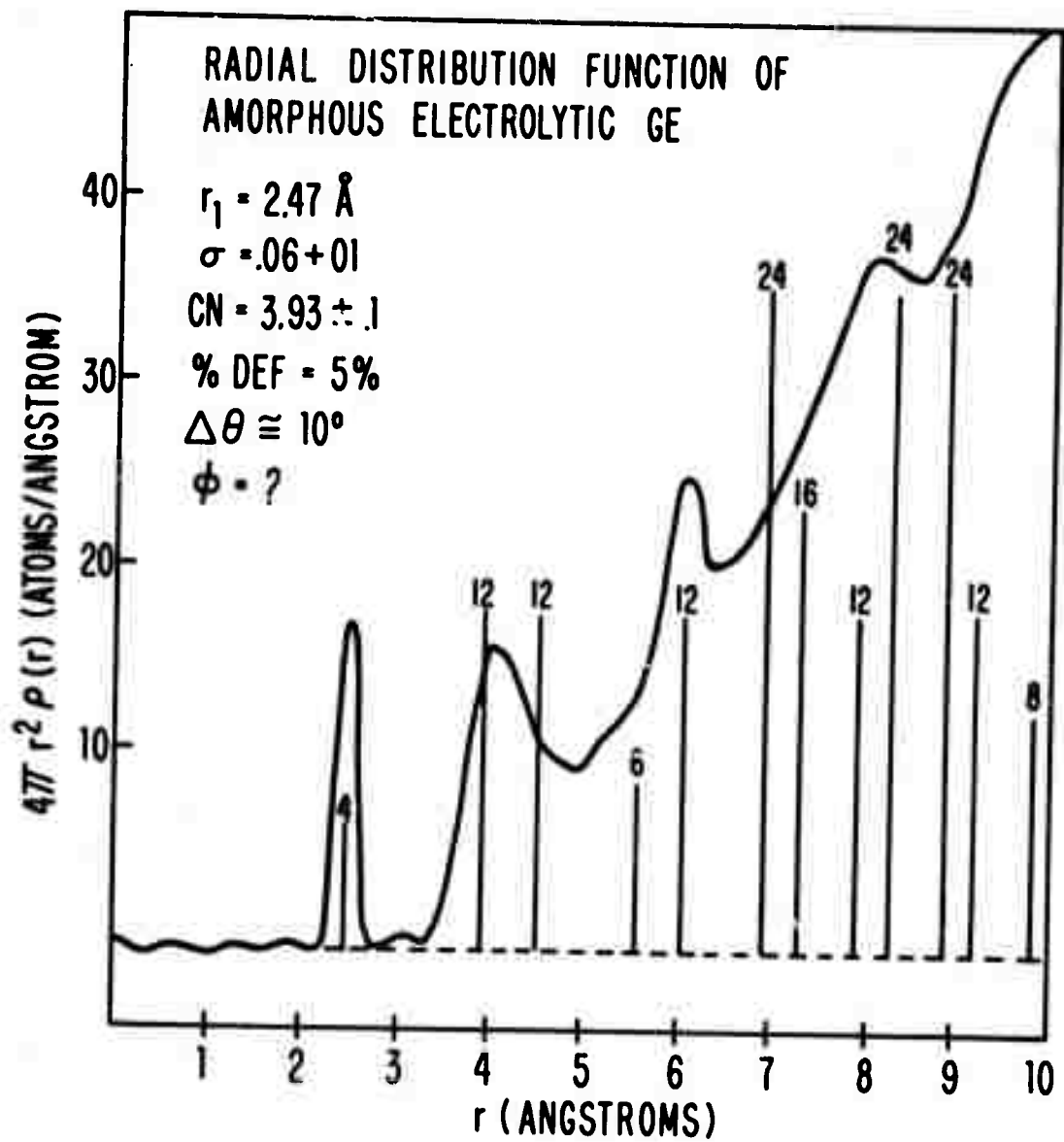
FIG. 7-6   CRYSTALLINE RDF GENERATED BY SCHEME I COMPARED
WITH   EXPERIMENTAL RDF OF AMORPHOUS ELECTRO-
DEPOSITED Ge.
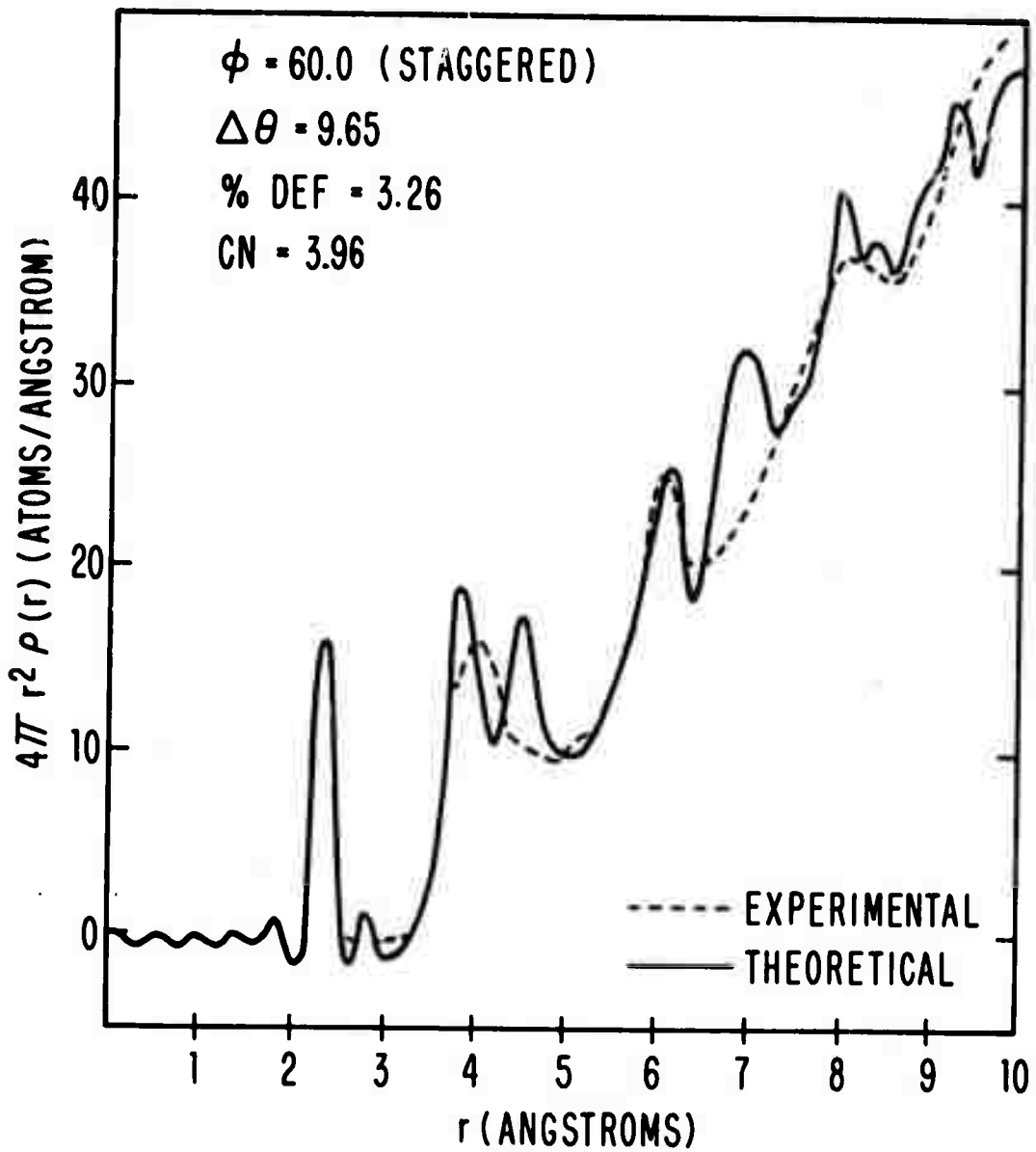
FIG. 7-7 RDF GENERATED BY SCHEME I WITH ϕ = 60°

new distances uncommon to the crystalline RDF appear, as is shown in Figure 7-8. The density deficit is 2%, the rms bond angle uncertainty is 8.8° and the coordination number is 3.92. In particular, we note the absence of a peak at the third crystalline neighbor distance and the appearance of peaks at 5.1 Å and 6.7 Å.

For ϕ 60° away from the crystalline value, which is the eclipsed configuration, the most ordered of all structures occurs (see Figure 7-9). In addition to the peaks at 2.45 Å and 3.9 Å, very strong peaks occur at 5.5 Å and 7.8 Å. These peak positions happen to be the positions associated with the undistorted amorphon; hence, to a degree, the formation of amorphons is taking place. We cannot at this time say whether entire closed amorphons are being formed, but at least several five membered rings must be linked up to explain the strong peak occurring at 7.8 Å. This RDF has a shape which is strikingly similar to the experimental RDF, but unfortunately the third and fourth peaks are in the wrong positions.

Another point of interest is that the coordination number of this structure is near 4.0, with CN = 3.95, but the density deficit, 10%, is the highest for all the structures genenerated. This suggests that the density and the number of broken bonds are not necessarily related. As first recognized by Turnbull and Polk[12], structures containing a very high density of pentagonal rings must also enclose holes of about 4 Å diameter, resulting in a decreased den-
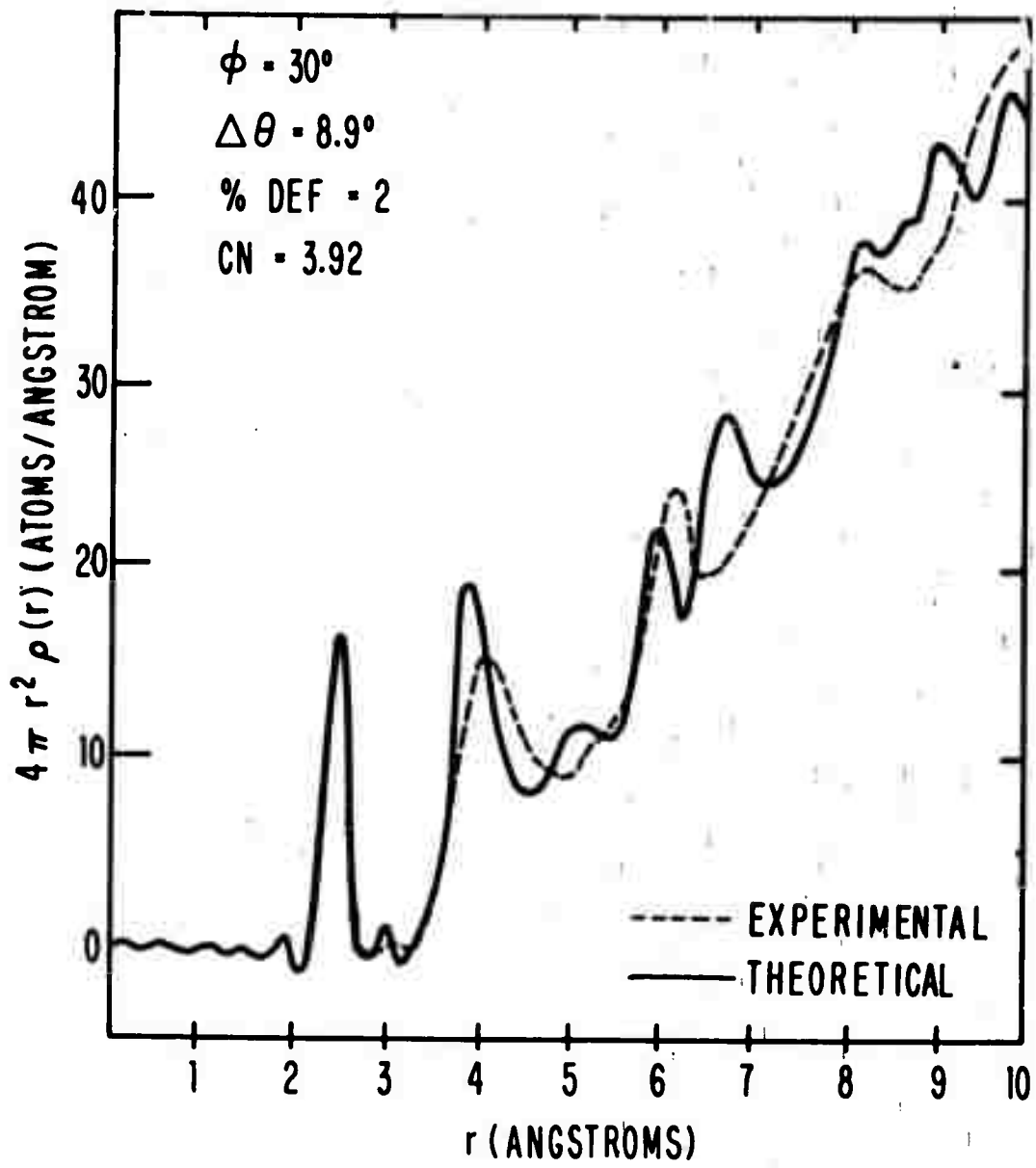
FIG. 7-8 RDF GENERATED BY SCHEME I WITH $\phi = 30°$.
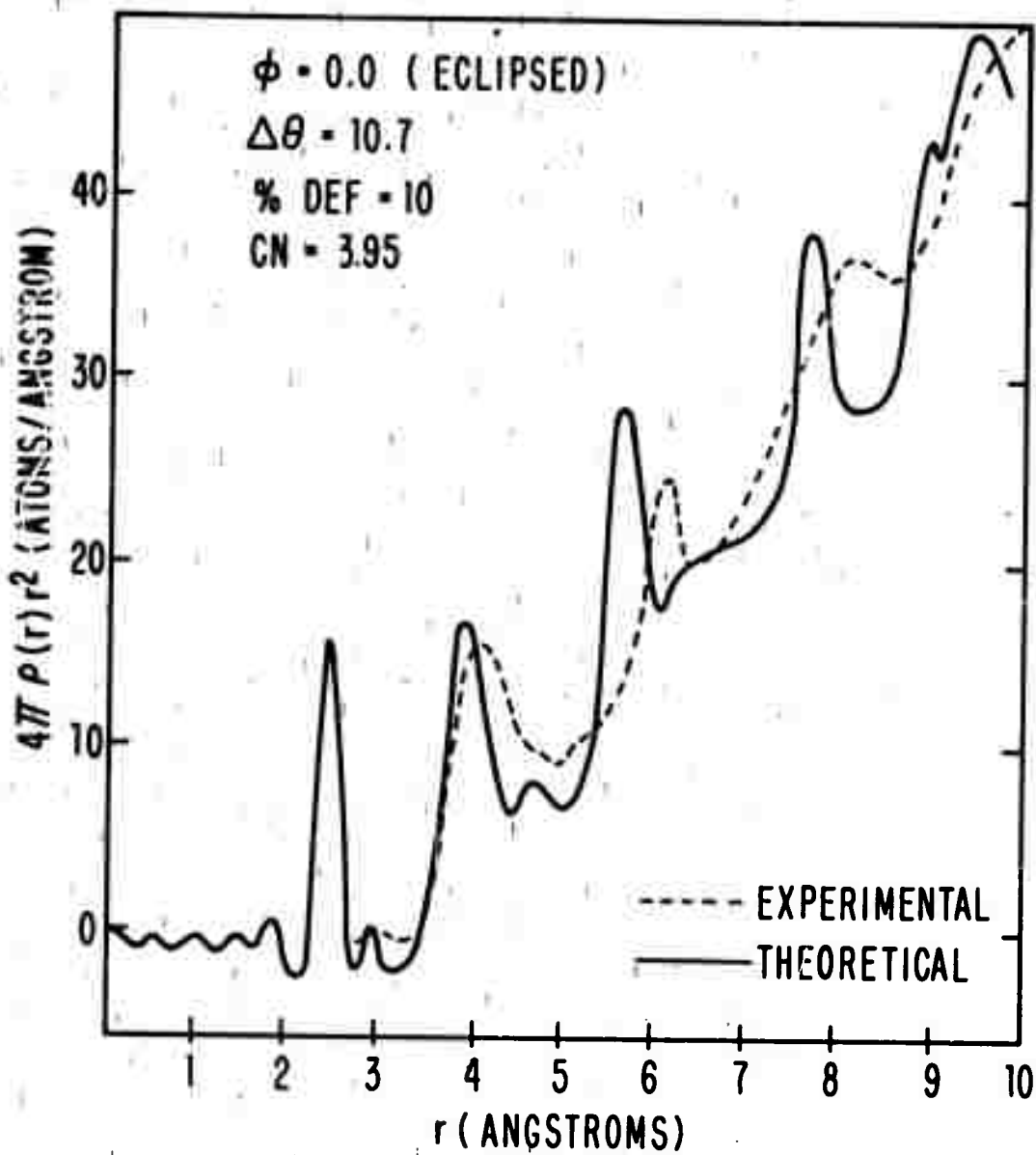
FIG. 7-9 RDF GENERATED BY SCHEME I WITH $\phi = 0°$

sity.   This observation has been substantiated here.

Next we generate a structure in which ϕ is a distri-
bution of values rather than a single value as in the other
runs. We randomly choose ϕ , after placing each atom, to
be either staggered of eclipsed with equal probabilities.
This in a rough way represents one of the structures that
has been suggested by Grigorovici and Manaila[2], in which
the staggered and the eclipsed configurations are intimately
mixed. Figure 7-10 shows that the fit to the experimental

RDF is unsatisfactory since the peak at 4.5 $\overset{o}{A}$, which is
associated   with the crystalline third neighbor, and the
peak at 5.5 $\overset{o}{A}$, which is associated with the amorphon third
neighbor, are not experimentally observed. This RDF also,
as one expects,bears some resemblance to the structure
built with ϕ midway between the staggered and the eclipsed
configurations. It appears that no combination of the
staggered and the eclipsed configurations can simultaneously
suppress the peaks occurring at 4.5 and 5.6 $\overset{o}{A}$.

Finally for Scheme I, ϕ is chosen after positioning
each atom to be any value between the staggered and the
eclipsed configurations. The resulting RDF shown in Fi-
gure 7-11 is in very good agreement with the experimental
RDF; even the peaks at 6.1 and 8.0 $\overset{o}{A}$ occur in this RDF.
However, the coordination number has fallen to 3.77 and the
density deficit has risen to 7 %.

ϕ = 50/50 RANDOM MIX
$\triangle\theta$ = 8.8
% DEF = 5.0
CN = 3.9

----- EXPERIMENTAL
—— THEORETICAL
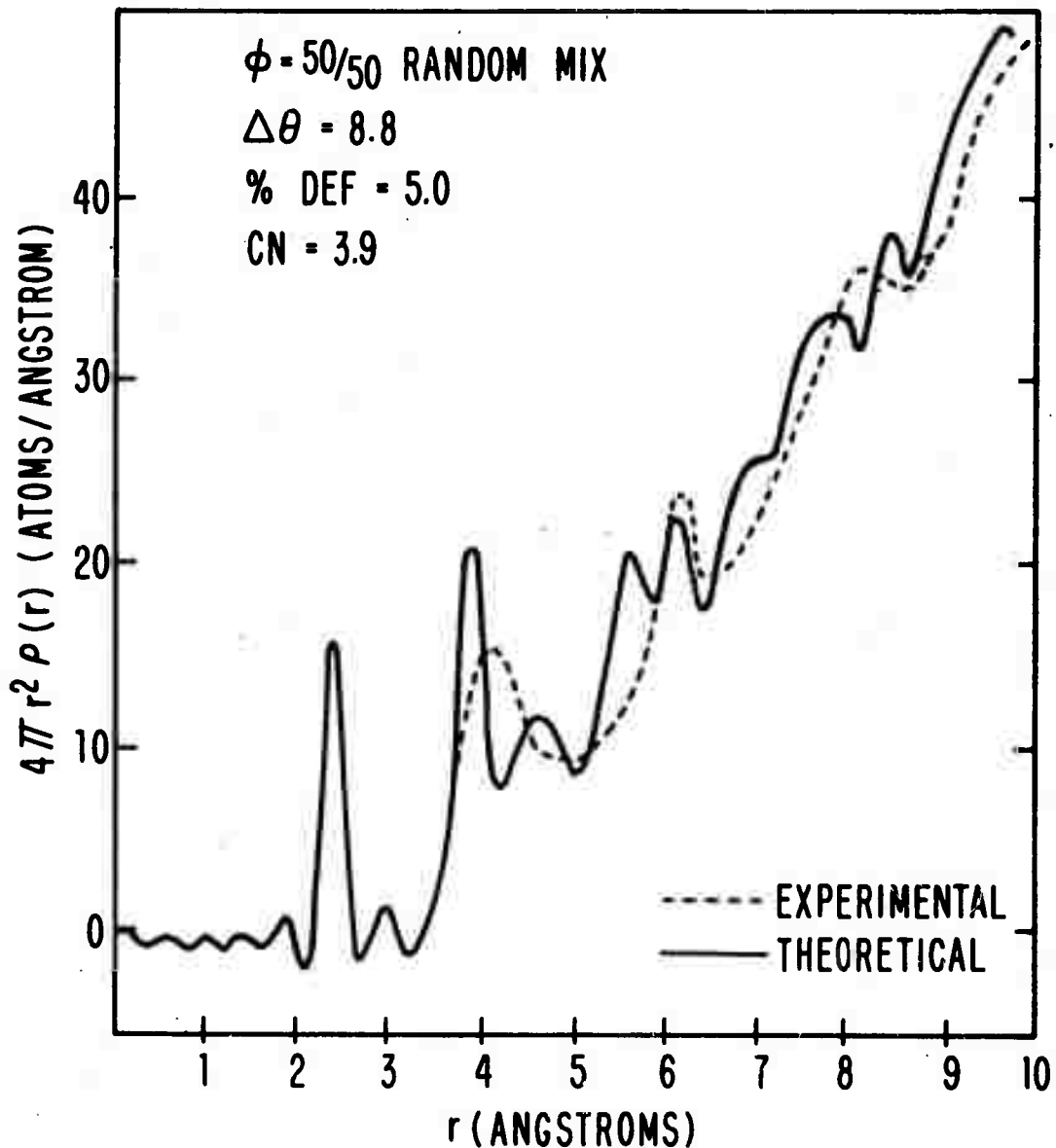
FIG. 7-10 RDF GENERATED BY SCHEME I WITH ϕ CHOSEN TO
BE EITHER STAGGERED OR ECLIPSED WITH EQUAL
PROBABILITIES.
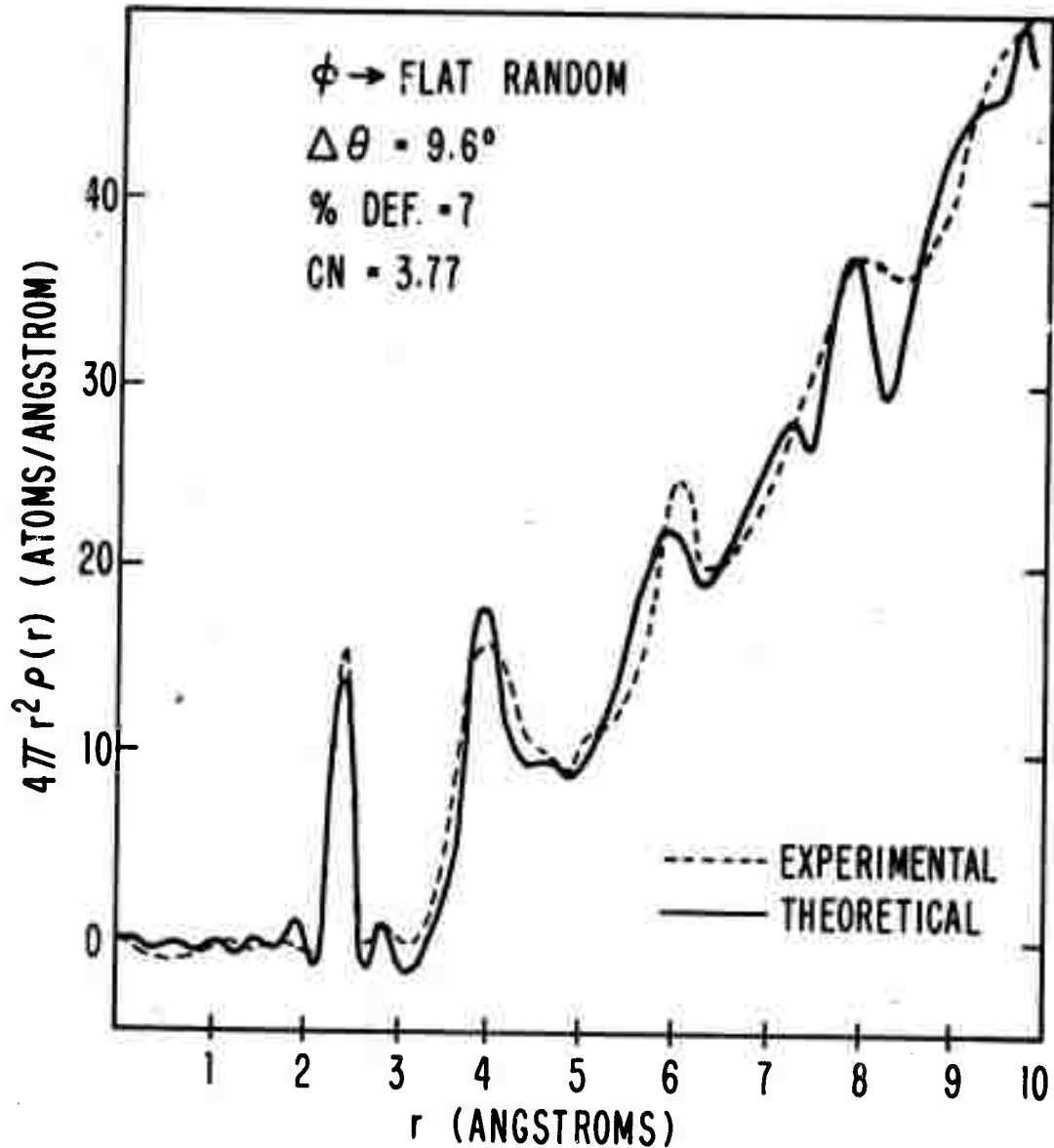
FIG. 7-11 RDF GENERATED BY SCHEME I WITH ϕ CHOSEN
TO BE ANY VALUE BETWEEN THE STAGGERED
AND THE ECLIPSED CONFIGURATIONS WITH
EQUAL PROBABILITIES.

Figure 7-12 shows a typical bond angle distribution

for the structures generated by Scheme I. All look very much

much the same with a large peak at the origin and the

number of bonds falling off roughly linearly with $\Delta\theta$.

Since the rms bond angle distortion has been found to be

about the same for all of these structures, the energies

of these structures may not be so different. This suggests

that the real solid may have several different structural

possibilities to choose from, and hence, the deposition

conditions may be important in determining in which struc-

ture the atoms will arrange themselves.

E. <u>Results and discussion of Scheme II</u>

Figure 7-13 shows that the RDF resulting from Scheme

II fits the experimental PDF even better than any of the

RDF's resulting from Scheme I. We note that in particular,

the peaks at 6.1 and 8.0 $\overset{o}{R}$ are well fitted. The average

coordination number of the 90 atoms in the inner sphere

about which the RDF has been calculated is 3.80, and hence,

about 5% of the bonds are broken. For the innermost 500

atoms, the number of broken bonds is about 8%, suggesting

that if the structure were indefinitely extended, about

5-8% of the bonds would be broken.

The number of second nearest neighbors, found by taking

twice the area under the RDF from 3.2 to 4.0 $\overset{o}{R}$, is 11.6

which further indicates that the basic tetrahedral unit is
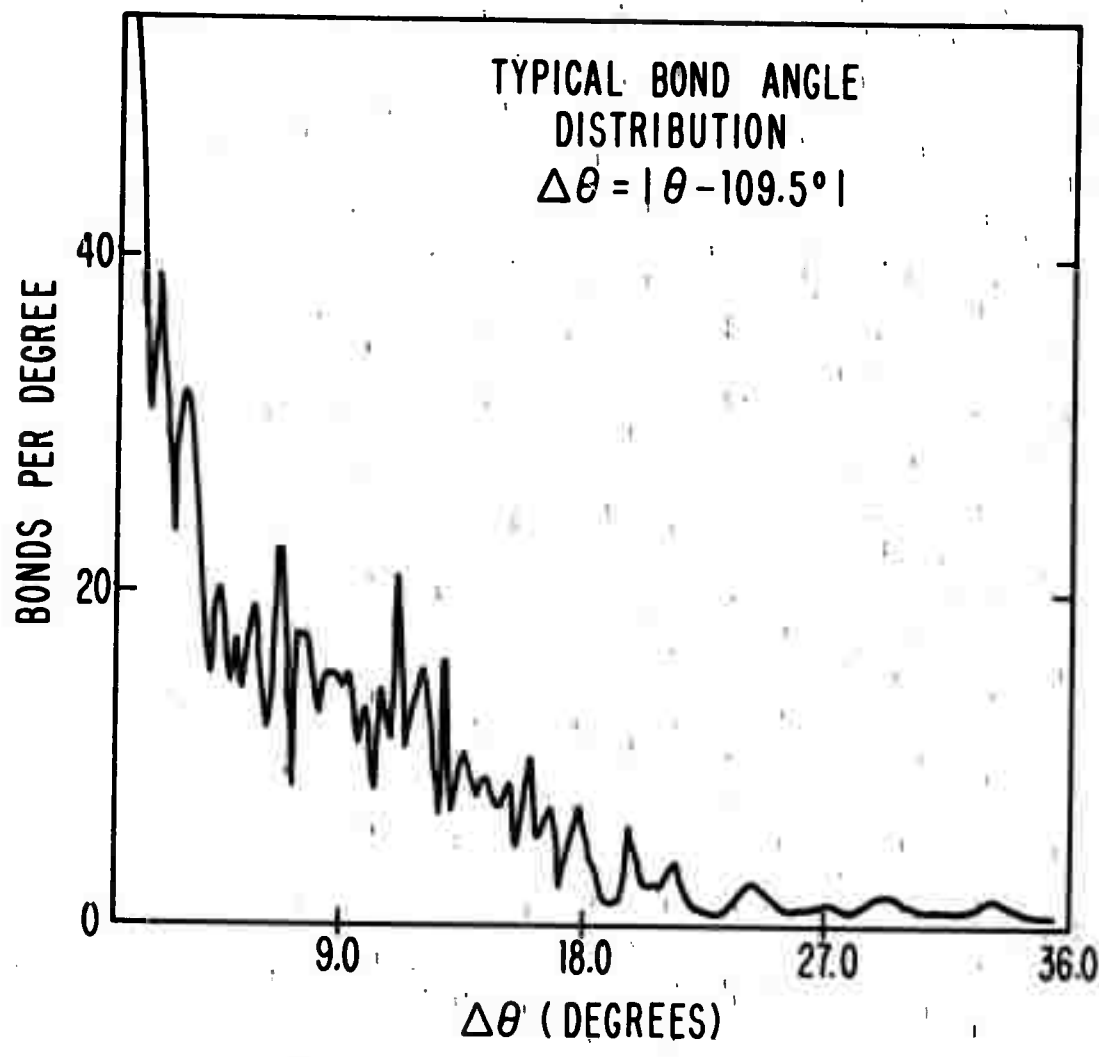
FIG. 7-12 TYPICAL BOND ANGLE DISTRIBUTION OF STRUCTURES GENERATED BY SCHEME I.
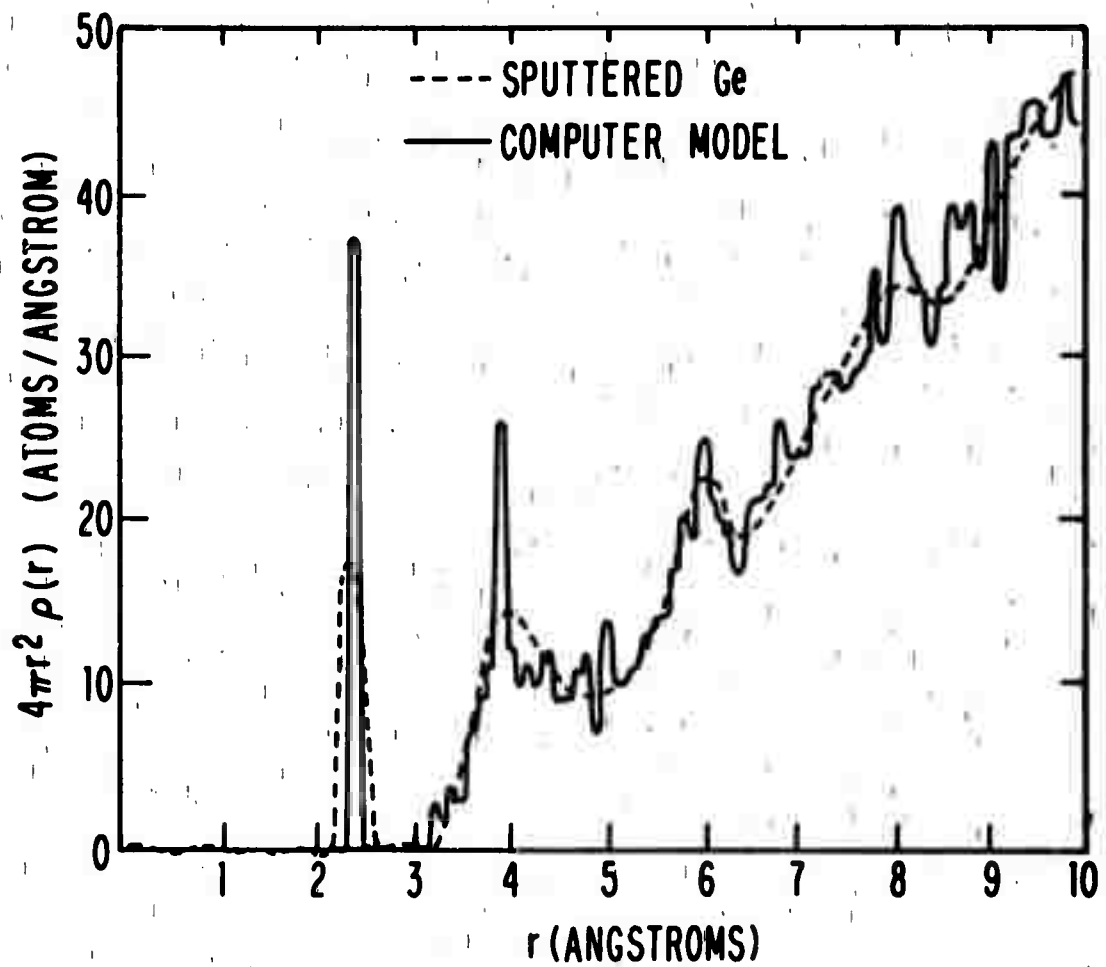
FIG. 7-13 RDF GENERATED BY SCHEME II COMPARED WITH
RDF OF AMORPHOUS SPUTTERED Ge
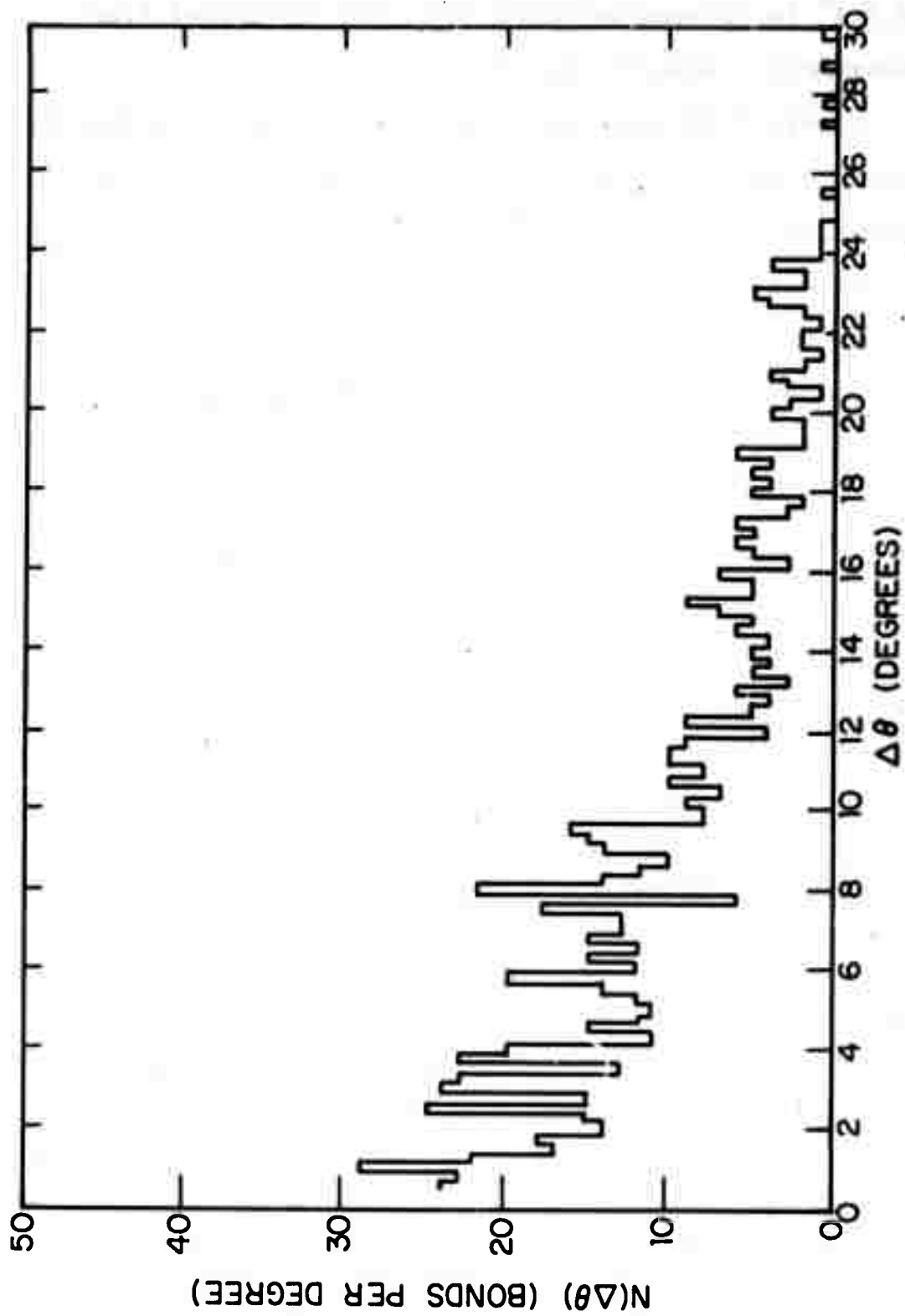
FIG. 7-14 BOND ANGLE DISTRIBUTION OF STRUCTURE GENERATED BY SCHEME II.

well preserved. The rms spreading of the bond angle of 9.9° is in good agreement with that estimated from experiment. (see Chapter 5)

Figure 7-15 shows that the dihedral angle distribution of the cluster is flat, as has been suggested from the results of Scheme I and from the experimental RDF in Chapter 5. However, it may be possible that there is no connection between the structures of Scheme I and II except that statistically they are the same. However, the results of Scheme I have at least suggested that it is a necessary condition that the dihedral angle distribution be flat in order that the RDF agree with experiment. This contention concerning the flatness of the dihedral angle distribution is further substantiated by this Scheme II where no constraints are put on the dihedral angles.

The density deficit of the inner sphere is 3% and the deficit of the outer sphere is 11%. The density deficit of the outer sphere, we believe, represents a good upper bound on the density deficit for the ideal amorphous Ge. Since not all of the bonds have been satisfied, it is believed that the density can be made even higher with a more sophisticated routine that can more completely satisfy the bonding. We believe that such a routine would have to abandon the one atom approximation and would have to tear down and reassemble
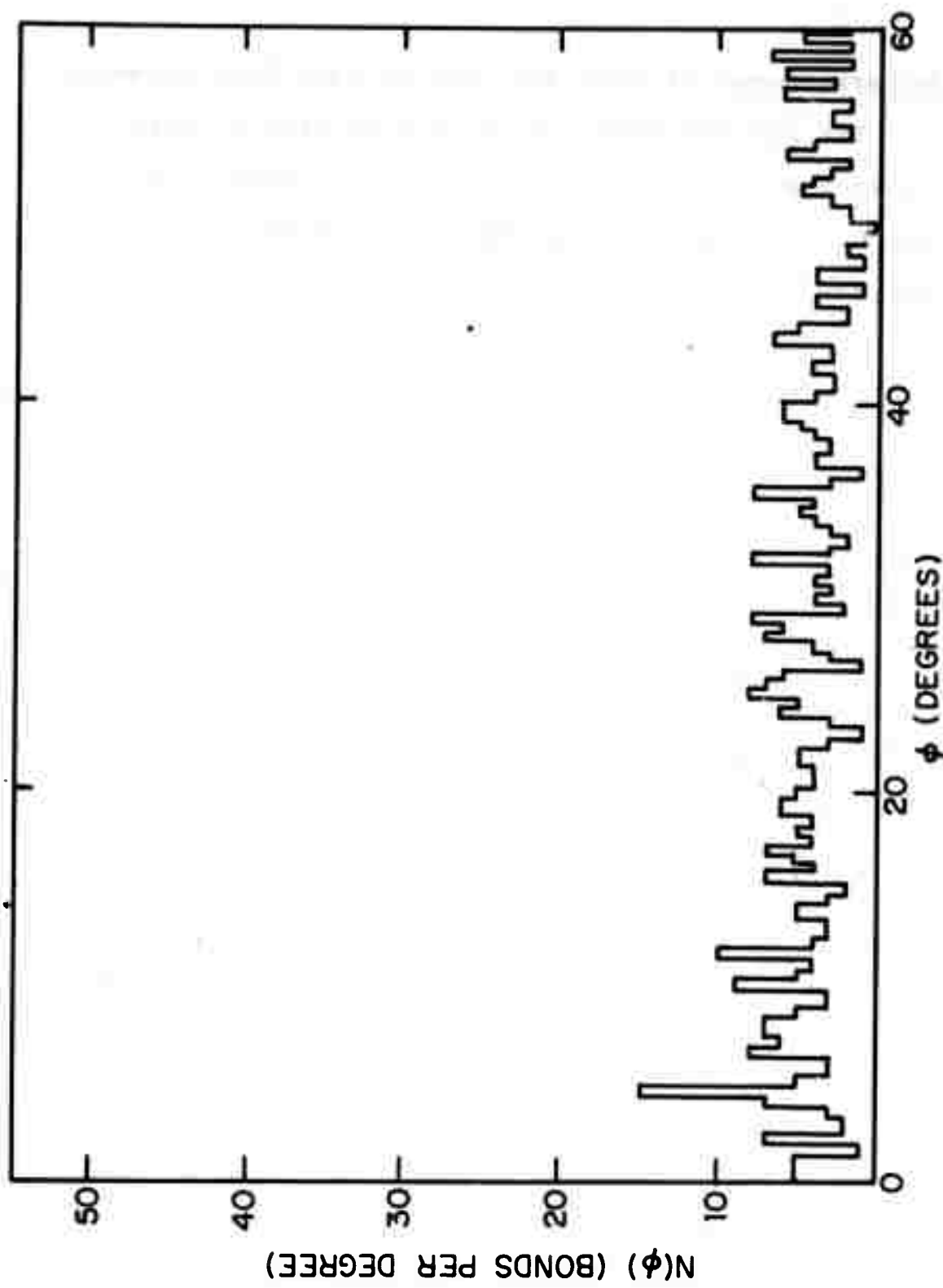
FIG. 7-15 DIHEDRAL ANGLE DISTRIBUTION OF STRUCTURE GENERATED BY SCHEME II.

any arrangement of atoms that had too many dangling bonds.

The ring statistics for this model have not been computed since with the computer space available, this requires a considerable amount of computation time with the program in its present form.

It still remains puzzling why the peaks at 6.1 and 8.0 $\mathring{A}$ persist even though the dihedral angle distribution is flat, Richter and Breitling[13] have suggested that these are the distances associated with the undistorted zig-zag chains of Ge atoms, and that these are the distances least sensitive to the disorder. It may be that no structural unit is reoccurring, but these bumps merely represent a rise in the probability of certain distances within a random structure subjected to the constraints on the bond lengths and angles.

Under the constraints imposed on the bond angle distortions in this simulation, the fractions of single, double, and triple sites which the adatom finds are .45, .50, and .05 respectively. Since the bond angle limitations imposed on the generated structure are close to those observed experimentally, we expect these fractions to roughly represent the fractions of such sites that the real adatom encounters on the surface for deposition temperatures near room temperature.

Despite the success of the routine in fitting the RDF, it is still lacking in some respects. The large numbers of broken bonds may make this model inadequate for use in

calculations of the electronic properties, since we expect the structure of real materials deposited near room temperature to have far fewer than 5-8% broken bonds. However, we may expect materials deposited at very low temperatures, where all movement is suppressed, to have large numbers of broken bonds and to be more accurately described by this model. Nevertheless, the model even in its present crude form does show that the continuous random network model fits the gross structure in the RDF, even at high r values.

F. Summary and Conclusions

We believe that this investigation has at least shown that computer modeling of the deposition process to obtain the structure of amorphous Ge is both practicable and feasible.

The most important result of this investigation is that the RDF of the computer generated structure of Scheme II fits not only the first two peaks in the experimental RDF, as does Polk's model, but also fits all the major peaks occurring up to $r = 10$ Å, thus more convincingly demonstrating the correctness of the continuous random network models for tetrahedrally coordinated semiconductors. The details of this Scheme II structure are:

1) The distribution of the nearest neighbor separations is a delta function occuring at the crystalline interatomic separation.

2) The distribution of the bond angles has an rms spread of $\pm10^{\circ}$, with a cut off at about 30°.

3) The distribution of the dihedral angles is flat. (Polk also has suggested that his model has a flat distribution)

4) The density is at least within 10% of the crystalline value.

Also we can draw some conclusions about the real deposition process. We have shown that structures built with the one atom approximation can adequately fit the experimental RDF, suggesting that many atom rearrangements are unimportant in determining the gross structure of amorphous Ge. Since the Scheme II RDF fits the experimental RDF the best, we conclude that the dihedral rotations are unrestrained as described in the text.

We have also found that as long as we permit a $0-30^{O}$ bond angle distortion, several other structures can be generated that, although not entirely in agreement with the experimental RDF's, at least are in agreement with the observed density and coordination number. These results suggest that the amorphous structure may not/well defined even in a statistical sense, and that under different deposition conditions or with atoms having some restrictions on the dihedral angles, various structures may emerge.

REFERENCES

1. D.E. Polk, J. Non-Cryst. Solids $\underline{5}$, 365 (1971)

2. R. Grigorovici and R. Manaila, Thin Sol. Films, $\underline{1}$, 343 (1967)

3. R. Kaplow, T.A. Rowe, B.L. Averbach, Phys. Rev. $\underline{168}$, 1068 (1968)

4. D. Henderson and F. Herman, J. Non-Cryst. Solids, (1972) (in the press)

5. D. Henderson, (private communication and to be published)

6. C. Bennett, Ph.D. Thesis, Harvard University, 1971

7. J.L. Finney, Ph.D. Thesis, Univ. London, (1968)

8. G.S. Cargill III, J. Appl. Phys. $\underline{41}$, 2248 (1970)

9. D. Weaire, (private communication)

10. M.L. Rudee, Phys. Stat. Sol. (b), $\underline{46}$, (1971) kl

11. L. Pauling, Nature of the Chemical Bond, Third Edition Cornell Univ. Press (1961)

12. D, Turnbull and D.E. Polk, J. Non-Cryst. Solids (1972), (in the press)

13. H. Richter and G. Breitling, Z. Naturforschg. $\underline{13a}$, 988 (1958)

APPENDIX I

COMPTON DOWNSCATTERING CORRECTIONS

In radial distribution analysis, small corrections in the experimental scattered x-ray intensity become important when the data are extended to high k values, where not only does the intensity fall, but so does the relatives magnitude of the information carrying oscillations. These corrections become particularly crucial when the high angle normalization method is used, since important quantities of the radial distribution function, such as the density and coordination number depend directly on the accuracy of the normalization.

Use of a crystal monochromator does not guarantee that Compton processes at high angle can be neglected. Although the monochromator is effective in removing the Compton scattering produced by the energy band to which it is tuned, it is relatively ineffective in removing Compton scattered radiation produced from the high energy shoulder of the incident beam, since some of the Compton scattering produced by the high energy shoulder can lie in the monochromator band pass.

An estimate of the "Compton downscattering" contribution to the observed intensity necessitates knowledge of $E(\lambda)$ the intensity as a function of wavelength of the incident beam. The incident beam wavelength profile can in general be approximated, as is shown in Figure I-1, by a sharp peak of height E_o and of width $\Delta\lambda_o$, and a flat shoulder lying at wave-
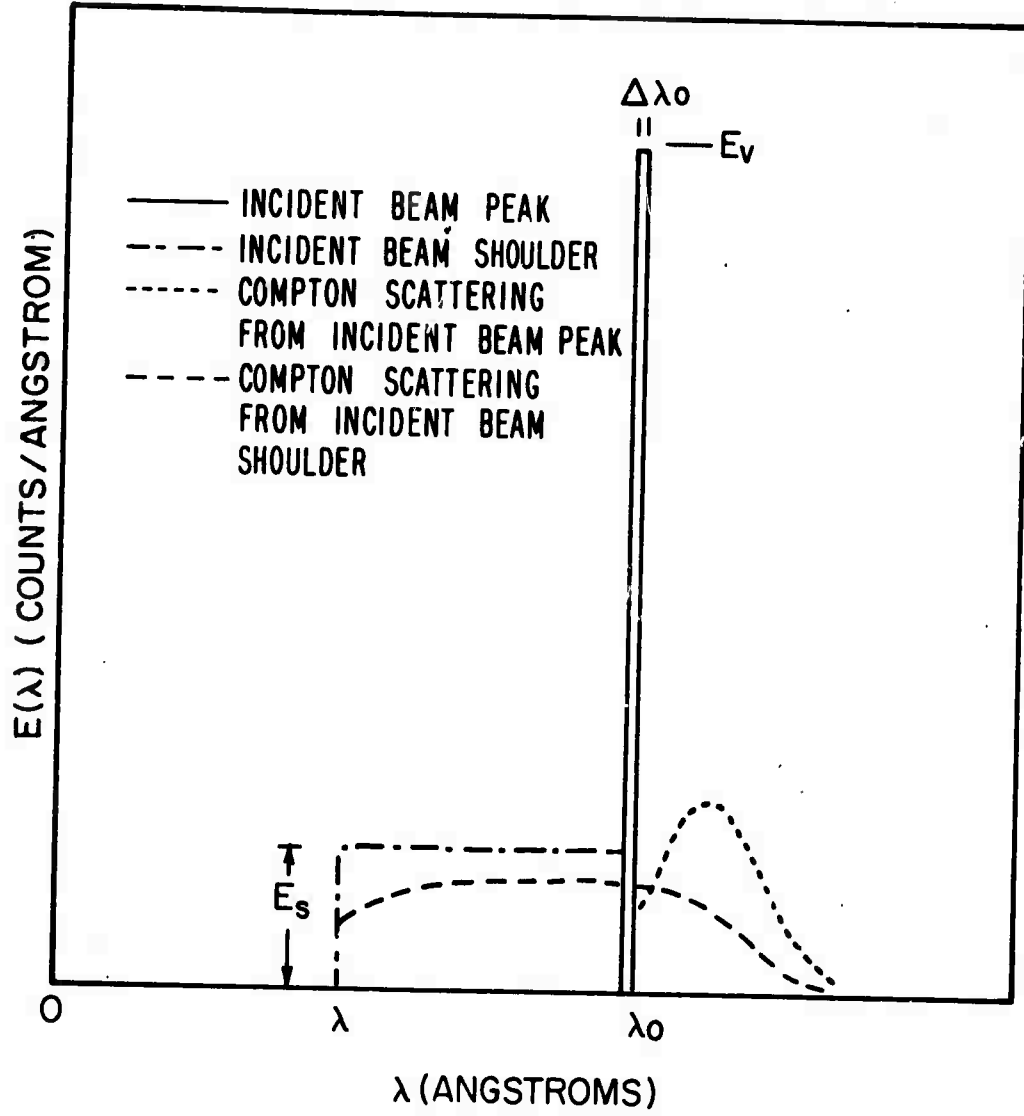
FIG. I-1   THE INCIDENT BEAM AND COMPTON
SCATTERED WAVELENGTH PROFILES

lengths shorter than λ_o with a height E_s. We ignore the part of the continuum that lies at longer wavelengths, since we do not expect the Compton scattering produced in this range to pass through the monochromator. In normal diffraction experiments, λ_o is the wavelength, usually a characteristic line in the x-ray spectrum, to which the monochromator is tuned. The shoulder has a cut off at λ_1 which arises from either a cutoff in the excitation energies of the electrons incident on the anode of the x-ray tube, or from the use of a metal filter in the incident beam.

Following Ruland,[1] the Compton profile, i.e., the distribution in wavelengths of the modified scattered radiation, produced by a delta function incident beam of wavelength λ' can be represented by a profile function of form:

$$\frac{1}{\Delta\lambda}\ h\ (\frac{\lambda-\lambda'-\Delta\lambda c}{\Delta\lambda}) \qquad \text{for} \quad \lambda > \lambda' \tag{I-1}$$

$$O \qquad \text{for} \quad \lambda < \lambda'$$

where $\Delta\lambda c$ is average change in the photon wavelength and $\Delta\lambda$ is the width of the Compton profile.[1]

Note that this distribution is zero for wavelengths less than the incident beam. This is because it is unlikely from conservation of energy to have a photon scattered with an energy more than a few electron volts greater than the incident photon energy in x-ray scattering.

We take the distribution to be normalized so that

$$\frac{1}{\Delta\lambda}\ \int_{-\Delta\lambda c}^{\infty} h(\frac{u}{\Delta\lambda})du\ =\ \text{finc}(k) \tag{I-2}$$

where $f_{inc}(k)$ is the Compton scattering factor for the material under investigation and k is the total momentum transfer between the incident photon momentum and the scattered photon momentum.

The total Compton intensity per unit wavelength downscattered from the white radiation shoulder is given by:

$$E_{CD}(\lambda_0) = E_S \int_{\lambda_1}^{\lambda_0} \frac{1}{\Delta\lambda} h(\frac{\lambda_0 - \lambda' - \Delta\lambda c}{\Delta\lambda}) d\lambda' = E_S \int_{-\Delta\lambda_c}^{\lambda_0 - \Delta\lambda c - \lambda_1} \frac{1}{\Delta\lambda} h(\frac{u}{\Delta\lambda}) du$$

$$(I-3)$$

For any profile function which decays with wavelengths away from the center of the profile, and for which the integral has converged at the upper limit, the profile width and position are lost in the integration and we have the simple result that the total downscattered Compton radiation is:

$$E_{CD}(\lambda_0) = E_S f_{inc}(k) \qquad (I-4)$$

However, if the integral has not converged, such as in the case where $\lambda_0 - \lambda_1 - \Delta\lambda c \sim \Delta\lambda$, we can approximate the long wavelength side of the distribution with a Lorentzian. The total downscattered Compton intensity per unit wavelength becomes for $\lambda_0 - \Delta\lambda c - \lambda_1 > \Delta\lambda c$:

$$E_{cd}(\lambda_0) = E_S f_{inc}(k) \left\{ 1/2 + \frac{\tan^{-1}}{\pi} (\frac{\lambda_0 - \Delta\lambda c - \lambda_1}{\Delta\lambda}) \right\} \qquad (I-5)$$

The total observed downscattered intensity, $I_{CD}(k)$, is simply the downscattered Compton intensity per unit wave-

length times the monochromator band pass width, b or :

$$I_{CD}(k) = b \ E_{cd}(\lambda_0) \qquad (I-6)$$

The total Compton scatterd intensity by the peak at λ_0 is $f_{inc}(k) E_0 \Delta \lambda_0$, but the observed intensity is decreased by a factor $Q(k)$, the monochromator efficiency.[1] Hence, the total observed incoherent Compton scattered intensity is the sum of these two components, or:

$$I_C(k) = Q(k) \cdot E_0 \ \Delta \lambda_0 \ f_{inc}(k) + b \ E_S \ f_{inc}(k) \left\{ \frac{1}{2} + \frac{\tan^{-1}}{\pi} \ (\frac{\lambda_0 - \Delta \lambda_C - \lambda_1}{\Delta \lambda}) \right\}$$

$$(I-2)$$

which can be written in the more convenient form:

$$I_C(k) = E_0 \Delta \lambda_0 \ f_{inc}(k) \ (Q(k) + CD) \qquad (I-8)$$

where

$$CD = \frac{E_S \ b}{E_0 \ \Delta \lambda_0} \left\{ \frac{1}{2} + \frac{1}{\pi} \tan^{-1} (\frac{\lambda_0 - \Delta \lambda_C - \lambda_1}{\Delta \lambda}) \right\}$$

The net effect of this downscattering contribution is to make the monochromator less efficient by adding to $Q(k)$ an almost constant term, CD. As long as the band pass, b, is wider than $\Delta \lambda_0$, this contribution becomess smaller with decreasing b. If the incident beam is monochromatic, the downscattering does not enter; however, the loss in intensity required to make the incident beam monochromatic may not be worthwhile. In some cases it may be better to maintain the full intensity of a polychromatic incident beam and make

this correction to the data.

It has been the author's experience in RDF analysis of amorphous Ge to find that failure to make this correction leads to an undernormalization of about 5-10% and subsequently an F(k) which sags at intermediate k values.

REFERENCES

1. Ruland, W., Brit. J. Appl. Phys. (1964) 15, 1301

APPENDIX II

CONVERGENCE OF ITERATION PROCEDURE USED
IN COLLIMATION CORRECTIONS

We wish to show that the iteration given in Equation 4-29,

$$I_{SA}^{n+1}(y) = I_{SA}^{n}(y) + (I_{exp}(y) - M \cdot I_{SA}^{n}(y)) \qquad (II-1)$$

converges to the solution of

$$I_{exp}(y) = M \cdot I_{SA}(y) = \int_{0}^{\infty} K(u) I_{SA}(\sqrt{u^2 + y^2}) du \qquad (II-2)$$

where

$$\int_{0}^{\infty} K(u) du = 1 \text{ and } K(u) > 0 \text{ for } u > 0 \qquad (II-3)$$

A specific $K(u)$ has been used in Chapter 4, but here we show that all $K(u)$'s that satisfy the above criteria also allow this procedure to converge.

We take as our initial guess to the solution, $I_{SA}^{o}(y) = I_{exp}(y)$. We can write the initial guess as: $I_{SA}^{o}(y) = I_{SA}(y) + \phi(y)$, where $\phi(y)$ is the difference between the experimental intensity and the actual intensity. In general, the difference between the actual and the experimental intensity, $\phi(y)$ is a rapidly decreasing monotonic function. We shall exploit this fact in proving convergence.

Substituting the initial guess into Equation II-1 the iteration after n times gives the very simple result:

$$I_{SA}^{(n+1)}(y) = I_{SA}(y) + (1 - M)^{n} \phi(y) \qquad (II-4)$$

It suffices to show only that $(1 - M)^n \phi(y)$ tends to 0 as n increases.

Since $|\phi(y)|$ is a monotonic decreasing function and $K(u)$ is normalized to unity, we have the condition:

$$0 < \frac{M \cdot \phi(y)}{\phi(y)} = a(y) < 1$$

We can write in general:

$$(1 - M)^n \phi(y) = \prod_i^n (1 - a_i(y))^n \phi(y)$$

Since $0 < a_i(y) < 1$, then $0 < 1 - a_i(y) < 0$ for all $a_i(y)$ and hence, the above must tend to 0 as n tends to infinity. Also note that this term also goes to o if $\phi(y)$ is monotonically increasing such that:

$$2 > \frac{M(\phi(y))}{\phi(y)} > 1$$

and hence, the iteration procedure must also converge to the correct solution for $\phi(y)$ satisfying this condition. Combining these two results, the sufficient condition for convergence is:

$$0 < \frac{M(\phi(y))}{\phi(y)} < 2$$

APPENDIX III

CALCULATION OF THE THERMAL SPREADING

It is important that we know whether the spread in the near neighbor shells represents real static disorder or is merely thermal broadening. Since there does not exist a well established theory which treats vibrational modes in an amorphous solid, we must resort to calculations based on crystalline models, and hope that these results approximately apply to amorphous solids.

We can use Debye-Waller theory to get an estimate of the thermal spreading of the peaks in the experimental RDF's. The displacement of an atom at position r, away from its equilibrium position is given by

$$U_o = \sum_j \sum_k a_{kj} e^{ik \cdot r - i\omega_{kj}t} \epsilon_{kj} \qquad \text{(III-1)}$$

where k = the wave propagation vector of a phonon mode

$\quad j$ = the polarization mode of a phonon mode

a_{kj} = the amplitude of a phonon mode

ω_{kj} = the frequency of vibration of a phonon mode

ϵ_{kj} = the polarization vector of a phonon mode.

As shown by James[1] the mean square independent displacement of each atom about its equilibrium position is given by:

$$\langle U_o^2 \rangle = \sum_i \sum_j |a_{kj}|^2 = \frac{3\hbar^2}{mk_B\theta_m^2} T \qquad \text{(III-3)}$$

where θ_m = the Debye x-ray temperature

If we have atom o at the origin and atom i in shell i, the corresponding mean square thermal width of this shell observed in the RDF is given by

$$\sigma_i^2 = ((U_o - U_i(r))^2 = 2U_o^2(1-\gamma(r)) \text{ where } \gamma(r) = \frac{< U_o U_i(r) >}{U_o^2} \quad \text{(III-4)}$$

The term $1 - \gamma(r)$ denotes the degree of coupling that exists between the atom at the origin and the atom in shell i. For the first coordination shell we expect that $\gamma(r)$ is close to 1, but for shells far away we expect that the coupling tends to 0, and hence, the mean square width becomes equal to the sum of the independent motions of each atom.

Exact evaluation of the coupling is very complex, since it requires summing over the entire phonon spectrum. We can get an estimate of the coupling by evaluating it for a cubic monoatomic system.

For the simple monoatomic cubic crystal, assuming a spherical phonon zone boundary and an energy dispersion relation that goes as $\omega_{kj} = ck$, where c is a constant and using the relation $a_{kj} = \frac{2}{m} \frac{kT}{\omega_{jk}^2}$, the $\gamma(r)$ function becomes after integrating over the angles:

$$\gamma(r) = \frac{\int_0^{k_o} \frac{\sin(kr)}{kr} dk}{\int c \, dk} = \frac{1}{x_o} \int_0^{x_o} \frac{\sin(x)}{x} dx = \frac{S_i(x_o)}{x_o} \quad \text{(III-5)}$$

where $x = kr$, and $x_o = k_o r$

We choose $k_o = \frac{\pi}{r_1}$ so that it corresponds to the cut off

k value for a one dimensional chain with an interatomic distance r_1.

The function $Si(\pi x)/\pi x$ is plotted in Figure III-1. From it, we find that for the materials with distances found in the diamond cubic structures, the coupling term is 0.59 for the nearest neighbor shell, and 0.39 for the second neighbor shell; for shells lying beyond r greater than 4 interatomic spacings, the coupling drops to less than 0.1 so that the atoms in these shells are vibrating almost independently of the atom at the origin.

FIG. III·I   PLOT OF $\dfrac{Si(\pi x)}{\pi x}$